

DEVELOPMENT OF A NOVEL LASER-INDUCED SIDE  
TRANSFER PROCESS FOR BIOPRINTING

HAMID EBRAHIMI ORIMI

A THESIS  
IN  
THE DEPARTMENT  
OF  
MECHANICAL, INDUSTRIAL AND AEROSPACE ENGINEERING

PRESENTED IN PARTIAL FULFILLMENT OF THE REQUIREMENTS  
FOR THE DEGREE OF DOCTOR OF PHILOSOPHY  
CONCORDIA UNIVERSITY  
MONTRÉAL, QUÉBEC, CANADA

JANUARY 2022

© HAMID EBRAHIMI ORIMI, 2022

CONCORDIA UNIVERSITY  
School of Graduate Studies

This is to certify that the thesis prepared

By: **Mr. Hamid Ebrahimi Orimi**  
Entitled: **Development of a novel laser-induced side transfer process for bioprinting**

and submitted in partial fulfillment of the requirements for the degree of

**Doctor of Philosophy (Mechanical Engineering)**

complies with the regulations of this University and meets the accepted standards with respect to originality and quality.

Signed by the final examining committee:

_____	Chair
Dr. T. Popa	
_____	Thesis Supervisor
Dr. S. Narayanswamy	
_____	Thesis Supervisor
Dr. C. Boutopoulos	
_____	Examiner
Dr. R. Sedaghati	
_____	Examiner
Dr. J. Dargahi	
_____	Examiner
Dr. A. Bagchi	
_____	External Examiner
Dr. P. Gregorčič	

Approved by \_\_\_\_\_  
Dr. I. Contreras, Graduate Program Director

February, 11, 2022 \_\_\_\_\_  
Dr. M. Debbabi, Ph.D., Dean  
Faculty of Engineering and Computer Science

# Abstract

## Development of a novel laser-induced side transfer process for bioprinting

Hamid Ebrahimi Orimi, Ph.D.

Concordia University, 2022

Bioprinting technologies enable precise delivery of bio-inks for the fabrication of living constructs. An open challenge in the bioprinting field is to fabricate a vascular network. For this, ability to print a wide range of viscosity, micrometric printing resolution, negligible impact on the cell viability, high-speed and multi-scale printing are required. The current research aims to simulate, develop and validate a novel laser induced side transfer (LIST) technique for bioprinting. The method uses low energy nanosecond laser pulses to generate a transient microbubble inside a microcapillary that contains the bio-ink. Microbubble expansion results in the ejection of the bioink perpendicular to the irradiation axis. We presented a hybrid model to simulate the technique. We investigated the dynamics of the laser-induced bubble in confining geometries, to show the self-limiting effect on the growth of the bubble. Understanding the effect of geometry confinement on bubble dynamics is required to optimize existing and engineer future applications.

We developed LIST setup and determined optimal conditions of bioprinting and investigated the functionality of LIST-printed human umbilical vein endothelial cells (HUVECs). Our investigations show that LIST-printed HUVECs present negligible loss of viability and maintain their abilities to migrate, proliferate and form intercellular junctions. We explored the effect of hydrogel-based matrices on the LIST-printed HUVECs. Our investigation showed that printing Fibrinogen/HUVECs droplets on Matrigel/Thrombin-based matrix provided firm adhesion maintaining the initial printing pattern. This matrix also led the HUVECs to form intercellular junctions. We investigated the effects of pro- and anti-angiogenic factors on sprouting in the LIST-printed lines and in the formation of the tube-like structures. In all conditions, the cells were able to partially create the tube-like formation. However, bone

morphogenetic protein9 (BMP9) as an anti-angiogenic factor significantly increased the lumen length.

In the present study, we showed that LIST is capable of printing cells with negligible loss in viability ( $>93.1\%$ ), with micrometric resolution (165 and 325  $\mu\text{m}$ ) and with high speed (potentially 2500 Hz) for bioinks with viscosity upto 300 mPa.s. These features make LIST complementary to existing bioprinting approaches and pave the path to fabricate functional tissues/organs for drug screening and tissue regeneration.

# Acknowledgments

I wish to thank Professor Sivakumar Narayanswamy for supervising me and for his valuable guidance. It was impossible to make through this study without his effective support and continuous encouragement throughout my doctoral study.

I would also wish to express my deepest gratitude to Professor Christos Boutopoulos for supervising me during this journey. My research would have been impossible without his aid, continuous supports and work-related trainings.

I am also profoundly grateful to Professor Bruno Larrivée for his valuable suggestions, comments and technical supports which extremely helped me in this study.

I also appreciate Professor Santiago Costantino for his constructive comments and technical supports.

I would like to pay my special regards to my research partner, Sara Hosseini, for her assistance and giving invaluable help in the lab through my research experiments.

I would also like to thank Dr. Erika Hooker and Dr. Mikhail Sergeev for their trainings and patiently supporting my research.

Here, I appreciate Concordia University and the Fonds de Recherche du Québec Nature et technologies (FRQNT) for all the supports they have given me during this journey.

This thesis would not be possible without the warm support of my family. I like to thank them deeply for their constant encouragement and their deep understanding through these years.

*This dissertation is dedicated to my parents, my sister and my brother, who taught me to pursue my true passion and supported me with their love and encouragement.*

# Contribution of authors

Followings are the authors contribution in the papers presented in this study:

*Chapter 2: Ebrahimi Orimi, Hamid, Leonardo Arreaza, Sivakumar Narayanswamy, and Christos Boutopoulos. "Self-limited nanosecond laser-induced bubble growth in sealed containers." Applied Physics Letters 119, no. 6 (2021): 064101.*

Here is the contribution of authors to this study:

- Hamid Ebrahimi Orimi: contributed in conceptualization, methodology, software, data curation, writing - original draft, visualization.
- Leonardo Arreaza: contributed in conceptualization, methodology and data curation.
- Sivakumar Narayanswamy: contributed in conceptualization, supervision.
- Christos Boutopoulos: contributed in conceptualization, methodology, writing - review/editing, supervision, funding acquisition.

*Chapter 3: Orimi, Hamid Ebrahimi, Sivakumar Narayanswamy, and Christos Boutopoulos. "Hybrid analytical/numerical modeling of nanosecond laser-induced microjets generated by liquid confining devices." Journal of Fluids and Structures 98 (2020): 103079.*

Here is the contribution of authors to this study:

- Hamid Ebrahimi Orimi: contributed in conceptualization, methodology, software, data curation, writing - original draft, visualization.
- Sivakumar Narayanswamy: contributed in conceptualization, supervision.
- Christos Boutopoulos: contributed in conceptualization, methodology, writing - review/editing, supervision, funding acquisition.

*Chapter 4: Orimi, Hamid Ebrahimi, Sayadeh Sara Hosseini Kolkooch, Erika Hooker, Sivakumar Narayanswamy, Bruno Larrivé, and Christos Boutopoulos. "Drop-on-demand cell bioprinting via Laser Induced Side Transfer (LIST)." Scientific Reports 10, no. 1 (2020): 1-9.*

Here is the contribution of authors to this study:

- Hamid Ebrahimi Orimi: co-designed the LIST setup, performed experiments (bio-printing, jet dynamics and microscopy), analyzed data and wrote the first version of the manuscript.
- Sayadeh Sara Hosseini Kolkooch: contributed to bio-ink and printing substrate preparations.
- Erika Hooker: contributed ideas on HUVECs manipulations and helped with HUVECs culture maintenance.
- Sivakumar Narayanswamy: contributed ideas on instrumentation. Bruno Larrivé: contributed ideas on HUVECs manipulations and provided relevant resources.
- Christos Boutopoulos: oversaw the project and finalized the manuscript with input from all authors.

*Chapter 5: Orimi, Hamid Ebrahimi, Sayadeh Sara Hosseini Kolkooch, Erika Hooker, Sivakumar Narayanswamy, Bruno Larrivé, and Christos Boutopoulos. "Spatially-guided endothelial tubulogenesis by laser-induced side transfer (LIST) bioprinting of HUVECs", under review, Biofabrication.*

Here is the contribution of authors to this study:

- Hamid Ebrahimi Orimi: performed experiments (bio-printing, and microscopy), analyzed data and wrote the first version of the manuscript.
- Sayadeh Sara Hosseini Kolkooch: performed experiments (printing substrate/bioink preparations, angiogenesis treatments), performed microscopy characterization and contributed to data analysis.
- Erika Hooker: contributed ideas on HUVECs manipulations, helped with HUVECs culture maintenance, angiogenesis treatments and microscopy.

- Sivakumar Narayanswamy: contributed ideas on instrumentation. Bruno Larivée: contributed ideas on HUVECs manipulations and provided relevant resources.
- Christos Boutopoulos: oversaw the project and finalized the manuscript with input from all authors.

# Contents

<b>List of Figures</b>	<b>xv</b>
<b>List of Tables</b>	<b>xxvi</b>
<b>List of Abbreviations</b>	<b>xxvii</b>
<b>List of Symbols</b>	<b>xxx</b>
<b>1 Introduction and literature review</b>	<b>1</b>
1.1 Bioprinting techniques . . . . .	2
1.1.1 Extrusion-based bioprinting (EBB) . . . . .	4
1.1.2 Droplet-based bioprinting (DBB) . . . . .	5
1.1.3 Light-based bioprinting (LBB) . . . . .	8
1.2 Bioprinting applications . . . . .	11
1.2.1 Pharmaceuticals/drug screening . . . . .	11
1.2.2 Tissue regeneration . . . . .	12
1.3 Bioprinting technologies for vascular printing . . . . .	13
1.3.1 Bioprinting of microvascular constructs . . . . .	15
1.4 Cavitation bubbles and applications of laser-based bubble . . . . .	23
1.5 Modeling of bubble dynamics and bubble-induced microjets . . . . .	31
1.5.1 Analytical simulation of spherical bubbles . . . . .	31
1.5.2 Bubble and microjet dynamics in the confining conditions . . . . .	34
1.6 Problem statement and motivation . . . . .	41
1.7 Thesis objective and scope . . . . .	42
1.8 Thesis contribution . . . . .	43
1.9 Organization of the thesis in manuscript-based format . . . . .	44

<b>2</b>	<b>Self-limited nanosecond laser-induced bubble growth in sealed containers</b>	<b>48</b>
2.1	Introduction . . . . .	48
2.2	Material and methods . . . . .	49
2.3	Results and discussion . . . . .	50
2.4	Conclusion . . . . .	55
<b>3</b>	<b>Hybrid analytical/numerical modeling of nanosecond laser-induced microjets generated by liquid confining devices</b>	<b>57</b>
3.1	Introduction . . . . .	57
3.2	Device and model overview . . . . .	59
3.3	Description of the model . . . . .	60
3.3.1	Model assumptions . . . . .	60
3.3.2	Bubble dynamics analytical model . . . . .	61
3.3.3	Calculation of $R_0$ . . . . .	62
3.3.4	Calculation of $P_g$ . . . . .	63
3.3.5	Calculation of $P_l$ . . . . .	64
3.3.6	Rebound and damping . . . . .	64
3.3.7	Bubble dynamics implementation in FSI . . . . .	65
3.3.8	Membrane dynamics and V outlet calculation with FSI . . . . .	65
3.3.9	Liquid ejection dynamics . . . . .	65
3.3.10	Mesh selection . . . . .	67
3.4	Results and discussion . . . . .	68
3.4.1	Bubble dynamics in open/closed chambers and liquid semi-confining devices . . . . .	68
3.4.2	Liquid ejection dynamics . . . . .	70
	The effect of the nozzle diameter . . . . .	72
	The effect of the membrane thickness . . . . .	72
	The effect of the laser energy . . . . .	74
3.5	Conclusion . . . . .	75
<b>4</b>	<b>Drop-on-demand cell bioprinting via laser-induced side transfer</b>	<b>78</b>
4.1	Introduction . . . . .	78
4.2	Material and methods . . . . .	81

4.2.1	Laser beam delivery system . . . . .	81
4.2.2	Drop-on-demand unit . . . . .	81
4.2.3	Microjet visualization system and analysis . . . . .	81
4.2.4	Bio-ink formulation . . . . .	82
4.2.5	Printing substrates . . . . .	82
4.2.6	Printing protocol . . . . .	83
4.2.7	Viability assay . . . . .	83
4.2.8	Visualization of intercellular junctions . . . . .	83
4.3	Results and discussion . . . . .	84
4.3.1	Laser-induced side transfer (LIST) . . . . .	84
4.3.2	Optimizing the printing process . . . . .	84
4.3.3	LIST printed HUVECs maintain their ability to migrate and proliferate . . . . .	88
4.3.4	LIST printed HUVECs present marginal loss of viability compared to control deposited HUVECs . . . . .	88
4.3.5	LIST-printed HUVECs form intracellular junctions . . . . .	89
4.3.6	High speed LIST printing . . . . .	91
4.4	Conclusion . . . . .	92
<b>5</b>	<b>Spatially guided angiogenesis assay and tube-like formation by laser-induced side transfer (LIST) bioprinting of HUVECs</b>	<b>94</b>
5.1	Introduction . . . . .	94
5.2	Material and methods . . . . .	96
5.2.1	Bioink preparation . . . . .	96
5.2.2	Live-dead assay for red dye cytotoxicity assessment . . . . .	96
5.2.3	Matrices . . . . .	97
5.2.4	Printing setup and protocol . . . . .	97
5.2.5	Immunofluorescence imaging . . . . .	97
5.2.6	Lumen segmentation and quantification . . . . .	98
5.2.7	Sprouting Angiogenesis assays . . . . .	98
5.2.8	Anti- and pro-angiogenic treatments . . . . .	99
5.3	Results . . . . .	99
5.3.1	Droplet and line printing by Laser-induced side transfer . . . . .	99

5.3.2	The effect of the support matrix on HUVECs self-assembling and adhesion . . . . .	100
5.3.3	LIST-printed HUVECs lines regress with time . . . . .	101
5.3.4	Evaluating the affect of pro- and anti- angiogenic factors on sprouting from LIST-printed patterns . . . . .	103
5.3.5	Evaluating the effects of pro- and anti- angiogenic factors on guided tubulogenesis . . . . .	104
5.4	Discussion . . . . .	106
5.5	Conclusion . . . . .	109
<b>6</b>	<b>Conclusions, limitations and future studies</b>	<b>110</b>
6.1	Conclusions . . . . .	110
6.2	Limitations . . . . .	115
6.3	Future studies . . . . .	116
	<b>Bibliography</b>	<b>118</b>
<b>A</b>	<b>Supplementary of chapter 2</b>	<b>146</b>
A.1	Complete schematic of the experimental setup . . . . .	146
A.2	Container preparation, degassing and sealing protocol . . . . .	147
A.3	Cavitation threshold and energy balance . . . . .	148
A.4	Calculation of $R_0$ . . . . .	149
A.5	Calculation of $P_g$ . . . . .	150
A.6	Initial conditions and constants used in Keller-Miksis model . . . . .	150
<b>B</b>	<b>Supplementary of chapter 3</b>	<b>152</b>
B.1	Video S1 . . . . .	152
B.2	Video S2 . . . . .	152
B.3	Video S3 . . . . .	152
B.4	Video S4 . . . . .	152
<b>C</b>	<b>Supplementary of chapter 4</b>	<b>153</b>
C.1	HUVECs migration post LIST-printing . . . . .	153
C.2	Time point to the first frame . . . . .	155

<b>D</b>	<b>Supplementary of chapter 5</b>	<b>156</b>
D.1	Allura red dye toxicity test with dye exclusion method . . . . .	156
D.2	HUVECs network formation study on Fibrin, Matrigel and Matrigel/thrombin using conventional cell seeding . . . . .	157
D.3	Conventional assays for similar conditions show random or no network formation . . . . .	158

# List of Figures

1.1	Existing bioprinting methods, schematics of (a) extrusion-based bioprinter, (b) inkjet bioprinter and (c) light-based bioprinter including laser-induced forward transfer (LIFT) and stereolithography (SL) bioprinters [3]. . . . .	3
1.2	EBB systems with (a) pneumatic actuator, (b) mechanical actuator and (c) solenoid actuator [4]. . . . .	4
1.3	Classification of droplet-based bioprinting into inkjet, acoustic, and micro-valve bioprinting modalities. Inkjet bioprinting is further classified into continuous inkjet, drop-on-demand and electrohydrodynamic jetting modalities. Drop-on-demand inkjet [11]. . . . .	6
1.4	Mechanisms of droplet-based bioprinting, (a) micro-valve (solenoid) bioprinting, (b) acoustic-droplet ejection and (c) inkjet bioprinting techniques including continuous-ink-jetting, thermal drop-on-demand bioprinting, piezoelectric drop-on-demand bioprinting, electrostatic bioprinting, electrohydrodynamic jetting [11]. . . . .	7
1.5	Schematic representation of projection stereolithography apparatus [31].	9
1.6	Laser-induced forward transfer (LIFT), featuring all the parameters involved in the process [33]. . . . .	10
1.7	(a) HUVEC branch/stem structure 1 day post-printing [78] and (b) live/dead (green/red) staining after 24 h. The red line indicates the original printed pattern prior to 24 h in culture [79]. . . . .	16
1.8	Crossed circle pattern, (a) schematic of the pattern design, (b) shows macrophotography of calvaria in two months and (c) The right column shows fluorescence microscopy images of HUVECs vascular networks two months post-printing. White circles show the bone defect delimitation [80]. . . . .	16

1.9	(a) Arrangement of printed cells using LIFT after 24 h: Human MSC were prestained with PKH26 and patches were stained with polyclonal goat anti-Pecam1 and (b) patch implantation in-vivo: After LAD-ligation rats received the cardiac patch sutured onto the area of blanched myocardium [81]. . . . .	17
1.10	(a) Images of Y-shaped alginate tubes printed using 8% sodium alginate solution and (b) images of cellular tubes printed with 2% alginate and bioink [82]. . . . .	18
1.11	(a) Schematic of the patterning process and (b) brightfield images of tube-like formation, and confocal microscopy and 3D reconstruction of endothelial tube [83]. . . . .	19
1.12	(a) Schematic of the bioprinting platform, (b) fluorescent images indicating the heterogeneous cell-laden tissue construct. HUVECs (red) are encapsulated in the intended channels and hepatoma G2 (HepG2) (green) are encapsulated in the surrounding area and (c) confocal microscopy images show HUVECs (Green) and supportive mesenchymal cells (Purple) within the patterned channel regions with different vessel sizes [84]. . . . .	20
1.13	(a) Schematic of DOPsL printing setup and (b) scanning electron microscope (SEM) image of a vascular network in PEGDA [85]. . . . .	20
1.14	(a) Model and printed graft of the heterogeneous dual construct, endothelial progenitor cell (EPC)-laden Matrigel (left), multipotent stromal cell (MSC)-laden Matrigel part with added biphasic calcium phosphate (BCP) (right) and (b) fluorescence microscopy images of EPCs (red) and MSCs (green) printed within one tubes-in-cube construct [86].	21
1.15	(a) Schematic of cell printed scaffold fabrication steps, (b) SEM image of a freeze-dried 3D scaffold and (c) confocal microscopy image of capillary network formation by HUVECs in the printed collagen line at day 14 [87]. . . . .	22

1.16	(a) Schematic cross-sectional view of a section of $\mu$ VN illustrating, (b) schematic of microfluidic collagen scaffolds after fabrication and (c) confocal microscopy images of endothelialized microfluidic vessels, Z-stack projection of horizontal sections of the network, its corner view and branching sections Red, CD31; blue, nuclei [88]. . . . .	23
1.17	(a) Schematic illustration of tissue fabrication process, (b) printed tissue construct within a perfusion chamber, (c) printed tissue construct removed from the perfusion chamber and d) confocal microscopy of HUVECs (red) lining vascular network supported by HNDF-laden (green) matrix at 45 days of perfusion [89]. . . . .	24
1.18	(a) Experimental setup for cavitation-based sonic cutting, Laser-induced focused ultrasound creates micro-cavitation in a sample mounted on a motorized stage, (b) schematics of the sonic cutting of tissue-mimicking gel (1 mm thick) for a square hole. Ultrasonic micro-cavitation is sequentially applied on four imaginary cutting surfaces and (c) other primitive shapes (circle and triangle) produced by the sonic cutting [110].	25
1.19	PLACS operation, (a) schematic of the cell sorter. The sample flow is hydrodynamically focused on the waste channel, (b) time-resolved images of the cavitation bubble generated by the focused pulsed laser beam in the microfluidic cell sorter and (c) fluorescent particle switching in PLACS without switching [97,98]. . . . .	26
1.20	(a) Schematic of the pulse laser-driven peristaltic membrane pump, (b) the synchronized laser-induced cavitation bubbles deform the thin membranes in sequence to push the fluid in the sample channel forward, (c) a laser pulse focused in the middle of a wide channel excites an explosive bubble that quickly expands the channel width and d) two different pumping rates [111]. . . . .	27
1.21	(a) Schematic of laser droplet generator device and (b) time-resolved images of on-demand droplet generation [113]. . . . .	28
1.22	(a) Illustration of the sequential mechanisms of the laser-based microjet generation and (b) image of repeated microjet without refilling [100,101].	29

1.23	Ex-vivo study, (a) cross-sectional and top view of the porcine tissue after injections via laser focusing and (b) snapshots of dyed water injection into the porcine tissue from the glass capillary [116]. . . . .	29
1.24	(a) Top view of the time-resolved imaging setup, (b) side view of the microcapillary in which the droplets are generated, (c) series of time-resolved images of the jet formation and (d) array of droplets with rabbit and mouse immunoglobulin G (IgGs) imaged with a bright-field microscope and the same array imaged under fluorescence (performing an immunoassay with fluorescent-labeled secondary anti-IgGs against rabbit) [120]. . . . .	30
1.25	(a) The process of a laser-induced cavitation bubble, a laser pulse is focused in the liquid (i) which causes the growth of the bubble to its maximum radius ( $R_{max}$ ) (ii) and then the bubble collapses and oscillates toward the equilibrium state with the radius $R_{eq}$ (iii) and (b) the bubble radius vs time [124]. . . . .	31
1.26	(a) Schematic of a laser-induced cavitation bubble placed near two, (b) Dynamics of a bubble placed near two perpendicular rigid walls for $\gamma_h = 1.08$ , $\gamma_v = 0.88$ , $R_{max} = 0.85$ mm. Frame interval $10 \mu s$ . Frame width 3 mm [139], (c) schematic of bubble place near a rigid boundary and an elastic membrane and (d) Bubble dynamics positioned near the boundary, pulse energy 10 mJ, gap width $300 \mu m$ , $\gamma_M = 0$ [141]. . . . .	35
1.27	Shadowgraph frames of laser-induced bubble dynamics in water at (a) $1 \times 10^5$ Pa, (b) $3 \times 10^5$ Pa and (c) maximum bubble volume and radius vs the external pressure applied to the ambient water [144]. . . . .	36
1.28	(a) Computational model, (b) experimentally measured bubble profile with the fitted profile and (c) jet-front displacement vs. time for a range of laser energy from 4.7 to $7.3 \mu J$ (d) Experimental and simulation simulation results of droplet dynamics from a $5 \mu m$ donor film using $5.4 \mu J$ [146]. . . . .	38

1.29	(a) Computational domain of needleless injector, (b) two-dimensional axisymmetric needle-free device simulation results for $p_{bubble} = 5 \times 10^7$ Pa and the standard meniscus shape [148] and (c) experimental (background image) and simulation of jet formation (solid lines), the absorbed energy is $365 \mu\text{J}$ and distance between the laser spot and meniscus is $600 \mu\text{m}$ . Pressure amplitude is 1581 bar with 50 ns duration [149].	39
1.30	(a) Schematic of the physical domain, (b) experimental frame of the spark bubble droplet formation and (c) simulation result corresponding to the frame presented in b [150]. . . . .	40
1.31	Schematic of laser-induced side transfer (LIST). . . . .	44
2.1	Schematic overview of the experimental setups used to study self-limited bubble growth in sealed containers. (a) Simultaneous measurement of bubble dynamics and liquid pressure, and (b) measurement of bubble maximum radius. . . . .	50
2.2	Self-limited bubble growth in sealed containers, (a) Indicative bubble dynamics traces (i.e., inverted photodiode signal) and bubble images for sealed containers (0.3 mL, 0.6 and 1.9 mL) and an open control container (15 mL). Bubbles were generated at 1.75 mJ and images were acquired using sufficiently long integration time ( $100 \mu\text{s}$ ) to depict max bubble size. The dependence of the maximum bubble radius, (b) and bubble lifetime and (c) on the laser energy for sealed and control containers. The dependence on the laser energy is fitted for $E_l \geq 2E_{th}$ .	52
2.3	Pressure profiles for sealed and control containers, a) Indicative ( $E_l = 2.5$ mJ) liquid pressure recordings (top) and corresponding bubble dynamics traces (bottom) (i.e., inverted photodiode signal) for sealed containers (0.3 mL, 0.6 and 1.9 mL) and an open control container (15 mL). The raw data were filtered to remove the high frequency component (noise and/or shockwaves), b) The dependence of the maximum pressure variance on the laser energy for sealed and control containers.	53

2.4	Keller-Miksis bubble modeling using the experimentally measured pressure profiles. (a) KM bubble modeling for sealed containers (0.3 mL, 0.6 and 1.9 mL) and an open control container (15 mL). $E_l = 1.5$ mJ, the dependence of the experimentally measured and modeled bubble behavior on the laser energy for open and sealed containers: (b) maximum bubble size and (c) time of bubble maximum size. . . . .	56
3.1	Schematic of the simulated dual chamber liquid-confining device, (a) laser-induced optical breakdown, (b) generation of a cavitation bubble and (c) elastic membrane deformation, and (d) generation of a microjet.	59
3.2	Sketches of the computational domains for (a) FSI and (b) TPF. . . .	60
3.3	(a) Irradiance distribution and (b) representation of the bubble initial volume for $\lambda = 532$ nm, $NA = 0.5$ and $E_l = 200 \mu\text{J}$ . . . . .	63
3.4	(a) Snapshots of bubble dynamics in the FSI model, (b) bubble radius and (c) bubble wall velocity for $200 \mu\text{J}$ laser energy and $532$ nm wavelength. A video with the complete bubble dynamics can be found in the supplementary material (section B.1-Video S1). . . . .	66
3.5	(a) Membrane average velocity profile and (b) integral of volumetric flow rate for $200 \mu\text{J}$ laser energy (c) spatiotemporal evolution of the membrane's velocity profile. . . . .	67
3.6	(a) Outlet velocity for different meshing sizes and (b) its variation on the meshing size for $E_l = 200 \mu\text{J}$ . . . . .	68
3.7	(a) Jet-front for different meshing sizes and (b) its variation on the meshing size $E_l = 200 \mu\text{J}$ . . . . .	69
3.8	The effect of a closed chamber on bubble dynamics and for $E_l = 200 \mu\text{J}$ . Simulated (a) bubble dynamics and (b) $P_l$ temporal profile for open (constant $P_l$ ) and closed (variable $P_l$ ) chambers. . . . .	70
3.9	The effect of laser energy on bubble dynamics: (a) bubble maximum radius and (b) bubble lifetime as a function of laser energy for open (constant $P_l$ ) and closed chambers (variable $P_l$ ). . . . .	71
3.10	Simulated bubble dynamics for the liquid confining-device presented in Figure 3.2 considering $V_{outlet}$ . (a) bubble radius and (b) bubble wall velocity. . . . .	71

3.11	Numerical simulation of laser-induced liquid ejection from the liquid confining device presented in Figure 3.2 for 70 $\mu\text{J}$ laser energy: (a) bubble and membrane dynamics (FSI simulation) and (b) liquid ejection dynamics (TPF simulation). Videos with the complete bubble and ejection dynamics can be found in the supplementary material (section B.3-Video S3 and section B.4-Video S4). . . . .	73
3.12	The effect of the nozzle size variation on the liquid ejection dynamics for an otherwise identical liquid confining device (see Figure 3.2). The jet front trace for 70 $\mu\text{J}$ laser energy and 150 $\mu\text{m}$ nozzle size corresponds to a non-detached oscillating liquid meniscus. . . . .	74
3.13	The effect of the membrane thickness on the liquid ejection dynamics for an otherwise identical liquid confining device (see Figure 3.2). The jet front trace for 70 $\mu\text{J}$ laser energy and 600 $\mu\text{m}$ / 400 $\mu\text{m}$ diameter thickness corresponds to a non-detached oscillating liquid meniscus. . . . .	75
3.14	The effect of the laser energy on the liquid ejection dynamics for the liquid-confining device of Figure 3.2 (nozzle size 75 $\mu\text{m}$ , membrane thickness 200 $\mu\text{m}$ ). The jet front traces for 25 and 40 $\mu\text{J}$ laser energy correspond to non-detached oscillating liquid menisci. . . . .	76
3.15	The effect of the laser energy on the liquid ejection dynamics for the liquid-confining device of Figure 3.2 (nozzle size 50 $\mu\text{m}$ , membrane thickness 200 $\mu\text{m}$ ). The jet front traces for 25 $\mu\text{J}$ laser energy correspond to non-detached oscillating liquid menisci. . . . .	76
4.1	Overview of LIST (a) schematic side view representation of LIST bioprinting (left) and indicative high-speed imaging of bio-ink ejection from capillary tip to the substrate (right) and (b) schematic of the complete LIST bioprinting setup. . . . .	80
4.2	Sequences of snapshots showing microjet evolution and drop formation for different laser energies. The laser pulse was focused at the middle point of the capillary and 500 $\mu\text{m}$ above its distal end. . . . .	86

4.3	(a) The dependence of the bio-ink jet front position on the laser energy. Gray symbols represent data points and black lines represent the best fitted curve, $N = 10$ (per energy) and (b) the dependence of the droplet volume (dotted line) and droplet diameter (solid line) on the laser energy, $N = 10$ (per energy). . . . .	87
4.4	(a) Optical microscopy images of LIST-printed HUVECs for various laser energies and (b) the number of the cells per droplet for various laser energies. . . . .	87
4.5	(a,b) Fluorescence microscopy images of LIST printed cells at $90 \mu\text{J}$ , (c) Combined imaging channels, including algorithm-generated cell labeling marks. Green crosses indicate live cells and red crosses indicate dead cells and (d) The dependence of the HUVEC cell viability on the laser energy for 0, 1 and 3-days post printing. $N_d$ indicates the number of droplets. . . . .	90
4.6	Confocal microscopy images of (a–c) LIST-printed ( $100 \mu\text{J}$ ) and (d–f) control HUVECs. Green indicates CD31 staining, red shows VE Cadherin and blue indicates cell nuclei staining with DAPI. . . . .	91
4.7	Sequences of snapshots showing microjet evolution for (a) 10 Hz, (b) 20 Hz and (c) 30 Hz. The laser energy was kept constant at $100 \mu\text{J}$ . The laser pulse was focused at the middle point of the capillary and $500 \mu\text{m}$ above its distal end. . . . .	92
4.8	The dependence of the HUVEC cell viability on the printing speed. The laser energy was kept constant at $100 \mu\text{J}$ . . . . .	93
5.1	(a) Schematic showing the LIST bioprinting process and indicative high-speed imaging of droplet ejection. (b) an array of LIST-printed HUVECs-laden droplets (c) a LIST-printed line using 20 % overlap between adjacent droplets. . . . .	100

5.2	(a) Schematic of LIST-printing of HUVECs lines on different matrices; two days post-printing observation of LIST-printed HUVECs with optical microscopy shows (b) non-directional HUVECs proliferation on fibrin-coated substrate, (c) cord-like HUVECs self-assembling on Matrigel-coated substrate combined with poor adhesion and sprouting, and (d) cord-like HUVECs self-assembling on Matrigel/Thrombin-coated substrate combined with strong adhesion and sprouting. . . .	102
5.3	(a) Optical microscopy images of LIST-printed HUVECs. Drastic self-assembling occurs in day 1, (b) the evolution of LIST-printed lines thickness over time. Error bars represent standard deviation of 5 biological replicates. One-way ANOVA test was used for mean comparison. Significant differences are indicated by asterisks ( $P < 0.0001 = ****$ ).	103
5.4	(a) Bright field microscopy images of HUVECs printed lines treated by pro-angiogenic factors (BMP6 and VEGF) and control media (2% FBS). (b) The average number of sprouts and the average length of sprouts for (BMP6 and VEGF) and control (Basal Media-2% FBS) treatments, (c) bright field microscopy images of HUVEC-printed lines treated by anti-angiogenic factors (BMP9 and FLT1-FC) and control (Complete Medium (CM)), (b) the average number of sprouts and the average length of sprouts for (BMP9 and FLT1-FC) and control (CM) treatments. Error bars represent standard deviation of 3 biological replicates. One-way ANOVA test was used for mean comparison. Significant differences are indicated by asterisks ( $P < 0.05 = *$ and $P < 0.01 = **$ ) . . . . .	105

5.5	(a-c) Day 5 confocal microscopy of LIST-printed HUVECs lines including cross sectional views. The lines were treated by anti-angiogenic factors (BMP9 and FLT1-FC) or control (CM), (d-f) day 5 confocal microscopy of LIST-printed HUVECs lines including cross sectional views. The lines were treated by pro-angiogenic factors (BMP6 and VEGF) or control (Basal Media-2%FBS). Green indicates CD31 and blue indicates cell nuclei staining with DAPI, (g-h) capillary-like length over potential lumen length for anti-angiogenic factors (BMP9 and FLT1-FC) or CM, (g) for pro-angiogenic factors (BMP6 and VEGF) or control (Basal media-2%FBS). Error bars represent standard deviation of 3 biological replicates. One-way ANOVA test was used for mean comparison. Significant differences are indicated by asterisks ( $P < 0.01 = **$ ).	107
A.1	Complete schematic of the experimental setup used to capture bubble dynamics and liquid pressure increase in sealed containers.	146
A.2	(a) Cavitation probability versus pulse energy (b) Laser to bubble energy conversion versus laser pulse energy.	148
A.3	(a) Irradiance distribution and (b) representation of the bubble initial volume for $\lambda = 532$ nm, NA = 0.1 and E = 1.75 mJ.	150
C.1	HUVECs migration post LIST printing. (a-c) Phase contrast (PC) optical microscopy images of LIST-printed (100 $\mu$ J) HUVECs 0 h, 36 h and 72 h post printing. (d-e) Fluorescence (FL) microscopy and (f) combined BF/PC images 72 h post printing. Calcein AM (green) stains live cells and Hoechst 33342 (blue) stains all cells.	154
C.2	Flow chart showing the steps implemented to assign a time point to the first frame of an image sequence acquired by fast imaging.	155
D.1	Evaluating potential cytotoxicity effects for Allura red. The effect of the Allura red dye (10 mM and 50 mM) on HUVECs viability for 0-, 1- and 3-days post exposure. Error bars represent standard deviation (N=3). Two-way ANOVA test was used for comparison ( $P < 0.01 = *$ ).	156

D.2	HUVECs network formation on Fibrin, Matrigel and Matrigel/thrombin using conventional cell seeding, (a) schematic of conventional HUVECs seeding on three different matrices (left). After seeding the samples were placed into an incubator for further analysis (right); HUVECs (2-days after seeding) on (b) fibrin, (c) Matrigel, and (d) Matrigel/thrombin.	157
D.3	Verifying the effect of anti- (BMP9 and FLT1-Fc) and pro- angiogenic (VEGF and BMP6) compounds using a conventional angiogenesis assay. Indicative fluorescence images of random HUVECs networks on fibrin stained with Calcein AM. . . . .	158
D.4	Verifying the effect of anti- (BMP9 and FLT1-Fc) and pro- angiogenic (VEGF and BMP6) compounds using a conventional angiogenesis assay. (a) number of junctions per field and (b) total length in a conventional angiogenesis assay for treatments with by pro- and anti-angiogenic factors. Significant differences are indicated by asterisks ( $P < 0.05 = *$ , $P < 0.01 = **$ and $P < 0.001 = ***$ ). . . . .	159

# List of Tables

1.1	Comparison of tissue engineering methods [1]. . . . .	2
1.2	Comparison of existing bioprinting techniques [37]. . . . .	10
3.1	Mesh settings tested for the FSI and TPF mesh dependence studies. . . . .	68
A.1	The initial conditions used in the Keller-Miksis model. . . . .	151
A.2	Constants used in the Keller-Miksis model. . . . .	151

# List of Abbreviations

DNA	Deoxyribonucleic acid
ECM	Extracellular matrix
2D	Two-dimensional
3D	Three-dimensional
EBB	Extrusion-based bioprinting
MBB	Microextrusion-based bioprinting
DBB	Droplet-based bioprinting
LBB	Light-based bioprinting
CT	Computed tomography
MRI	Magnetic resonance imaging
CAD	Computer-aided design
CIJ	Continuous inkjet
DOD	Drop-on-demand
EHD	Electrohydrodynamic
LIFT	Laser-induced forward transfer
SL	Stereolithography
DMM	Digital micro-mirrors
UV	Ultraviolet
HTS	High-throughput screening
COVID19	Coronavirus disease of 2019
GelMA	Gelatin-Methacryloyl
PLGA	Poly lactic-co-glycolic acid
HUVEC	Human umbilical vein endothelial cell
HUVSMC	Human umbilical vein smooth cell
VEGF	Vascular endothelial growth factor

hMSC	Human mesenchymal stem cell
PEUU	Polyesterurethane urea
LAD	Left anterior descending
$\mu$ COB	Microscale continuous optical bioprinting
PEGDA	Poly (ethylene glycol) diacrylat
DOPsL	Dynamic optical projection stereolithography
EPC	Endothelial progenitor cell
MPSC	Multi-potent stromal cell
HepG2	Hepatoma G2
SEM	Scanning electron microscope
PCL	Poly(caprolactone)
HUASMC	Human umbilical arterial smooth muscle cell
HBVPC	Human brain vascular pericyte
HNDF	Human neonatal dermal fibroblast
CNT-PDMS	Carbon nanotube polydimethylsiloxane
PLACS	Pulsed laser activated cell sorting
IgG	Immunoglobulin G
RP	Rayleigh–Plesset
KM	Keller-Miksis
GA	Gilmore-Akulichev
FSI	Fluid structure interaction
TPF	Two-phase flow
NA	Numerical aperture
LED	Light emitting diode
BLF	Bubble lifetime
LIST	Laser-induced side transfer
GUI	Graphical user interface
PFA	Paraformaldehyde
BSA	Bovine serum albumin
PBS	Phosphate buffered saline
FBS	Fetal Bovine Serum
BMP9	Bone morphogenetic protein 9
BMP6	Bone morphogenetic protein 6

ANOVA      Analysis of variance

# List of Symbols

$R$	Instantaneous bubble radius
$\rho_l$	Liquid density
$P_l$	Liquid pressure at a long distance from the bubble
$P_g$	Gas pressure in the bubble
$P_{g0}$	Initial gas pressure in the bubble (t=0)
$\nu$	Kinematic viscosity
$\sigma_l$	Surface tension
$\gamma$	Heat capacity ratio
$P_v$	Saturated vapor pressure in the bubble
$R_0$	Bubble initial radius (t=0)
$C$	Speed of sound in the liquid
$n$	Instantaneous number of moles
$n_0$	Initial number of moles
$R_{0n}$	Time-varying g equilibrium bubble radius
$H$	The enthalpy of the liquid
$E_l$	Laser energy
$f$	Focal length
$E_{th}$	Cavitation threshold
$t_{BLF}$	Bubble lifetime
$E_b$	Bubble energy
$R_{max}$	Bubble maximum radius
$V_c$	Liquid initial volume
$E_c$	Compressibility energy
$\beta$	Compressibility coefficient
$\lambda$	Laser wavelength

$W_0$	Spot size at the focus
$r$	Coordinate in radial direction
$W_z$	Laser beam width at position $z$
$I_0$	Peak irradiance
NA	Numerical aperture of the lens
$Z_r$	Rayleigh range
$P_{l0}$	Initial liquid pressure
$\Delta V_c$	Liquid volume difference
$V_c$	Liquid initial volume
$V_{outlet}$	Integral of outlet volumetric flow rate
$I_c$	Channel intensity
$I_b$	Background intensity
$\sigma_{I_b}$	Standard deviation of $I_b$
$\Delta l$	The jet front position
$V_{avg}$	Average velocity of the microjet
$t_0$	Time stamp of to the first frame of the fast imaging sequence

# Chapter 1

## Introduction and literature review

The demand for tissues and organs for transplantation has been increasing in recent years. Calamities as donor organ shortage, rejection, incompatibility, and trafficking, led scientists to seek an alternative for organ donation. Tissue engineering is one such method with which tissues and artificial organs using living cells can be engineered. Initially, methods such as porous scaffolds and molding were used to create living tissues. Recently, bioprinting has emerged as a viable alternative to create living tissues owing to its advantages, as listed in the table 1.1 [1].

To print functional constructs, a set of factors for the environment (in which the printing takes place), the equipment, and bioink<sup>1</sup> need to be provided. The most important of which are as follows [2]:

- The bioprinter and the printing environment must be sterilized to avoid contamination during the printing process.
- Adequate temperature and humidity for cell viability and biomaterial durability must be ensured during printing.
- One of the determining factors that affects printability and printing resolution is the size of the nozzle. In the case of nozzle-free bioprinters, the properties of the donor substrate need to be carefully selected.
- Since thermal or shear stresses undermine the viability of the cells, bioprinters must expose the cells with minimum shear and thermal stresses. Therefore,

---

<sup>1</sup>Bioink is the material used to produce engineered tissue using bioprinters.

Table 1.1: Comparison of tissue engineering methods [1].

	Assembly method		
	Bioprinting	Molding	Porous scaffolds
Materials	Natural and synthetic polymers; High concentration cell solutions	Natural and synthetic polymers; High concentration cell solutions; Cell sheets	Natural and synthetic polymers; Ceramics; Metals
Resolution	10-1000 $\mu\text{m}$	>500 nm	100 nm-1000 $\mu\text{m}$
Advantages	Control of tissue geometry across a wide range of scales; rapid production of scaffolds; precise cell and material patterning	Accurate control of small (<100 $\mu\text{m}$ ) features; scaffold fabrication is rapid and often the molds are reusable; gentle on encapsulated cells	Controllable material properties (e.g. porosity, modulus); wide range of materials available for use
Disadvantages	Printing techniques may reduce cell viability or have unknown consequences; limited material selection due to crosslinking speed	Scaffolds are generally homogenous and require combination of multiple scaffolds to create patterns	Scaffold geometry is less controllable, technique may damage encapsulated cells or require seeding after assembly; less control of cell patterning
Techniques	Extrusion; Laser-assisted; Inkjet; Stereolithography	Cell sheet stacking; Lithography; Injection molding	Electrospinning; Phase separation; Freeze drying; Self-assembly

choosing an appropriate printing mechanism according to the cell types and bioinks properties lead to the fabrication of living functional constructs.

- Selecting an optimal bioinks and ECM plays a significant role in the bioprinting of living tissues. It could preserve the printed pattern and provide an environment that supports cell-cell and cell-ECM interactions.

## 1.1 Bioprinting techniques

In general, bioprinters are divided into three main categories according to their working principles:

1. Extrusion-based bioprinting (EBB) figure 1.1a
2. Droplet-based bioprinting (DBB) figure 1.1b
3. Light-based bioprinting (LBB) figure 1.1c

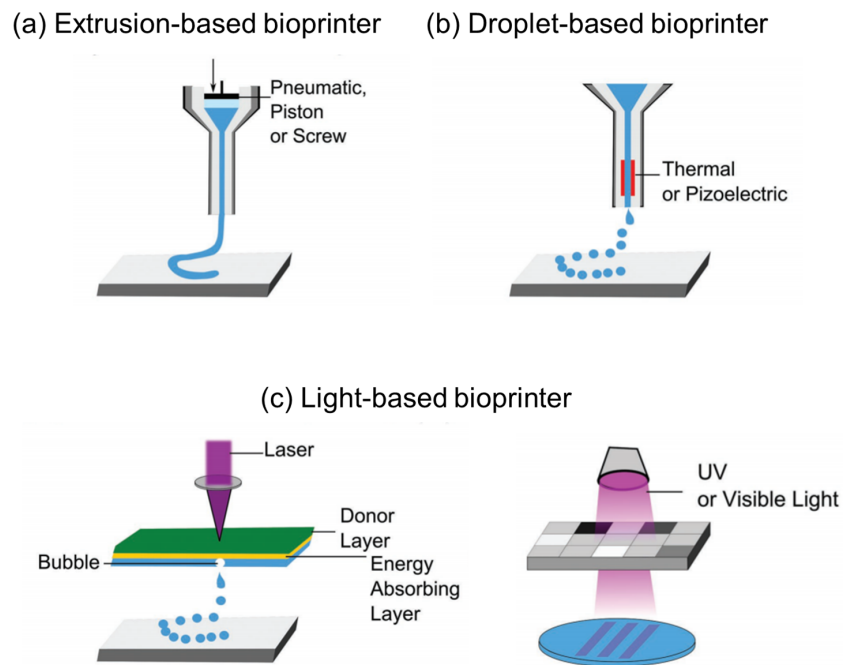


Figure 1.1: Existing bioprinting methods, schematics of (a) extrusion-based bioprinter, (b) inkjet bioprinter and (c) light-based bioprinter including laser-induced forward transfer (LIFT) and stereolithography (SL) bioprinters [3].

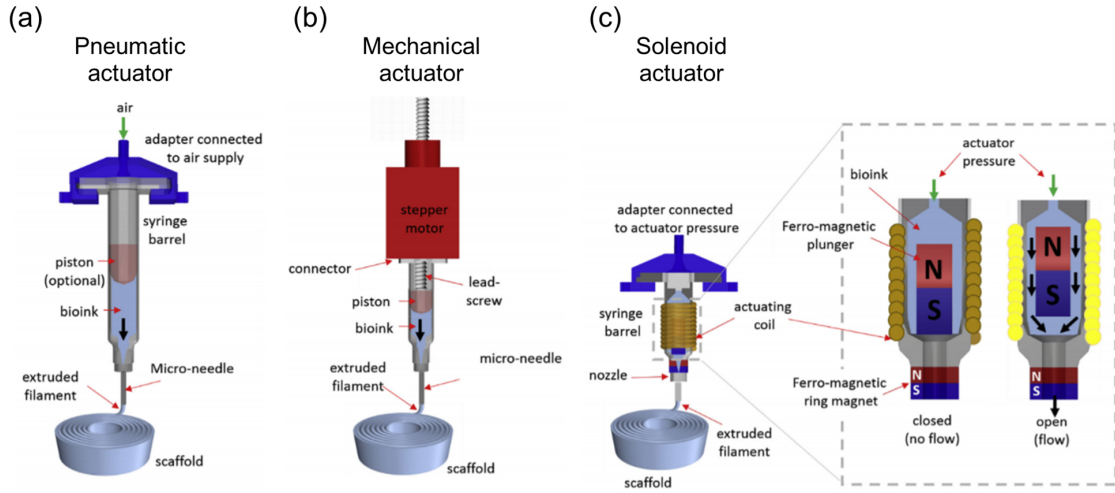


Figure 1.2: EBB systems with (a) pneumatic actuator, (b) mechanical actuator and (c) solenoid actuator [4].

### 1.1.1 Extrusion-based bioprinting (EBB)

EBB is a printing technique in which a fluid dispensing unit is synchronized with an automated robotic system for the extrusion of biomaterials in a spatially-controlled manner [4]. During bioprinting, bioink is deposited using pneumatic [5], mechanical (hydraulic [6], screw-driven [7, 8]) or solenoid-based [9] actuators presented in figure 1.2. It results in the accurate placement of cells encapsulated in the filaments of bioink. The pneumatic actuator is preferable for high-precision applications due to its controlled pressure [4]. Mechanical actuators can be used for dispensing bioinks with high viscosities where direct control on the flow rate is required. However, they may create a pressurized environment that is harmful for the loaded cells. Solenoid actuator utilizes an electromagnetic field to control the bioinks flow by applying magnetic force between a ferromagnetic plunger and the ring. EBB employs computer-aided design (CAD) files that contain 3D printing pattern [4]. The CAD file can be generated by a CAD modeling software or by medical imaging (e.g. computed tomography (CT) scans and magnetic resonance imaging (MRI)). Processing of CAD files precisely controls the relative motion between the stage and the bioprinter head, while depositing bioinks layer by layer to form the 3D shape.

EBB offers high printing speed and greater deposition compared to other types of bioprinting methods. Extrusion-based bioprinters are capable to print a wide

range of bioinks including cell-laden hydrogels<sup>2</sup>, decellularized<sup>3</sup> matrix components and micro-carriers, compared to the other types of bioprinters that are capable to exclusively print cell-laden hydrogels [4]. Currently, printing viscous bioinks with high cell concentrations is achievable only EBB. However, the process of extrusion causes large pressures and shear stresses on the loaded cells which can play a crucial role in the loss of viability and functionality of the printed primary cells and stem cells [10]. Printing resolution is quite low compared to other printing methods that results in imprecise cell patterning. Since the bioink is supposed to be deposited in the form of cylindrical filaments, the bioink used in this technology should have shear thinning ability to avoid forming droplets during the extrusion process [4].

### 1.1.2 Droplet-based bioprinting (DBB)

DBB is a bioprinting method that has a spatially-controlled unit and bioinks deposition mechanism. In this approach, droplets of bioinks with a controlled volume are generated with acoustic, thermal, and piezoelectric<sup>4</sup> actuators. The droplets are then precisely deposited at the desired coordinates [11]. Given the fact that the cells-laden droplets are well-positioned, this method facilitates the fabrication of spatially-heterocellular constructs. DBB is classified into three main categories: inkjet [12,13], acoustic droplet ejection [14] and micro-valve bioprinting [15–18]. Based on the mechanism, inkjet bioprinters can further be classified as continuous inkjet (CIJ) [19], drop-on-demand (DOD) [20–27] and electrohydrodynamic<sup>5</sup> (EHD) [28–30] methods, as shown in the figure 1.3.

Several studies examined the impact of printing process on the printed cells viability and the functionality in micro-valve bioprinting. Generally, this technique needs low working pressure for deposition of droplets compared to other DBB methods (figure 1.4a) resulting in reduced cell damage. However, the droplets generated by this method are larger than the droplets made by other DBB modalities with identical configuration, thus, micro-valve bioprinting reduces the printing resolution. Acoustic bioprinting presented in figure 1.4b employs a gentle pressure on bioinks for droplet

---

<sup>2</sup>a 3D network of polymers that can swell in water and maintain the structure due to chemical or physical cross-linking of polymer chains.

<sup>3</sup>Decellularization is the process for isolation of ECM of a tissue from its inhabiting cells.

<sup>4</sup>Piezoelectric is a solid material that accumulates electric charge.

<sup>5</sup>Electrohydrodynamics is the study of interaction ionized particles with electric fields.

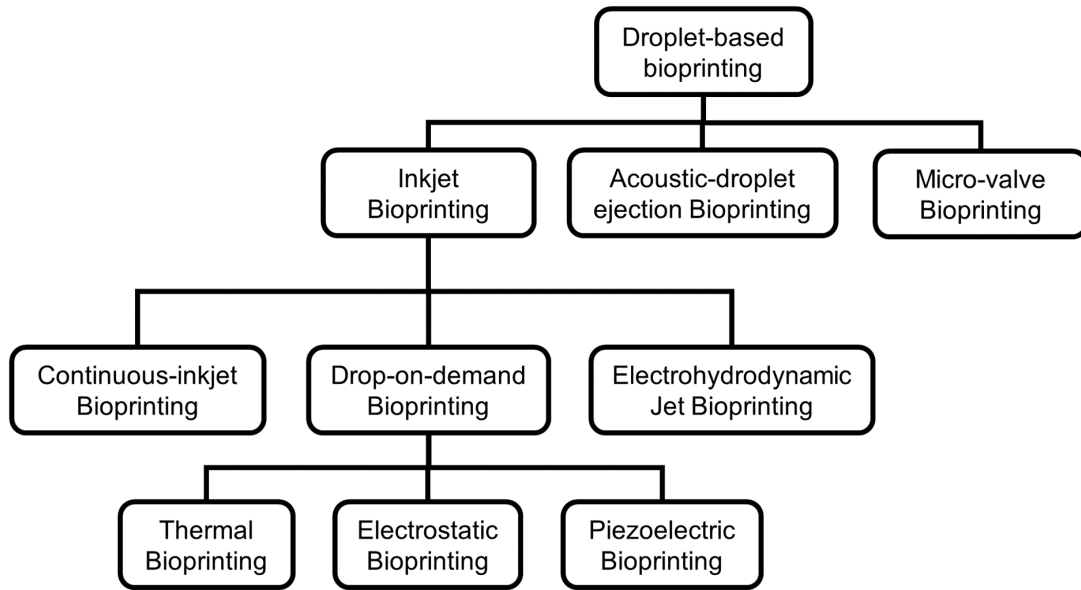


Figure 1.3: Classification of droplet-based bioprinting into inkjet, acoustic, and micro-valve bioprinting modalities. Inkjet bioprinting is further classified into continuous inkjet, drop-on-demand and electrohydrodynamic jetting modalities. Drop-on-demand inkjet [11].

ejection. It results in negligible loss of cell viability and has less impact on functionality of the printed cells as the cells are not exposed to high pressure, heat, large voltage, or significant shear stress. However, the movement of either the printing head or the substrate introduces undesirable disturbance causing uncontrolled droplet ejection. Moreover, the pressure generated with acoustic field may not be sufficient for droplet ejection of viscous bioinks or bioinks with high cell concentrations.

Inkjet printers are commonly used for both non-biological and biological applications. The inkjet bioprinters are categorized into electrohydrodynamic, continuous inkjet and drop-on-demand bioprinters. Electrohydrodynamic bioprinters propel the bioinks by generating an electric field. Electrostatic stress generates a droplet by overcoming the surface tension at the orifice. During the droplet ejection, the cells experience very high pressure and significant shear stress, which may cause a loss in cell viability. In continuous inkjet bioprinting, a continuous stream of bioinks droplets is created via the Plateau-Rayleigh instability<sup>6</sup>. The droplet patterning is performed

<sup>6</sup>Plateau-Rayleigh instability describe how and why a falling fluid flow breaks up into smaller parts.

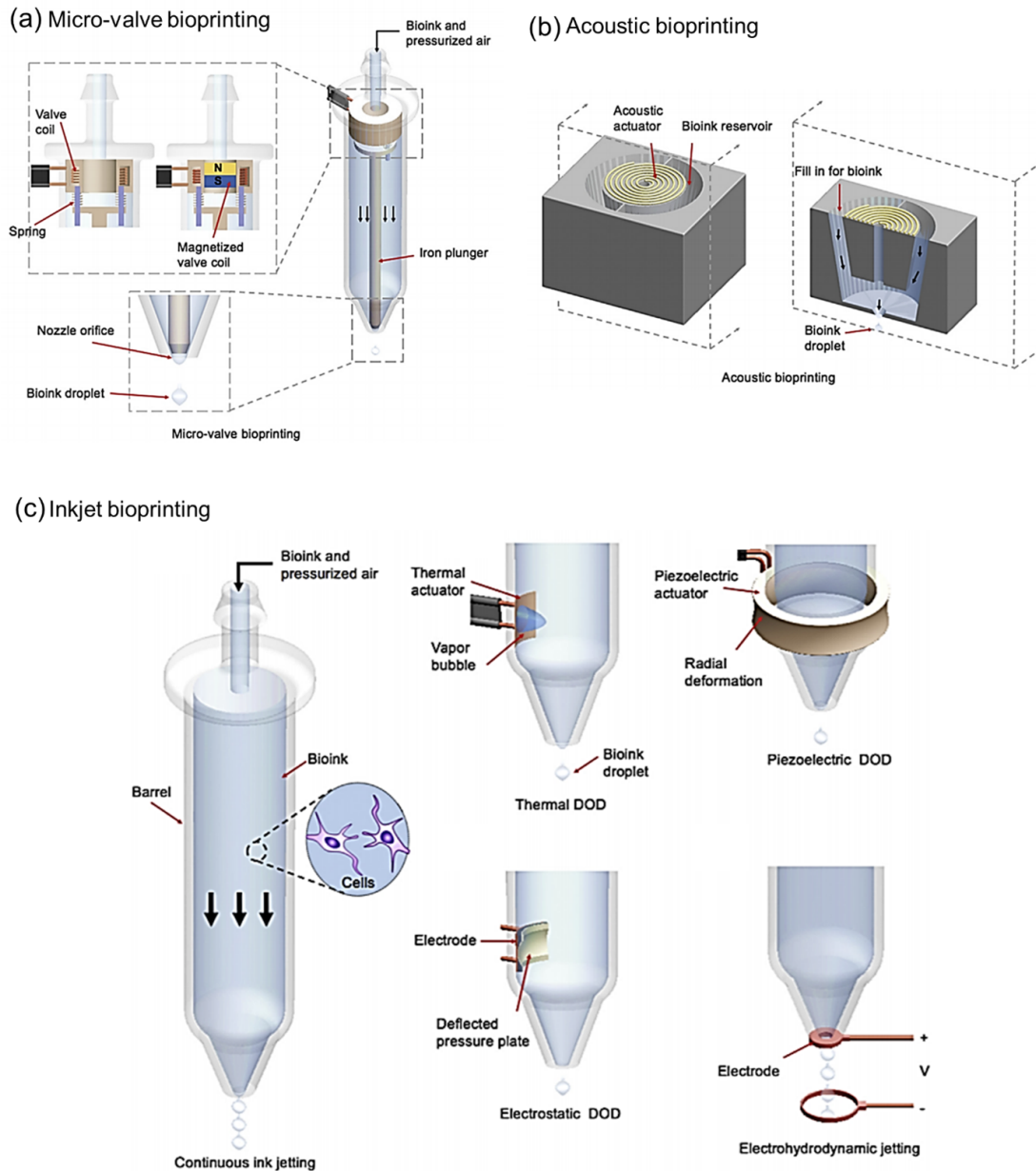


Figure 1.4: Mechanisms of droplet-based bioprinting, (a) micro-valve (solenoid) bioprinting, (b) acoustic-droplet ejection and (c) inkjet bioprinting techniques including continuous-ink-jetting, thermal drop-on-demand bioprinting, piezoelectric drop-on-demand bioprinting, electrostatic bioprinting, electrohydrodynamic jetting [11].

by charge and deflector electrodes. Since there is no on-demand control on the droplet generation, this technique is not convenient to pattern the biologics.

Drop-on-demand technique, on the other hand, comprises of thermal, piezoelectric and electrostatic bioprinting. The working principles are based on vapor bubble expansion, rapid and temporary deformation of the reservoir, and sudden volume variation in the container using pressure plate, respectively. Thermal and piezoelectric inkjet printers are the main varieties that can generate pressure to eject the droplet from the nozzle. Thermal inkjet has high printing speed, low cost and wide availability. However, it presents non-uniform droplet size, mechanical stresses and risk of exposing the bioinks to heat in some cases (resulting in temperature rise of 4-10 °C). In piezoelectric inkjet bioprinting, a piezoelectric crystal generates acoustic waves that break the liquid into droplets at fixed time intervals. This kind of inkjet bioprinter can produce uniform droplets and reduce the risk of exposing the bioinks to thermal or mechanical stresses. However, this technology is incompatible with viscous bioinks primarily due to the limited driving force available for liquid ejection (figure 1.4c).

### **1.1.3 Light-based bioprinting (LBB)**

LBB is a nozzle-free bioprinting technique that has been developed as a promising alternative to improve precision and bioinks compatibility. Most common LBB approaches are based on stereolithography (SL) and laser-induced forward transfer (LIFT). SL is a technique based on polymerization of light-sensitive materials with spatially-controlled light. The desired coordinates are illuminated by an ultraviolet (UV) light source coupled with digital micro-mirrors (DMM) to deflect the unwanted beams [31]. The technique provides high printing quality, speed and cell viability [32]. However, it has been reported that the UV light can be injurious to the DNA of the cells. Moreover, multi-material printing with this method is quite challenging (figure 1.5).

LIFT enables direct deposition of functional materials from a donor substrate called “ribbon”, to a receiving substrate, in a controlled and precise fashion. A LIFT “ribbon” consists of a transparent substrate (e.g. glass) covered by a thin light-absorbing layer (e.g. 5-100 nm thick gold or titanium layer), and a liquid film (5-20  $\mu\text{m}$  thick). Irradiation by a focused pulsed laser beam at the substrate-liquid film

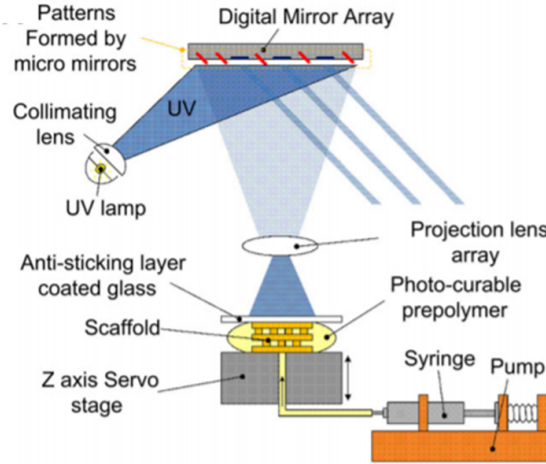


Figure 1.5: Schematic representation of projection stereolithography apparatus [31].

interface enables confined energy deposition and subsequent generation of an expanding microbubble. In turn, this propels a small volume of the liquid film towards a receiving substrate placed adjacent to the donor substrate (figure 1.6) [33–36]. LIFT technology can be successfully used for tissue- and organ-engineering applications; however, it is not as frequently used as inkjet or extrusion-based methods for bioprinting. Since LIFT is a nozzle-free printing approach, there is no clogging which is a key issue in EBB and DBB. Hence, LIFT can be compatible with a wide range of bioinks viscosities. However, ribbon preparation is time-consuming for printing multiple cell types or materials. Nevertheless, the non-uniformity of the ribbon coating results in low resolution and quality. Importantly, the limitation in the ribbon geometry significantly restrains the size of the 3D constructs up to a few  $\text{mm}^3$ .

From the aforementioned discussions on the different bioprinting approaches, the most important parameters that can affect the printing feasibility, and functionality of the printed constructs include:

- Viability of the printed cells,
- Biomaterial viscosity range that can be covered,
- Printing resolution,
- Printing speed and preparation time,

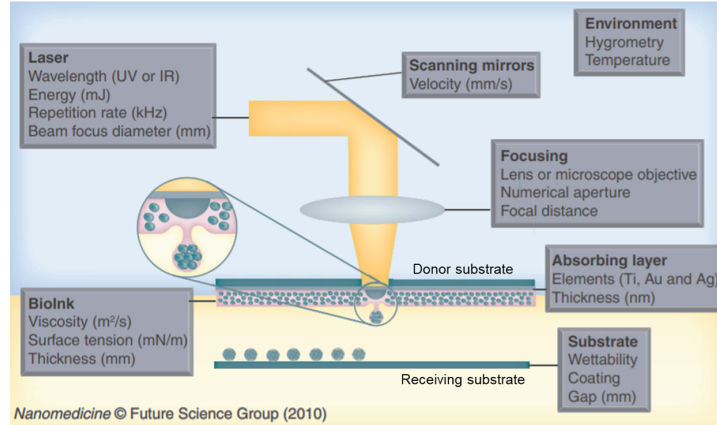


Figure 1.6: Laser-induced forward transfer (LIFT), featuring all the parameters involved in the process [33].

- Printing scale,
- Ability to print multiple materials.

Table 1.2 provides a comparison between the abovementioned parameters in the existing bioprinters. Clearly, EBBs facilitate bioprinting of viscous bioinks and bioinks with a high concentration of cells. DBBs provide fast printing speed and high resolution. LBBs present higher (>95 %) cell viability and micrometric resolution. Overall, any of these three existing bioprinting approaches can be chosen based on the biomaterials, tissue types and applications.

Table 1.2: Comparison of existing bioprinting techniques [37].

	Bioprinting		
	Extrusion-based	Inkjet	Laser assisted
Material viscosity	30 mPa.s to $6 \times 10^7$ mPa.s	3.5-12 mPa.s	1-300 mPa.s
Preparation time	Low to medium	Low	Medium to high
Print speed	Slow (10-50 $\mu\text{m/s}$ )	Fast (1-1000 droplets per s [38])	Medium to fast (200-1600 mm/s)
Resolution or droplet size	5 $\mu\text{m}$ to millimeters wide	>300 pl droplet (>50 $\mu\text{m}$ )	Microscale resolution
Cell viability	40-80%	>85%	>95%
Cell density	High	Low (< $10^6$ cells/ml)	Medium ( $10^8$ cells/ml)
Printer cost	Medium	Low	High

## 1.2 Bioprinting applications

Many attempts have been made by scientists for printing living tissues. The bioprinted tissues with existing bioprinters have been widely used in pharmaceuticals/drug screening and cancer research. However, printing tissues/organs (i.e. tissue regeneration) for transplantation purposes still remains under development.

### 1.2.1 Pharmaceuticals/drug screening

High-throughput screening (HTS) is a common method that allows researchers to quickly conduct a wide range of chemical, genetic and pharmaceutical tests in the preclinical stage for compound and drug discovery. In recent years, this has been the primary method for preclinical tests prior to drug and compound approval. However, 2D cell culture for cell growth is being used in HTS. 2D cell cultures poorly mimic in-vivo<sup>7</sup> cell-cell and cell-matrix interactions due to different phenotypes and different genomic profiles of many cell types in 3D cultures [39]. Recently, researchers used spheroid culture in HTS to model the 3D interaction of cells more accurately. However, the interaction between the cell and the matrices remains unanswered, which is necessary to simulate in-vivo conditions in preclinical trials. Bioprinters have been proven to mimic the spatial and chemical attributes of human tissues by creating 3D in-vitro<sup>8</sup> tissue models [39]. Thus, the widespread use of the printed tissues in HTS for the preclinical stage can prevent catastrophic failures in the subsequent clinical stage by providing reliable evaluation. Printing living constructs has been a promising technique in drug discovery and toxicology research for in-vitro models of liver [40], heart tissue [41–43], vascularized constructs [44,45] and cancer [46,47] models. The in-vitro tissue models are categorized into three main types, which include mini-tissue, organ-on-a-chip and tissue/organ construct.

Mini-tissue approach has been widely utilized in drug discovery and accelerates HTS with a low dose. In tissues that function independently, this method is effective for drug discovery purposes without the need for large tissues or complex organs. However, lack of tissue interface, static culture condition, microenvironment

---

<sup>7</sup>In-vivo is the study that is performed on living organisms.

<sup>8</sup>In-vitro is the study that is carried out with microorganisms, cells, or biological molecules in a labware.

and not being identical to in-vivo model are the main limitations of this approach. The technique enables the fabrication of microspheroidal organoids [48] using electro-assisted [49] or airflow-assisted [50] bioprinters. In this method, extrusion-based bioprinters are employed to print fiber-shaped tissues and reconstruct these tissues like muscle strips [51], nerve bundles [52] and blood vessels [53]. The mini-tissue array, where Optical projection stereolithography is commonly used, is another type of fabrication in the mini-tissue category [54].

Organ-on-a-chip organ is another technique in drug discovery that addresses the limitations posed by the Mini-tissue method. The important advantages of this method are dynamic cell culture, dynamic perfusions<sup>9</sup> that mimic the blood stream, controlled microenvironment that reduces sample consumption, and complex physical/chemical stimuli. These features provide a convenient platform for in-vitro biological analysis with the physiological correlation of in-vitro models and better simulation of in-vivo environments. The method can be classified as integrated cell/organ-on-a-chip, modular microfluidic chip and multi-organ system. In integrated cell/organ-on-a-chip, cells are deposited by perfusions in a microfluidic chip. Several studies were conducted to develop integrated cell/organ-on-a-chip platforms such as lung-on-a-chip to simulate severe acute respiratory diseases like coronavirus disease of 2019 (COVID19) [55–57] and liver-on-a-chip [58–60] to evaluate the hepatotoxic<sup>10</sup> effects of drugs.

In cases where the cell deposition and the bioprinting of 3D structures on the chips are not convenient or where the tissues and organs in the studies are complex, the modular microfluidic technique is utilized. According to human physiology, the organs of the body interact together. This interaction plays a crucial role in drug discovery in the preclinical stage.

### 1.2.2 Tissue regeneration

One of the ultimate goals of bioprinting is to fabricate functional tissues for tissue regeneration or organ transplantation. Given that this method can regenerate human tissues with their own living cells, the tissue/organ rejection may not occur [61]. However, to achieve this, there are several major challenges that must be addressed

---

<sup>9</sup>Perfusion is the process of passing fluids through the circulatory system to an organ or tissue.

<sup>10</sup>Hepatotoxicity is the liver damage caused by drugs.

by bioprinting techniques, such as tissue vascularization, integrating multiple cell types in the creation of complex functional organs and mechanical and structural integrity [62]. Despite remarkable efforts to print and transplant functional organs in the murine model, research has not been successfully transferable to human organ fabrication due to the organ size and the physiological conditions of mice which are not closely relevant to human organs [63]. To make functional human organs with a clinically relevant size, the above-mentioned limitation must be addressed. To date, successful attempts have been made to print human tissues with simple, flat, and hollow geometry. These include tissues such as skin [64–66], cartilage [67, 68] and cornea [69–71] that have been bioprinted, validated and are currently in the clinical stage. The main reason for the rapid validation process and reaching the clinical stage for these type of tissue is their structural simplicity and the absence of vascularization. Currently, research is being focused on the bioprinting of blood vessels, urethras and tracheas tissues and the validation process has been carried out to a considerable extent. These tissues are likely to enter the clinical phase in the near future. Their success in the clinical stage will enable the bioprinting processes to reconstruct complex tissues such as the kidney.

To date, numerous bioprinting techniques with vast potential applications have been developed. Since the thesis is on development of a bioprinting approach using laser-induced bubbles for fabrication of microvascular constructs, a detailed review on bioprinting technologies for vascular printing (section 1.3), cavitation bubbles and their applications (section 1.4), modeling of bubble dynamics and bubble-induced microjets (section 1.5) will be presented henceforth.

### **1.3 Bioprinting technologies for vascular printing**

As mentioned in the previous sections, one of the challenges in printing functional tissue is the need for tissue vascularization that delivers the oxygen and nutrients needed by cells and collects the waste and carbon dioxide produced by the cells. Recently, various bioprinting techniques have been used to fabricate multiscale structure<sup>11</sup> of the vascular network within the complex constructs [72]. In these methods, the formation process of blood vessels, with anatomically precise, physiologically relevant

---

<sup>11</sup>Multiscale structure is a structure in which multiple constructs at different scales are used.

and stable mechanical features, is widely different.

The use of sacrificial bioprinting is an approach to create hollow structures in vascular formation. The sacrificial biomaterials are dissolved through thermal modification or chemical reactions such as enzymatic degradation to fabricate perfusable blood vessels. In several studies, EBB has been used to print sacrificial channels loaded with cellular components and hydrogels. As an example, Bertassoni et al. printed agarose as a sacrificial material with cell-laden gelatin-Methacryloyl (GelMA) hydrogels using EBB [45]. Also, some studies have used pluronic F127 as a thermosensitive sacrificial material, that melts at 4°C within Collagen, composite of Matrigel and poly lactic-co-glycolic acid (PLGA) [73–75], GelMA [76]. In summary, the researchers were able to print the sacrificial bioinks using EBB techniques, and after removing the material, the lumen<sup>12</sup> opening is lined with the cells to form the vessel. EBB methods lead to the construction of vascular constructs with larger dimensions compared to DBB and LBB methods [72].

The use of EBB approaches to create microstructures is very challenging. As an alternative, DBB or LBB methods have been used for creating micro-capillaries. Nakamura et al. printed an alginate-based bioink into a calcium chloride solution using DBB [77]. Through this method, they were able to produce channels of about 200  $\mu\text{m}$ . Also, Pataky et al. were able to create a vascular structure after 21 days by 2D printing of alginate-based and thrombin-calcium-based bioinks on fibrinogen surface [25]. The results of printing in these studies show the ability of this method in making microdroplets of bioink, which makes this method suitable for creating capillary structures. However, one of the limitations of this method is nozzle clogging that limits the viscosity range of bioinks that can be printed.

LBB techniques are not only able to provide a better printing resolution than EBB and DBB methods, but also possess the lowest cell damage with cell viability of over 95%. LIFT has been widely used to print endothelial cells (e.g. Human umbilical vein endothelial cells (HUVECs)) in 2D and form a capillary structure using their self-assembly feature. For printing 3D structures using LBB method, SL is used. However, the limitations of SL include the need for photocurable hydrogels and the possibility of light toxicity.

---

<sup>12</sup>Lumen is the interior of tubular structure.

### 1.3.1 Bioprinting of microvascular constructs

In research to date, a limited number of studies have showed the fabrication of blood vessels using LBB techniques. In this section, recent efforts to create vascular structures using different technologies have been reviewed and criticized in order to understand the trends and difficulties of creating a vascular network via bioprinting technologies. Wu et al. printed HUVECs on Matrigel using LIFT technique followed by 24 h incubation [78]. On day 1 of printing, a layer of human umbilical vein smooth cells (HUVSMCs) has been printed above the HUVEC layer (figure 1.7a). Comparison between the printed HUVECs with or without a layer of HUVSMCs shows that the presence of HUVSMCs leads to more stability of the printed structure. HUVSMCs also limit the over-growth and migration<sup>13</sup> of HUVECs so that they can maintain their original structure for a longer period. Despite the stability of the printed structure, no investigation has been done on the internal structure of the printed pattern to examine the lumen formation in this study.

Pirlo et al. presented a laser-based bioprinter to pattern the HUVECs in 2D on poly-lactide-co-glycolide biopaper substrates loaded with Collagen Type I and Matrigel (figure 1.7b) [79]. The printed HUVECs differentiated and maintained their original structure by forming intercellular junction. Also, to check the stackability of the printed structures, the biopapers with imprinted HUVECs were stacked for 4 days. The results showed that the cells were viable and functional in the multilayer structure. Despite the creation of HUVECs network in this research, no study has been done on the tube-like formation of the printed structure.

K erour edan et al. presented direct LIFT-printing of HUVECs into a mouse bone [80]. The printing area was covered with collagen and vascular endothelial growth factor (VEGF). The results illustrated significant improvement in vascularization rate between control and disc/crossed circle patterns. They were able to introduce LIFT as a promising tool for in-situ<sup>14</sup> prevascularization (figure 1.8). However, in this research, the development of the tube-like formation has not been studied and also the generated networks do not offer precise control over each endothelial branch that was formed.

---

<sup>13</sup>Migration is the process of cells movement in response to mechanical/chemical signals.

<sup>14</sup>In-situ is the study that is performed in place where it occurs.

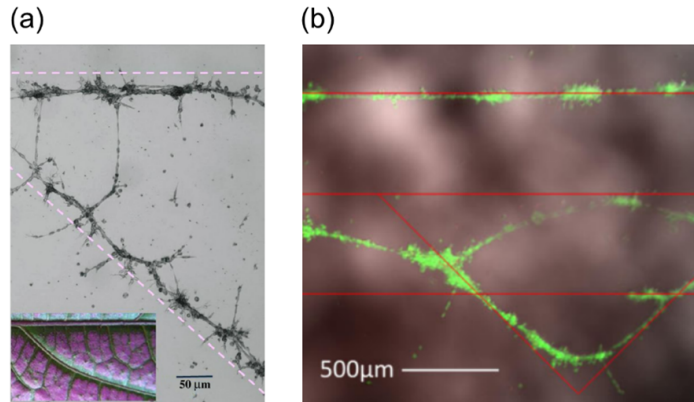


Figure 1.7: (a) HUVEC branch/stem structure 1 day post-printing [78] and (b) live/dead (green/red) staining after 24 h. The red line indicates the original printed pattern prior to 24 h in culture [79].

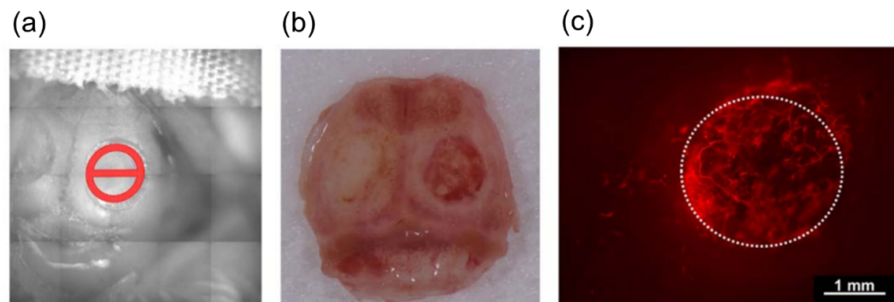


Figure 1.8: Crossed circle pattern, (a) schematic of the pattern design, (b) shows macrophotography of calvaria in two months and (c) The right column shows fluorescence microscopy images of HUVECs vascular networks two months post-printing. White circles show the bone defect delimitation [80].

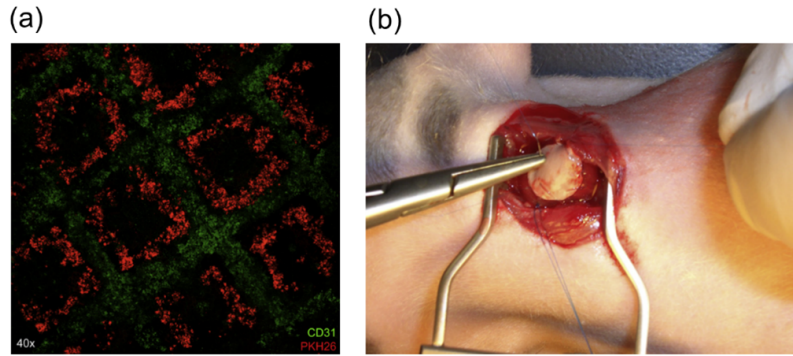


Figure 1.9: (a) Arrangement of printed cells using LIFT after 24 h: Human MSC were prestained with PKH26 and patches were stained with polyclonal goat anti-Pecam1 and (b) patch implantation in-vivo: After LAD-ligation rats received the cardiac patch sutured onto the area of blanched myocardium [81].

Cardiac patches<sup>15</sup> including cells such as HUVECs have been shown to enhance myocardial infarction treatment and wound healing. Gaebel et al. used LIFT to pattern HUVECs and human mesenchymal stem cells (hMSC) to make a cardiac patch for cardiac regeneration purposes [81]. The cardiac patch made with Polyesterurethane urea (PEUU) was transplanted in a rat heart zone that was infarcted. Eight weeks later, due to the type of pattern with interwoven HUVECs and hMSC, the printed cardiac patch significantly increased vascular formation (figure 1.9). As a result, it improved the function of the heart exposed to myocardial infarction<sup>16</sup> compared to controls.

Xiong et al. printed 3D constructs using the laser printing approach [82]. In this method, the authors used a laser-based nozzle-free bioprinter to form straight and Y-shape tubes using alginate solution and alginate-based mouse fibroblast suspension. To construct a 3D structure, the print was done on a moving platform and filled with crosslinking and supporting solutions (figure 1.10). After 24 hours of printing, the viability of the printed cells in both 3D structures was over 60%.

Hribar et al. presented a method to generate a 3D vascular network using a near-infrared femtosecond laser [83]. For this purpose, gold nanorods were dispersed in cell-encapsulating collagen hydrogels. By emitting focused laser light, they were able

<sup>15</sup>Cardiac patch is a laboratory-made heart tissue is used in replacing the patient's damage tissue.

<sup>16</sup>Myocardial infarction occurs when the coronary artery is blocked.

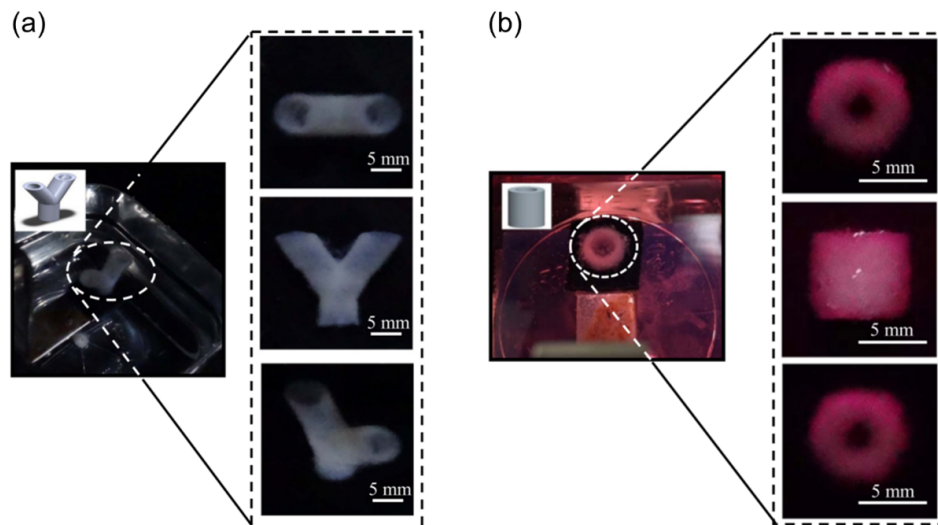


Figure 1.10: (a) Images of Y-shaped alginate tubes printed using 8% sodium alginate solution and (b) images of cellular tubes printed with 2% alginate and bioink [82].

to locally cause denaturation<sup>17</sup> in the collagen due to the release of energy absorbed by the gold nanorods in the hydrogel, resulting in channel formation. In the final step, the cells migrate, proliferate, and align. The presented results show that by changing the scanning speed of laser light and laser power, the resolution of the structure improves, and it maintains cell viability above 90 % (figure 1.11). However, creating structures that require modeling of several types of cells and biomaterials with this method is challenging. Also, parameters such as matrix stiffness and nonuniform cell migration affect the quality of the channels created.

Zhu et al. presented a 3D laser-based bioprinting technique called microscale continuous optical bioprinting ( $\mu$ COB) [84]. In their approach photosensitive hydrogel was polymerized to create a 3D structure in which HUVECs were encapsulated. It has a high resolution and printing speed along with flexibility and scalability. HUVECs and mesenchymal cells, which are the basic components of vascular tissues, are evenly distributed in the hydrogel. By providing adequate control on the properties of the biomaterials, HUVECs in the in-vitro model were able to form a tube structure. After the tube-like formation was implanted in the in-vivo model, Anastomosis<sup>18</sup> between the printed HUVECs and host circulation with functional vessels was seen (figure

<sup>17</sup>Denaturation is the process of breaking weak bonds/linkages

<sup>18</sup>An anastomosis is a surgical connection between two tubular structures.

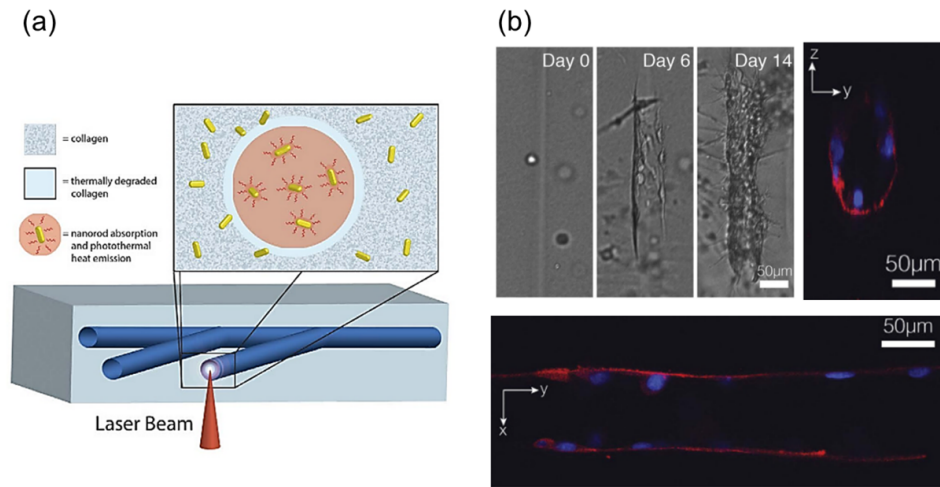


Figure 1.11: (a) Schematic of the patterning process and (b) brightfield images of tube-like formation, and confocal microscopy and 3D reconstruction of endothelial tube [83].

1.12). The main advantage of this printing approach is that there is no need for sacrificial materials or perfusions to enable tube-like formation.

Zhang et al fabricated a complex 3D vascular structure using a soft and degradable biomaterial called poly (ethylene glycol) diacrylate (PEGDA) [85]. To form the 3D structure, a laser-based method called dynamic optical projection stereolithography (DOPsL) was used on a photosensitive biomaterial (figure 1.13). The study showed the potential of using this method to create 3D tissue models, however, further studies are required for this purpose.

Fedorovich et al. used extrusion-based bioprinter to fabricate engineered bone grafts<sup>19</sup> including vascularization [86]. They printed the goat endothelial progenitor cells (EPCs) and multi-potent stromal cells (MPSCs) in the form of porous constructs that included alginate and Matrigel (figure 1.14). Six weeks after the transplantation in the mouse, perfused blood vessels formed inside the bone grafts, however, it had poor mechanical stability.

The fabrication of engineered liver tissue using 3D printing of HUVECs, hepatocytes, and normal human lung fibroblasts was presented by Lee et al. [87]. In this study, to achieve the excellent mechanical properties, poly(caprolactone) (PCL) as framework material and collagen as bioink have been used. Seeding of the cells into

<sup>19</sup>Graft is a piece of living tissue that can be transplanted.

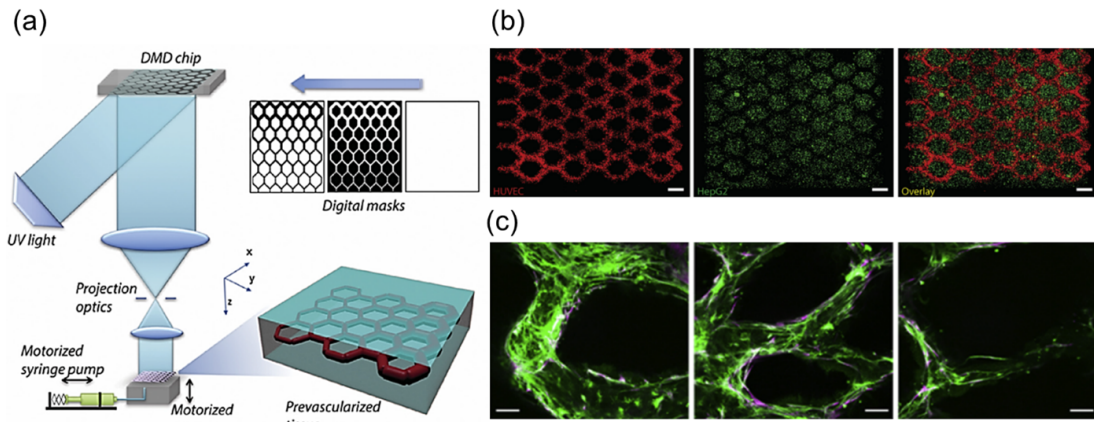


Figure 1.12: (a) Schematic of the bioprinting platform, (b) fluorescent images indicating the heterogeneous cell-laden tissue construct. HUVECs (red) are encapsulated in the intended channels and hepatoma G2 (HepG2) (green) are encapsulated in the surrounding area and (c) confocal microscopy images show HUVECs (Green) and supportive mesenchymal cells (Purple) within the patterned channel regions with different vessel sizes [84].

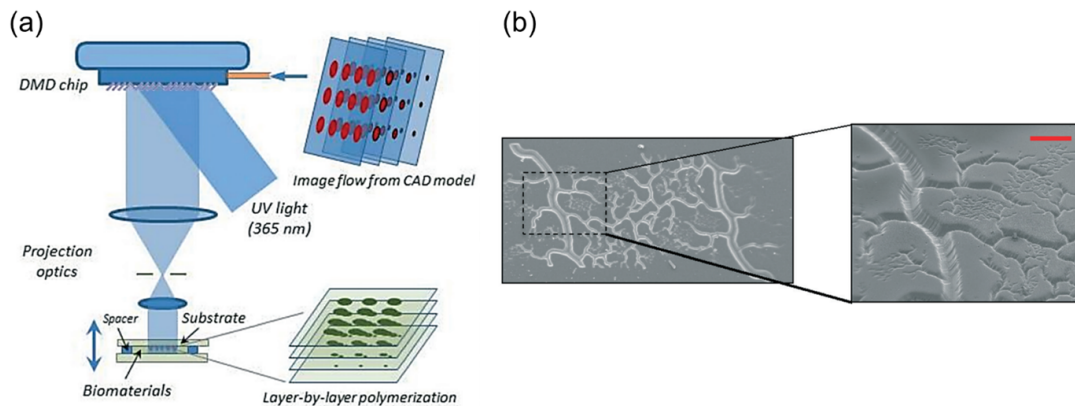


Figure 1.13: (a) Schematic of DOPsL printing setup and (b) scanning electron microscope (SEM) image of a vascular network in PEGDA [85].

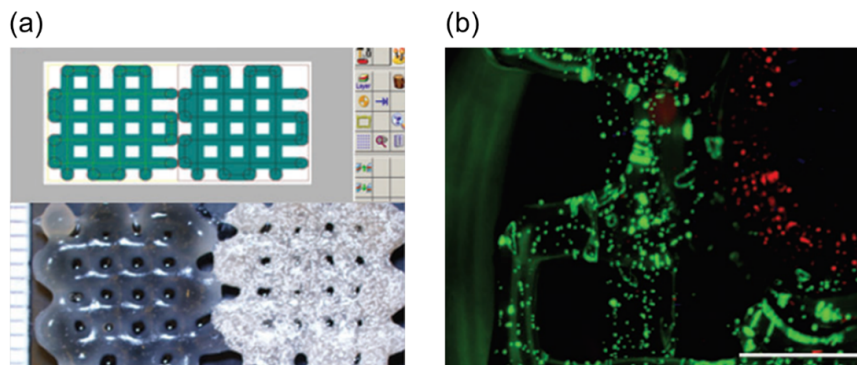


Figure 1.14: (a) Model and printed graft of the heterogeneous dual construct, endothelial progenitor cell (EPC)-laden Matrigel (left), multipotent stromal cell (MSC)-laden Matrigel part with added biphasic calcium phosphate (BCP) (right) and (b) fluorescence microscopy images of EPCs (red) and MSCs (green) printed within one tubes-in-cube construct [86].

PCL canals led to the formation of a tube-like structure and 3D liver cells growth and proliferation. The interaction of endothelial and nonparenchymal cells and their interactions have increased the viability and functionality of endothelial cells to make a tube-like formation (figure 1.15). This contribution can be valuable in liver tissue regeneration.

To form endothelialized microfluidic vessels, molding microstructures were applied on native collagen type I with injection molding techniques [88]. HUVECs were seeded within the microstructures leading to successful microvessel formation along with lumen development. The interactions of this three-dimensional microvascular network with perivascular cells such as human umbilical arterial smooth muscle cells (HUASMCs) or human brain vascular pericytes (HBVPCs) seeded in collagen matrix were investigated. Angiogenesis<sup>20</sup> in healthy and pathological scenarios and thrombosis<sup>21</sup> under quiescent and inflammatory conditions were analyzed. (figure 1.16).

To overcome current limitations in thick tissue generation, Kolesky et al, constructed a thick (e.g., over 1 cm) vascularized bone tissue, printed on a 3D perfusable chip and with long term perfusion (6 weeks), by applying indirect extrusion (figure 1.17) [89]. First, a perfusion chip was printed using a silicone ink. Then, pluronic

<sup>20</sup>Angiogenesis is the process of new blood vessel formation.

<sup>21</sup>Thrombosis happens when the veins or arteries are blocked by the blood clots.

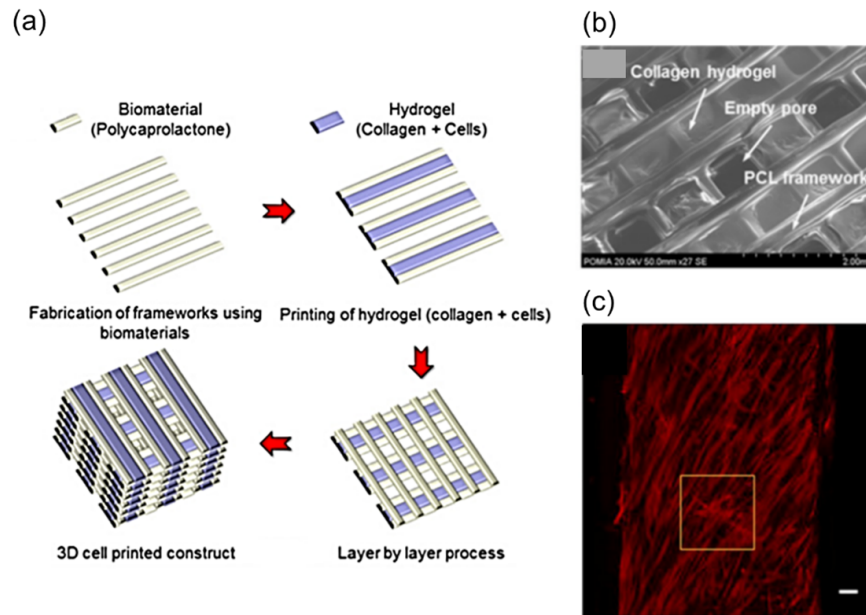


Figure 1.15: (a) Schematic of cell printed scaffold fabrication steps, (b) SEM image of a freeze-dried 3D scaffold and (c) confocal microscopy image of capillary network formation by HUVECs in the printed collagen line at day 14 [87].

F127-thrombin blend fugitive ink and cell-laden bioink were printed into the 3D perfusion chip. The cell-laden bioink contained human bone marrow-derived mesenchymal stem cells (hMSCs), fibrinogen and gelatin. To form an ECM matrix, a composite material including human neonatal dermal fibroblasts (HNDFs), gelatin, fibrinogen, thrombin and transglutaminase was then cast over the printed inks. After matrix solidification through cross-links of fibrin and gelatin, the sacrificial bioink was evacuated. The hollow tubes were then perfused with HUVECs with an external pump to form vessels. Not only this study featured the advantage of fabricating a thick vascularized tissue, but also the confocal images demonstrated lumen development of the formed vascular network figure 1.17.

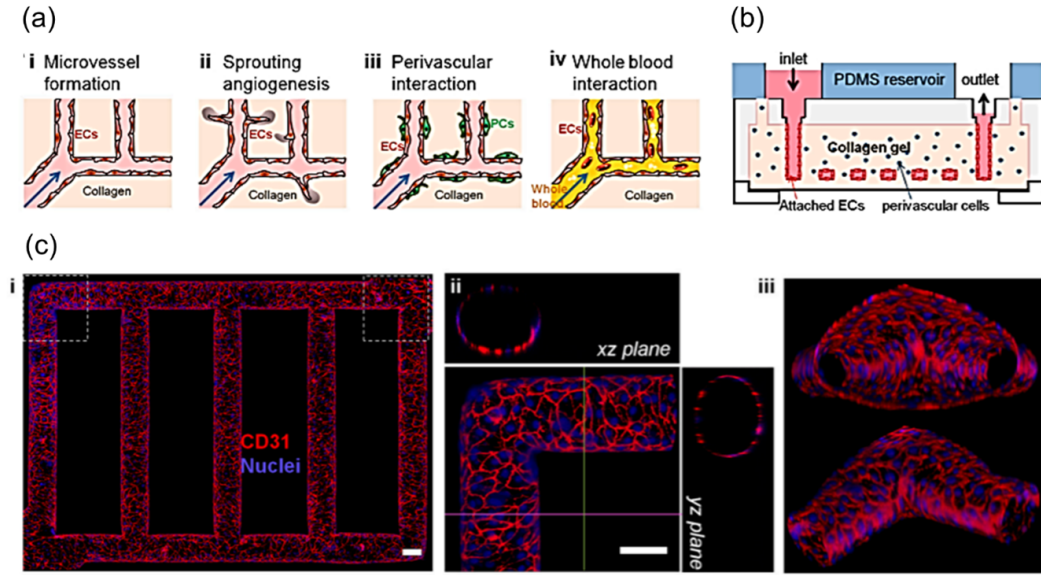


Figure 1.16: (a) Schematic cross-sectional view of a section of  $\mu$ VN illustrating, (b) schematic of microfluidic collagen scaffolds after fabrication and (c) confocal microscopy images of endothelialized microfluidic vessels, Z-stack projection of horizontal sections of the network, its corner view and branching sections Red, CD31; blue, nuclei [88].

## 1.4 Cavitation bubbles and applications of laser-based bubble

In the method presented in this thesis, a laser-induced cavitation bubble is used to print the cells. Therefore, the following sections concentrate on a brief description of the cavitation bubble, its applications (section 1.4) and modeling of bubbles and microjets dynamics (section 1.5).

Cavitation bubbles occur where the liquid pressure is locally lower than the saturated vapor pressure at a given temperature. This phenomenon can be produced by spark discharge [90], ultrasonic [91,92] and laser pulses [93–95]. Because of the high controllability of the bubbles created by laser pulses, the bubbles formed in this way have gained many applications in biomedical engineering including eye surgery [96], high-speed cell sorting [97–99], needle-free injection [100–105], printing [106], laser lithotripsy [107–109].

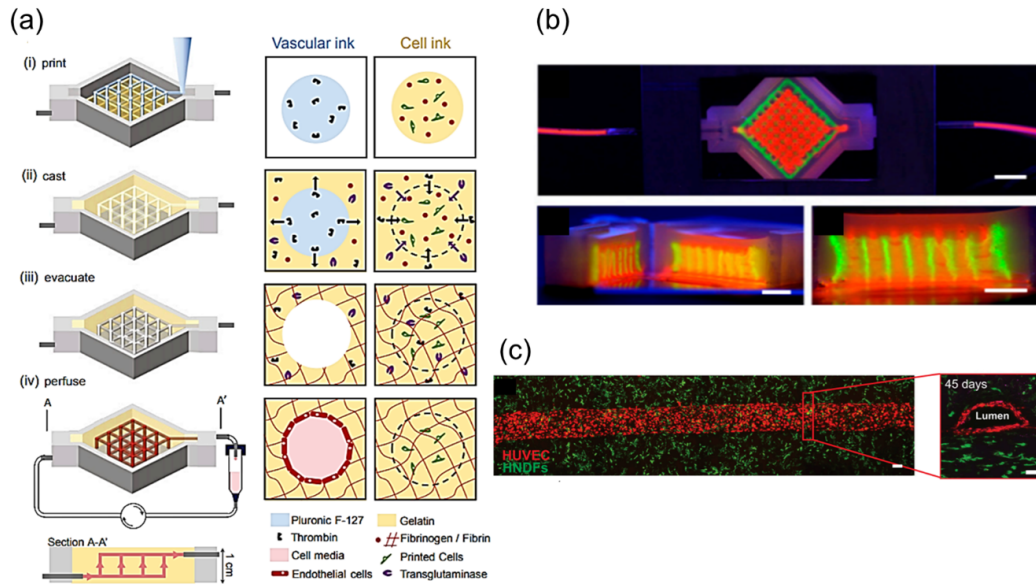


Figure 1.17: (a) Schematic illustration of tissue fabrication process, (b) printed tissue construct within a perfusion chamber, (c) printed tissue construct removed from the perfusion chamber and d) confocal microscopy of HUVECs (red) lining vascular network supported by HNDF-laden (green) matrix at 45 days of perfusion [89].

## Lithotripsy

One of the laser-induced bubble applications is in laser lithotripsy which is a minimally invasive method for fragmentation of kidney stones with a fiber-guided pulsed laser. The laser energy transfers to the urinary stone via a vapor bubble. The absorbed energy then fragments the stones due to the photothermal mechanism [107, 108]. The variation in the fiber optic tips offers different bubble dynamics and forward pressure [109].

## Soft tissue scalpel

Additionally, the laser-induced bubbles can be used as and scalpel in soft tissues. Lee et al. designed a laser-induced focused ultrasound to generate micro-cavitation for soft tissue cutting and ablation purposes [110]. In this method, a focused photoacoustic pulse is produced by radiating a pulsed laser beam on the carbon nanotube-polydimethylsiloxane (CNT-PDMS) coated on a concave lens. The focused photoacoustic pulse creates free-field and controllable micro-cavitation in water (Figure

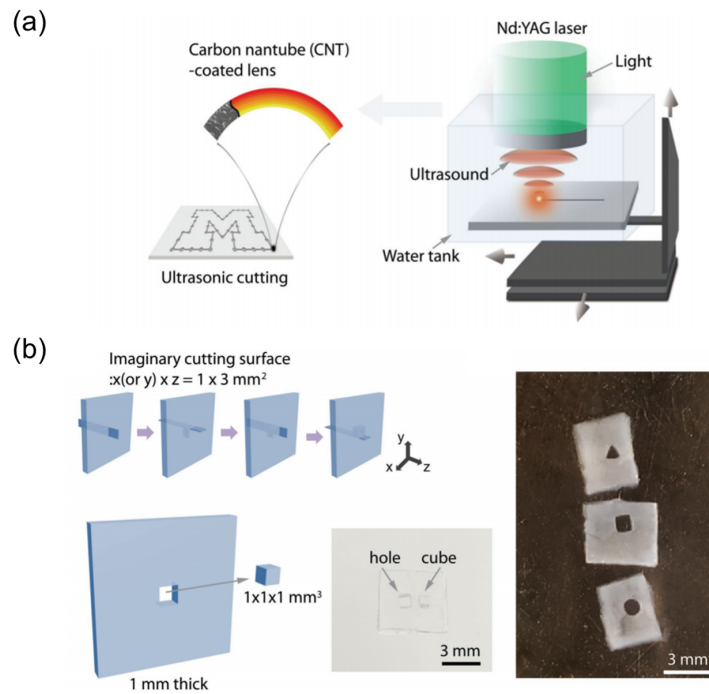


Figure 1.18: (a) Experimental setup for cavitation-based sonic cutting, Laser-induced focused ultrasound creates micro-cavitation in a sample mounted on a motorized stage, (b) schematics of the sonic cutting of tissue-mimicking gel (1 mm thick) for a square hole. Ultrasonic micro-cavitation is sequentially applied on four imaginary cutting surfaces and (c) other primitive shapes (circle and triangle) produced by the sonic cutting [110].

1.18). Such cavitation is spatially-regulated within the focal volume and is able to cut water-rich material such as soft tissues with micrometric resolution. The advantage of this cavitation-based approach over the conventional laser cutting methods is in its ability to cut opaque tissues. In these tissues, incisions are not made efficiently using a laser light due to the low penetration depth.

## Cell sorting

Wu et al. introduced a Pulsed Laser Activated Cell Sorting (PLACS) in which the laser-induced microbubble is used for switching purposes in a microfluidic device [97,98] (Figure 21.19). The microbubble expansion generates a high-speed horizontal microjet ( $<30 \mu\text{s}$ ). The microjet deflects the desired cell towards the collection channel for sorting right after being detected by the fluorescence detection region. The method presents high-purity and high-speed because of bubble reproducibility

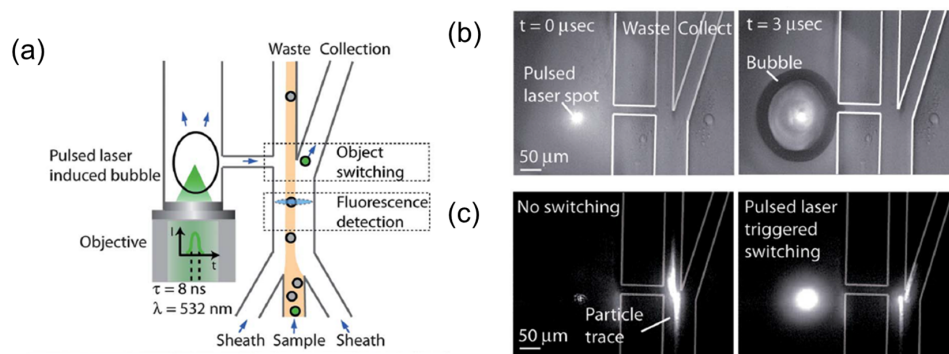


Figure 1.19: PLACS operation, (a) schematic of the cell sorter. The sample flow is hydrodynamically focused on the waste channel, (b) time-resolved images of the cavitation bubble generated by the focused pulsed laser beam in the microfluidic cell sorter and (c) fluorescent particle switching in PLACS without switching [97,98].

and high-speed microjet, respectively. Chen et al. developed a 3D PLACS based on microfluidic [99]. The parabolic flow velocity profile causes a variation in the velocity of the cells at different vertical positions. Therefore, the cells arrived at the switching point with different delays after the fluorescence detection. The variation in the delay impacts the sorting purity. The method utilized multilayer 3D channels to improve the purity by third-dimensional flow.

### Micro-pump in microfluidic device

Fluid transfer within micro-channels can be done by pneumatically-controlled pumps. However, interfacing external tubing on the micro-devices is time-consuming and microfluidic circuitries become complicated with increased number of channels. Chen et al. presented a laser pulse-driven microfluidic pump to eliminate the drawbacks of conventional methods [111]. The force that guides the flow in the micro-channel is generated by scanning laser-induced bubbles. The bubbles have been generated in the secondary channel to avoid any potential contaminants resulting from the cavitation process (Figure 1.20). Dijkink et al. showed laser-induced bubbles in microfluidic are reproducible and can control the volume precisely in the order of picoliters [112]. The amount of pumped liquid can be adjusted by the distance of the bubble from the channel and the variation in laser energy.

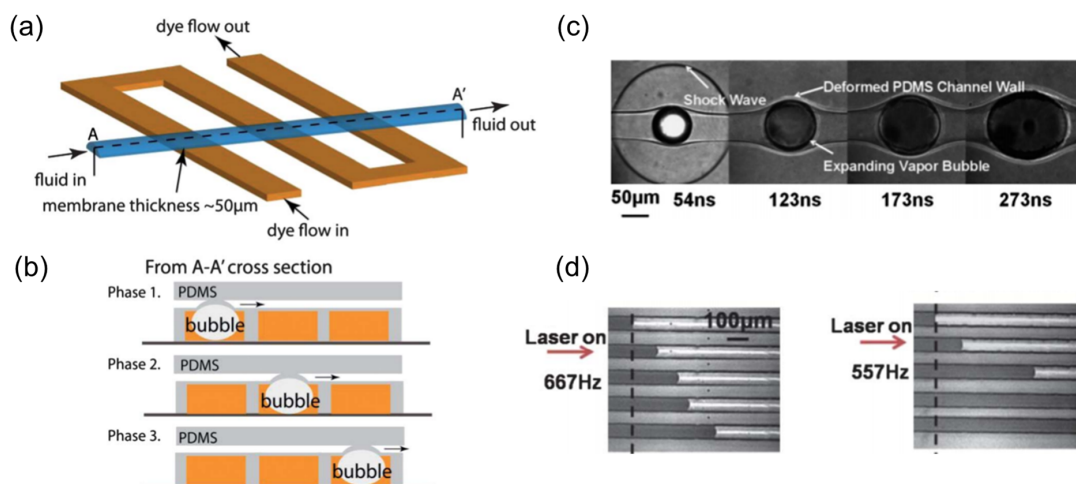


Figure 1.20: (a) Schematic of the pulse laser-driven peristaltic membrane pump, (b) the synchronized laser-induced cavitation bubbles deform the thin membranes in sequence to push the fluid in the sample channel forward, (c) a laser pulse focused in the middle of a wide channel excites an explosive bubble that quickly expands the channel width and d) two different pumping rates [111].

## Laser generated microdroplet/jet applications

**Droplet generator in microdevices** Generating droplets are required for microfluidic applications. Using laser-induced cavitation bubble, Park et al demonstrated the high speed and on-demand droplet generator (Figure 1.21) [113]. Figure 1.21b shows the time-resolved images of a single droplet. It indicates a 1 kHz to 10 kHz droplet generation speed.

**Needle-free injection** Han et al. introduced the laser-based injector for needle-free drug delivery purposes [100]. The device consists of two reservoirs split by an elastic membrane. Laser-induced bubble deforms the membrane. The deformation generates high-speed (average velocity: 264 m/s) micro-droplets of drugs. By controlling the laser parameters, Jang et al. showed that optimal quantity of drugs can be delivered at the desired penetration depth [101]. To enhance the performance and prepare the device for clinical use, added a stepper motor to provide uniform pressure in the drug reservoir before an ejection (Figure 1.22). It could compensate the drug based on the jet characteristics including velocity and volume. Variation in the laser energy (400-1200 mJ) changes the microjet velocity. Then, it precisely reaches 400-1800  $\mu\text{m}$

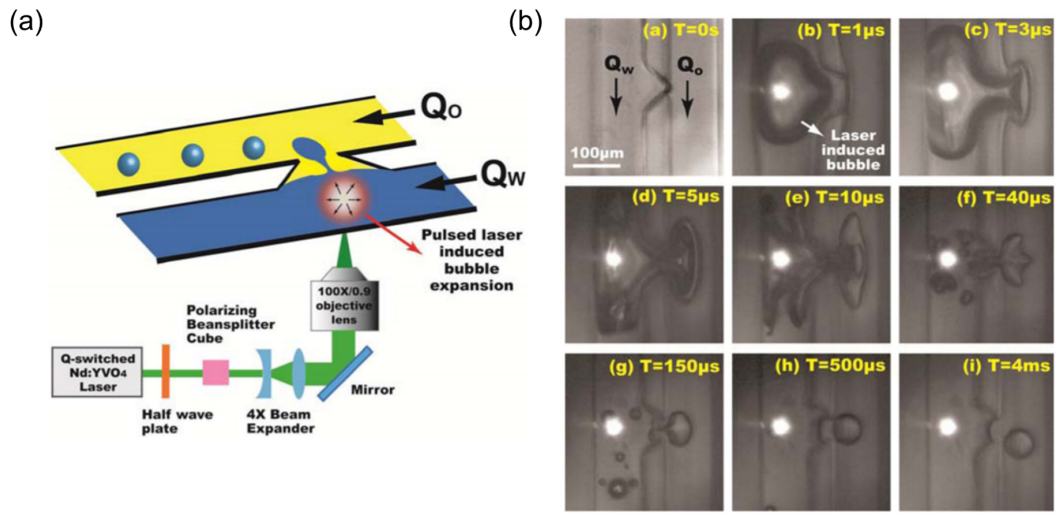


Figure 1.21: (a) Schematic of laser droplet generator device and (b) time-resolved images of on-demand droplet generation [113].

skin depth [102, 103] or into fat tissue [104] with the exact amounts and uniform delivery [105].

Tagawa et al. developed a needle-free injection method using highly-focused high-speed microjets (as high as 850 m/s) [114, 115]. The technique uses a focused laser pulse in a micro-capillary to generate a microbubble. Rohilla et al. used the same approach to investigate the efficacy of needle-free injection on gelatine substrates and ex-vivo tissue samples shown in Figure 1.23 [116]. They found that geometry characteristics (including capillary diameter and laser focal point) and fluid properties such as viscosity affect the transient penetration dynamics and dispersion pattern. For deep penetration to the stiff tissue, Krizek et al. presented a repetitive regime of microjets to mitigate bruising and pain associated with conventional injectors [117]. Using a similar technique, delrot et al. demonstrated depth-controlled liquid injection in soft gelatin. They were able to deliver picoliter doses up to sub-mm depth without any reloading steps [118, 119].

**Printing** The printable viscosity range in existing drop-on-demand (DOD) units is limited to 100 mPa.s. Delrot et al. developed a laser-induced printing approach for patterning viscous inks upto 210 mPa.s [120]. Figure 1.24 illustrates the schematic of the technique.

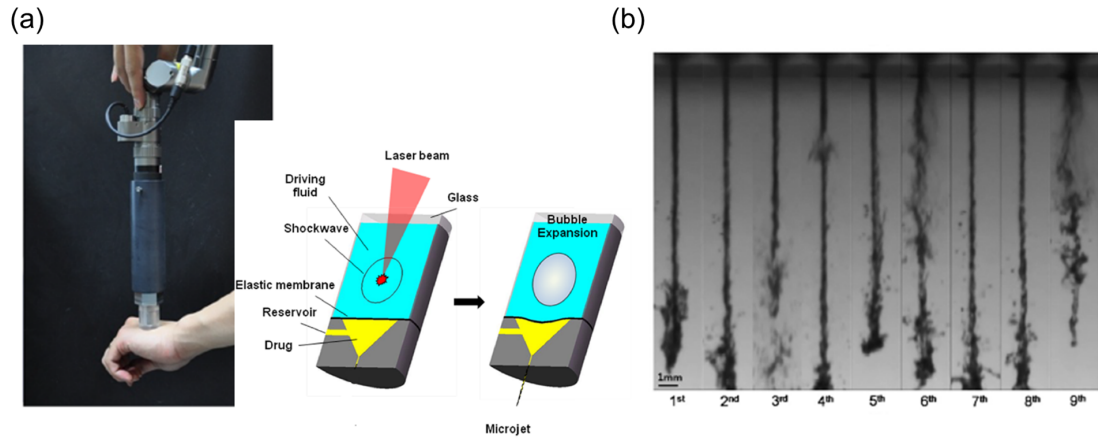


Figure 1.22: (a) Illustration of the sequential mechanisms of the laser-based microjet generation and (b) image of repeated microjet without refilling [100, 101].

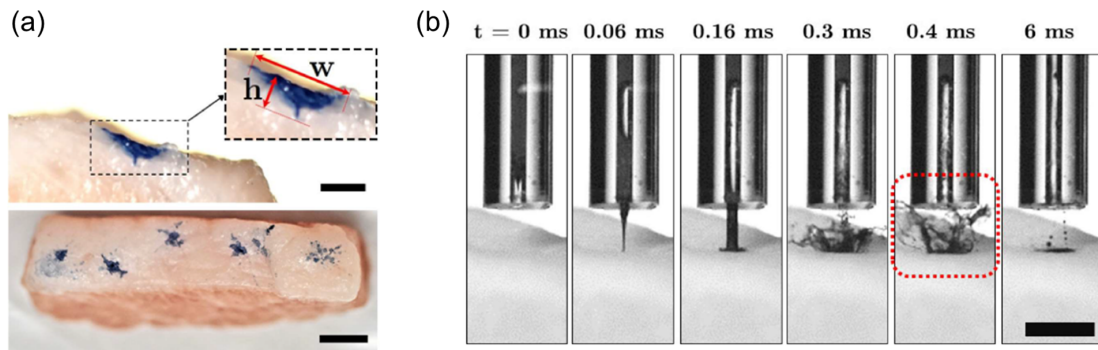


Figure 1.23: Ex-vivo study, (a) cross-sectional and top view of the porcine tissue after injections via laser focusing and (b) snapshots of dyed water injection into the porcine tissue from the glass capillary [116].

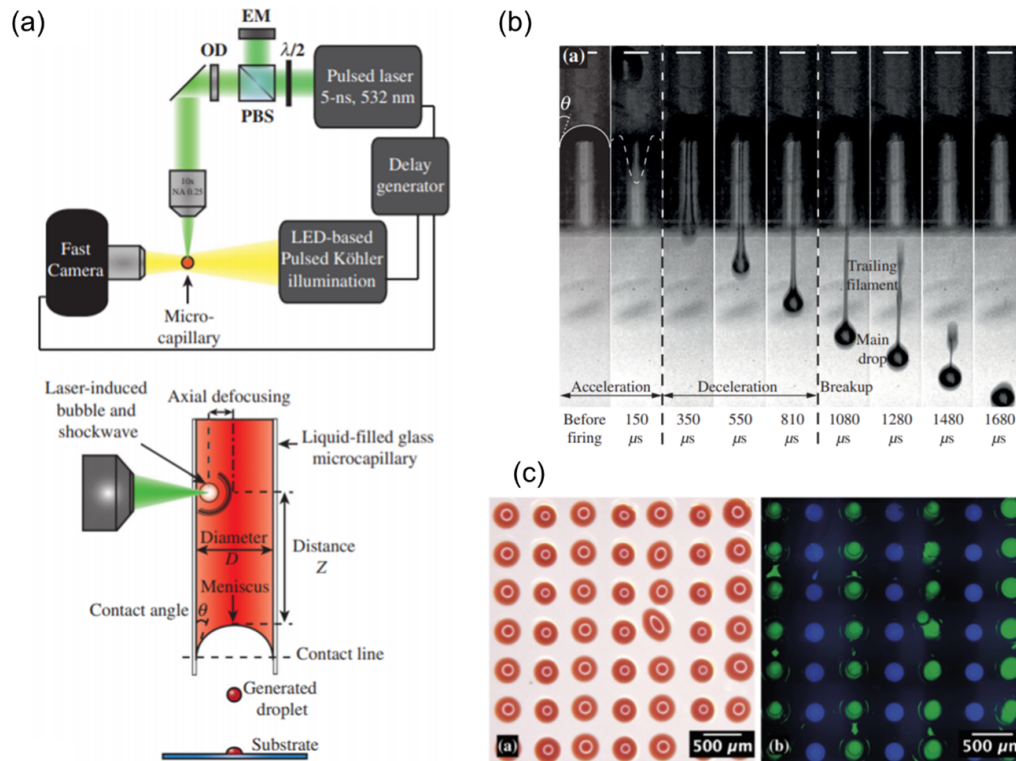


Figure 1.24: (a) Top view of the time-resolved imaging setup, (b) side view of the microcapillary in which the droplets are generated, (c) series of time-resolved images of the jet formation and (d) array of droplets with rabbit and mouse immunoglobulin G (IgGs) imaged with a bright-field microscope and the same array imaged under fluorescence (performing an immunoassay with fluorescent-labeled secondary anti-IgGs against rabbit) [120].

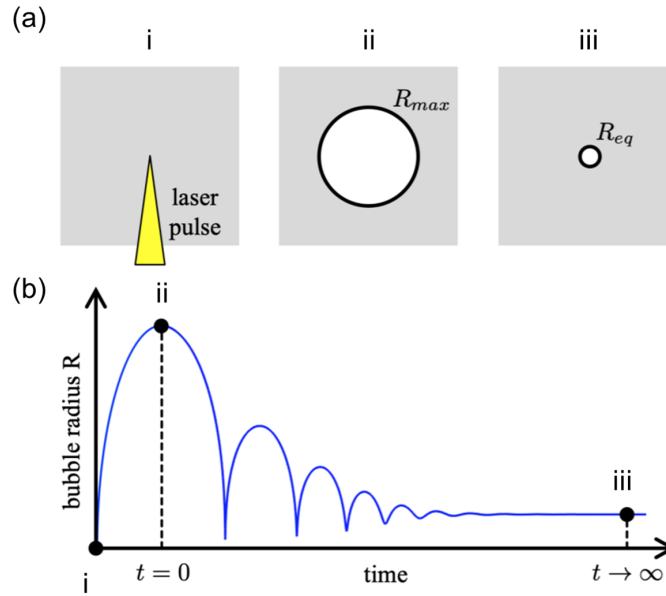


Figure 1.25: (a) The process of a laser-induced cavitation bubble, a laser pulse is focused in the liquid (i) which causes the growth of the bubble to its maximum radius ( $R_{max}$ ) (ii) and then the bubble collapses and oscillates toward the equilibrium state with the radius  $R_{eq}$  (iii) and (b) the bubble radius vs time [124].

## 1.5 Modeling of bubble dynamics and bubble-induced microjets

### 1.5.1 Analytical simulation of spherical bubbles

Cavitation bubbles occur where the liquid pressure is locally lower than the saturated vapor pressure at a given temperature. This phenomenon can be produced by spark discharge [90, 121], ultrasonic [91, 92] and laser pulses [95, 122, 123]. Because of the high controllability and the fact that it is non-contact process, the bubbles formed by laser pulses have gained many applications in biomedical engineering. Figure 1.25 shows the process of a laser-induced spherical bubble and the bubble radius versus time [124].

The bubble dynamics vary with the variation in the properties of the liquid in which the bubbles are formed. Predictable dynamics of the bubbles under different conditions (i.e. properties of liquid and environmental parameters where the bubble is generated) leads to their optimal use in their applications. Currently, there are

analytical models to describe the bubble dynamics while considering the liquid properties. The most important of which are Rayleigh-Plesset (RP) [125], Keller-Miksis (KM) [126] and Gilmore-Akulichev (GA) [127, 128] models.

### Rayleigh Plesset model

Rayleigh made the first attempt to describe the spherical bubble dynamics. There are three underlying assumptions in the proposed model [125, 129, 130]: i) the gas in the bubble is affected by the isothermal process<sup>22</sup>; ii) no mass can be transferred between the gas and the liquid; iii) the liquid is incompressible<sup>23</sup>. Also, the effect of surface tension and fluid viscosity was neglected. Using the momentum equation, Rayleigh showed that the bubble boundary  $R(t)$  follows the Eq. 1:

$$R\ddot{R} + \frac{3}{2}\dot{R}^2 = \frac{P(R) - P_l}{\rho} \quad (1)$$

Where  $\rho$  is the liquid density,  $P_l$  is the liquid pressure at a long distance from the bubble and  $P(R)$  is liquid pressure at the bubble boundary. Although surface tension and fluid viscosity were not considered in the Rayleigh equation, the above equation can be extended to account for the effect of these two parameters. Since the viscosity effect is only on the boundary conditions,  $P(R)$  can be written as follows (Eq. 2):

$$P(R) = P_g - \frac{2\sigma_l}{R} - \frac{4\mu}{R}\dot{R} \quad (2)$$

Where  $P_g$  is the gas pressure in the bubble,  $\mu$  is the dynamic viscosity; and  $\sigma_l$  is the surface tension. Rayleigh-Plesset model extended the Rayleigh equation by considering Eq. 2 as the governing equation of liquid pressure at the bubble boundary (Eq. 3):

$$R\ddot{R} + \frac{3}{2}\dot{R}^2 = \frac{P_g - P_l}{\rho} - 4\nu\frac{\dot{R}}{R} - \frac{2\sigma_l}{\rho R} \quad (3)$$

$\nu$  is the kinematic viscosity, Assuming the whole process is adiabatic, RP equation can be rewritten as follows (Eq. 4):

$$R\ddot{R} + \frac{3}{2}\dot{R}^2 = \frac{P_{g0}}{\rho}\left(\frac{R_0}{R}\right)^{3\gamma} - \frac{P_l - P_v}{\rho_0} - 4\nu\frac{\dot{R}}{R} - \frac{2\sigma_l}{\rho R} \quad (4)$$

---

<sup>22</sup>Isothermal process is a thermodynamic process in which the temperature remains constant.

<sup>23</sup>Incompressible liquid is a fluid in which the density remains constant.

$\gamma$  is heat capacity ratio,  $R_0$  is the initial bubble radius ( $t = 0$ ),  $P_v$  is the saturated vapor pressure in the bubble, and  $P_{g0}$  is the initial gas pressure in the bubble ( $t = 0$ ). Rayleigh-Plesset equation describes the dynamics of a spherical bubble for different liquid properties (e.g. viscosity [131,132] and density [133]) which have been experimentally studied for years.

### **Keller Miksis model**

Keller and Miksis updated the RP model to describe the dynamics of the bubble in which the fluid compressibility and the wave motion of the bubble radius are taken into account [126,134,135]. Since KM model considers liquid compressibility, it accurately describes the bubble dynamics compared to RP model. KM equation is a second-order nonlinear ordinary differential equation for fluid dynamics which is given as follows (Eq. 5):

$$\begin{aligned}
& \left(1 - \frac{\dot{R}}{c}\right)R\ddot{R} + \frac{3}{2}(\dot{R})^2\left(1 - \frac{\dot{R}}{3c}\right) = \\
& \frac{1}{\rho}\left(1 + \frac{\dot{R}}{c}\right)\left[\left(P_g - P_v + \frac{2\sigma_l}{R_0}\right)\left(\frac{R_0}{R}\right)^{3\gamma} + P_v - P_l\right] - 4\nu\frac{\dot{R}}{R} - \frac{2\sigma_l}{\rho R} \\
& - \frac{3}{c\rho}\left(P_g - P_v + \frac{2\sigma_l}{R_0}\right)\left(\frac{R_0}{R}\right)^{3\gamma}\dot{R}
\end{aligned} \tag{5}$$

Where  $C$  is the speed of sound at the bubble wall. Mach number in KM equation is one of the factors for simulating fluid compressibility. KM model estimates the maximum radius and lifetime of the bubble more accurately. While the RP equation is only able to model the bubble's first cycle, the key element in KM model is the potential to simulate bubble oscillation after the primary bubble. The radius of these oscillations is smaller and has a shorter lifetime than the primary bubble as per KM model.

### **Gilmore Akulichev model**

The model proposed by Gilmore-Akulichev describes the dynamics of the bubble considering liquid compressibility. In KM and RP, the gas content of the bubble is considered constant. This assumption is often inaccurate since gas diffusion occurs

when the gas densities of different materials are different [127]. During the formation and expansion of the bubble, more gas flows from the liquid to the bubble and during the collapse, the gas flows into the liquid. Considering the gas diffusion, the gas pressure considered in Eq. 2 and Eq. 3 is no longer constant and depends on the number of moles and bubble radius as shown in Eq. 6 [127, 128]:

$$P_g = (P_{g0} + \frac{2\sigma}{R_0}) \frac{n}{n_0} (\frac{R_0}{R})^{3\gamma} (\frac{R_{0n}}{R_0})^{3(\gamma-1)} \quad (6)$$

Where  $n$  and  $n_0$  are instantaneous and the initial number of moles in the bubble, respectively.  $R_{0n}$  is the time-varying equilibrium bubble radius. Considering the effect of gas diffusion and compressibility, the Gilmore-Akulichev equation is well suited for high pressure condition and is described as follows (Eq. 7-11) [127, 128, 136, 137]:

$$(1 - \frac{\dot{R}}{c})R\ddot{R} + \frac{3}{2}(\dot{R})^2(1 - \frac{\dot{R}}{3c}) = (1 + \frac{\dot{R}}{C})H + \frac{\dot{R}}{C}(1 - \frac{\dot{R}}{C})R\frac{dH}{dR} \quad (7)$$

$$P = A(\frac{\rho}{\rho_0})^m - B \quad (8)$$

$$A = \frac{C_l^2 \rho}{P_0 m}, m = 7, B = A - 1 \quad (9)$$

$$H = \int_{P_\infty}^{P(R)} \frac{dP}{\rho} \quad (10)$$

$$P(R) = P_g - \frac{2\sigma}{R} - \frac{4\mu}{R}\dot{R} \quad (11)$$

Where  $H$  is the enthalpy of the liquid.

## 1.5.2 Bubble and microjet dynamics in the confining conditions

### Bubble dynamics

It can be concluded from the analytical models presented in section 1.5, fluid properties such as density and viscosity, gas pressure trapped in the bubble and liquid

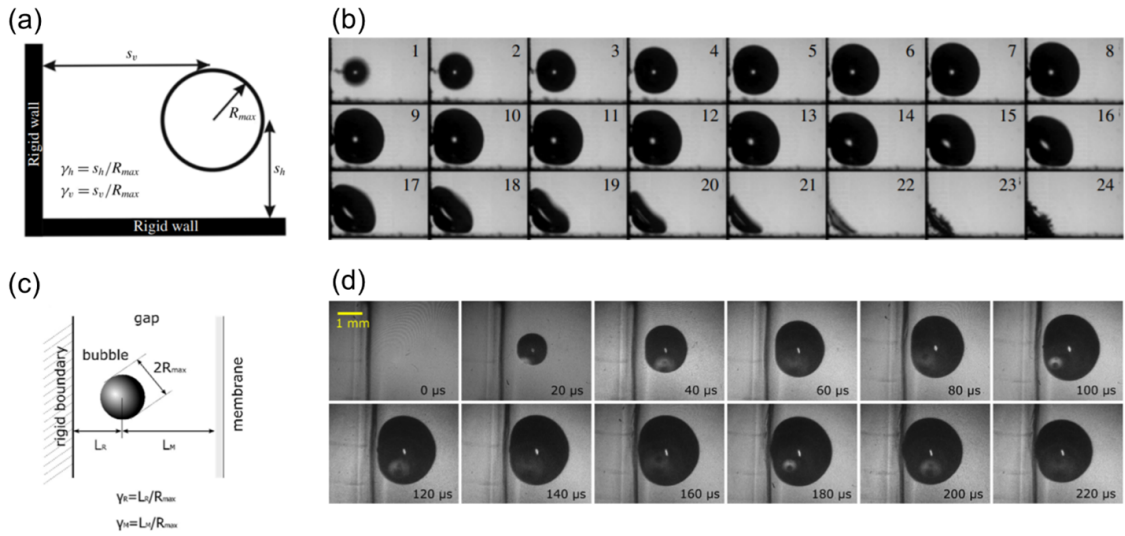


Figure 1.26: (a) Schematic of a laser-induced cavitation bubble placed near two, (b) Dynamics of a bubble placed near two perpendicular rigid walls for  $\gamma_h = 1.08$ ,  $\gamma_v = 0.88$ ,  $R_{max} = 0.85$  mm. Frame interval  $10 \mu s$ . Frame width 3 mm [139], (c) schematic of bubble place near a rigid boundary and an elastic membrane and (d) Bubble dynamics positioned near the boundary, pulse energy 10 mJ, gap width  $300 \mu m$ ,  $\gamma_M = 0$  [141].

pressure in the reservoir have a significant effect on bubble dynamics. The application described in section 1.4 mostly used bubbles in confined geometry. Hence, the effects of geometry and liquid pressure in the reservoir play a key role in accurately describing the bubble dynamics. To this end, many attempts have been made to illustrate the dynamics of the bubble near the boundaries. Pozar et al. showed that pressure builds up in the liquid by creating bubbles near a rigid concave surface [138]. Brujan et al. presented their investigation on the laser-induced cavitation bubble near two perpendicular rigid walls and the effect of distance between the walls and the bubble on the bubble dynamics [139] (figure 1.26a and b). The results show that the greater the ratio of the maximum radius to the distance of the bubble from the wall, the more compressed the bubble becomes. Research on bubble dynamics near flexible walls also reveals changes in bubble radius and its uniformity [140]. Also, research has been done on the simultaneous effect of flexible and rigid walls by Horvat et al. [141]. They presented that the bubble evolution is significantly dependent on the position of the bubble to the boundary by examining the dynamics of the bubble in the gap between a rigid boundary and an elastic membrane (figure 1.26c and d).

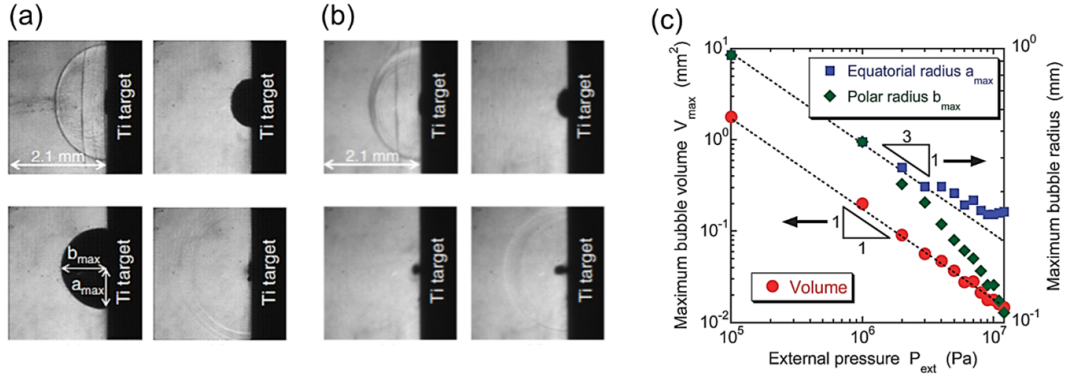


Figure 1.27: Shadowgraph frames of laser-induced bubble dynamics in water at (a)  $1 \times 10^5$  Pa, (b)  $3 \times 10^5$  Pa and (c) maximum bubble volume and radius vs the external pressure applied to the ambient water [144].

Limiting bubbles with such boundaries significantly reduces the bubble radius and shortens its lifetime. The main reason is local variation in the liquid density due to local compressibility. Lauterborn et al. indicated that the pressure of the liquid near the wall and the bubble boundary increases significantly with the growth of the bubble [142], and Lechner et al. pointed to a local pressure increase in the liquid due to bubbles generation near a rigid wall [143].

According to the aforementioned, the increase in liquid pressure can be considered a key parameter on the variation of bubble dynamics. Research has been done on the effect of the liquid pressure on the maximum bubble radius and its lifetime [144, 145]. Sasaki et al. have shown that the maximum volume of the bubble is inversely proportional to the liquid pressure (figure 1.27a and b) [144]. For example, increasing the pressure of the liquid in the reservoir to 100 atm reduces the maximum volume of bubbles by 100 times in the pressurized reservoir. It has also been shown that increasing the liquid pressure significantly reduces the lifetime of the bubbles (figure 1.26c).

From the above discussion, we can conclude the following:

1. The generation of bubbles near the wall changes the bubble dynamics due to the liquid pressure increase.
2. There is a sharp decrease in the bubble radius and its lifetime by increasing the pressure in the reservoir.

As the bubble grows inside the confined geometry, the pressure of the liquid in the reservoir increase. This time-dependent increase in the liquid pressure inside the confined geometry prevents the bubble from freely growing. To the best of our knowledge, the self-limiting effect of bubbles in the reservoir has not been investigated. Experimental and analytical studies to measure the liquid pressure in the reservoir during a bubble's lifetime and its effect on bubble dynamics will provide valuable information. This information can be used for the applications that cavitation bubbles have in medical sciences.

### **Bubble-induced microjets**

As mentioned in the section 1.4, lasers have been extensively used for microjet and droplet generating devices, such as the LIFT, needle-free injectors, and printers. Efforts have been made to simulate the droplets or microjets generators for optimization purposes. By presenting a computational model, Brown et al. studied the dynamics of the droplet/microjets produced by LIFT [146]. In this study, the bubble dynamics is simulated as moving boundaries in the fluid domain. It should be noted that these deformations were recorded experimentally. The mass and momentum conservation equations were discretized using the finite volume method. With the presented model in this research, the effect of fluid properties such as viscosity, surface tension, and laser energy on the dynamics of the droplet/microjet was parametrically studied for optimization purposes [146, 147].

Kyriazis et al. presented the simulation of the bubble generated in the laser-induced droplet generator [148]. The model simulated the bubble and microjet dynamics applying the initial bubble pressure in the model. In this study, the effect of meniscus shape on microjet dynamics was investigated; and it was shown that trumpet shape meniscus produces a more concentrated jet. Peter et al. also modeled the effect of bubbles on the fluid in the form of a pressure wave to simulate the laser-induced droplet/microjet generators [149]. The effect of bubble location and contact angle on bubble dynamics was parametrically investigated.

As mentioned in section 1.4, the bubbles in the microjet/droplet generators can also be generated through sparks or heating. Tan proposed a model for simulating bubbles and droplets created in inkjet printers that work with thermal actuators. Dadvand et al. also presented a numerical model for simulating droplets created

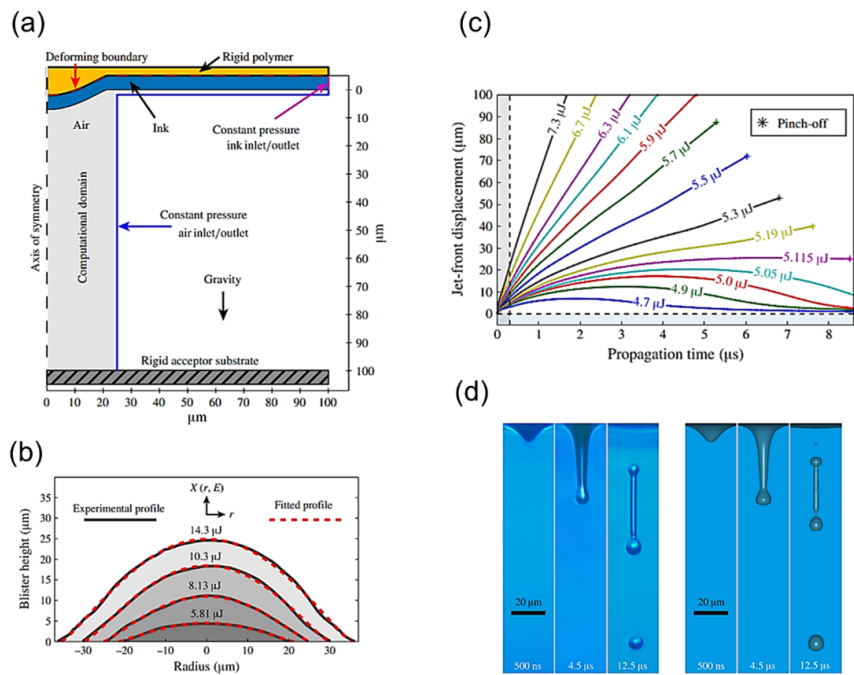


Figure 1.28: (a) Computational model, (b) experimentally measured bubble profile with the fitted profile and (c) jet-front displacement vs. time for a range of laser energy from 4.7 to 7.3 μJ (d) Experimental and simulation simulation results of droplet dynamics from a 5 μm donor film using 5.4 μJ [146].

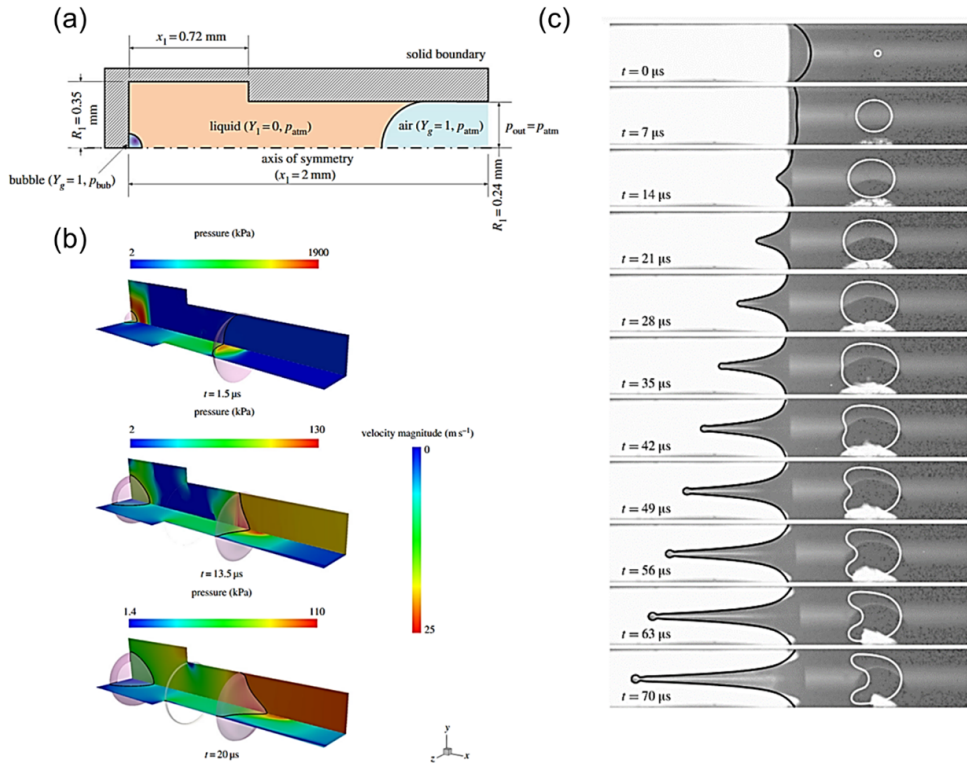


Figure 1.29: (a) Computational domain of needleless injector, (b) two-dimensional axisymmetric needle-free device simulation results for  $p_{bubble} = 5 \times 10^7$  Pa and the standard meniscus shape [148] and (c) experimental (background image) and simulation of jet formation (solid lines), the absorbed energy is  $365 \mu\text{J}$  and distance between the laser spot and meniscus is  $600 \mu\text{m}$ . Pressure amplitude is 1581 bar with 50 ns duration [149].

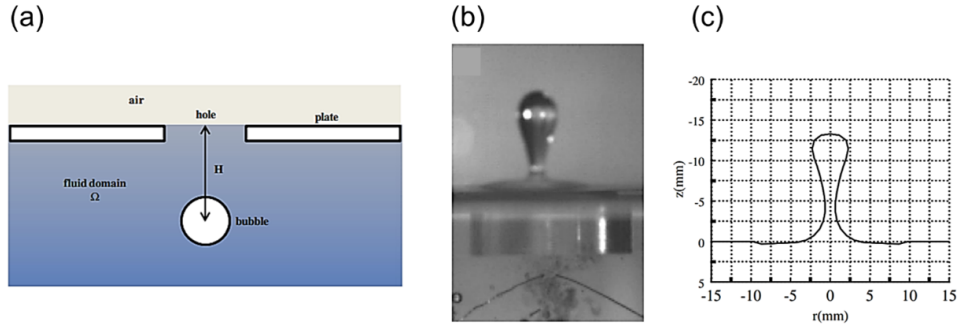


Figure 1.30: (a) Schematic of the physical domain, (b) experimental frame of the spark bubble droplet formation and (c) simulation result corresponding to the frame presented in b [150].

by spark bubbles [150]. In this study, the pressure wave caused by the bubble was considered as a driving force. It was also shown that the bubble position and outlet size have a considerable effect on droplet dynamics. Also, various methods have been used for numerical modeling of bubbles, including the work done by Sato et al. They used the boundary integral method to simulate the bubble profile at different time intervals [151]. In their model, the effect of reservoir confinement and bubble proximity to the wall on the liquid pressure and bubble dynamics was investigated. Similarly, the effect of geometric confinement on bubble dynamics in a narrow tube [152, 153], for the bubble generated near a rigid wall [154] and inside cylindrical /conical tubes filled with viscous liquid [155] was presented.

In many cases, the discharged energy and the shock wave created during the bubble generation impact the liquid properties and properties of the droplets. To reduce these impacts, an elastic membrane can be placed between the bubble reservoir and the reservoirs in which the ejecting liquid is stored. The pressure wave generated by the bubble transmits through the membrane to produce the droplets with minimal impact on the ejecting liquid properties. This approach has numerous applications in medical science, some of which are listed in the section 1.4. For optimization purposes, it is necessary to simulate the bubble dynamics under the confinement, the interaction between bubbles with an elastic membrane, and the simulation of droplet dynamics created by the pressure wave transmitted by the membrane. To the best of our knowledge, no research comprehensively incorporates these three points and parametrically examines the effect of geometry on droplet dynamics.

## 1.6 Problem statement and motivation

Bioprinting is a technique for creating living tissues that finds many applications ranging from drug discovery to tissue regeneration. There is a need for a vascular network within the printed tissues for functional tissue construction. Vascular networks deliver oxygen and nutrients into the tissue and carry waste and carbon dioxide from the tissue. Many efforts have been made to address this need (presented in section 1.3). However, printing micro-vessels using existing methods is quite challenging. EBB approaches print biomaterials with poor resolution and moderate cell viability. In inkjets, the printability is limited to a narrow range of bioinks viscosity ( $<3.5\text{-}12$  mPa.s [37]). The bioink source is restricted to the size of the donor substrate in LIFT. Therefore, it is required to have a bioprinting method that improves the shortcomings of the existing methods, as well as the ability to print multiple bioinks at high speed.

Hence, a novel bioprinting technique using laser-induced cavitation is presented in this thesis. The laser pulses focus in the bioink reservoir, causing cavitation and consequently a bubble. The pressure wave created by the bubble in a few hundred microseconds ejects a droplet of bioink. The pressure amplitude can be tuned by changing the laser energy to print bioinks with different viscosities. To optimize the process, it is required to know the exact dynamics of the bubbles in a confining geometry. Moreover, there is a need to simulate physics such as fluid-structure interaction and two-phase flow in multiphysics software.

In addition to developing the bioprinting device, its performance must be evaluated. Moreover, the functionality of primary cells (i.e. HUVECs) after the printing needs to be studied, including viability assay, formation of intercellular junctions and live imaging to record their proliferation and migration. Another motivation of this study is to create a tube-like formation by printing of HUVECs. Moreover, the printing protocol of the cells for tubulogenesis<sup>24</sup> needs to be defined including:

- Alignment of the optical components and tuning the laser energy,
- Selection and preparation of bioink compounds and hydrogel-based matrices,

---

<sup>24</sup>Tubulogenesis is the process of tube-like formation.

- Treatment of LIST-printed HUVECs using the pro-<sup>25</sup> and anti-angiogenic factors<sup>26</sup>.

## 1.7 Thesis objective and scope

The overall objective of this thesis is to develop a laser-based approach for cell bioprinting to construct a micro-sized tube-like formation with a high aspect ratio. The specific objectives of this research are:

1. Experimentally investigating the bubble dynamics in the confining reservoirs
  - (a) Development of a pump-probe experimental setup for bubble dynamics study,
  - (b) Development of a protocol for the confining reservoir preparation including degassing and liquid pressure wave recording,
  - (c) Investigation on the effect of the laser energy and reservoir volume on the bubble and the liquid pressure dynamics.
2. Simulation of the laser-induced droplet generator in a multi-physics software
  - (a) Development of a mathematical model to simulate the laser-induced bubble in the confining devices using MATLAB,
  - (b) Simulation of the bubble, fluid and structure (an elastic membrane) interactions in fluid-structure interaction (FSI) module of COMSOL,
  - (c) Simulation of the droplet dynamics in two-phase flow (TPF) module of COMSOL,
  - (d) Investigation on droplet dynamics by parametrically studying the laser energy and geometry (i.e. nozzle size and membrane thickness) with COMSOL.
3. Validation of laser-induced side transfer (LIST) bioprinting technique
  - (a) Design and construction of the experimental system,

---

<sup>25</sup>Pro-angiogenic factors are the factors that increase the growth of new blood vessels.

<sup>26</sup>Anti-angiogenic factors are the factors that reduce the growth of new blood vessels.

- (b) Experimental investigation on the droplet dynamics by varying the laser energy,
  - (c) Investigation on the viability and the functionality of the LIST-printed HUVECs,
  - (d) Investigation on the droplet dynamics and HUVECs viability using LIST in high-speed printing mode.
4. Fabrication of tube-like formation using LIST bioprinting of HUVECs
- (a) Investigation on the bioink and the matrices where HUVECs are printed for tubulogenesis purpose,
  - (b) Development of a protocol for LIST-printing of HUVECs for tubulogenesis.

## 1.8 Thesis contribution

The main contribution of this work is to develop and utilize a droplet-based bioprinter, for printing of HUVECs having negligible loss of their viability and functionality. Figure 1.31 shows the developed system configuration. The specific contributions of the present thesis are as follows:

- The first contribution of this thesis is to investigate the effect of reservoir confinement on the pressure wave profile and bubble dynamics.
- For the first time, a comprehensive simulation for the laser-induced droplet generating devices was presented. This simulation involves bubble dynamics modeling, its interaction with the liquid and the elastic membrane, and finally simulating the dynamics of the created droplets.
- As the third contribution, the development of a laser-based bioprinting technique is presented in this thesis. The device performance including the droplet dynamics, the printed HUVECs viability and functionality is evaluated. Moreover, LIST could be widely adapted for applications requiring multiscale bioprinting capabilities and can potentially print at high-speed (upto 2500 droplets per s).

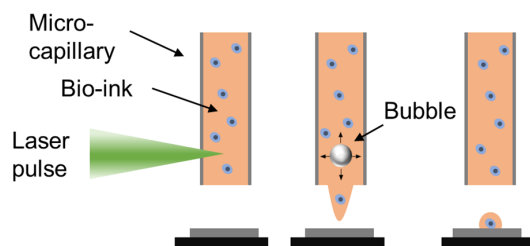


Figure 1.31: Schematic of laser-induced side transfer (LIST).

- In this thesis, a study was performed on the combination of bioink and hydrogel-based matrices to obtain the optimal condition to accelerate the formation of a tube-like structure. The fourth contribution of this thesis is to present the protocol for printing HUVECs for tubulogenesis purposes.

LIST will provide researchers a powerful tool they need for patterning of primary cells including HUVECs for drug discovery and regenerative medicine applications. Moreover, the method has a negligible impact on the printed cells (viability of over 90%), micrometric resolution and an unending supply of bioinks. It can potentially print viscous and multiple bioinks at high-speed.

## 1.9 Organization of the thesis in manuscript-based format

This manuscript-based thesis is organized into six chapters. In the present chapter, an introduction about bioprinting techniques, cavitation bubble, their applications, a literature review, the problem statement and motivation, the objective and scope, and the contribution of this thesis are presented. Chapters 2 to 5 are duplicated from three published journal articles and a journal article under review. The chapters are organized in a cohesive manner to address the objectives of the thesis defined in section 1.7 and formatted according to “Thesis Preparation and Thesis Examination Regulations” of the School of Graduate Studies at Concordia University. In the duplicated articles, sections, figures, equations, and tables are numbered according to the thesis preparation regulations. A single comprehensive reference list rather than individual papers reference list is presented in the Reference section. Conclusions of

the thesis, limitations and future recommendations are presented in Chapter 6.

*Chapter 2 is based on the following article published in Applied Physics Letters [156].*

*Ebrahimi Orimi, Hamid, Leonardo Arreaza, Sivakumar Narayanswamy, and Christos Boutopoulos. "Self-limited nanosecond laser-induced bubble growth in sealed containers." Applied Physics Letters 119, no. 6 (2021): 064101.*

We demonstrate that nanosecond laser-induced bubbles, generated in sealed containers, can experience self-limiting effects. We experimentally study such effects using simultaneous pressure and bubble dynamics recordings. We show that self-limiting effects can be drastic for mm-sized bubbles generated in sub-cm<sup>3</sup> sized containers, resulting in 0.5-fold decrease in their size and 4-fold decrease in their lifetime compared to those generated in non-sealed control containers. We use the Keller-Miksis equation to model the self-limiting effects and discuss their technological implications in applications that exploit bubble growth in confined geometries.

*Chapter 3 presents the following article published in the Journal of Fluids and Structures [157].*

*Orimi, Hamid Ebrahimi, Sivakumar Narayanswamy, and Christos Boutopoulos. "Hybrid analytical/numerical modeling of nanosecond laser-induced microjets generated by liquid confining devices." Journal of Fluids and Structures 98 (2020): 103079.*

The generation of microjets with pulsed laser irradiation is a key enabling technique for microfluidic devices, printers and needle-free drug injectors. Modeling approaches for such devices are essential to optimize their design and performance. Here we present a hybrid analytical/numerical model to simulate nanosecond laser-induced microjets generated by a dual-chamber liquid confining device. The simulated device consists of two chambers; the first one is closed and filled with a propellant liquid and the second is filled with the liquid to be ejected and equipped with a nozzle. Laser-induced cavitation is generated in the first chamber, which is separated by an elastic membrane from the second one, to reduce the thermo-mechanical impact of the absorbed laser energy on the liquid to be ejected. By modifying the generalized form of the Rayleigh–Plesset equation to account for the pressure variation inside the chamber, we show that the geometry of the liquid confining device affects drastically laser-induced bubble dynamics and the resulting jet ejection dynamics. We also demonstrate the effect of the membrane size, laser energy and nozzle size variation on

the microjet dynamics. We found that such devices can generate microjets (velocity: 0.93 m/s to 48.39 m/s) suitable for micro-drop printing (volume: 0.097 nL to 7.68 nL). Although we focused on printing applications, the modeling approach presented here can be widely adapted for designing and optimizing needle-free drug injectors and microfluidic devices.

*Chapter 4 presents the following article published in Scientific Reports [158].*

*Orimi, Hamid Ebrahimi, Sayadeh Sara Hosseini Kolkooh, Erika Hooker, Sivakumar Narayanswamy, Bruno Larrivé, and Christos Boutopoulos. "Drop-on-demand cell bioprinting via Laser Induced Side Transfer (LIST)." Scientific Reports 10, no. 1 (2020): 1-9.*

We introduced and validated a drop-on-demand method to print cells. The method uses low energy nanosecond laser (wavelength: 532 nm) pulses to generate a transient microbubble at the distal end of a glass microcapillary supplied with bio-ink. Microbubble expansion results in the ejection of a cell containing microjet perpendicular to the irradiation axis, a method we coined Laser Induced Side Transfer (LIST). We show that the size of the deposited bio-ink droplets can be adjusted between 165 and 325  $\mu\text{m}$  by varying the laser energy. We studied the corresponding jet ejection dynamics and determined optimal conditions for satellite droplet-free bioprinting. We demonstrated droplet bio-printing up to a 30 Hz repetition rate, corresponding to the maximum repetition rate of the used laser. Jet ejection dynamics indicate that LIST can potentially reach 2.5 kHz. Finally, we show that LIST-printed human umbilical vein endothelial cells (HUVECs) present negligible loss of viability and maintain their abilities to migrate, proliferate and form intercellular junctions. Sample preparation is uncomplicated in LIST, while with further development bio-ink multiplexing can be attained. LIST could be widely adapted for applications requiring multiscale bioprinting capabilities, such as the development of 3D drug screening models and artificial tissues.

*Chapter 5 presents the following article submitted to Biofabrication.*

*Orimi, Hamid Ebrahimi, Sayadeh Sara Hosseini Kolkooh, Erika Hooker, Sivakumar Narayanswamy, Bruno Larrivé, and Christos Boutopoulos. "Spatially-guided endothelial tubulogenesis by laser-induced side transfer (LIST) bioprinting of HUVECs", under review, Biofabrication.*

The ability to bioprint microvasculature networks is central for drug screening

and for tissue engineering applications. Here we used a newly developed bioprinting technology, termed laser-induced side transfer (LIST), to print human umbilical vein endothelial cells (HUVECs) and to spatially guide endothelial tubulogenesis. We investigated the effect of three bioprinting matrices (fibrin, Matrigel and Matrigel/thrombin) on HUVECs self-assembling. Furthermore, we studied the effect of pro- and anti- angiogenic compounds on sprouting angiogenesis and tubulogenesis. We found that HUVECs self-assembling is optimal on Matrigel/thrombin due to the formation of fibrin stripes that enhance HUVECs confinement and adhesion. Importantly, we showed that treatment of printed HUVEC lines with the anti-angiogenic factor bone morphogenetic protein 9 (BMP9) significantly improves the percentage of lumen coverage. Our results showcase LIST as a powerful bioprinting technology to study tubulogenesis and to screen compounds targeting microvasculature pathologies.

*Chapter 6 presents conclusion, summary and limitation of the thesis work, and future recommendations*

# Chapter 2

## Self-limited nanosecond laser-induced bubble growth in sealed containers

This chapter is based on the manuscript published in Applied Physics Letter, where the self-limited bubble dynamics are presented. This chapter covers the objective “1(a-c)” of the “Thesis objective and scope” in Section 1.7.

### 2.1 Introduction

Laser-induced cavitation bubbles are central in a variety of biomedical applications, including eye surgery [96], high-speed cell sorting [97], needle-free injection [157], bio-printing [158], and laser lithotripsy [159]. In most of the cavitation bubble-enabled applications, bubble growth is confined or semi-confined in a liquid container. The understanding of how confined geometries affect bubble dynamics (i.e., their size and lifetime) is essential to optimize existing applications and to eventually engineer future applications that can benefit from bubble confinement effects. Significant efforts have been made towards understanding bubble growth near rigid [138, 141] and elastic [140, 160] boundaries, or between them [139]. Limiting bubbles with such boundaries significantly reduces their size and lifetime due to local liquid compressibility [142, 143]. Previous studies have also shown that varying the externally applied pressure to a sealed container can drastically affect bubble dynamics [144, 145]. For

example, laser-induced bubbles in a 3 MPa pressurized chamber, have  $\approx 30$ -times smaller volume and  $\approx 17$ -times shorter lifetime compared to those generated in a non-pressurized chamber using identical laser conditions [144]. Historically, fundamental studies on laser-induced bubble dynamics have been conducted in large containers, where self-limiting effects are negligible (i.e., external pressure is 1 atm). Interestingly, bubble confinement effects were observed both experimentally and theoretically in ballistic penetration of reservoirs filled with a liquid, where the generation of highly energetic bubbles is common [161]. The work described in here is motivated by the absence of studies reporting self-limiting effects in laser-induced bubbles and by the importance of those effects in virtually any applications that exploits bubbles generation in confined or semi-confined reservoirs, such as microfluidic chambers and microcapillaries. Here we sought to address such self-limiting effects and designed an experimental setting to reveal them. In this chapter, we show that self-limiting effects appear when laser-induced mm-sized bubbles are generated in small sealed containers. We investigate the self-limiting effects using simultaneous bubble dynamics and liquid pressure recordings. We show that pressure waves generated by the bubble expansion can in turn modulate bubble growth (i.e., self-limiting effect), resulting in drastic spatiotemporal bubble confinement. Finally, we use Keller-Miksis modelling to explain the self-limiting effects and discuss their technological implications.

## 2.2 Material and methods

We generated cavitation bubbles using ns laser pulses (Nano L series, Litron Lasers, 6 ns, 532 nm). We used microcentrifuge tubes with built-in optical windows (glass cover slips) as sealed containers (Figure 2.1). We filled the containers with thoroughly degassed distilled water and sealed them hermetically using a protocol provided in the Supplementary Material (section A.2). The laser beam was expanded to  $\approx 12$  mm in diameter and focused at the center of the containers using a  $4\times$  objective lens (PLN4X, NA=0.1, Olympus). We used two measuring systems to monitor simultaneously bubble dynamics and pressure increase inside the container. Briefly, we used a continuous wave laser beam (633 nm) to measure bubble dynamics and a hydrophone (rise time: 50 ns) (Muller-Platte Needle Probe, Muller Instruments), placed inside the sealed container, to record liquid pressure (Figure 2.1a). Finally, images of

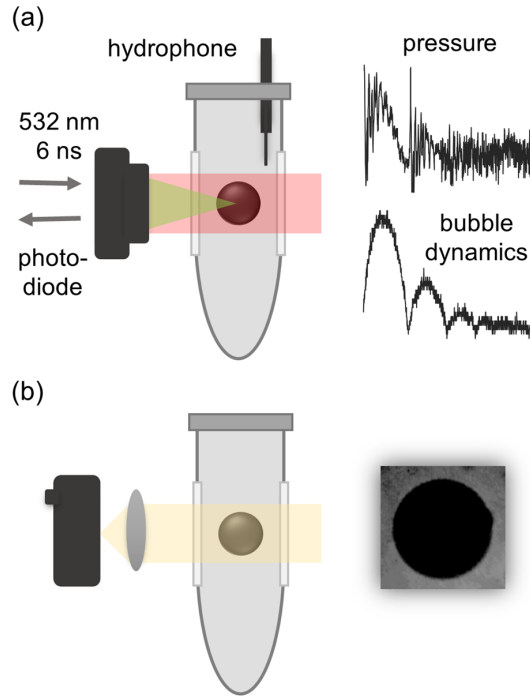


Figure 2.1: Schematic overview of the experimental setups used to study self-limited bubble growth in sealed containers. (a) Simultaneous measurement of bubble dynamics and liquid pressure, and (b) measurement of bubble maximum radius.

the bubbles were taken using a high-speed camera (Chronos 1.4, Kron Technologies) (Figure 2.1b). We used a beam sampling approach to measure the laser energy. We recorded the energy of each laser pulse using a pyroelectric sensor (QE12LPS-MB, Gentec Electro-Optics). Then, we used the transmission coefficient of the setup to deduce the energy at the sample level, which is the reported value throughout the study. A detailed schematic of the experimental setup is presented in Figure A.1.

## 2.3 Results and discussion

With previous theoretical work, we have shown that laser-induced bubbles experience self-limited growth in confined geometries due to water compressibility [157]. Here, we sought to investigate experimentally this “damping” effect and its dependence on key experimental settings, such as the container volume and bubble energy. We used three sealed containers: 0.3 mL, 0.6 mL, and 1.9 mL and varied the laser pulse energy from 1.5 mJ to 3.25 mJ. Note that we determined the cavitation threshold

(80% cavitation probability) for our irradiation setting to be  $E_{th} = 1.25$  mJ (see Figure A.2a). We also used a large (50 mL) non-sealed container to perform control experiments. Figure 2.2a shows the results of an indicative series of experiments, where bubbles were generated at 1.75 mJ in different containers. We found that bubbles in sealed containers had much shorter lifetime (53  $\mu$ s for 0.3 mL, 79  $\mu$ s for 0.6 mL, 111  $\mu$ s for 1.9 mL) compared to those generated in an open control container (123  $\mu$ s). Furthermore, bubbles generated in sealed containers had smaller size (535  $\mu$ m for 0.3 mL, 572  $\mu$ m for 0.6 mL, 627  $\mu$ m for 1.9 mL) compared to those generated in an open container (731  $\mu$ m). These results reveal a predominant self-limiting effect in bubble growth that strongly depends on the volume of the sealed container,  $V_c$ . We systematically studied this effect as function of the laser energy (Figure 13b),  $E_l$ . For  $E_l \geq 2E_{th}$  and control open container, we found that  $R_{max} \sim E_l^{0.32}$ , which is consistent with the extended literature in large containers [93, 162], and reflects the energy balance when liquid pressure is equal to 1 atm. However, this relation changes for sealed containers in a volume-dependent manner:  $R_{max} \sim E_l^{0.26}$  for  $V_c = 1.9$  mL,  $R_{max} \sim E_l^{0.19}$  for  $V_c = 0.6$  mL, and  $R_{max} \sim E_l^{0.25}$  for  $V_c = 0.3$  mL. We will show later that lower exponent values for sealed containers compared to the open container, do not represent bubbles of lower energy. We found a similar effect for the bubble lifetime,  $t_{BLF}$ :  $t_{BLF} \sim E_l^{0.39}$  for the control open container,  $t_{BLF} \sim E_l^{0.455}$  for  $V_c = 1.9$  mL,  $t_{BLF} \sim E_l^{0.044}$  for  $V_c = 0.6$  mL, and  $t_{BLF} \sim E_l^{0.001}$  for  $V_c = 0.3$  mL (Figure 2.2c). There are two important practical implications of those findings: (i) for a given laser energy, the maximum bubble size depends on the volume of the sealed container, and (ii) the bubble lifetime is virtually independent of the laser energy for small sealed containers.

The liquid pressure inside the container,  $P_l$ , is a key factor affecting bubble dynamics. Therefore, we sought to measure the time-dependent  $P_l$  for both open and sealed containers. Figure 2.3a presents  $P_l$  along with the corresponding bubble temporal profile in both sealed and open containers for  $E_l = 2.5$  mJ. We found only marginal  $P_l$  variations for the open container, indicating that bubble growth is not affected by the container itself. For all sealed containers, we found significant  $P_l$  modulation that is strongly correlated to the bubble dynamics. First, there is an increase in  $P_l$ , up to a maximum value, corresponding to the bubble growth phase. Note that the time point of maximum bubble size coincides with that of maximum  $P_l$  for all sealed

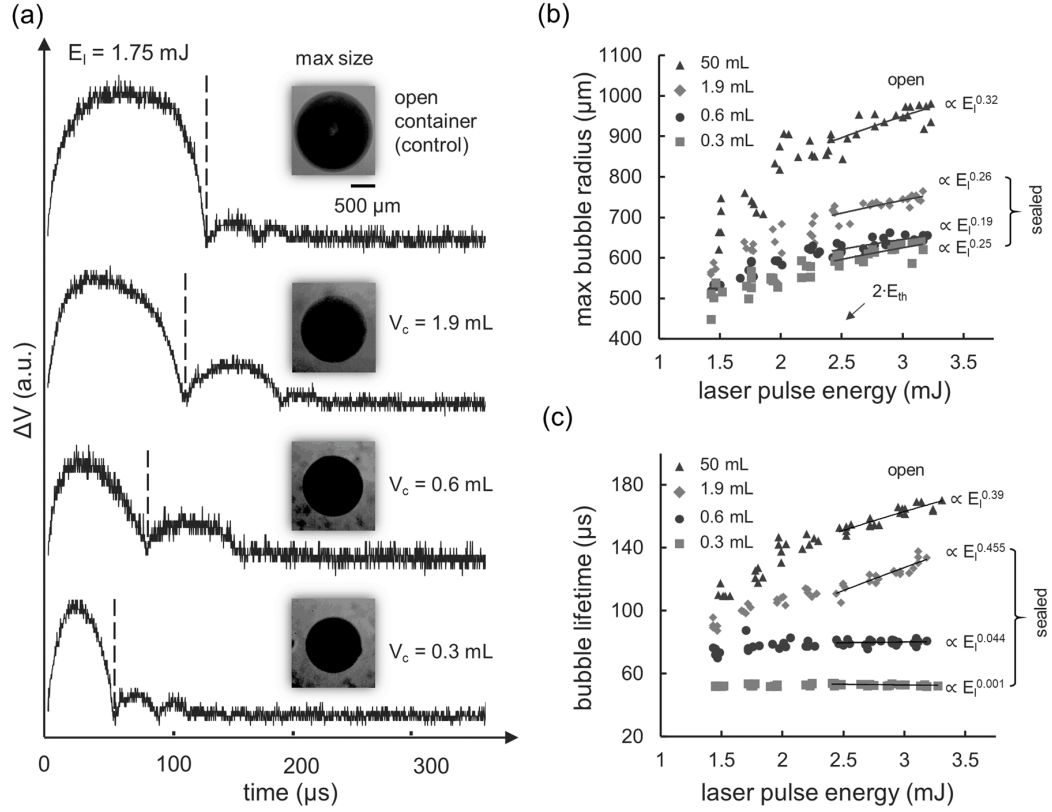


Figure 2.2: Self-limited bubble growth in sealed containers, (a) Indicative bubble dynamics traces (i.e., inverted photodiode signal) and bubble images for sealed containers (0.3 mL, 0.6 and 1.9 mL) and an open control container (15 mL). Bubbles were generated at 1.75 mJ and images were acquired using sufficiently long integration time ( $100 \mu\text{s}$ ) to depict max bubble size. The dependence of the maximum bubble radius, (b) and bubble lifetime and (c) on the laser energy for sealed and control containers. The dependence on the laser energy is fitted for  $E_l \geq 2E_{th}$ .

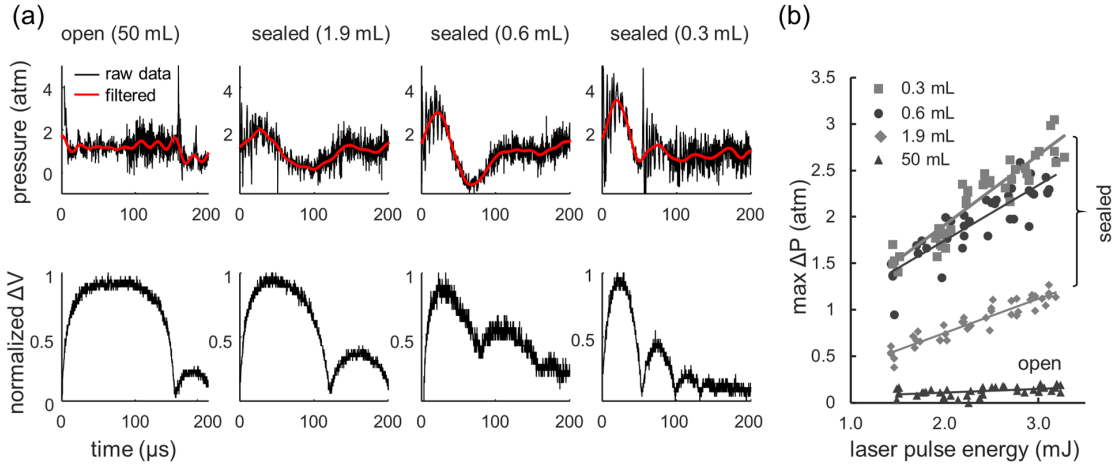


Figure 2.3: Pressure profiles for sealed and control containers, a) Indicative ( $E_l = 2.5$  mJ) liquid pressure recordings (top) and corresponding bubble dynamics traces (bottom) (i.e., inverted photodiode signal) for sealed containers (0.3 mL, 0.6 and 1.9 mL) and an open control container (15 mL). The raw data were filtered to remove the high frequency component (noise and/or shockwaves), b) The dependence of the maximum pressure variance on the laser energy for sealed and control containers.

containers. Next,  $P_l$  decreases due to bubble contraction and reaches a minimum value at bubble collapse. We filtered the raw hydrophone data to remove shockwave generation, shockwave reflections and noise components. Using the filtered signal (red line in Figure 2.3a), we calculated the maximum increase in  $P_l$  as a function of the laser energy for all containers.  $P_l$  increase was marginal and independent of  $E_l$  for the controlled container. However, we found a strong correlation between the laser energy and maximum  $P_l$  for all sealed containers (Figure 2.3b). Overall, these results indicate that bubble growth in sealed containers results in the generation of a pressure wave due to liquid compression. Both the laser energy and the sealed container volume affect the amplitude of the pressure wave, while its temporal profile follows the bubble dynamics. For the examined settings, we found that the maximum amplitude of the liquid pressure wave was 3.8 bar (sealed 0.3 mL), which is one order of magnitude smaller compared to that of a decaying shock wave released upon bubble generation and collapse [163]. The life span of the generated pressure waves ( $\approx 55$  to  $160 \mu\text{s}$ ) is two orders of magnitude larger compared to that of the corresponding shock waves.

To examine if the laser to bubble energy conversion efficiency is maintained in the

different settings, we used the following equation (Eq. 12) to calculate the bubble energy for sealed and controlled containers:

$$E_b = \frac{4}{3}\pi(P_l - P_v)R_{max}^3 \quad (12)$$

where,  $P_l$  is the liquid pressure far from the bubble when it reaches its maximum radius,  $P_v$  is the saturated vapor pressure in the bubble and  $R_{max}$  is the maximum bubble radius. Using the maximum  $P_l$  (Figure 2.3b) and maximum bubble radius (Figure 2.2b) we found that the bubble energy conversion efficiency ( $E_{bubble}/E_{pulse}$ ) is relatively constant ( $\approx 12\%$  for  $E_l \geq 2E_{th}$ ) independently of the container volume and configuration (i.e., open/sealed) (Figure A.2b). Next, we sought to validate whether the implementation of the experimentally measured  $P_l$  in a bubble model would allow modeling of the confinement effect. To do so, we used the Keller-Miksis (KM) equation (Eq. 13):

$$\begin{aligned} (1 - \frac{\dot{R}}{c})R\ddot{R} + \frac{3}{2}(\dot{R})^2(1 - \frac{\dot{R}}{3c}) = \\ \frac{1}{\rho}(1 + \frac{\dot{R}}{c})[(P_g - P_v + \frac{2\sigma_l}{R_0})(\frac{R_0}{R})^{3\gamma} + P_v - P_l] - 4\nu\frac{\dot{R}}{R} - \frac{2\sigma_l}{\rho R} \\ - \frac{3}{c\rho}(P_g - P_v + \frac{2\sigma_l}{R_0})(\frac{R_0}{R})^{3\gamma}\dot{R} \end{aligned} \quad (13)$$

Where  $c$  is the speed of sound in the liquid,  $\rho_l$  is the liquid density,  $\gamma$  is the heat capacity ratio,  $R$  is the bubble radius,  $R_0$  is the bubble initial radius ( $t = 0$ ),  $\nu$  is the kinematic viscosity,  $\sigma_l$  is the surface tension, and  $P_g$  is the initial gas pressure in the bubble ( $t = 0$ ). Our modeling approach consists of two steps: First, for a given laser energy, we determined a set of initial conditions ( $R_0, P_g$ ). We have previously reported in details our approach to determine the initial conditions [157]. We present in the supplementary material (sections A.4 and A.5) the adaptation of this approach for the KM model. For a given energy, the initial conditions were considered independent of both the container volume and configuration (i.e., open/sealed). Next, for a given laser energy and container configuration, we used the experimentally measured  $P_l$  profile (Figure 2.3a) to calculate bubble growth. All modeling parameters can be found in the supplementary material (section A.6-table A.1 and table A.2). Figure

2.4 summarizes our modeling results on the self-limited bubble growth. In accordance with the experimental results, the KM model shows that both  $R_{max}$  and bubble lifetime are suppressed in sealed containers due to  $P_l$  increase (Figure 2.4). For  $R_{max}$ , there is a very good agreement between the KM model and the experiments for the entire spectrum of the tested settings (Figure 2.4b). This reflects the preservation of the laser to bubble energy conversion efficiency (Figure A.2b). Although, the KM model shows temporal confinement of the bubble as well (Figure 2.4a), there is a systematic overestimation of the bubble maximum size time point. Note that we compare this time point instead of the bubble lifetime (Figure 2.4b), since bubble collapse did not occur for several experimental settings due to the pressure wave (i.e.,  $V_c = 0.6$  ml in Figure 2.4a), an effect we also observed experimentally (Figure 2.3a,  $V_c = 0.6$  ml). The differences between the modeled and experimental temporal profiles can be attributed to the limitations of our experimental setting. In fact,  $P_l$  is being measure far from the bubble, thus the model underestimates the actual pressure experienced by the bubble wall during the expansion phase. Note that the KM model assumes spherical bubbles. In our experimental setting, fast bubble imaging showed that this condition is met during the bubble growth phase. However, there is a loss of spherical symmetry in the late stage of the bubble collapse phase, which also limits the accuracy of our model.

## 2.4 Conclusion

In conclusion, we showed that laser-induced bubble growth in sealed containers can be spatiotemporally self-limited. Using both experimental measurements and modeling, we attributed the self-limiting effect to the generation of a pressure wave; whose amplitude and lifespan depends on the laser energy and the volume of the container. Interestingly, the self-limiting effect is predominant on the bubble lifetime, which becomes virtually independent of the laser energy for small sealed containers. We also found that laser to bubble energy conversion efficiency is preserved in self-limited bubbles. The technological implications of these findings are important for designing devices that exploit bubble growth in small volume containers, such as laser-actuated microfluidics and laser-induced microjet devices.

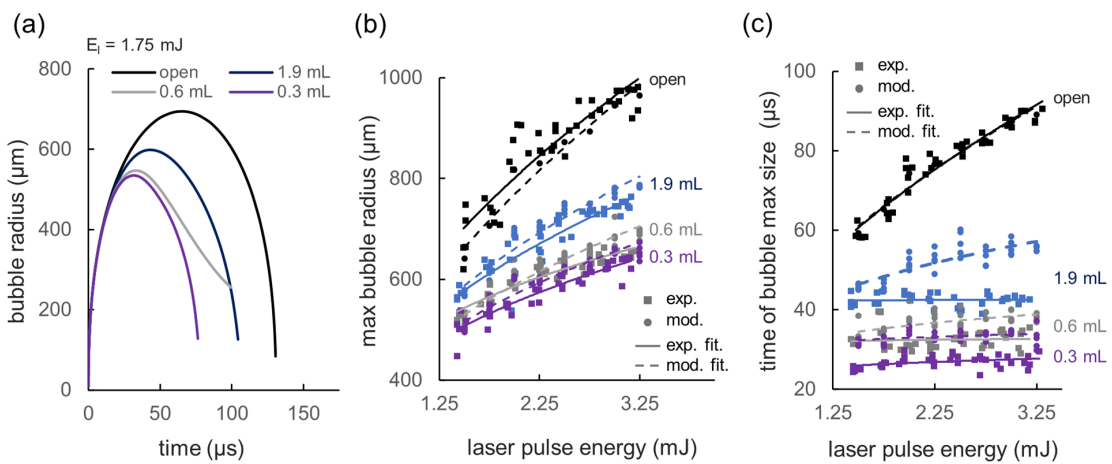


Figure 2.4: Keller-Miksis bubble modeling using the experimentally measured pressure profiles. (a) KM bubble modeling for sealed containers (0.3 mL, 0.6 and 1.9 mL) and an open control container (15 mL).  $E_l = 1.5 \text{ mJ}$ , the dependence of the experimentally measured and modeled bubble behavior on the laser energy for open and sealed containers: (b) maximum bubble size and (c) time of bubble maximum size.

# Chapter 3

## Hybrid analytical/numerical modeling of nanosecond laser-induced microjets generated by liquid confining devices

This chapter is based on the manuscript published in the Journal of Fluids and Structures, where the simulations of laser-induced bubble and microjets dynamics are presented. This chapter covers the objective “2(a-d)” of the “Thesis objective and scope” in Section 1.7.

### 3.1 Introduction

Cavitation bubbles can cause destructive mechanical impact [140,164]. However, the ability to control their spatiotemporal growth provides an efficient method to induce directional liquid displacement and enables a wide range of applications in biomedical engineering [165]. Laser-induced cavitation plays a central role in such applications due to its simplicity and versatility. It has been used for tissue ejection [166], in eye surgery [96], for high-speed cell sorting [99], as a scalpel [110] and for various microjet ejection applications as discussed in details below.

The expansion and collapse of laser-induced bubbles create pressure waves and liquid displacement. Laser-induced forward transfer (LIFT) is a powerful printing

technique [34, 146, 147, 167] that exploits such phenomena to generate liquid microjets. It uses pulsed laser irradiation of non-confined liquid films, i.e., bio-ink layers of few micrometers in thickness deposited on a transparent support. An alternative way to generate high-speed microjets uses laser-induced bubbles in a nozzle bearing reservoirs. This concept has been used in needle-free drug injectors [101, 103] and for microdroplet generation in microfluidic devices [113, 168]. The jet-injection mechanism in such devices implies pressure increase inside a semi-confined chamber, a process that may not be confused with the LIFT jet-generation mechanism, i.e. bubble oscillation close to a rigid boundary.

Modeling works on laser-induced jet-ejection have used a variety of approaches to account for laser energy to liquid pressure and kinetic energy conversion, including implementation of pressure waves [149], bubble pressure [148], and moving boundaries with experimentally determined displacement [146, 147, 153]. Previous works have simulated microjet generation by spark-generated bubbles [150], thermally-generated bubbles [169] and laser-induced bubbles within glass microcapillaries [148, 149]. Importantly, liquid confining chambers affect laser-induced bubble dynamics [151, 152, 154, 155], compared to open chambers, where expanding bubbles experience constant pressure and no rigid boundaries. Importantly, the application of an external pressure to a closed chamber can suppress drastically bubble expansion and shorten its life time [144]. Here, we report the simulation of a laser-driven liquid-confining device tailored for bio-printing applications. The architecture is inspired from previous experimental works on needle-free drug injection [101, 103]. Although we focus on bio-printing, the modeling approach presented here can be easily adapted for drug injectors. The simulated device consists of two chambers; the first one is closed and filled with water and the second is filled with the liquid to be ejected and equipped with a nozzle. Laser-induced cavitation is generated in the first chamber, which is separated by an elastic membrane from the second one, to reduce the thermo-mechanical impact of the absorbed laser energy on the liquid to be ejected with a jet formation. The jet generation mechanism implies pressure increase within the semi-confined chamber (Figure 3.1). The optimization of such a device is challenging, requiring coupled modeling components accounting for bubble dynamics, fluid-structure interaction and two-phase flow. Although there is extensive experimental work on similar devices for needle-free drug delivery [101, 103], as of

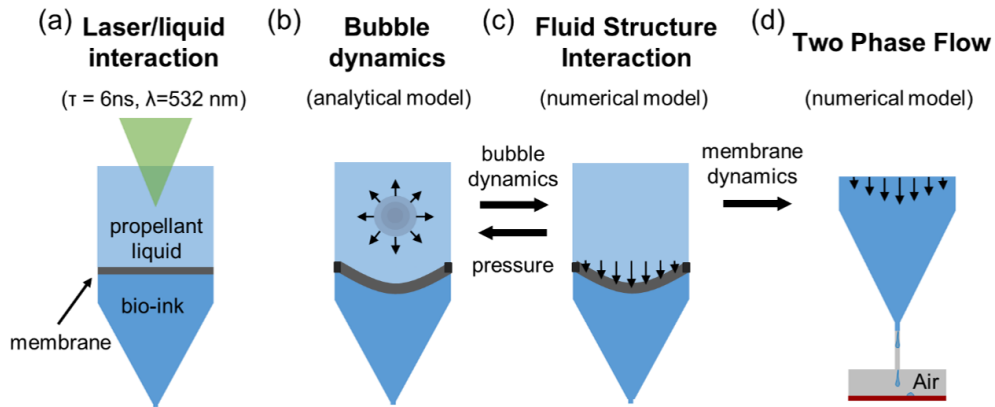


Figure 3.1: Schematic of the simulated dual chamber liquid-confining device, (a) laser-induced optical breakdown, (b) generation of a cavitation bubble and (c) elastic membrane deformation, and (d) generation of a microjet.

today, no modeling approaches have been reported.

We developed a hybrid numerical/analytical model for studying laser-induced bubble dynamics in a dual-chamber liquid-confining device in which there is no interference between the bubble and microjet generation. We considered a nanosecond (ns) pulsed laser (wavelength: 532 nm; pulse duration: 6 ns) for our work. By modifying the generalized form of the Rayleigh–Plesset (RP) equation, we show that the geometry of the liquid confining device affects drastically laser-induced bubble dynamics and the resulting jet ejection dynamics. We also show that dual-chamber liquid-confining devices can generate microjets (velocity: 0.93 m/s to 48.39 m/s) suitable for microdrop printing (volume: 0.097 nL to 7.68 nL).

## 3.2 Device and model overview

Figure 3.1 illustrates a schematic of the simulated dual chamber liquid-confining device. The architecture is similar with the one presented in previous experimental works on needle-free drug injection [101, 103]. However, the size of the device has been scaled down for bioprinting applications. We considered the following mechanism for liquid ejection. Two chambers, containing a propellant liquid and a bio-ink, are separated by an elastic membrane. A focused (ns) laser pulse induces optical breakdown (Figure 3.1a) and a resulting cavitation bubble in the propellant liquid chamber (Figure 3.1b). The bubble expansion deforms the elastic membrane, which

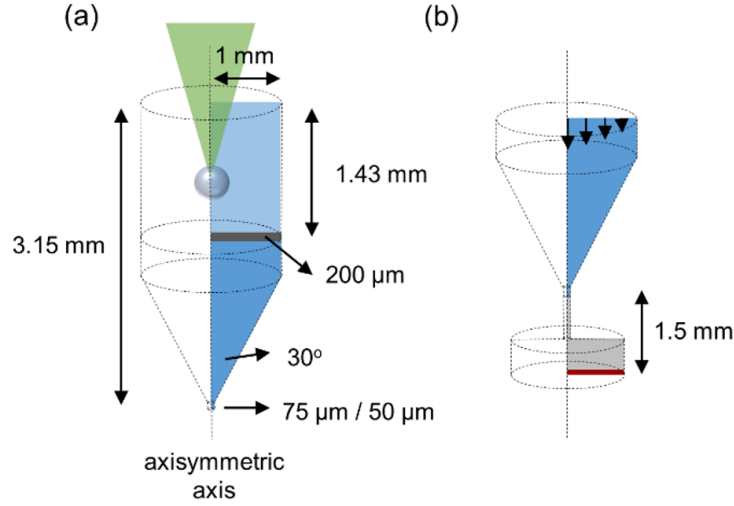


Figure 3.2: Sketches of the computational domains for (a) FSI and (b) TPF.

in turn increase the pressure in the bio-ink reservoir (Figure 3.1c), causing liquid ejection from the nozzle (Figure 3.1d). For the hybrid analytical/numerical modeling presented we used three major components. First, we developed an analytical model of bubble dynamics based on the solution of the RP equation. Note that we coupled RP to Tait equation to account for the pressure increase in the propellant liquid chamber. Then, we performed numerical simulation of the membrane velocity using the fluid-structure interaction (FSI) module of COMSOL coupled to the analytical model of bubble dynamics. Finally, we used the calculated membrane velocity as an input for the two-phase flow (TPF) module of COMSOL to calculate the microjet ejection dynamics. To decrease the computational time, we used an axisymmetry model in respect to the reservoir's center axis for FSI and TPF simulations. Figure 3.2a and 3.2b show sketches of the FSI and TPF computational domains. Both the propellant liquid and the liquid to be ejected were considered water throughout this work, while the membrane material was considered rubber.

### 3.3 Description of the model

#### 3.3.1 Model assumptions

We neglected the effect of shock wave propagation in our model. Shock wave propagation upon ns laser optical breakdown in liquid can result in liquid ejection. However,

experimental data show that the shock wave has a much smaller contribution on liquid ejection compared to bubble growth [100]. For the analytical calculation of bubble dynamics, we considered the bubble initial volume ( $t = 0$ ) a sphere, whose volume corresponds to the ellipsoid at which the laser irradiance exceeds the optical breakdown threshold ( $2.5 \times 10^7$  mJ/cm<sup>2</sup>) in water for 6 ns pulsed laser at 532 nm [166]. Finally, we considered the two chambers entirely filled with water at 20 °C.

### 3.3.2 Bubble dynamics analytical model

The RP equation has been widely used to describe ns laser-induced cavitation dynamics in open liquid containing chambers [95, 145, 170–176], where the pressure far from the cavitation bubble can be considered equal to the atmospheric pressure. In this work, we used the RP equation (Eq. 14) as the basis for our bubble dynamics analytical model, while we also introduced a key modification to account for the pressure increase induced by the bubble growth in a confined chamber. The RP equation in its generalized form [125] is given below:

$$R\ddot{R} + \frac{3}{2}\dot{R}^2 = \frac{P_g}{\rho} \left(\frac{R_0}{R}\right)^{3\gamma} - \frac{P_l - P_v}{\rho_0} - 4\nu\frac{\dot{R}}{R} - \frac{2\sigma_l}{\rho R} \quad (14)$$

Where  $\rho_l$  is the liquid density,  $P_l$  is the liquid pressure far from the bubble,  $\gamma$  is heat capacity ratio,  $R$  is the bubble radius,  $R_0$  is the bubble initial radius ( $t = 0$ ),  $\nu$  is the kinematic viscosity,  $\sigma_l$  is the surface tension,  $P_v$  is the saturated vapor pressure in the bubble, and  $P_g$  is the initial gas pressure in the bubble ( $t = 0$ ). To consider the effect of liquid compressibility in a closed container, we calculated the energy required ( $E_c$ ) to compress the liquid to pressure  $P_l$  (Eq. 15) [177]:

$$E_c = \frac{\beta}{2} V_c P_l^2 \quad (15)$$

Where  $\beta$  is compressibility coefficient,  $V_c$  is liquid initial volume and  $P_l$  is the liquid pressure. To implement the compressibility energy loss term in the RP equation, we introduced the derivative of Eq. 15 in respect to  $R$  (Eq. 16).

$$R\ddot{R} + \frac{3}{2}\dot{R}^2 = \frac{P_g}{\rho} \left(\frac{R_0}{R}\right)^{3\gamma} - \frac{P_l - P_v}{\rho_0} - 4\nu\frac{\dot{R}}{R} - \frac{2\sigma_l}{\rho R} - \frac{1}{4\pi R^2 \rho_l} \frac{\partial E}{\partial R} \quad (16)$$

In the following sections we will present how  $R_0$  and  $P_g$  were calculated for a given

laser energy and how  $P_l$  was implemented as a time dependent variable. We will also present our approach to consider energy losses for the bubble rebounds.

### 3.3.3 Calculation of $R_0$

We considered a focused Gaussian beam to calculate the bubble initial radius,  $R_0$ . Our key assumption is that  $R_0$  corresponds to the laser focal volume at which the laser irradiance exceeds the optical breakdown threshold. We considered the optical breakdown threshold equal to  $2.5 \times 10^7$  mJ/cm<sup>2</sup>, which is the experimental value reported for ns laser ( $\lambda = 532$  nm) cavitation in water [166]. We used a Gaussian function (Eq. 17) to calculate the irradiance distribution,  $I_G(r,z)$ :

$$I_G(r, z) = I_0 \left( \frac{W_0}{W_z} \right)^2 \exp\left[-2 \left( \frac{r^2}{W_z^2} \right)\right] \quad (17)$$

where ( $W_0$ ) is the spot size at the focus,  $r$  is the coordinate in the radial direction,  $W_z$  is the laser beam width at position  $z$  along the beam propagation axis, and  $I_0$  is the peak irradiance.  $W_0$  and  $I_0$  can be calculated using the following equations (Eq. 18 and Eq. 19):

$$W_0 = \frac{1.22 \lambda}{NA} \quad (18)$$

$$I_0 = 2I_{av} = \frac{2E_l}{\pi W_0^2} \quad (19)$$

where  $\lambda$  is the laser wavelength, NA is the numerical aperture of the lens and  $E_l$  is the laser energy.  $W_z$  can be calculated by Eq. 20.

$$W = W_0 \sqrt{1 + \left( \frac{Z}{Z_r} \right)^2} \quad (20)$$

Where  $Z_r$  is the Rayleigh range (Eq. 21):

$$Z_r = \frac{\pi W_0^2}{\lambda} \quad (21)$$

Figure 3.3a illustrates the irradiance distribution for  $\lambda = 532$  nm, NA = 0.5 and  $E_l = 200$   $\mu$ J. The equivalent focal volume considered for the  $R_0$  calculation is shown in Figure 3.3b.

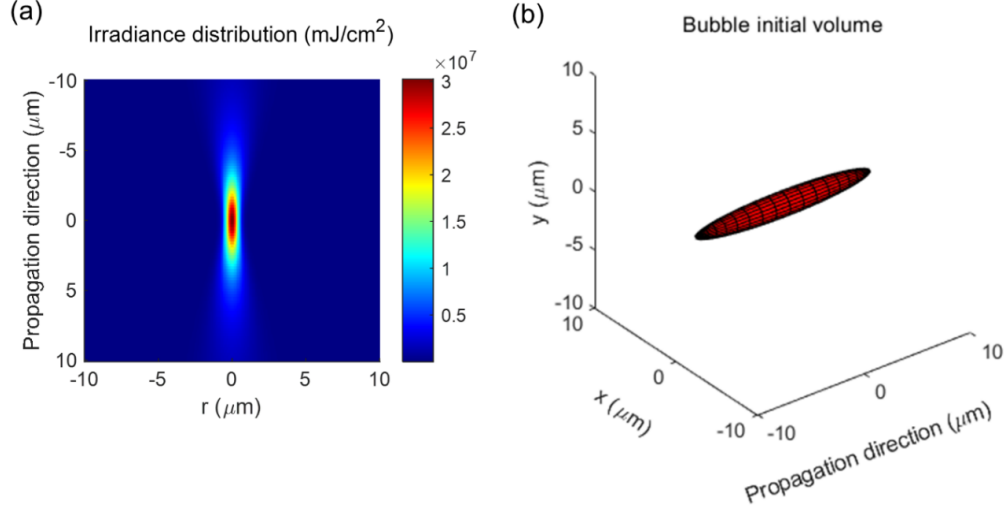


Figure 3.3: (a) Irradiance distribution and (b) representation of the bubble initial volume for  $\lambda = 532$  nm,  $\text{NA} = 0.5$  and  $E_l = 200$   $\mu\text{J}$ .

### 3.3.4 Calculation of $P_g$

We calculated  $P_g$  for given  $E_l$  and  $R_0$  by using a fitting process so as the maximum bubble radius  $R_{max}$ , extracted by the RP equation, would match the its experimentally documented relationship on  $E_l$ . For these calculations we used the following equation [93, 162, 163, 178] to calculate  $R_{max}$  as a function of the bubble energy,  $E_b$  (Eq. 22):

$$R_{max} = \left( \frac{3E_b}{4\pi \times (P_l - P_v)} \right)^{\frac{1}{3}} \quad (22)$$

It is well documented in the literature that ns laser-induced cavitation in water result to a  $\approx 20\%$  laser to bubble energy conversion efficiency [163, 179–181]. Thermal effects have a negligible effect in the examined laser-induced cavitation setting. Bubble growth is inertially controlled. Laser to bubble energy conversion can be considered instantly occurring. Initially, the energy is stored as potential energy. Our model considers its conversion to liquid kinetic energy, potential energy in compressed liquid, and to membrane mechanical energy.  $R_{max}$  can be related to  $E_l$  by the following equation (Eq. 23):

$$R_{max} = \left( \frac{3E_b}{20\pi \times (P_l - P_v)} \right)^{\frac{1}{3}} \quad (23)$$

Note that the validity of Eq. 22 and Eq. 23 has been confirmed experimentally for laser energies well above the cavitation threshold,  $E_{th}$ . We estimate that the laser energies used throughout this work range from  $\approx 4 \times E_{th}$  to  $\approx 20 \times E_{th}$ , thus lie within the experimentally documented validity domain of Eq. 22 and Eq. 23 [162,182]. For given laser energy,  $E_l$ , we first calculated  $R_0$  (see section 3.3.3) and then varied  $P_g$  so as the  $R_{max}$  calculated by the RP equation (Eq. 14) would match the one given by Eq. 22. For these calculations, we considered  $P_l = 1$  atm and  $P_v = 2330$  Pa.

### 3.3.5 Calculation of $P_l$

Contrary to bubble dynamics in an open chamber configuration [171, 176], liquid pressure  $P_l$  may not be assumed constant in a closed chamber configuration because bubble expansion results to  $P_l$  increase. Subsequently,  $P_l$  increase can affect drastically bubble dynamics (i.e., damp bubble growth). To account for such effects, we considered the Tait equation [183] to calculate  $P_l$  (Eq. 24):

$$P_l = (B + P_{l0})\left(1 - \frac{\Delta V_c}{V_c}\right)^{-7} - B \quad (24)$$

where  $B = 314$  MPa,  $P_{l0}$  is the initial liquid pressure (1 atm),  $\Delta V_c$  is the liquid volume difference, and  $V_c$  is liquid initial volume. Next, we considered  $\Delta V_c$  equal to the bubble volume and coupled to Eq. 16 (during bubble expansion), Eq. 14 (during bubble collapse), and Eq. 24 to calculate analytically the bubble dynamics in a closed chamber. This model allows for a time-dependent calculation of  $P_l$  and its effect on bubble dynamics. For a semi-confined geometry, bubble growth can result to liquid ejection from the nozzle and  $P_l$  release. To account for this, we considered the calculated by the FSI numerical model  $V_{outlet}$  (see section 3.3.8) to determine  $\Delta V_c$  and  $P_l$ . We coupled the analytical model to the COMSOL solver so as both time-dependent  $P_l$  and  $V_{outlet}$  were considered for bubble dynamics.

### 3.3.6 Rebound and damping

The collapse of the initial bubble is followed by rebounds and significant energy loss due to shock wave emission upon collapse and heat conduction [93, 184]. The generic RP equation does not account for bubble damping because of such phenomena. Considering the importance of the rebounds and damping in liquid ejection dynamics,

we implemented a rebound model based on experimentally available data [93, 163] for bubble energy loss and damping. We assumed two rebounds and considered that the first one has 1.3% of the laser pulse energy and the second one 0.2%. Subsequently, the dynamics of the bubble rebounds were calculated using the methodology presented in the previous sections for the first bubble.

### 3.3.7 Bubble dynamics implementation in FSI

Given that COMSOL Multiphysics has no built-in module simulating bubble dynamics, we developed our own modeling strategy to implement the analytical bubble dynamics model into the FSI module. We used a moving mesh (Figure 3.4b) to account for the bubble wall radius and a moving wall (Figure 3.4c) to account for the bubble wall velocity. Figure 3.4a presents a snapshot of the bubble growth for 200  $\mu\text{J}$  laser energy and 532 nm wavelength. The corresponding bubble radius and wall velocity can be found in Figure 3.4b and 3.4c.

### 3.3.8 Membrane dynamics and V outlet calculation with FSI

The simulated device consists in two chambers separated by the elastic membrane (Figure 3.1). Following the implementation of the analytical bubble dynamics model in COMSOL and its coupling to the numerical solver, we modeled the entire device with the FSI module. The key outputs of the FSI model were the membrane dynamics and  $V_{\text{outlet}}$ . Figure 3.5a shows the membrane average velocity and Figure 3.5b presents the average volume of liquid exiting the nozzle tip for 200  $\mu\text{J}$  laser energy. The spatiotemporal evolution of the membrane's oscillations can be found in Figure 3.5c. High amplitude oscillations can be observed at the center of the membrane for certain time frames (e.g.,  $\approx 60 \mu\text{s}$ ). The cause of these oscillations is the formation of transient air bubbles right below the center of the membrane. We provide in the supplementary information the corresponding TPF simulations showing the bubble formation below the central part of the membrane (section B.2-Video S2).

### 3.3.9 Liquid ejection dynamics

We used the two-phase flow (TPF) module of COMSOL to calculate the dynamics of the liquid exiting the nozzle. The TPF module uses as input the membrane dynamics

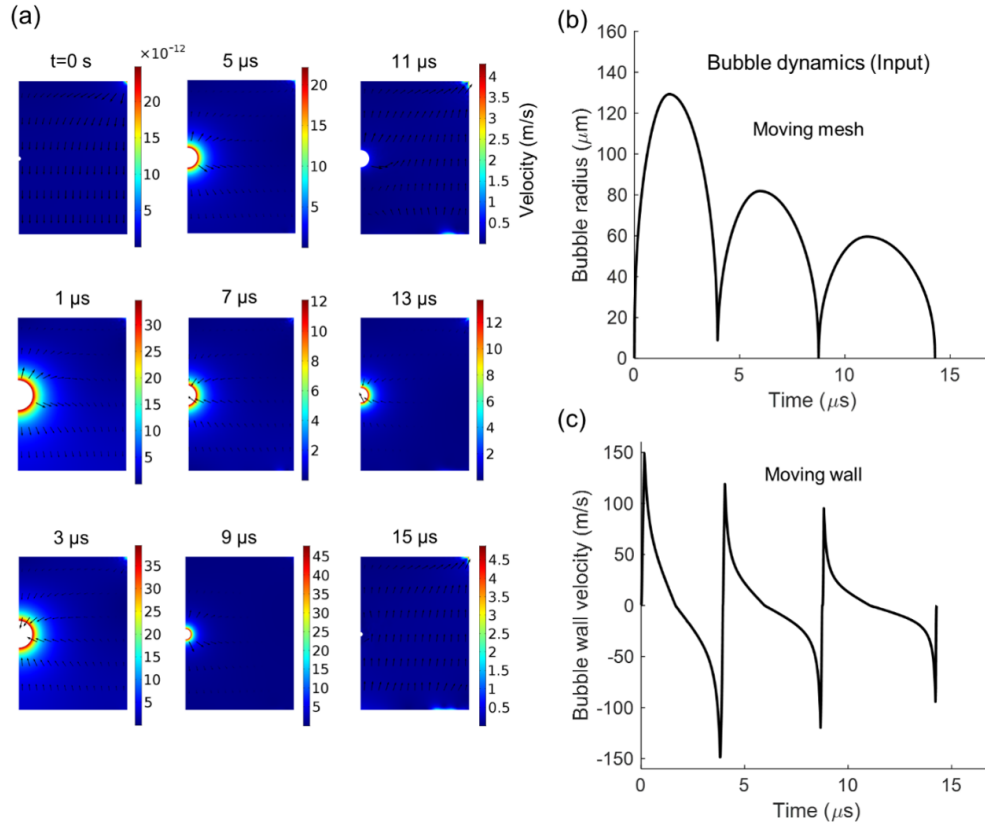


Figure 3.4: (a) Snapshots of bubble dynamics in the FSI model, (b) bubble radius and (c) bubble wall velocity for 200  $\mu\text{J}$  laser energy and 532 nm wavelength. A video with the complete bubble dynamics can be found in the supplementary material (section B.1-Video S1).

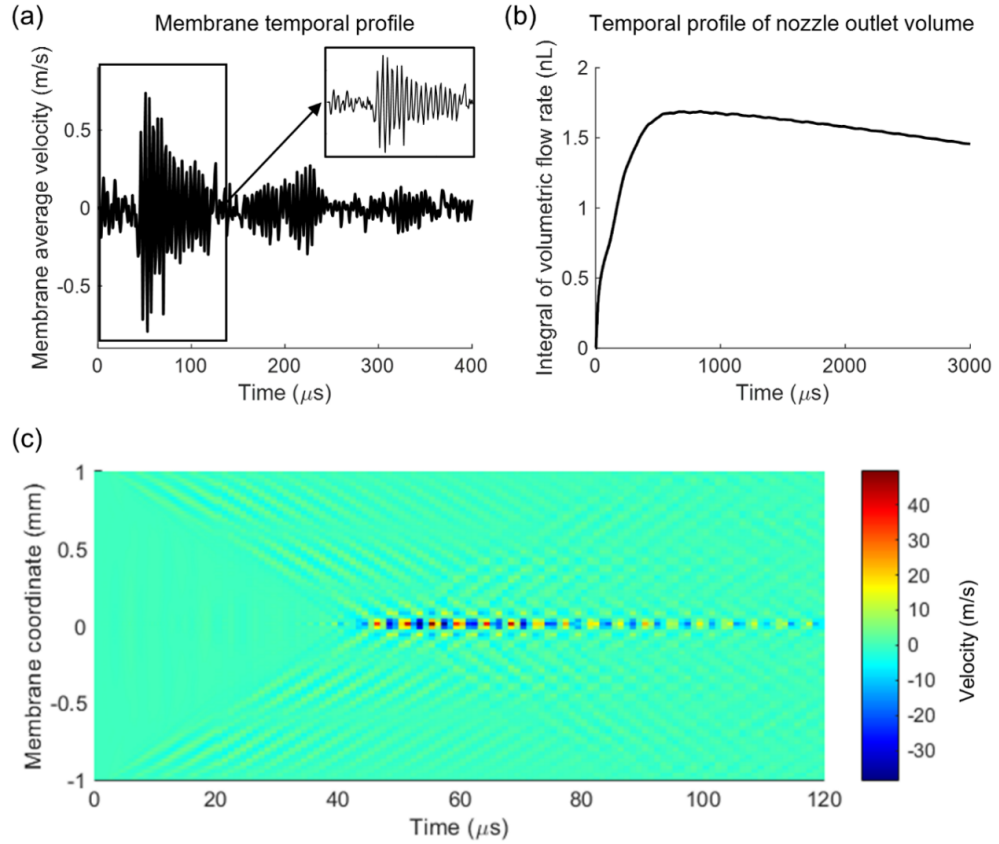


Figure 3.5: (a) Membrane average velocity profile and (b) integral of volumetric flow rate for 200  $\mu\text{J}$  laser energy (c) spatiotemporal evolution of the membrane's velocity profile.

(Figure 3.5) extracted by the FSI module.

### 3.3.10 Mesh selection

For FSI simulations we conducted a mesh independence study to test whether the simulation results are independent of the mesh resolution. We used the time-dependent and spatially averaged outlet velocity profile and volume for this study and ran the same simulation for four different mesh densities shown in Table 3.1. We found negligible differences in the results (Figure 3.6). Therefore, considering the computational time cost, we opted for “Finer” mesh having maximum and minimum element size equal to 98  $\mu\text{m}$  and 1.4  $\mu\text{m}$ , respectively.

For TPF simulations we conducted a similar study. We calculated the jet-front for four different mesh densities shown in Table 3.1. Considering the robustness

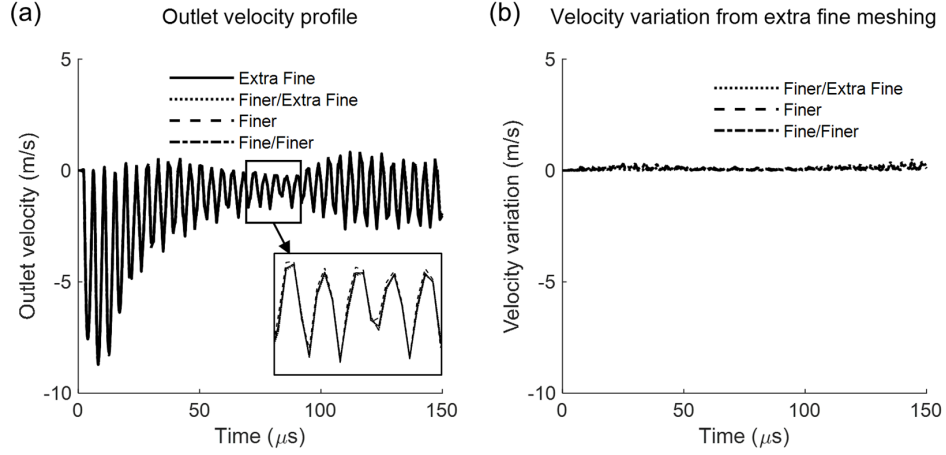


Figure 3.6: (a) Outlet velocity for different meshing sizes and (b) its variation on the meshing size for  $E_l = 200 \mu\text{J}$ .

of the solutions (Figure 3.7) and the computational time together, we opted for “Finer/ExtraFine” mesh having maximum and minimum element size equal to  $5.0 \mu\text{m}$  and  $2.5 \mu\text{m}$ , respectively. Note that we used adaptive meshing for TPF.

Table 3.1: Mesh settings tested for the FSI and TPF mesh dependence studies.

	Maximum element size(mm)		Minimum element size(mm)	
	FSI	TPF	FSI	TPF
Extra Fine	0.04550	0.0025	0.0005250	0.00125
Finer/Extra Fine	0.07175	<b>0.005</b>	0.0009625	<b>0.0025</b>
Finer	<b>0.09800</b>	0.0075	<b>0.0014000</b>	0.00375
Fine/Finer	0.11050	0.01	0.0024500	0.005

## 3.4 Results and discussion

### 3.4.1 Bubble dynamics in open/closed chambers and liquid semi-confining devices

PI variation can have a dominant effect on bubble growth and collapse [144, 174, 185–187]. Indicatively, experimental data show that ns laser-induced bubbles, generated in a 3 MPa pressurized chamber, have  $\approx 30$ -times smaller volume and  $\approx 17$ -times shorter life time compared to those generated in a non-pressurized chamber using

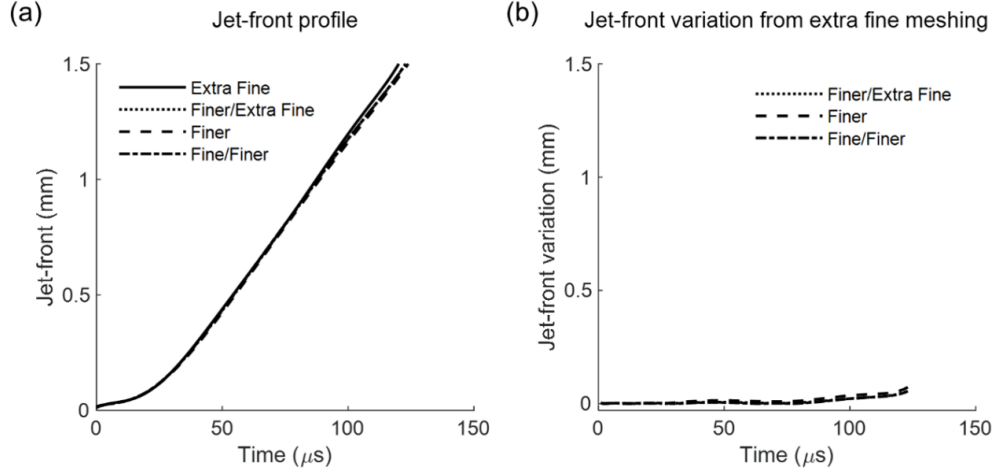


Figure 3.7: (a) Jet-front for different meshing sizes and (b) its variation on the meshing size  $E_l = 200 \mu\text{J}$ .

identical laser conditions [144]. A key feature of the developed model is the ability predict bubble dynamics in closed or semi-confined chambers, where bubble expansion itself affects  $P_l$ .

To illustrate such an effect, we used our analytical model to simulate bubble dynamics in closed chambers having different volumes ( $272 \mu\text{l}$  and  $6.344 \mu\text{l}$ ) for  $E_l = 200 \mu\text{J}$ . For comparison, we also considered bubble dynamics in an open chamber, where  $P_l$  is constant and equal to 1 atm. Figure 3.8a shows how  $P_l$  variation confines the spatiotemporal bubble growth for a given laser energy. The effect is predominant for the smallest chamber ( $6.344 \mu\text{L}$ ), where a 3-times smaller maximum bubble size and a 19-times shorter bubble lifetime is simulated compared to an open chamber. The corresponding  $P_l$  is shown in Figure 3.8b, where the peak pressure was found to reach 0.59 MPa for the  $272 \mu\text{L}$  chamber and 3.44 MPa for the  $6.344 \mu\text{L}$  chamber.

Given that the laser energy is a key experimental factor for controlling bubble dynamics, we simulated its effect on bubble maximum radius and bubble life time (Figure 3.9). The maximum bubble radius scales with the laser energy as  $R_{max} \sim E_l^{0.33}$  for an open chamber, where  $P_l$  is constant and equal to 1 atm. For closed chambers, the scaling relationship change to  $R_{max} \sim E_l^{0.20}$  for  $V_c = 272 \mu\text{L}$  and  $R_{max} \sim E_l^{0.17}$  for  $V_c = 6.344 \mu\text{L}$ , reflecting the predominant confinement of the bubble growth because of the  $P_l$  increase (Figure 3.9a). Unlike the open chamber case, bubble lifetime declines with the laser energy for closed chambers (Figure 3.9b). It is evident from Figure

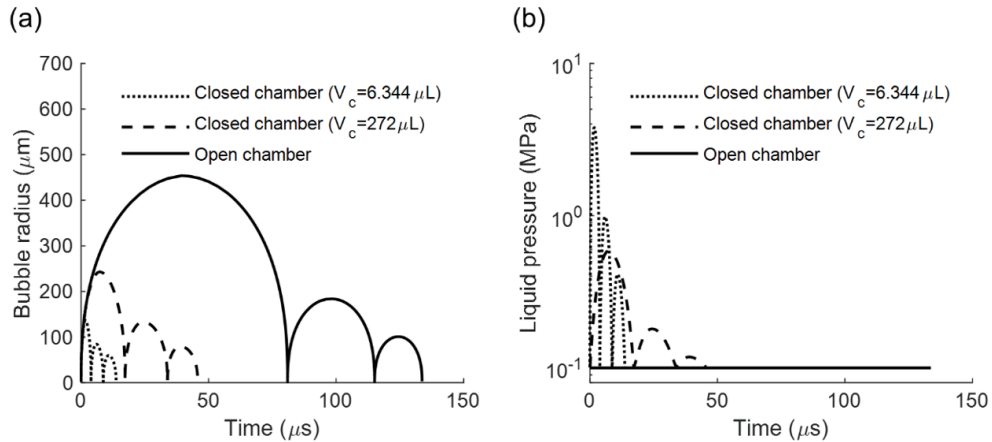


Figure 3.8: The effect of a closed chamber on bubble dynamics and for  $E_l = 200 \mu\text{J}$ . Simulated (a) bubble dynamics and (b)  $P_l$  temporal profile for open (constant  $P_l$ ) and closed (variable  $P_l$ ) chambers.

3.11 that the volume of the chamber,  $V_c$ , dictates the spatiotemporal dynamics of confined bubbles. One would expect such an effect because  $V_c$  is the key determinant of  $P_l$  (Eq. 24).

Although the analytical model provides accurate solutions for hermetically sealed chambers, it cannot be applied directly to liquid ejection devices because liquid ejection ( $V_{outlet}$ ) causes  $P_l$  release. To overcome this limitation, we coupled the analytical model to the FSI module of COMSOL, calculating  $V_{outlet}$  (see section 3.3.5). We used the coupled model to simulate bubble dynamics generated by the device presented in Figure 3.2. Figure 3.10 presents indicative bubble dynamics for laser energies ranging from 50 to 450  $\mu\text{J}$ . Interestingly, the bubble life time declines with the increase of the laser energy. In addition, the first cycle has a shorter life than the second cycle, which in turn has a shorter lifetime than the third cycle. These behaviors are inverted compared to open chambers (i.e.,  $P_l \approx 1 \text{ atm}$ ) [93], demonstrating the significant impact of a variable  $P_l$  on bubble dynamics.

### 3.4.2 Liquid ejection dynamics

The geometry of a liquid-confining device as well as the rheological properties of the liquid and the laser energy are key experimental parameters affecting laser-induced liquid ejection dynamics. The desired ejection dynamics may vary depending on the application. For example, ejection of fast liquid jets is desirable for drug delivery

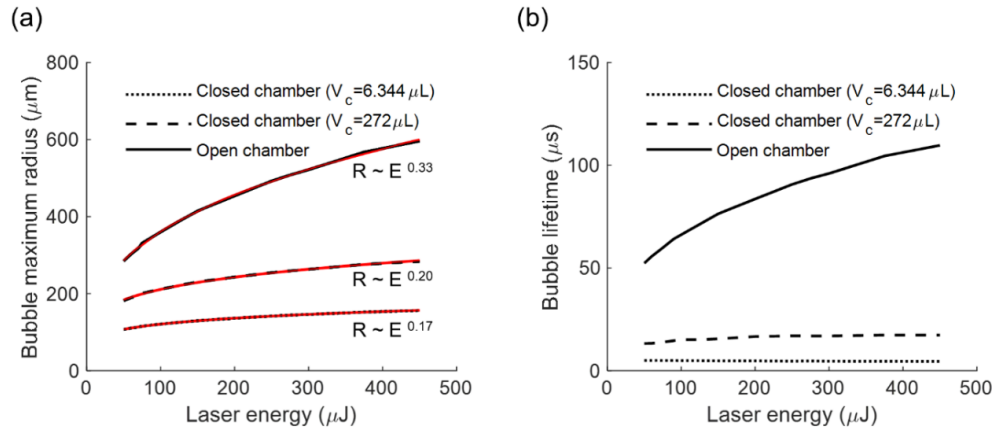


Figure 3.9: The effect of laser energy on bubble dynamics: (a) bubble maximum radius and (b) bubble lifetime as a function of laser energy for open (constant  $P_l$ ) and closed chambers (variable  $P_l$ ).

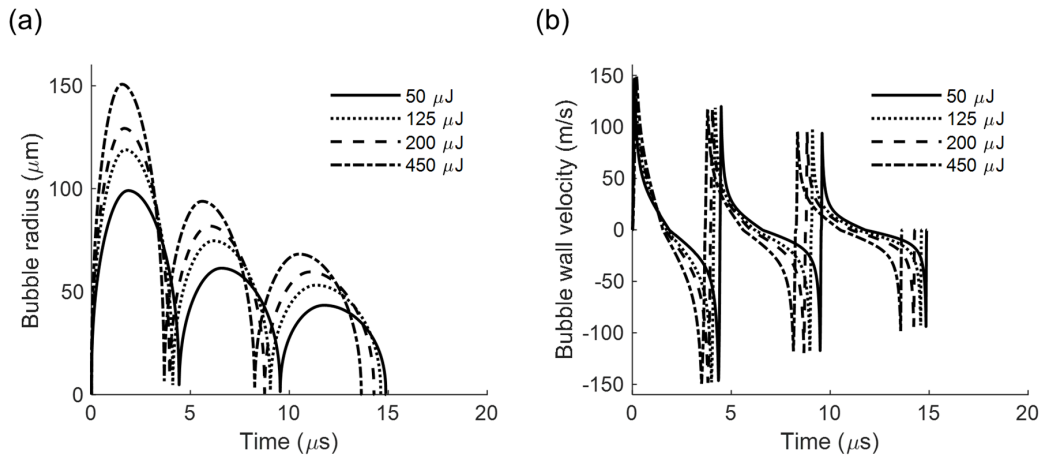


Figure 3.10: Simulated bubble dynamics for the liquid confining-device presented in Figure 3.2 considering  $V_{outlet}$ . (a) bubble radius and (b) bubble wall velocity.

application [101], while smooth jet ejection is preferable for printing applications [120]. In this work, we considered a printing application and used our model to study the effect of the liquid-confining device geometry (i.e., nozzle size and membrane thickness) and laser energy on the ejection dynamics. Figure 3.11 shows representative snapshots of FSI and TPF simulations at different time frames post cavitation for 70  $\mu\text{J}$  laser energy. We systematically analyzed such dynamics to conduct the parametric studies present in the following sections. Note that in the numerical model, the initial bubble is assumed spherical even though it is elliptical, while an equivalent radius is considered (i.e., resulting to the same volume). Experimental studies show that initially elliptical ns laser-induced bubbles increase drastically their symmetry within a fraction of a  $\mu\text{s}$  and turn spherical within few  $\mu\text{s}$  [93]. In this context, our assumption concerns a short time period ( $< 25\%$ ) compared to the bubble lifetime. For this timeframe, the volume of the bubble represents less than 15.5% of its maximum volume. Since the bubble volume is the key determinant of pressure increase and liquid displacement, it is reasonable to expect that the spherical assumption has only a minor effect on the jet ejection modeling.

### **The effect of the nozzle diameter**

We first investigated the effect of the nozzle diameter on the ejected liquid dynamics by monitoring the front position of the ejected jet for two laser fluences (70 and 200  $\mu\text{J}$ ), determined by a preliminary laser energy scan (Figure 3.12). For these simulations, the membrane size was 200  $\mu\text{m}$  and the nozzle diameters varied from 50 to 150  $\mu\text{m}$ . We found that the velocity of the ejected liquid increases with the decrease of the nozzle diameter. We also found that the smaller the nozzle size the lower the laser energy ejection threshold for an otherwise identical geometry. These results suggest that the smaller nozzle diameters of 50  $\mu\text{m}$  or 75  $\mu\text{m}$  would be more efficient for a bioprinting application because the lower the laser energy ejection threshold the lower the thermal impact to the bio-ink. Therefore, we selected these values for the parametric laser energy scan (see section 3.4.2).

### **The effect of the membrane thickness**

Next, we investigated the effect of the membrane thickness on the ejected liquid dynamics for two laser fluences (70 and 200  $\mu\text{J}$ ) (Figure 3.13). For these simulations,

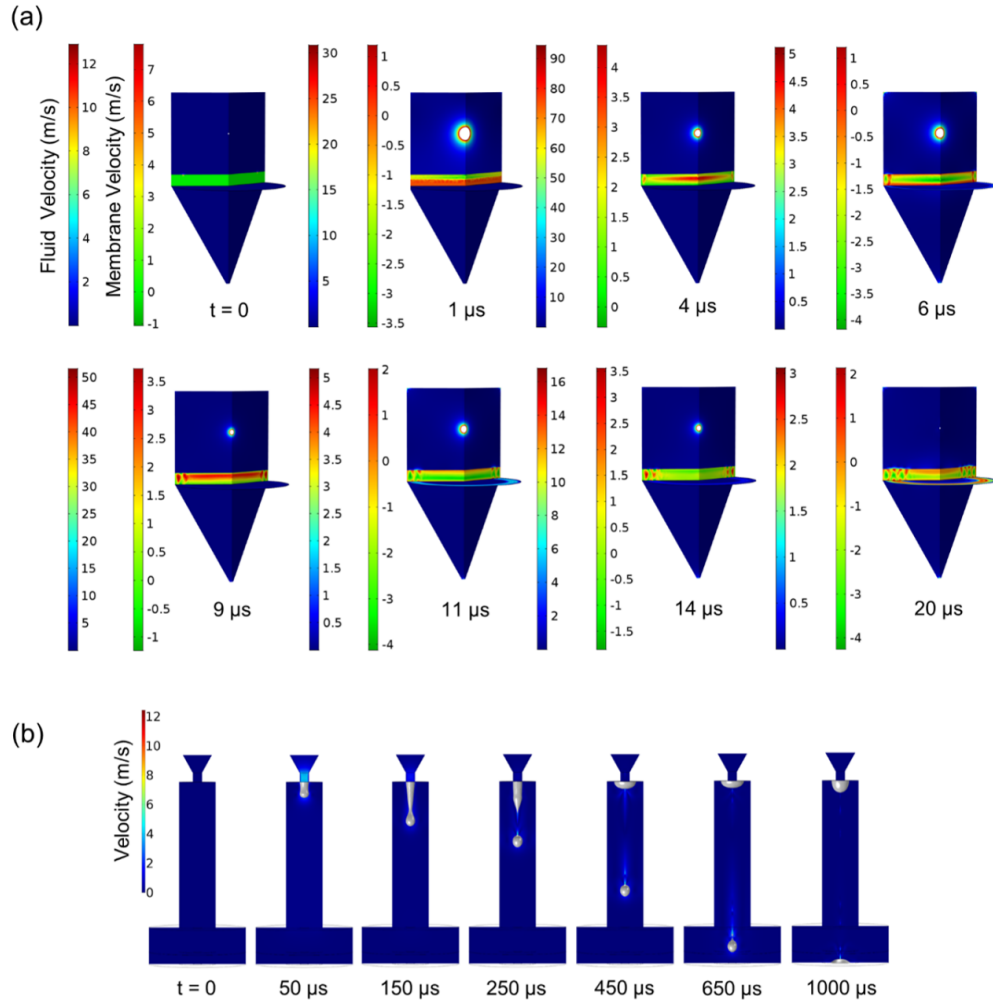


Figure 3.11: Numerical simulation of laser-induced liquid ejection from the liquid confining device presented in Figure 3.2 for  $70 \mu\text{J}$  laser energy: (a) bubble and membrane dynamics (FSI simulation) and (b) liquid ejection dynamics (TPF simulation). Videos with the complete bubble and ejection dynamics can be found in the supplementary material (section B.3-Video S3 and section B.4-Video S4).

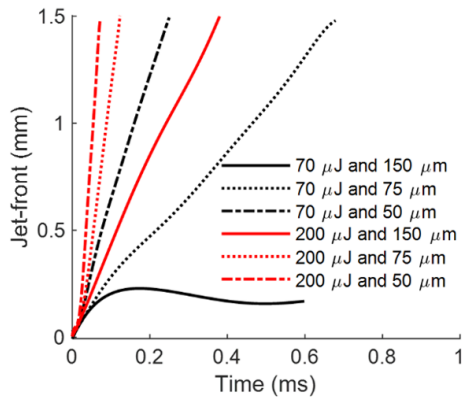


Figure 3.12: The effect of the nozzle size variation on the liquid ejection dynamics for an otherwise identical liquid confining device (see Figure 3.2). The jet front trace for 70  $\mu\text{J}$  laser energy and 150  $\mu\text{m}$  nozzle size corresponds to a non-detached oscillating liquid meniscus.

the nozzle diameter was 200  $\mu\text{m}$  and the membrane thickness varied from 200 to 600  $\mu\text{m}$ . We found that the velocity of the ejected liquid decreases with the increase of the membrane thickness. Indicatively, for laser energy of 200  $\mu\text{J}$ , the simulated average jet velocity is 12.2 m/s and 2.6 m/s for membrane thickness of 200  $\mu\text{m}$  and 600  $\mu\text{m}$ , respectively. Accordingly, the simulations show that the thinner the membrane the lower the laser energy ejection threshold for an otherwise identical geometry. This is an expected behavior because the thicker the elastic membranes the higher the damping capacity for the liquid's kinetic and pressure energy. We opted for 200  $\mu\text{m}$  membrane thickness for next part of our study.

### The effect of the laser energy

Finally, we investigated the effect of the laser energy on the ejected liquid dynamics for two nozzle diameters: 75  $\mu\text{m}$  (Figure 3.14) and 50  $\mu\text{m}$  (Figure 3.15). The simulated jet front average ejection velocity increases with the increase of the laser energy for the scanned laser energy range (50 to 450  $\mu\text{J}$ ). From 0.94 m/s (75  $\mu\text{m}$ ) and 4.1 m/s (50  $\mu\text{m}$ ) at the laser energy ejection threshold to 19.9 m/s (75  $\mu\text{m}$ ) and 48.4 m/s (50  $\mu\text{m}$ ) for 450  $\mu\text{J}$ . The simulated ejected volume varies from 0.097 nL to 5.49 nL for 50  $\mu\text{m}$  nozzle size and from 0.49 nL to 7.68 nL for 75  $\mu\text{m}$  nozzle size. We determined the pinch off time, which indicates the droplet ejection repetition rate. It varies from 210 (4.76 kHz) to 837  $\mu\text{s}$  (1.19 kHz) for 75  $\mu\text{m}$  nozzle and from 240 (4.05 kHz) to 605

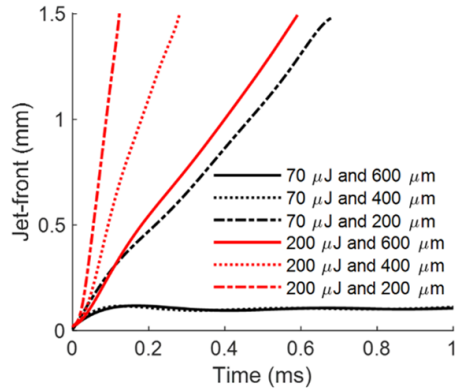


Figure 3.13: The effect of the membrane thickness on the liquid ejection dynamics for an otherwise identical liquid confining device (see Figure 3.2). The jet front trace for  $70 \mu\text{J}$  laser energy and  $600 \mu\text{m} / 400 \mu\text{m}$  diameter thickness corresponds to a non-detached oscillating liquid meniscus.

$\mu\text{s}$  (1.65 kHz) for  $50 \mu\text{m}$  nozzle. For a given laser energy the jet detaches faster for the  $50 \mu\text{m}$  nozzle compared to  $75 \mu\text{m}$  nozzle. In the context of a printing application, the size of the deposited drop would determine the spatial resolution of the printed pattern. However, the final drop size depends on the variety of factors, including the impact speed and wettability of the receiving substrate. Indicatively, we considered that the droplets land with no splashing and have a  $30^\circ$  contact angle on a substrate to evaluate the resulting drop size for the laser energies considered here. With such an assumption, we estimate that drops with diameter from  $120 \mu\text{m}$  to  $465 \mu\text{m}$  can be printed with the  $50 \mu\text{m}$  nozzle. The corresponding drop size for the  $75 \mu\text{m}$  nozzle varies from  $210 \mu\text{m}$  to  $525 \mu\text{m}$ .

### 3.5 Conclusion

We presented a hybrid analytical/numerical model suitable for modeling laser-induced microjet generation from liquid confining devices. For a given laser energy the analytical model predicts the bubble dynamics in a closed chamber. Importantly, by coupling the RP and Tait equations we account for the "self-confinement" of the bubble due to the pressure increase inside the chamber. With FSI and TPF numerical simulations we simulated the performance of such device in a bio-printing context. We show its capability to generate microjets (velocity:  $0.93 \text{ m/s}$  to  $48.39$

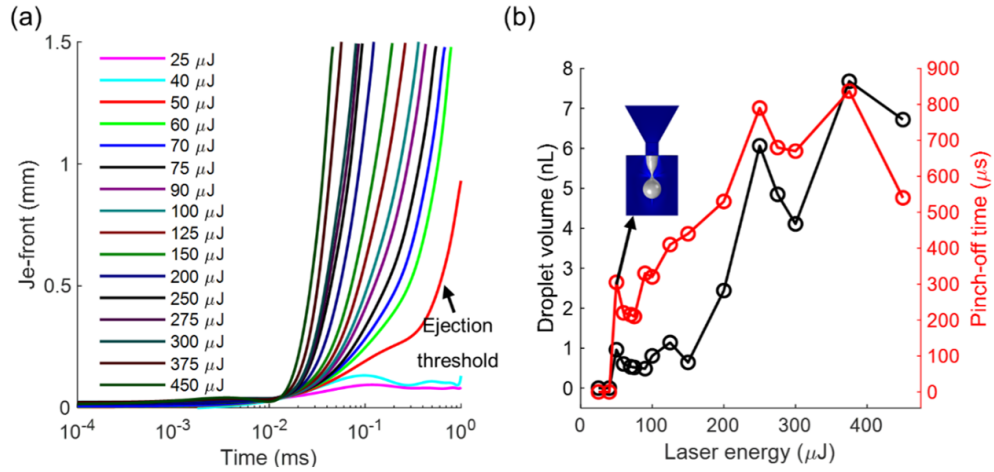


Figure 3.14: The effect of the laser energy on the liquid ejection dynamics for the liquid-confining device of Figure 3.2 (nozzle size 75  $\mu\text{m}$ , membrane thickness 200  $\mu\text{m}$ ). The jet front traces for 25 and 40  $\mu\text{J}$  laser energy correspond to non-detached oscillating liquid menisci.

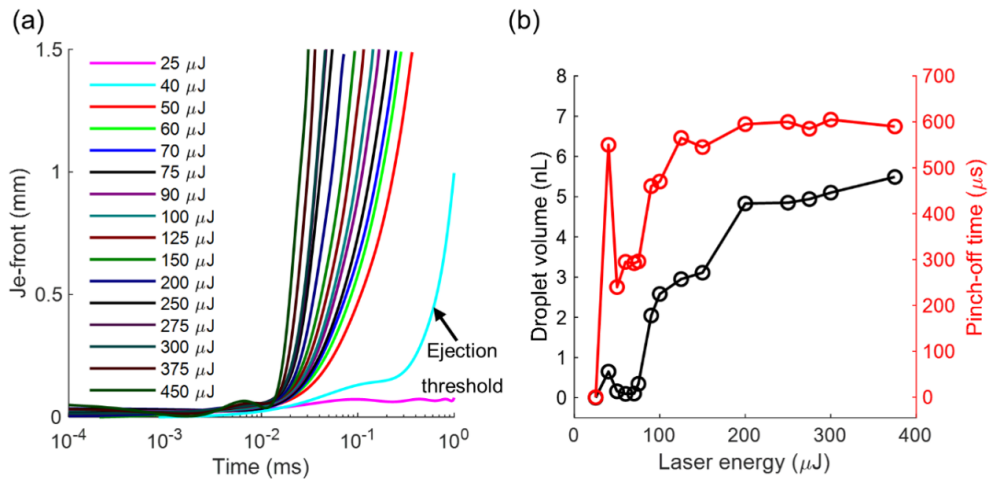


Figure 3.15: The effect of the laser energy on the liquid ejection dynamics for the liquid-confining device of Figure 3.2 (nozzle size 50  $\mu\text{m}$ , membrane thickness 200  $\mu\text{m}$ ). The jet front traces for 25  $\mu\text{J}$  laser energy correspond to non-detached oscillating liquid menisci.

m/s) suitable for microdrop deposition (volume: 0.097 nL to 7.68 nL) for laser energies ranging from 50  $\mu\text{J}$  to 450  $\mu\text{J}$ . Overall, the model provides insights on the effect of the device geometry, membrane thickness and laser energy on the ejection process. Beyond printing applications, it can be widely adapted for designing and optimizing needle-free drug injectors and microfluidic devices.

Since the publication of this article, Orimi et al. have presented a study in which self-limiting bubble dynamics has been experimentally studied [156]. Additionally, the results of the parametric study in this research have been employed by Schoppink et al. to provide insights for laser to jet energy conversion in laser-assisted jet injectors [188]. Knowledge of bubble dynamics in a confined geometry paves the path for optimization of methods in which laser-induced bubbles are used as a driving force. For example, the use of laser-induced bubbles in bioprinting [189] and non-contact injection [117] can be mentioned.

# Chapter 4

## Drop-on-demand cell bioprinting via laser-induced side transfer

This chapter is based on the manuscript published in Scientific Reports, where the development and validation of laser-induced side transfer (LIST) are presented. This chapter covers the objective “3(a-d)” of the “Thesis objective and scope” in Section 1.7.

### 4.1 Introduction

Cell bioprinting technologies aim to build living constructs with long term mechanical and biological stability suitable for transplantation, as well as to provide improved 3-dimensional (3D) drug discovery models [37, 190]. Central goal in cell-bioprinting is the positioning of multiple cell types on a supporting substrate in a precise manner. Post printing cell viability and spatial resolution are key determinants for the overall efficacy of the printing process. The main bioprinting technologies include drop-on-demand approaches [11], such as ink-jet printing [13, 191] and laser-induced forward transfer (LIFT) [192], as well as microextrusion [37, 193]. Depending on the printing mechanism, these technologies present partial only compatibility with available bio-ink formulations, with the bio-ink viscosity being the limiting factor [37]. For example, ink-jet printing is limited to the 3.5-12 mPa.s viscosity range and microextrusion from 30 mPa.s to  $>6 \times 10^7$  mPa.s [37]. LIFT does not use a nozzle. Such an implementation enables printability for an extended bio-ink viscosity range

(1 -300 mPa.s) [37]. In LIFT, a focused laser beam is used to propel a small quantity of a bio-ink film, previously spread on a transparent donor substrate, towards a receiving substrate. It has been successfully employed for 2D printing of a wide range of biomaterials, including living cells [194], proteins [106], isolated photosynthetic materials [195] and nucleic acids [196], with marginal cell viability compromise [33, 197–203]. Despite these significant developments, LIFT has yet to broadly reach tissue engineering laboratories. The main limitation of this technology is the necessity to apply and maintain a thin and uniform bio-ink film (5-20  $\mu\text{m}$ ) on the donor substrate. This step is technically challenging and limits 3D printing capabilities of LIFT. Indicatively, 3D bio-printing of a 1  $\text{cm}^3$  construct would require the preparation of a 1  $\text{m}^2$  bio-ink film. Laser-induced flow focusing has been used to print droplets of model (viscosity: 2–210 mPa.s) and protein solutions [120]. This approach has been initially implemented for the generation of supersonic microjets aiming to needle-free drug injection [114, 115, 149, 204]. Laser-induced flow focusing uses laser-induced bubble generation close to a liquid/air interface (i.e., the distal end of liquid filled microtube) to produce a microjet via the displacement of a concave shaped liquid surface. This technology has been largely exploited for supersonic jet generation, but it has not been tested for cell bioprinting. In this work, we present a non flow focusing variation of this approach as a method to print cells. The method, coined laser-induced side transfer (LIST), uses low energy laser pulses to generate a transient microbubble at the distal end of a glass microcapillary supplied with bio-ink. This causes the ejection of cell-containing microjet perpendicular to the irradiation axis (Figure 4.1a). We studied the jet ejection dynamics in LIST and determined optimal conditions for uniform bioprinting of a human umbilical vein endothelial cells (HUVECs) containing drops. We demonstrated droplet bio-printing up to a 30 Hz repetition rate and showed that LIST printed HUVECs presented marginal loss of viability and maintained their abilities to migrate, proliferate and form intercellular junctions.

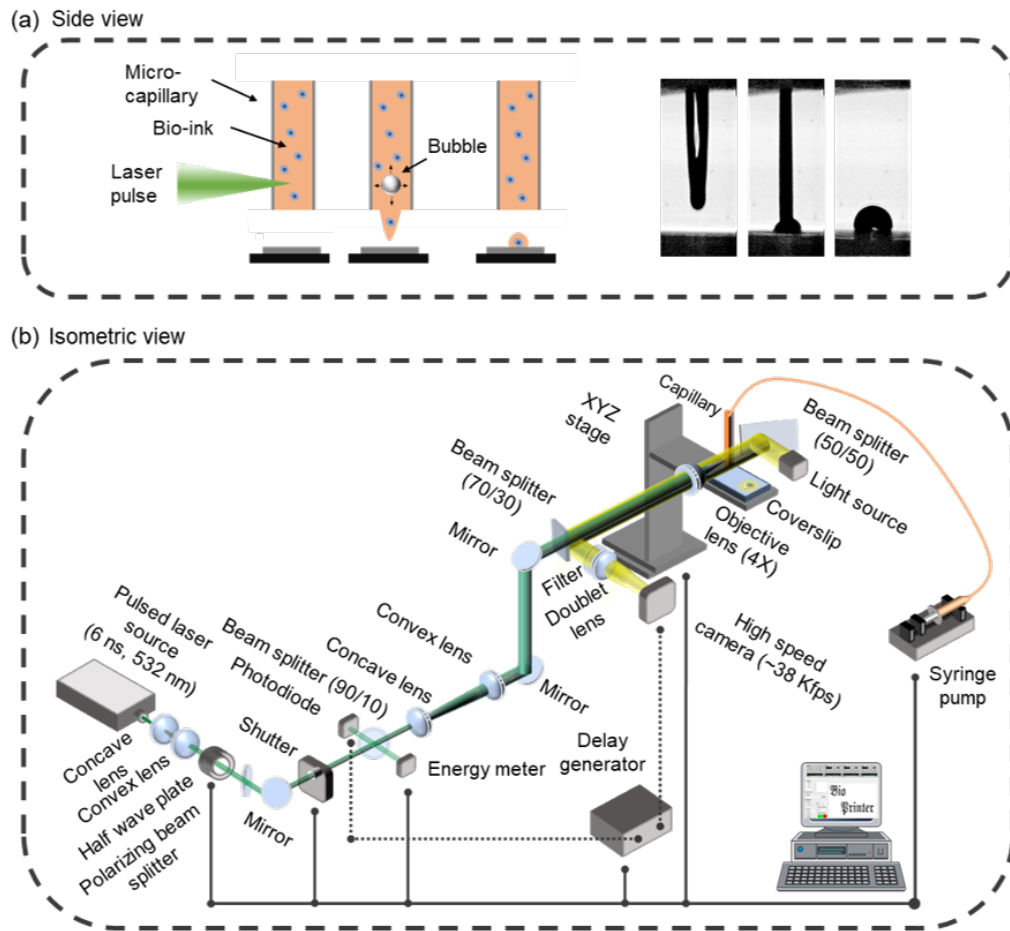


Figure 4.1: Overview of LIST (a) schematic side view representation of LIST bio-printing (left) and indicative high-speed imaging of bio-ink ejection from capillary tip to the substrate (right) and (b) schematic of the complete LIST bioprinting setup.

## 4.2 Material and methods

### 4.2.1 Laser beam delivery system

Figure 4.1b shows a schematic of the beam delivery system. We first expanded the exiting laser (Nano L series, Litron Lasers) beam from 4 mm to 8 mm in diameter by using a pair of concave ( $f = -50$  mm, LC1715-A-ML, Thorlabs) and convex lenses ( $f = 100$  mm, LA1509-A, Thorlabs). We used a motorized optical attenuator to control the laser energy, composed of a half-wave plate (WPMH05M-633, Thorlabs) a rotation stage (PRM1Z8, Thorlabs) and a polarizing beam splitter. On-line laser energy monitoring was attained by sampling the beam with a beam splitter (10:90 (R:T), BSN10, Thorlabs) and by measuring the energy of the sampled beam with a pyroelectric sensor (QE12LP-S-MB, Gentec-eo) to derive the energy at the sample. A second pair of lenses ( $f=-50$  mm, LC1715-A-ML, and  $f=150$  mm, LA1433-A-ML, Thorlabs) was used to further expand the beam from 8 mm to 24 mm in diameter and a pair of broadband dielectric mirrors (BB1-E02, Thorlabs) to elevate it to the desired level. Finally, the beam was focused at the middle of the capillary (Vitrocom hollow square capillary, inner size  $0.3 \text{ mm} \times 0.3 \text{ mm}$ ,  $0.15 \text{ mm}$  wall thickness, 50-mm long) by using a 4X objective lens (plan achromat,  $\text{NA} = 0.1$ , Olympus).

### 4.2.2 Drop-on-demand unit

The drop-on-demand unit uses a mechanical shutter (SH05, Thorlab) and an xyz motorized translational stage (PT1-Z8+ MAX 201, Thorlabs) to control the ejection of the droplets and their positioning on the receiving substrate (Figure 4.1b). The capillary is fixed during printing and the receiving substrate is displaced according to the desired printing pattern. A syringe pump (NE-1000, New Era Pump Systems Inc.) was used to refill the capillary at regular intervals.

### 4.2.3 Microjet visualization system and analysis

We used shadowgraphic imaging to study the microjet ejection dynamics in LIST (Figure 4.1b). Two approaches were implemented: (i) long-exposure imaging and (ii) fast-imaging. The first approach enabled the acquisition of single blur snapshots of microjets at pre-determined time points regarding laser firing (accuracy:  $\pm 1 \mu\text{s}$ ),

while the second approach enabled the acquisition of multiple jet snapshots of a microjet evolution at loosely determined time points (accuracy:  $\pm 31.5 \mu\text{s}$ ). By combining the two approaches we reconstructed the complete jet ejection dynamics for given laser conditions. For both approaches, we used a high-speed camera (Chronos 1.4, Kron Technologies) and back (light emitting diode) LED illumination (MCWHL5 and  $f = 150 \text{ mm}$ , AC254-150-A-ML, Thorlabs). A delay generator (DG535, Stanford Research Systems) and a photodiode (DET10A, Thorlabs) were used to synchronize the laser with the camera at desired time delays. For long-exposure imaging, we set the exposure time to  $50 \mu\text{s}$ . For high-speed imaging, we set the frame rate to 15870 fps (period  $63 \mu\text{s}$ ) and the exposure time to  $3 \mu\text{s}$ . For this imaging mode, the first frame had an arbitrary delay (0 to  $63 \mu\text{s}$ ) with respect to laser firing. We first used fast imaging to acquire multiple snapshots of jet dynamics generated at different energies. Then, we used long-exposure imaging at the same energies to estimate the speed of the ejected jets (section C.2- figure D.2). By knowing the jet ejection speed for a given energy, we assigned an approximate time stamp to the first frame of fast imaging (section C.2- figure D.2). Finally, we used MATLAB to process time-resolved images to extract the jet front as a function of time.

#### 4.2.4 Bio-ink formulation

HUVECs (Promocell) were cultured in EndoGRO-VEGF medium (Millipore). For the bio-ink we used  $10^6$  HUVECs per ml suspended in Basal medium (EndoGRO, Millipore), supplemented with fibrinogen ( $13.24 \mu\text{M}$ ) (F8630-5G; Sigma-Aldrich) and aprotinin ( $7.68 \mu\text{M}$ ) (10820-25MG; Sigma-Aldrich) that facilitated the gelation processes post printing. A red food dye, Allura red AC (458848-100G, Sigma-Aldrich), was also added to a final concentration of 10 mM to enhance light absorption by the bio-ink.

#### 4.2.5 Printing substrates

We used fibrin-coated  $24 \text{ mm} \times 50 \text{ mm}$  microscope cover glasses (12-545-F, Fisher Scientific) as printing substrates. For the fibrin gel coating ( $\approx 1 \text{ mm}$ -thick), we used  $1185 \mu\text{L}$  of a Basal medium (SCME001, Millipore), containing fibrinogen ( $13.24 \mu\text{M}$ ) (F8630-1G, Sigma) an aprotinin ( $7.68 \mu\text{M}$ ) (10820-25MG; Sigma-Aldrich) and 15

$\mu\text{L}$  of a thrombin solution (1.25 U/mL final concentration in the fibrin gel) (T7513-100UN, Sigma-Aldrich). We used drop-casting to deposit the two solutions onto the microscope cover glasses one hour before printing.

#### 4.2.6 Printing protocol

Freshly prepared bio-ink ( $\approx 100 \mu\text{L}$ ) was loaded to the squared capillary using the syringe pump. The laser beam was focused in the middle of the capillary,  $500 \mu\text{m}$  far from its distal end. The receiving substrate was placed on an xyz translation stage and placed  $500\text{-}700 \mu\text{m}$  far from the capillary tip. Laser energies at the sample varied from  $90$  to  $130 \mu\text{J}$ . Printing patterns consisted in arrays of individual droplets separated by a  $500 \mu\text{m}$  gap. After printing, samples were placed in an incubator ( $37^\circ\text{C}$ ,  $5\% \text{CO}_2$ ) for  $5\text{-}10$  minutes. Next, we rinsed the samples twice with EndoGRO-VEGF medium (Millipore) to dilute the light absorbing red dye and put them back in the incubator till further analysis.

#### 4.2.7 Viability assay

We used a Calcein AM viability assay to access the viability of the printed cells at different time points and for various printing conditions. Post printing, we used Hoechst 33342 ( $14.237 \mu\text{M}$ ) (14533-100MG; Sigma-Aldrich) to stain all printed cells and Calcein AM ( $0.402 \mu\text{M}$ ) (400146, Cayman chemical) to evaluate the presence of live cells. Fluorescence images were acquired by an inverted motorized microscope with live cell imaging capabilities (Zeiss AxioObserver Z1). We developed a MATLAB algorithm to process the images. The algorithm detects the nucleus of all printed cells, stained in blue by Hoechst 33342. For each cell, the intensity  $I_c$  at the green channel (Calcein AM) is registered. The background green channel intensity,  $I_b$ , as well as its standard deviation,  $\sigma_{I_b}$ , are considered. A cell is considered live (i.e., Calcein AM positive) if its green channel intensity satisfies the following formula  $I_c > I_b + 5 \times \sigma_{I_b}$ .

#### 4.2.8 Visualization of intercellular junctions

We used immunofluorescence to visualize intercellular junctions for LIST-printed and control deposited HUVECs 3-days post printing/deposition. We first incubated the samples with Paraformaldehyde (PFA)  $4\%$  for  $10$  to  $15$  minutes to fix the cellular

protein and subcellular structures in place. The samples were then incubated with a blocking solution containing 3% Bovine serum albumin (BSA) and 0.1% Triton X-100 in Phosphate buffered saline (PBS) (including  $Mg^{2+}$  and  $Ca^{2+}$ ) for 10-15 minutes to induce permeabilization. Samples were then incubated with CD 31 (1:500) and VE-Cadherin (1:40) antibodies diluted in permeabilization medium at 4°C in the dark overnight. The following day, the samples were treated with the secondary antibody (Alexa Fluor 647 chicken anti-rat) (1:200) for 3 hours in room temperature. Finally, the samples were imaged by an upright confocal microscope (Zeiss AxioExaminer Z1).

## 4.3 Results and discussion

### 4.3.1 Laser-induced side transfer (LIST)

In LIST, cell-containing droplets are generated by focusing a 6 ns laser pulse (wavelength 532 nm, pulse duration 6 ns, energy per pulse 50 to 150  $\mu$ J) in a hollow square glass capillary filled with bio-ink. The irradiance at the focal plane is tuned to exceed the cavitation threshold of the bio-ink, resulting in the generation of transient spherical bubble (Figure 4.1a). Bubble expansion propels the bio-ink toward the capillary opening, resulting in the ejection of cell-containing microjet (Figure 4.1a). The LIST setup consists of three main parts: a) a laser beam delivery system, b) a drop-on-demand unit, and c) a microjet visualization system (Figure 4.1b). The setup is automated and controlled by MATLAB via graphical user interface (GUI). We provide a complete description of the setup in Methods.

### 4.3.2 Optimizing the printing process

In the first part of our work we sought to study and optimize the printing process via the visualization of the bio-ink ejection from the microcapillary tip. Our primary objective was to determine the laser energy resulting in the deposition of uniform cell-containing droplets on fibrin receiving substrates. We varied the laser energy from 90  $\mu$ J (i.e., ejection threshold) to 130  $\mu$ J and found that the bio-ink is ejected in the form of a microjet that eventually reaches the substrate (Figure 4.2). The jetting behaviour is similar to that observed in previous studies on laser-induced flow focusing of model solutions for drug delivery applications [115, 204]. However here,

the bio-ink jets are less energetic and do not penetrate the substrate. Their impact to the substrate results in the formation of an oscillating droplet that can even bounce back for low energies (90  $\mu\text{J}$ ). For higher energies (120 and 130  $\mu\text{J}$ ), satellite droplet formation as well as “splashing” behavior can be observed. Note that the deposited droplets “relax” at different contact angle depending on the laser energy. Similar phenomena have been widely observed in the LIFT literature [167,205]. Figure 4.3a illustrates the jet-front position extracted from the jet-ejection visualization. The average jet-front velocity ranges from 3.2 to 11.60 m/s for the examined laser energies (90 to 130  $\mu\text{J}$ ). The average jet-front velocity is constant with time for high energies. However, jet-front slowing with time is observed for low ejection velocities (90 to 110  $\mu\text{J}$ ) indicating the predominant effect of viscous and surface forces on the ejection process. Similar behavior has been reported for LIFT generated microjets [146]. The diameter of the deposited droplets varied from 165 to 325  $\mu\text{m}$  for the examined laser energy (Figure 4.3b). The corresponding droplet volume varied from 1.675 to 6.1 nL (Figure 4.3b). It was calculated using the contact angle of the deposited droplets at relaxation around 2 ms (see last column in Figure 4.2).

We acquired optical microscopy images of LIST-printed droplets 30 minutes post printing to evaluate the printing quality and to measure the number of HUVECs contained in each droplet (Figure 4.4a). We found no significant change in the circularity of the deposited droplets within the 90 to 120  $\mu\text{J}$  laser printing energy range. However, we observed non-circular drops and satellite droplet deposition for 130  $\mu\text{J}$  (Figure 4.4a). We found that the number of HUVECs per drop ranged from  $105 \pm 47$  to  $175 \pm 66$  for the examined laser energies (90 to 120  $\mu\text{J}$ ) (Figure 4.4b). These findings agree with fast imaging, where “splashing” behavior was observed for high laser energy printing (Figure 4.2).

Compared to microjet generation by laser-induced flow focusing [120], we used similar laser energy density threshold at focus to generate stable microjets. The generated cell-containing microjets present slightly lower threshold ejection speed (3.2 m/s) compared to that (4-7 m/s) observed for model solutions in Ref. [120]. Contrary to work exploiting flow focusing effects [115,120,204], we do not apply hydrophobicity enhancement treatment to the microcapillary tip. Therefore, there is almost no meniscus concavity and to provoke such effects. Nevertheless, uniform printing is demonstrated in absence of flow-focusing. Furthermore, the spatial resolution for

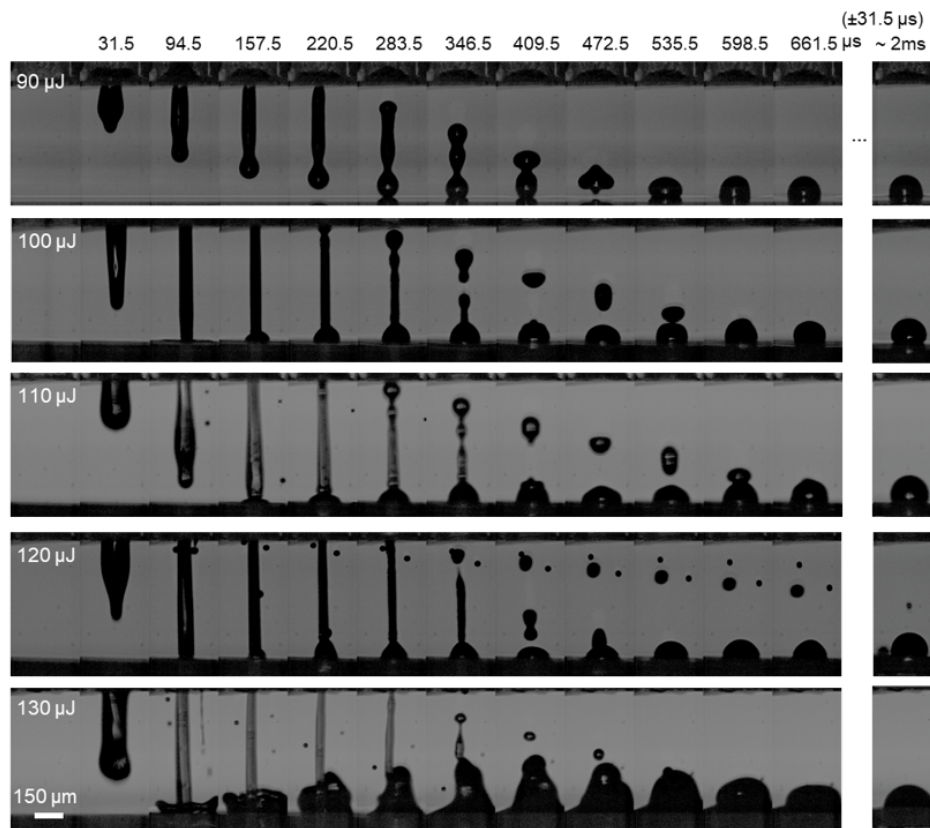


Figure 4.2: Sequences of snapshots showing microjet evolution and drop formation for different laser energies. The laser pulse was focused at the middle point of the capillary and  $500 \mu\text{m}$  above its distal end.

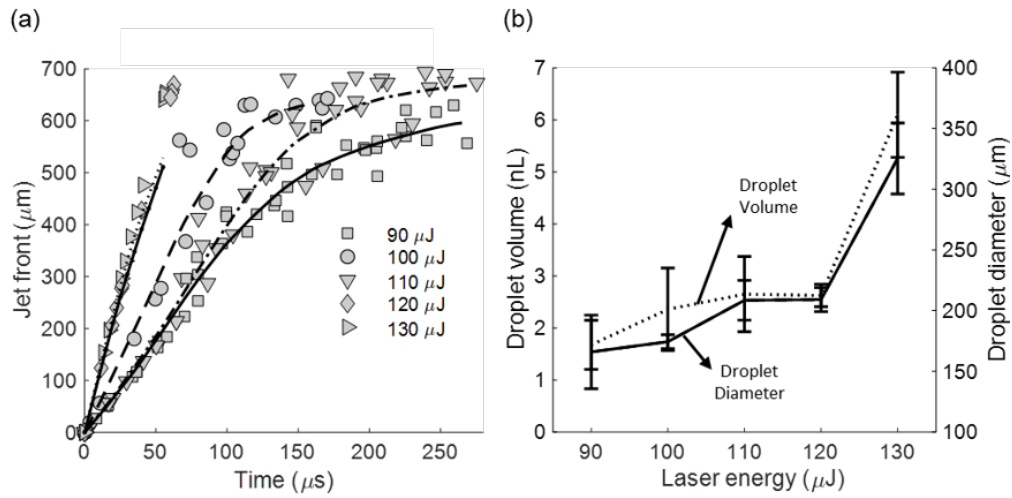


Figure 4.3: (a) The dependence of the bio-ink jet front position on the laser energy. Gray symbols represent data points and black lines represent the best fitted curve,  $N = 10$  (per energy) and (b) the dependence of the droplet volume (dotted line) and droplet diameter (solid line) on the laser energy,  $N = 10$  (per energy).

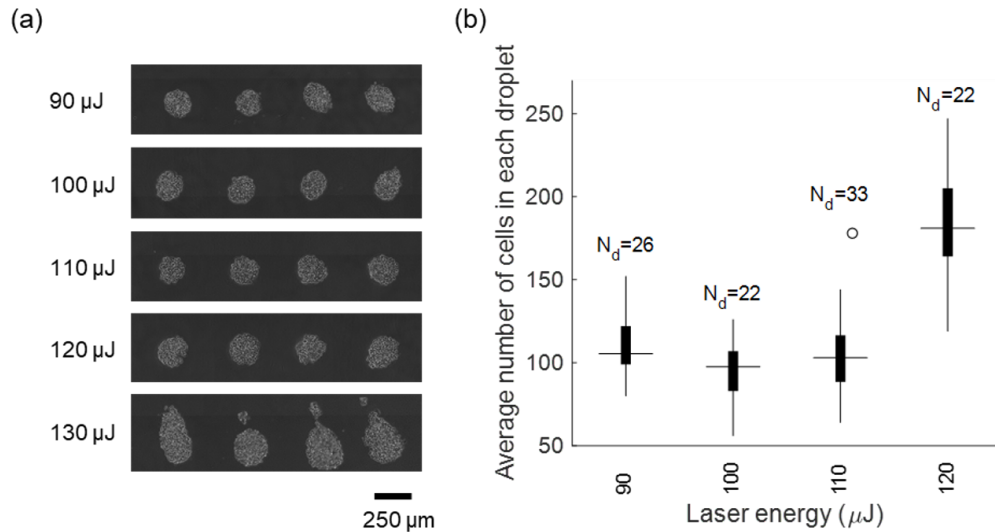


Figure 4.4: (a) Optical microscopy images of LIST-printed HUVECs for various laser energies and (b) the number of the cells per droplet for various laser energies.

our cell-bioprinting setting is  $165\ \mu\text{m}$ , similar to the one attained for model solution printing in Ref20 but lower than the one ( $10\text{-}140\ \mu\text{m}$ ) attained by LIFT for similar cell types [79, 206–208]. The use of microcapillaries of smaller size can potentially further improve the spatial resolution in LIST.

### **4.3.3 LIST printed HUVECs maintain their ability to migrate and proliferate**

The preservation of the cell migration and proliferation characteristics is central for bio-printing applications. We used live-cell time lapse imaging to assess the behavior of LIST-printed HUVECs. We focused on laser printing at  $100\ \mu\text{J}$  because it resulted in the deposition of uniform and reproducible droplets in the optimization study. HUVECs-containing drops were printed at a separation distance of  $500\ \mu\text{m}$  and followed for 3 days by optical microscopy. At day 3, we stained with Calcein AM and Hoechst 33342 to assess cell viability. We found that LIST-printed HUVECs progressively migrated from the initial area of deposition towards distant areas of the fibrin gel (section C.1- Figure C.1a to c). At day 3, the cells reached high confluency and covered uniformly the surface of the fibrin gel. Fluorescence imaging at day 3 indicated high cell viability (98%) post printing (section C.1- Figure C.1d to f). These results indicate that LIST printed HUVECs maintain their ability to migrate and proliferate.

### **4.3.4 LIST printed HUVECs present marginal loss of viability compared to control deposited HUVECs**

Given that LIST involves direct irradiation of a small section of the bio-ink, we sought to quantify potential effects on the viability of the deposited cells. We printed multiple droplets by varying the laser energy from  $90$  to  $120\ \mu\text{J}$ . We used the viability assay described in Methods to measure cell viability at 0, 1, and 3 days post printing. Figure 4.5a to 4.5c shows the typical steps implemented by the cell viability quantification algorithm. Hoechst 33342 stains the nucleus of all cells (Figure 4.5a) and facilitates automated cell counting and cell coordinates registration (blue crosses in Figure 4.5d). The cell coordinates are used to interrogate the intensity of Calcein AM (staining live cells only) in the green channel. The positions of dead cells in the combined channels

image are indicated by red crosses (Figure 4.5c). Right after printing, we found that the cell viability varied from 96.5% to 93.1% for the examined laser range (90 to 120  $\mu\text{J}$ ). There is marginal decrease in cell viability due to increase in laser energy. This can be explained by the increased thermomechanical impact on the cells at high energies compared to low energies, including higher pressure and temperature inside the capillary and generation of higher impact pressures upon jet collision to the fibrin gel. For days 1 and 3, cell viability increased up to level of the control. This is explained by the fact of not considering the cell division rate in our quantification. These results indicate that LIST has only a marginal effect on the viability of the printed cells for the examined laser energy. Similar viability has been observed for printing of HUVECs by LIFT [79, 206] (i.e.  $>90\%$ ). LIST involves direct irradiation of a small fraction of the deposited cells. Further studies are required to evaluate potential mutagenic effects on those cells. Genotoxic effects have been observed *in vitro* for laser irradiation of fibroblasts at 3  $\text{J}/\text{cm}^2$  (532 nm) and at 10  $\text{J}/\text{cm}^2$  (1064 nm) [209]. In this work we used 532 nm and exceeded this threshold at the focal point; thus, a tiny fraction of the deposited cells might be affected. Note that the 1064 nm wavelength presents not only higher threshold for the occurrence of genotoxic effects but also lower cavitation threshold in water compared to 532 nm. Future work on LIST at 1064 nm could eliminate the need to use a radiation absorber in the bio-ink and minimize potential mutagenic effects.

#### 4.3.5 LIST-printed HUVECs form intracellular junctions

Cultured endothelial cells such as HUVECs are known to form intercellular junctions. These junctions are composed of several cell adhesion molecules including PECAM-1/CD31, a cell adhesion and signaling molecule, and VE-cadherin, which has is essential for the formation of endothelial adherens junctions. We sought to investigate whether proper intracellular junctions were formed between LIST-printed HUVECs. We LIST-printed HUVECs at 100  $\mu\text{J}$ . 3-days post printing, the cells formed a relatively uniform and confluent layer on the fibrin gel. We performed immunofluorescence imaging to interrogate the presence of intercellular junctions (VE-cadherin and CD31) in both LIST-printed and control HUVECs (Figure 4.6). We found that LIST-printed HUVECs form intercellular junctions similar to control HUVECs cells. In fact, there was no apparent difference in the intensity and/or spatial distribution

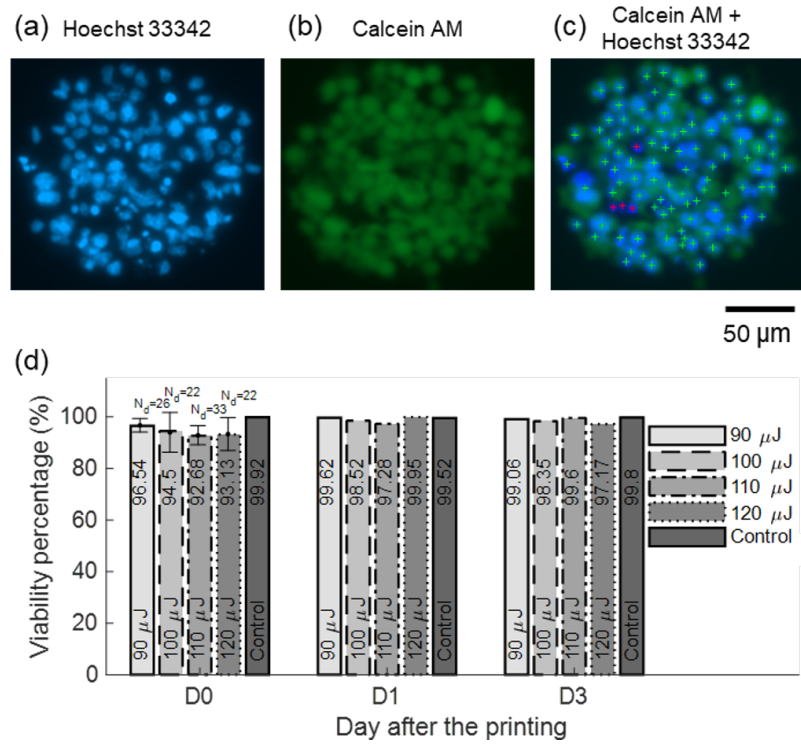


Figure 4.5: (a,b) Fluorescence microscopy images of LIST printed cells at  $90 \mu\text{J}$ , (c) Combined imaging channels, including algorithm-generated cell labeling marks. Green crosses indicate live cells and red crosses indicate dead cells and (d) The dependence of the HUVEC cell viability on the laser energy for 0, 1 and 3-days post printing.  $N_d$  indicates the number of droplets.

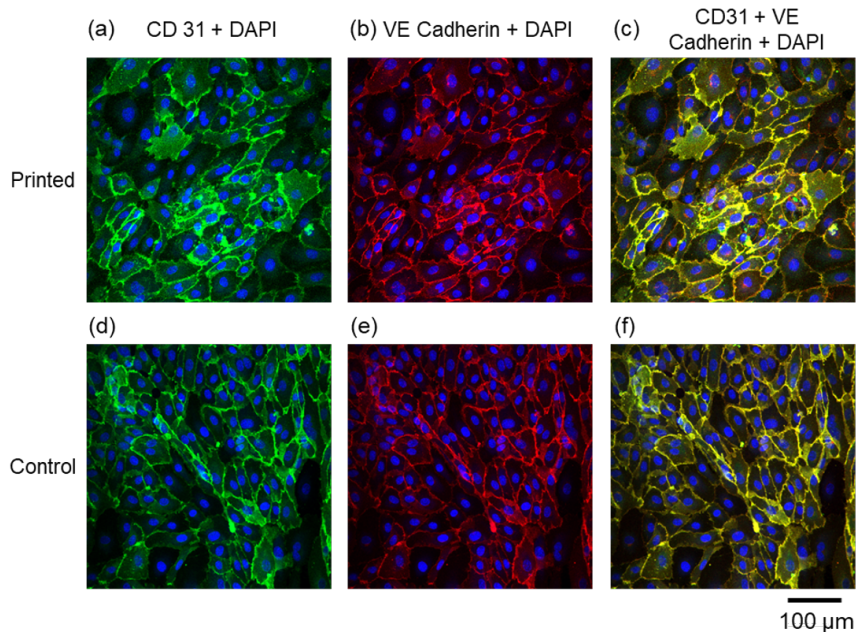


Figure 4.6: Confocal microscopy images of (a–c) LIST-printed ( $100 \mu\text{J}$ ) and (d–f) control HUVECs. Green indicates CD31 staining, red shows VE Cadherin and blue indicates cell nuclei staining with DAPI.

of the junction observed for the two groups. These results indicate the LIST-printed cells preserve their angiogenic junctional phenotype.

### 4.3.6 High speed LIST printing

Efficient printing of clinically relevant constructs (i.e.,  $1 > \text{cm}^3$ ) in a reasonable time period requires high-speed printing. In this context, we sought to study printing speed capabilities in LIST. We examined how the increase in the printing speed affects the jetting dynamics and the viability of the deposited cells. We increased the printing speed up to 30 Hz, which was the maximum repetition rate of our laser. We kept the laser energy constant ( $100 \mu\text{J}$ ) for this series of experiments and we did not use any substrate to prevent the perturbation of the ejected jets by already deposited material. We found that the ejected jets maintained similar spatiotemporal evolution for the tested printing speeds of 10, 20 and 30 Hz (Figure 4.7). However, for 30 Hz we observed the ejection of small satellite droplets on both sides of the main jet. We found insignificant differences on the jet-front ejection speed, i.e., 5.2 m/s for 1 Hz, 4.2 m/s for 10 Hz, 5.5 m/s for 20 Hz and 5.0 m/s for 30 Hz. Moreover, we found

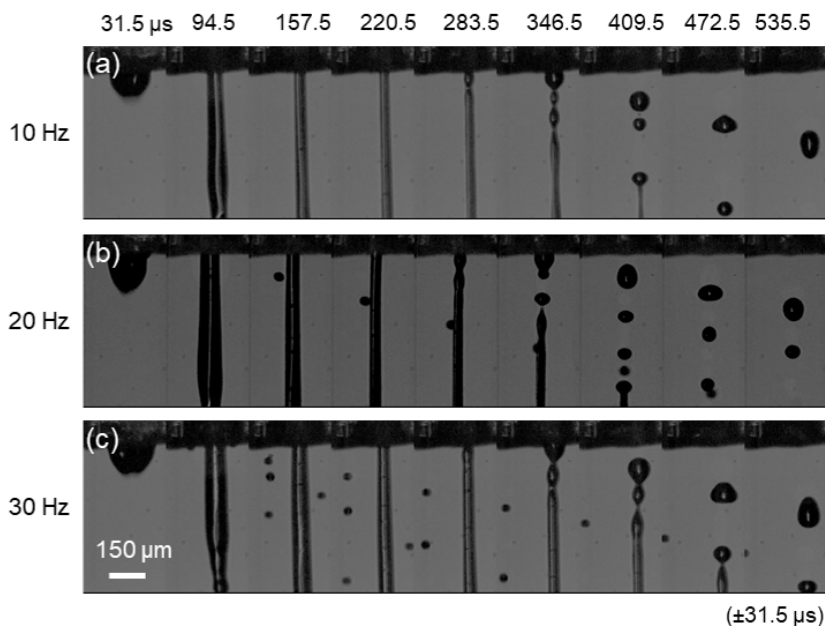


Figure 4.7: Sequences of snapshots showing microjet evolution for (a) 10 Hz, (b) 20 Hz and (c) 30 Hz. The laser energy was kept constant at  $100 \mu\text{J}$ . The laser pulse was focused at the middle point of the capillary and  $500 \mu\text{m}$  above its distal end.

that the microjet detachment occurs at a relatively constant time point for the tested conditions i.e., from  $315$  to  $378 \mu\text{s}$ . This indicates a potential printing speed up to  $2.5 \text{ kHz}$ . Indicatively, for LIST-printing at  $100 \mu\text{J}$ , one would need  $\approx 236 \text{ min}$  to print a  $1 \text{ cm}^3$  construct at  $30 \text{ Hz}$  and  $2.83 \text{ min}$  to print the same at  $2.5 \text{ kHz}$ . We further examined whether the increase of the printing speed affects the viability of the HUVECs. We found that the differences in the cell viability for  $10$ ,  $20$  and  $30 \text{ Hz}$  lied within the experimental error (Figure 4.8). These results indicate that with appropriate technical modifications, LIST has the potential to reach high printing speeds up to the range achieved by ink-jet printing.

## 4.4 Conclusion

We developed and validated a laser-assisted drop-on-demand method to print cell-containing droplets. Under optimal printing conditions (laser energy:  $100 \mu\text{J}$ ), uniform HUVECs containing droplets were deposited on fibrin coated substrates. Post printing, HUVECs maintain high viability and preserve their angiogenic junctional

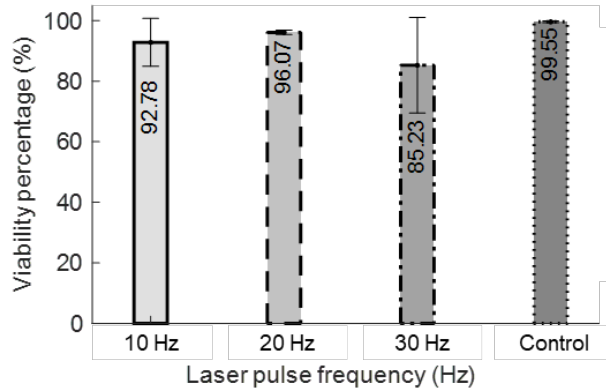


Figure 4.8: The dependence of the HUVEC cell viability on the printing speed. The laser energy was kept constant at  $100 \mu\text{J}$ .

phenotype. The minimum droplet size was  $165 \mu\text{m}$  for the tested conditions. Printing of smaller droplets should be possible by using thinner microcapillaries and/or by tuning the viscosity of the bio-ink. We showed droplet bio-printing up to a 30 Hz repetition rate, i.e., equal to the maximum repetition rate of the available laser. However, fast imaging of jet ejection dynamics indicate that LIST can potentially reach a printing speed of 2.5 kHz. Similar to ink-jet printing, simultaneous printing of multiple bio-ink is technically possible using multiple microcapillaries. LIST is technically uncomplicated and can foster 3D printing applications. It can potentially cover a technological gap in bioprinting technologies, between ink-jet printing and LIFT, as it could not only print bio-inks of high-viscosity but also support 3D printing of constructs with clinically relevant size.

Following the publication of the method presented in this chapter, the method has been used for neuron printing by Roversi et al. [189]. Using this approach, the biological analyzes presented a negligible impact on the functionality of this cell type. Moreover, This method has also been considered by researchers as an efficient method for printing primary cells [117, 210–213].

# Chapter 5

## Spatially guided angiogenesis assay and tube-like formation by laser-induced side transfer (LIST) bioprinting of HUVECs

This chapter is based on the manuscript to be submitted to Biofabrication, where the spatially-guided angiogenesis assay and the tube-like formation are presented. This chapter covers the objective “4(a-b)” of the “Thesis objective and scope” in Section 1.7.

### 5.1 Introduction

Bioprinting technologies aim to build living constructs with long term mechanical and biological stability suitable for transplantation, as well as to provide improved 3-dimensional (3D) drug discovery models [37,190]. Bioprinting of human umbilical vein endothelial cells (HUVECs) is the basis for creating microvasculature networks, which are of great interest for a variety of applications. Bioprinted living constructs of clinically relevant size require the incorporation of a fine-printed (resolution 100 to 200  $\mu\text{m}$ ) HUVECs capillary network (“capillary beds”) to ensure cell access to nutrients and oxygen as well as removal of metabolic wastes. This is essential for

the survival of the printed constructs in the long term [214–216]. Furthermore, bio-printed microvasculature can serve as a platform to study tubulogenesis and to screen compounds for microvasculature pathologies before initiating animal studies.

A central goal in bioprinting is the precise positioning of multiple cell types and/or biomaterials on a supporting substrate. Conventional bioprinting technologies include drop-on-demand (DOD) approaches, such as ink-jet printing [38, 217–219] and laser-induced forward transfer (LIFT) [192], as well as microextrusion-based bioprinting (MBB) [37, 193]. Depending on the printing mechanism, these technologies present only partial compatibility with bioink formulations, with bioink viscosity being the limiting factor [37]. MBB have been used to create vascular networks [87, 89, 220–224]. Yet, the printing resolution in MBB is not suitable for fine printing of microvascular networks. DOD bioprinting (e.g., inkjet [225, 226] and laser-induced forward transfer (LIFT) [78–81, 227, 228]) is an alternative for direct printing of HUVECs that attains better spatial resolution compared to MBB [37]. Recently, an alternative laser-based DOD bio-printing technique, termed laser-induced side transfer (LIST), was used to bioprint primary cells such as HUVECs and neurons [158, 189]. LIST printed HUVECs maintain the ability to proliferate, migrate and to form intercellular junctions [158].

Several 3D angiogenesis assays including tissue explants embedded in gels or isolated endothelial cells grown in gels can mimic the in-vivo environment, where endothelial cells surrounded by matrices can form tube-like structures in response to growth factors. These assays allow for rapid evaluation of angiogenic effects of growth factors but are limited to random network formation. The ability to bioprint spatially controlled capillary networks in a reproducible manner can address this limitation and can open new possibilities for studying tubulogenesis and for screening drugs for microvasculature pathologies.

The printing matrix has predominant effect on the self-organization of printed HUVECs. Cardiac patches [81] and collagen [79, 80] have been previously used as matrices LIFT printed HUVECs on Matrigel self-assembled in cord-like formations [78, 79]. However, lumen formation was not sufficiently documented in those early studies. LIFT printed HUVECs form similar cord-like formations on collagen [228]; however lumen formation has yet to be demonstrated. Pro- and anti-angiogenic factors modulate the microvasculature in-vitro and in-vivo [229, 230]. Several 3D angiogenesis assays including tissue explants embedded in gels or isolated endothelial cells grown

in gels can mimic the in-vivo environment, where endothelial cells surrounded by matrices can form tube-like structures in response to growth factors. These assays allow for rapid evaluation of angiogenic effects of growth factors but are limited to random network formation. The ability to bioprint spatially controlled capillary networks in a reproducible manner can address this limitation and can open new possibilities for studying tubulogenesis and for screening drugs for microvasculature pathologies.

Here we used the newly developed LIST to bioprint HUVECs networks on Matrigel, Fibrin and Matrigel/thrombin. We sought to investigate which matrix can better support guided tubulogenesis. We used microscopy to study HUVECs self-assembling post printing as well as an image processing algorithm to quantify lumen formation in printed HUVECs patterns. Finally, we exploited printed patterns as an assay to evaluate the effect of pro- and anti- angiogenic compounds on sprouting angiogenesis and tubulogenesis.

## **5.2 Material and methods**

### **5.2.1 Bioink preparation**

HUVECs (Promocell) were cultured in EndoGRO-VEGF medium (Millipore). The bioink formulation consisted of HUVECs ( $18.75 \times 10^6$  per ml) suspended in Basal medium (SCME-BM, Millipore), supplemented with fibrinogen ( $13.1 \mu\text{M}$ ) (F8630-5G; Sigma-Aldrich) and aprotinin ( $6.92 \mu\text{M}$ ) (10820-25MG; Sigma-Aldrich) and a red food dye Allura red AC (10 mM) (458848-100G, Sigma-Aldrich). The dye enhances light absorption by the bioink and facilitates printing at relatively low energy per laser pulse.

### **5.2.2 Live-dead assay for red dye cytotoxicity assessment**

We used a trypan blue exclusion test to assess potential cytotoxicity effects of the Allura red dye. HUVECs were exposed to Allura red (10 mM or 50 mM in culture medium) for 50 mins, corresponding to the typical exposure time during a bioprinting experiment. The samples were washed, and fresh medium was added. Trypan blue was used to assess viability 1-, 2- and 3-days post exposure to the dye (presented in section D.1).

### 5.2.3 Matrices

We prepared all gels on 18 mm  $\times$  18 mm microscope cover glasses (12-545-A, Fisher Scientific). For fibrin substrates, we used 314  $\mu$ L of a Basal medium (SCME-BM, Millipore), containing fibrinogen (14.11  $\mu$ M) (F8630-1G, Sigma), aprotinin (7.45  $\mu$ M) (10820-25MG; Sigma-Aldrich) and 10  $\mu$ L of a thrombin solution (3.09 U/mL final concentration in the fibrin gel) (T7513-100UN, Sigma-Aldrich). We used drop-casting to deposit the two solutions onto the microscope cover glasses one hour before printing. For Matrigel/thrombin substrates, 100  $\mu$ L Matrigel (35623, Corning) was thawed at room temperature and mixed with 5  $\mu$ L thrombin (4.76 U/mL final concentration in Matrigel) (T7513-100UN, Sigma Aldrich). The mixtures were drop-casted on cover glasses, which were then placed in an incubator (5% CO<sub>2</sub> at 37°C) for 3 hours. For Matrigel substrates, we used the same protocol without adding thrombin.

### 5.2.4 Printing setup and protocol

HUVECs were printed using a setup that has been previously described in detail [158]. Briefly, the gel-coated substrates were mounted on a motorized XYZ translation stage. A microcapillary (Vitrocom hollow square capillary, 0.3 mm inner dimension, 0.15 mm wall thickness and 50 mm long) was brought close ( $\approx$ 500  $\mu$ m) to the gel. The bioink was loaded to the microcapillary via a syringe pump (NE-1000, New Era Pump Systems Inc.). To eject bio-ink drops, we focused a nanosecond pulsed laser (Ultra compact pulsed Nd:YAG, Nano L series) in the middle of the microcapillary and 500  $\mu$ m far from its distal end using a 4 $\times$  Olympus plan achromat objective. The laser energy at the sample level was 110  $\mu$ J. Usually, four 10 mm-long line patterns were printed per sample. After printing, the samples were placed into an incubator for 10 minutes. Next, medium was added. The medium was changed after 30 minutes to remove the diffused red dye.

### 5.2.5 Immunofluorescence imaging

We used immunofluorescence to visualize intercellular junctions for LIST-printed HUVECs at day 5 of post printing. We first incubated the samples with PFA 4% for 10 to 15 minutes to fix the cellular protein and subcellular structures in place. The samples were then incubated with a blocking solution containing 3% BSA and 0.1%

Triton X-100 in PBS (including Mg<sup>2+</sup> and Ca<sup>2+</sup>) for 10–15 minutes to induce permeabilization. Samples were then incubated with CD 31 (1:500) antibodies diluted in permeabilization medium at 4°C in the dark overnight. The following day, the samples were treated with DAPI (1:2000). Finally, the samples were imaged by an upright confocal microscope (Zeiss AxioExaminer Z1).

### 5.2.6 Lumen segmentation and quantification

We developed a MATLAB algorithm to quantify lumen formation in printed HUVECs lines. We binarized fluorescence images (i.e., z-stack frames) to detect connected HUVECs using a thresholding approach detailed in the provided MATLAB code. For each z-stack frame the algorithm calculates the void area contained between connected HUVECs in both x and z axes. Note that lines are printed along the y axis. Void areas  $<25 \mu\text{m}^2$  or having length  $<75 \mu\text{m}$  along the y axis, or those that do not repeat in at least five consecutive slices (i.e.,  $4 \mu\text{m}$  thickness) were rejected. We summed the length of the remaining segmented areas per z-stack frame and used the frame with the largest value to report lumen length. The MATLAB code can be found in the Supplementary.

### 5.2.7 Sprouting Angiogenesis assays

In each well of a 24-well plate, we combined 12  $\mu\text{L}$  of a thrombin solution (1 U/mL final concentration in the fibrin gel) (T7513- 100UN, Sigma-Aldrich) and 50  $\mu\text{g}/\text{ml}$  aprotinin (10820-25MG; Sigma-Aldrich) with 400  $\mu\text{L}$  of fibrinogen (2.5 mg/ml, final concentration of 7.28  $\mu\text{M}$ ) dissolved in basal medium (SCME-BM, Millipore). For solidification purpose, we placed the well in the 37°C incubator for 30 mins. Next, we added 400  $\mu\text{L}$  fibrinogen containing HUVECs ( $\approx 2.5 \times 10^5$  cell per well) on top of the solid fibrin layer in each well. Again, we placed the wells in 37°C incubator to solidify for an hour. Once solidified, we added 400  $\mu\text{L}$  of complete media (EndoGRO-Millipore) containing IMR90 fibroblasts ( $\approx 2.5 \times 10^5$  cell per well). The next day (Day 1), we treated the cells with pro- and anti- angiogenic factors and monitored sprout formation on a daily basis. For fluorescence imaging, we removed the fibroblasts using 0.5 % trypsin and stained the HUVECs with 4  $\mu\text{g}/\text{ml}$  Calcein AM (400146, Cayman chemical) for imaging purposes.

### 5.2.8 Anti- and pro-angiogenic treatments

Sprouting HUVEC samples were treated with either anti-angiogenic recombinant human BMP9 protein (10 ng/ml) (3209-BP-010/CF, R&D Systems) or FLT1-FC (500 ng/ml) (7756-FL-050, R&D Systems) in complete endothelial media (CM). In order to establish conditions where pro-angiogenic factors could promote sprouting, pro-angiogenic compounds BMP6 (200 ng/ml) (120-06, Peprotech Inc) or VEGF (25 ng/ml) (293-VE-010, R&D Systems) were added to HUVECs in basal endothelial media supplemented with 2% FBS. Both pro- and anti-angiogenic treatments were added 1-day after printing or after seeding (conventional assays). Complete endothelial growth medium and basal endothelial medium supplemented with 2 % FBS were used as controls for anti- and pro-angiogenic treatments, respectively. Every other day, the medium was changed and the treatments were repeated.

## 5.3 Results

### 5.3.1 Droplet and line printing by Laser-induced side transfer

LIST is a drop-on-demand printing technology that uses focused laser pulses to eject bioink drops from a glass microcapillary towards a receiving substrate (Figure 5.1a). The high-power density of the laser pulse leads to a series of phenomena, including local ionization of the bioink, micro-bubble generation, liquid displacement, jet formation, and jet impingement at the substrate [158]. Figure 5.1a shows a schematic representation of the LIST working principle and indicative high-speed imaging of droplet ejection. LIST can be used to print arrays of cell-laden drops or continuous lines with appropriate adjustment of the overlap among adjacent droplets.

LIST uses a food dye additive (10 mM Allura red) in the bioink to enhance light absorption at 532 nm. We validated potential toxicity effects of the dye on HUVECs at 10 mM and 50 mM (i.e., 5-fold higher than the one used in the bioink), using a viability assay. We found no compromise in the cell viability for a 1-, 2-, and 3-days post-exposure (Figure D.1).

In this work we performed printing using a previously optimized laser pulse energy of 110  $\mu$ J per pulse [158]. An array of HUVEC-laden droplets is shown in Figure

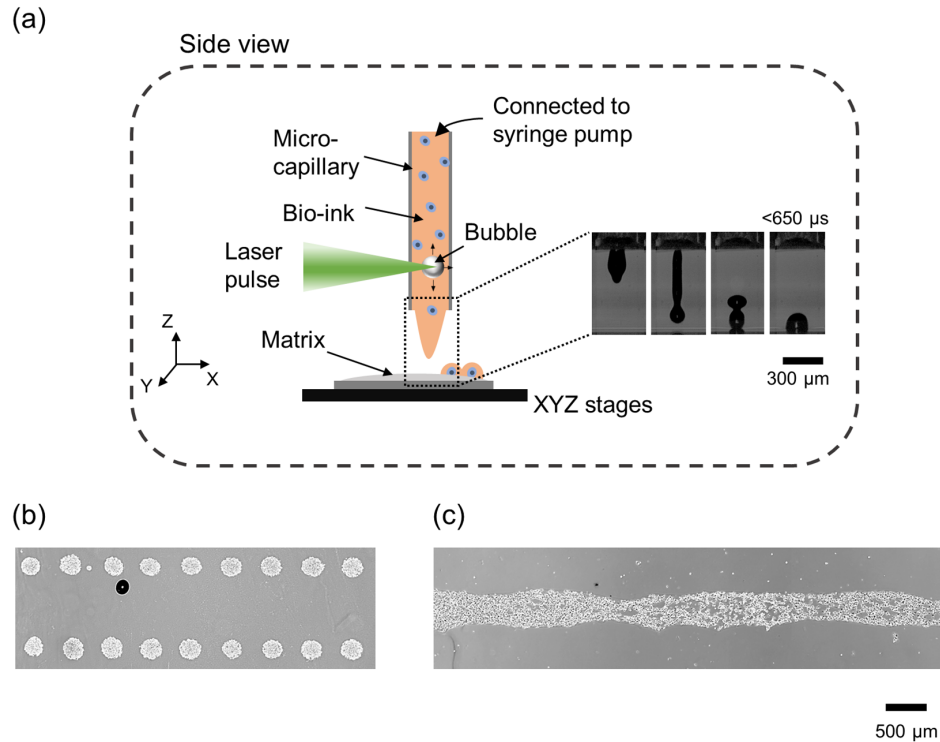


Figure 5.1: (a) Schematic showing the LIST bioprinting process and indicative high-speed imaging of droplet ejection. (b) an array of LIST-printed HUVECs-laden droplets (c) a LIST-printed line using 20 % overlap between adjacent droplets.

5.1b. A 200  $\mu\text{m}$  distance between adjacent droplets (20% overlap) was used to print continuous lines (Figure 5.1c).

### 5.3.2 The effect of the support matrix on HUVECs self-assembling and adhesion

After establishing a protocol for printing continuous lines, we sought to investigate the effect of the support matrix on HUVECs self-assembling. To do so, we printed HUVECs ( $18.75 \times 10^6$  HUVECs/mL in a bioink consisting of EBM-2 supplemented with fibrinogen, aprotinin and Allura red AC) lines on Fibrin-, Matrigel- and Matrigel/thrombin- coated substrates.

HUVECs proliferated on fibrin without preserving the initial footprint of the printed lines. 2-days after printing the cells invaded the available surface of the

matrix (Figure 5.2a). We observed similar behaviour in a control experiment, involving conventional seeding of HUVECs on fibrin (Figure D.2b). HUVECs printed on Matrigel showed cord-like self-assembling along the printed line (Figure 5.2b). We also observed HUVECs sprouting originating from the main cord-like formation. However, cord-like formations were unstable and started disintegrating 2-days post printing. A random and more stable HUVECs network was formed in a control experiment (Figure D.2c), involving conventional cell seeding on Matrigel. Poor cell adhesion in bioprinted lines might have occurred due to the smaller number of total cells compared to conventional cell seeding. Bioprinting on Matrigel/thrombin matrix resulted in the formation of well-resolved cord-like formations of HUVECs (Figure 5.2d). Since the bioink contained fibrinogen, a fibrin layer was formed along the printed lines. Although sprouting was observed, those cord-like formations maintained the initial printing geometry. Conversely, HUVECs showed random network formation in a control experiment of conventional cell seeding on Matrigel/thrombin substrate (Figure D.2c).

These results indicate that the matrix selection plays a predominant role in HUVECs self-assembling for otherwise identical printing conditions. The use of Matrigel/thrombin matrix provides a highly desirable combined effect: strong cell adhesion along the printed lines (fibrin) and poor cell migration towards the outer area (Matrigel/thrombin). Consequently, we selected the Matrigel/thrombin matrix as a platform to study the stability of bioprinted cord-like formations and to assess tubulogenesis.

### 5.3.3 LIST-printed HUVECs lines regress with time

To evaluate the evolution of the cord-like formations with time, we measured their thickness up to 5-days post printing. We found that the initial thickness of the structures was  $303 \pm 48 \mu\text{m}$  and that it progressively regressed to  $75 \pm 10 \mu\text{m}$  5-days post printing (Figure 5.3). Statistically significant regression takes place up to 2-days post printing (from  $303 \pm 48 \mu\text{m}$  to  $123 \pm 37 \mu\text{m}$ ), whereas the size of the structures remains stable past this time point. Given that we did not observe any contraction of the gel (i.e., the initial spacing of the lines was preserved with time), we attribute the thinning of the lines to dense self-assembling of the printed cells. We limited the analysis to 5-days post printing as cord-like formations start to disintegrate starting

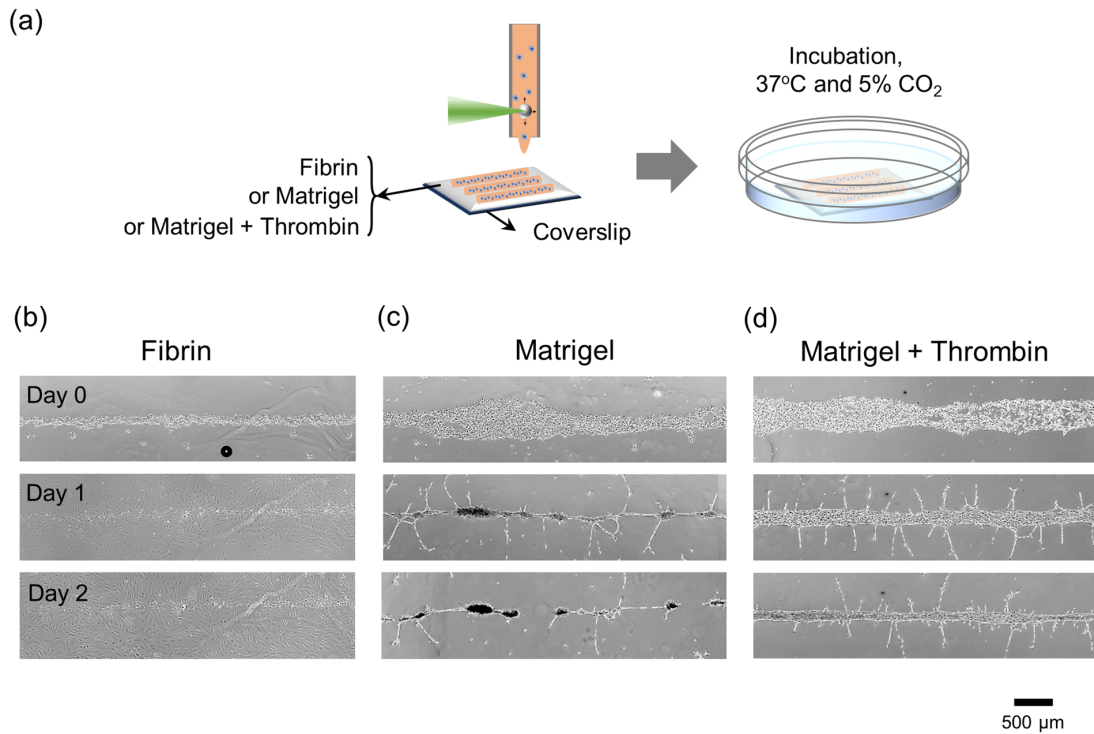


Figure 5.2: (a) Schematic of LIST-printing of HUVECs lines on different matrices; two days post-printing observation of LIST-printed HUVECs with optical microscopy shows (b) non-directional HUVECs proliferation on fibrin-coated substrate, (c) cord-like HUVECs self-assembling on Matrigel-coated substrate combined with poor adhesion and sprouting, and (d) cord-like HUVECs self-assembling on Matrigel/Thrombin-coated substrate combined with strong adhesion and sprouting.

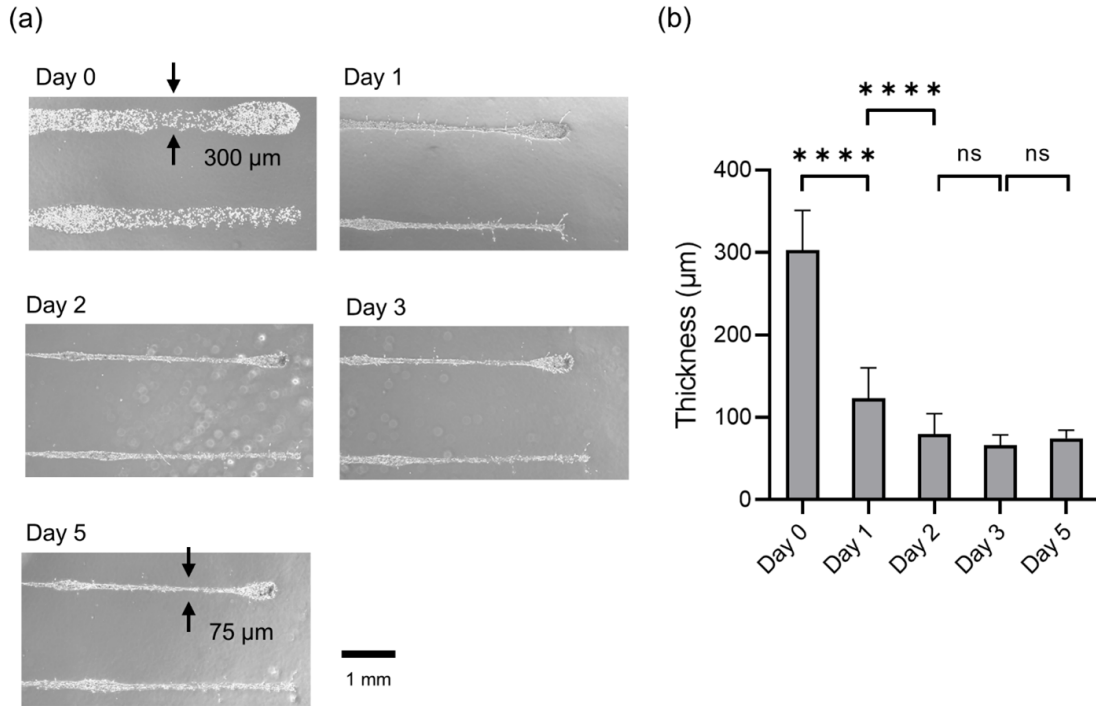


Figure 5.3: (a) Optical microscopy images of LIST-printed HUVECs. Drastic self-assembling occurs in day 1, (b) the evolution of LIST-printed lines thickness over time. Error bars represent standard deviation of 5 biological replicates. One-way ANOVA test was used for mean comparison. Significant differences are indicated by asterisks ( $P < 0.0001 = ****$ ).

from 6-days post printing. These results indicate that starting from 2-days post printing HUVECs have completed self-assembling.

### 5.3.4 Evaluating the affect of pro- and anti- angiogenic factors on sprouting from LIST-printed patterns

Next, we sought to investigate how anti- and pro- angiogenic factors affect sprouting angiogenesis from the printed lines. We selected two anti-angiogenic (BMP9 and FLT1-FC) and two pro-angiogenic (BMP6 and VEGF) compounds for this study. BMP9 and FLT1-FC were evaluated, as it was previously shown that they elicit potent anti-angiogenic effects in fibrin angiogenesis assays by modulating Alk1 and VEGF signaling, respectively [231, 232]. Conversely, the effects of VEGF and BMP6 were assessed, as they have been shown to reproducibly promote sprouting angiogenesis in

Matrigel and Fibrin HUVEC assays [233]. We first investigated the effect of those compounds using a conventional angiogenesis assay comprised of treating HUVECs seeded on fibrin. For VEGF treatment, we found more junctions and longer network length compared to control (Figures D.4 and D.3). BMP9 and FLT1-FC treatments resulted in a reversed effect (Figures D.4 and D.3). With BMP6 treatment being an exception (i.e., nonsignificant differences), these results confirm the anti- and pro-angiogenesis effect of the used compounds.

We applied similar stimulations to bio-printed lines by adding the various compounds in the culture media post printing. We then quantified the length and number of sprouts originating from the cord-like formations of HUVECs. We found a trend of more sprouts for VEGF treatments compared to control (2% FBS) (Figure 5.4a and b). We found a reversed trend for the average length of the sprouts for both BMP6 and VEGF treatments (Figure 5.4a and b). For 2-days post treatment with VEGF, the differences are statistically significant. For the evaluation of anti-angiogenic compounds (BMP9 and FLT1-FC), cultures were grown in complete ECGM2 medium, which include VEGF, FGF-2 and EGF as growth supplements. For 2- and 3-days post treatment, we found less sprouts for FLT-FC1 treatment (anti-angiogenic), whereas we found a similar trend for 1-day post treatment. (Figure 5.4c and d). We found less sprouts for BMP9 treatment compared to control for 3-days post treatment, whereas we found a similar trend for 1- and 2-days post treatment. (Figure 5.4c and d). FLT1-FC treatment resulted in longer sprouts 1-day post treatment, whereas a similar trend was observed for 2 and 3-days post treatment. Overall, these results are consistent with those obtained from the control assay (Figures D.3 and D.4). We applied all treatments in the next part of our study.

### **5.3.5 Evaluating the effects of pro- and anti- angiogenic factors on guided tubulogenesis**

Lumen formation must accompany the de novo growth of blood vessels during angiogenesis. Yet, in vitro assays do not always recapitulate this critical step of vascular development; HUVECs plated in conventional Matrigel assays do not make intercellular lumens, neither sprouting nor proliferation occur [234, 235]. As such, we sought to investigate whether a lumen was present in cord-like structures of printed HUVECs and whether pro- and anti- angiogenic factors could affect lumen formation.

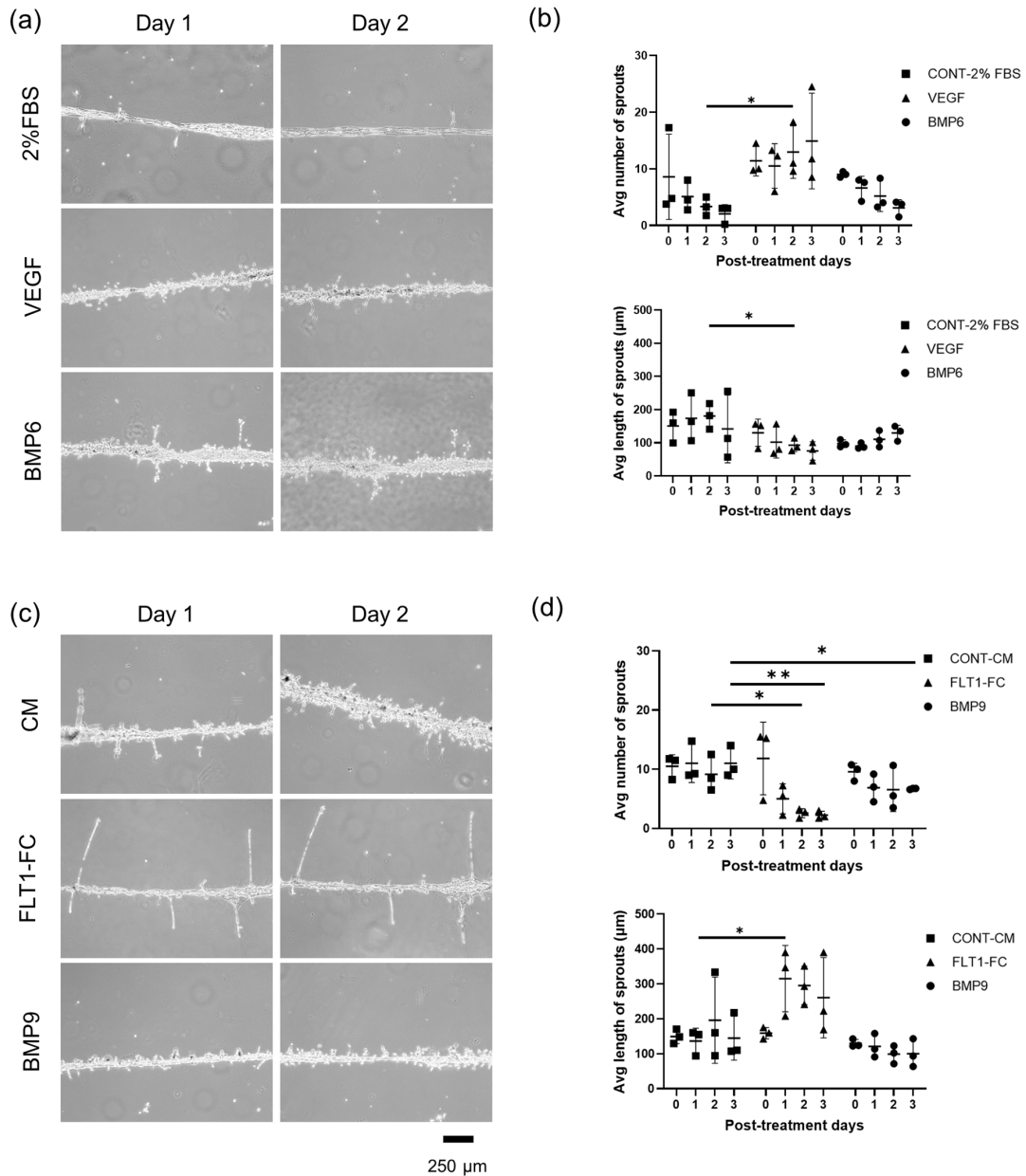


Figure 5.4: (a) Bright field microscopy images of HUVECs printed lines treated by pro-angiogenic factors (BMP6 and VEGF) and control media (2% FBS). (b) The average number of sprouts and the average length of sprouts for (BMP6 and VEGF) and control (Basal Media-2% FBS) treatments, (c) bright field microscopy images of HUVEC-printed lines treated by anti-angiogenic factors (BMP9 and FLT1-FC) and control (Complete Medium (CM)), (b) the average number of sprouts and the average length of sprouts for (BMP9 and FLT1-FC) and control (CM) treatments. Error bars represent standard deviation of 3 biological replicates. One-way ANOVA test was used for mean comparison. Significant differences are indicated by asterisks ( $P < 0.05 = *$  and  $P < 0.01 = **$ )

Pro-angiogenic (BMP6, VEGF) and anti-angiogenic (BMP9, FLT1-FC) factors were added to the medium 1-day post printing and the treatment was repeated every other day. Given that self-assembled formations remain stable up to 5-days post printing (Figure 5.3), we performed immunofluorescence (CD31 and DAPI) imaging at this time point. For all treatments, we found that HUVECs formed intercellular junctions (green staining) and self-assembled in 3D (Figure 5.5a to f). Further investigation of cross-sectional images revealed that a partial lumen was formed in the self-assembled patterns and that the different treatments clearly affected the characteristics of the lumen formation. A MATLAB algorithm was developed to quantify the extent of lumen formation. The algorithm quantifies the presence of contained (i.e., surrounded by cells) acellular volume within a printed pattern. We used the algorithm to calculate what fraction of a given line presents complete lumen formation (i.e., length of section(s) with lumen/total length).

We found that treatments with BMP9 significantly improved the tubulogenesis process compared to both FLT1-FC and control (Figure 5.5a to c, and g), consistent with a previous study showing that BMP9 participates in lumen formation and maintenance [236]. Printed lines treated with BMP9 presented complete lumen formation for 46.5% of their length, while lines exposed to complete medium for 18.2% of their length. We found no significant effects for pro-angiogenic treatments (BMP6 and VEGF). However, we did observe a trend of improved tubulogenesis for BMP6, compared to VEGF and control. Taken together these results indicate the LIST-printed HUVECs can self-assemble in 3D and that they can support tubulogenesis in a spatially guided manner. Yet, the lumen formation is partial along the printed structure, while anti-angiogenic treatment (BMP9) significantly improves tubulogenesis compared to complete medium.

## 5.4 Discussion

Bioprinting can spatially control tubulogenesis compared to conventional angiogenesis assays. Yet, HUVECs self-assembling and adherence to the matrix should be optimized in bioprinting. In agreement with the literature [234,237,238], our findings on conventional assays show that the HUVECs seeded on fibrin gel form randomly

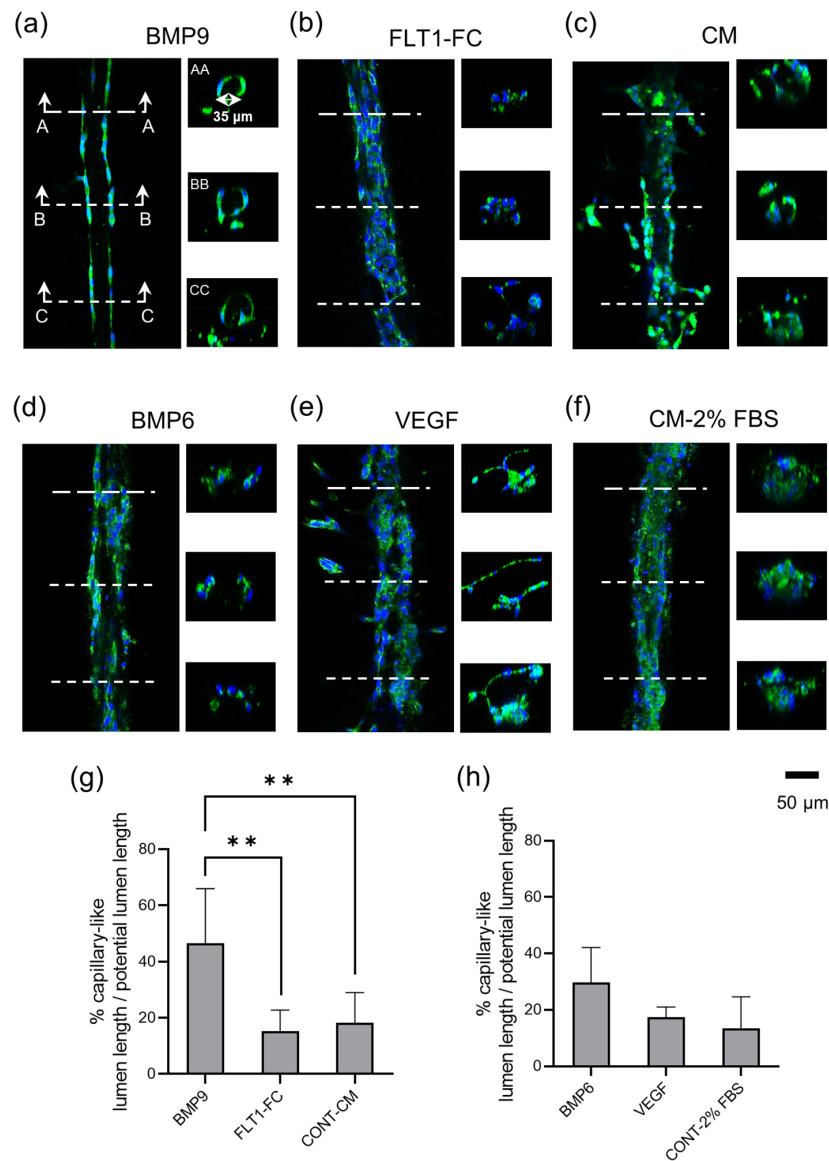


Figure 5.5: (a-c) Day 5 confocal microscopy of LIST-printed HUVECs lines including cross sectional views. The lines were treated by anti-angiogenic factors (BMP9 and FLT1-FC) or control (CM), (d-f) day 5 confocal microscopy of LIST-printed HUVECs lines including cross sectional views. The lines were treated by pro-angiogenic factors (BMP6 and VEGF) or control (Basal Media-2%FBS). Green indicates CD31 and blue indicates cell nuclei staining with DAPI, (g-h) capillary-like length over potential lumen length for anti-angiogenic factors (BMP9 and FLT1-FC) or CM, (g) for pro-angiogenic factors (BMP6 and VEGF) or control (Basal media-2%FBS). Error bars represent standard deviation of 3 biological replicates. One-way ANOVA test was used for mean comparison. Significant differences are indicated by asterisks ( $P < 0.01 = **$ ).

organized networks. Printed HUVECs lines on fibrin migrate and proliferate without preserving the initial pattern. The use of Matrigel as matrix confined HUVECs along the printed lines and promoted self-assembling in cord-like formations. For cells printed on Matrigel, we observed sporadic cell detachment starting from day-2 post printing. This can be attributed to poor cell-cell contacts [239] and/or to the reception of conflicting signaling from Matrigel and initiation of the apoptotic machinery [239]. LIFT bioprinted networks of HUVECs on Matrigel showed similar instability [78].

The relatively poor migration potential of HUVECs on Matrigel can be exploited to maintain the initial shape of the printed patterns. To prevent cell detachment, we added thrombin to Matrigel and fibrinogen in the bioink. This resulted in fibrin stripes with printed cells on Matrigel. Note that the addition of thrombin in Matrigel has been also shown to promote tubulogenesis both in-vitro and in-vivo [240]. HUVECs undergo rapid self-assembling on Matrigel/thrombin matrix. The lines take their final shape 2-days post printing; however, HUVECs printed lines are unstable and would likely require the supplementation of specific growth factors such as Angiopoietins [234] or TGFbeta [241] or the addition of support cells to maintain long-term stability. Indeed, it has been shown that HUVECs co-cultures containing support cells such as pericytes stabilize endothelial cell tube-like structures on Matrigel [241]. The addition of pericytes results in enhanced endothelial tube stability and limit the need for exogenous growth factors. In normal physiology, pericytes are essential for the maturation and stabilization of vasculature, and their dysfunction is associated in a variety of physiological disorders such as tumor angiogenesis [242]. In a variety in vitro co-culture, pericytes thus stabilize HUVEC tube networks via both direct cell-cell contacts and paracrine signaling pathways [243]. As such, the addition of support cells such as pericytes on HUVEC printed lines will likely improve the long-term stability of vascular structures and more closely mimic in vivo settings.

LIFT been previously used to pattern HUVECs on various matrices, including collagen [80], Collagen Type I and Matrigel impregnated biopapers [79], and Matrigel [78]. In those studies, cord-like structures were observed but lumen formation was not investigated [78–80]. Compared to LIFT, LIST bioprinting attains similar printing resolution and eliminates the donor preparation complexity.

Here, we found partial lumen formation for LIST printed HUVECs. Interestingly,

we found that the use of pro- and anti- angiogenic compounds has a profound effect on lumen formation. To the best of our knowledge, the effect of pro- and anti- angiogenic treatments on bioprinted HUVECs patterns has not been previously studied in bioprinted assays. For treatment with the anti-angiogenic factor of BMP9,  $46.5 \pm 19.4\%$  of the printed lines' length presented a complete lumen formation. Furthermore, BMP9 treated lines showed a uniform circular shape. While the mechanisms by which BMP9 promotes the formation of lumenized vascular structures are unclear, it has previously been reported that BMP9 can facilitate lumen formation in part by decreasing endothelial cell migration in blood vessels [236]. Thus, BMP9 signaling could trigger quiescence and changes in cytoskeletal organization in endothelial cells to enhance tube formation in printed HUVECs. Further improvement of the tubulogenesis can be attained by the printing of other cell types such as smooth muscle cells [78, 244], human mesenchymal stem cells (hMSCs) [245] and myoblasts [246] along with the printed HUVECs.

## 5.5 Conclusion

In conclusion, we showed spatially controlled endothelial tubulogenesis by LIST bioprinting a HUVECs – laden bioink containing fibrinogen. Central in achieving guided tubulogenesis is the selection of the matrix. We tested fibrin, Matrigel and Matrigel/thrombin matrices and found that HUVECs self-assembling is optimal in Matrigel/thrombin matrices due to the formation of fibrin stripes that enhance HUVECs confinement and self-assembling. Importantly, we found partial lumen formation for printed lines of HUVECs and showed that treatment with the anti-angiogenic factor BMP9 significantly improves the percentage of lumen coverage. By documenting treatment-dependent lumen formation and shape preservation in bioprinted patterns, our results showcase LIST as a powerful bioprinting technology to study tubulogenesis and screen compounds targeting microvasculature pathologies.

# Chapter 6

## Conclusions, limitations and future studies

### 6.1 Conclusions

The main goal of this thesis work is to design, develop and validate a novel laser-based drop-on-demand bioprinter to print viscous bioinks, maintaining the printed cell viability, and the cell functionality. The objectives were achieved by developing a bioprinter based on a novel laser-induced side transfer (LIST) technique. For validating the developed bioprinter, HUVECs were printed for tubulogenesis purposes. First, the dynamics of a laser-induced microbubble in the confining reservoir were experimentally investigated, since the bubble dynamics are different in the confining environment. Then, the hybrid analytical/numerical modelling of the laser-induced microjet generator was presented using MATLAB and COMSOL Multiphysics. Historically, laser-induced bubble dynamics studies used the RP, KM, and GA equations, However, these models do not account the pressure increase during the bubble expansion phase. In this thesis, an updated model considering the time-variant pressure changes and its effect on bubble dynamics was proposed. This contribution is particularly important for accurately simulating devices such as LIST and others that contain bubbles in a confining reservoir.

The geometry of the droplet generator was modified maintaining the working principle (presented in section 4).

After the development of the device, the effect of laser energy on the droplet's

dynamics was investigated. The viability and functionality of the LIST-printed cells were assessed. Results depict a negligible loss of viability even while applying the higher laser energy. Comparison of intercellular junction in the printed cells and the control indicated proper cell functionality after printing.

The ultimate goal of this thesis is to pattern human umbilical vein endothelial cells (HUVECs) and offer a suitable matrix for tubulogenesis purposes. The optimal combination of bioink and the matrix on which the cells are printed was selected by examining different natural hydrogel-based matrices. The LIST-printed patterns have been treated by pro- and anti-angiogenic factors to enhance the volume and length of the tube-like formation.

- In the literature review, overview of conventional bioprinting approaches, their benefits and their limitations were examined. Printing viscous bioink by inkjet and printing sizeable structures by LIFT is quite challenging. Printing viscous bioink and high-speed printing along with the ability to print sizeable structures are the features of extrusion-based bioprinters. However, this type of printing technique significantly affects the viability of the cells due to the mechanical stresses generated by the printing mechanism. Finally, it was concluded that a bioprinting approach that could print viscous bioink with negligible loss of cell viability and the ability to print a sizeable structure with the micrometric resolution is essential.
- In the introduction, the applications of bioprinters in recent years were discussed in detail. The current limitations to fabricating functional tissues and organs for transplantation were examined. One of the important uses of bioprinters is in the fabrication of human tissues to advance the preclinical research of drug discovery. The current challenges in the fabrication of efficient tissues or organs were presented. These include the capabilities of bioink multiplexing, geometric complexity and printing of vascular networks. The research done to construct blood vessels through bioprinters was reviewed in detail.
- Applications of microbubbles in medical science, such as lithotripsy, soft tissue scalpel, micropump, needle-free injection were thoroughly discussed. The analytical models which described the microbubble dynamics were presented in

detail. The most common of these models are Rayleigh-Plesset (RP), Keller-Miksis (KM) and Gilmore-Akulichev (GA) equations. In RP equation, the fluid is assumed to be incompressible. KM model considered the effect of fluid compressibility. Further, GA equation considered the effect of gas diffusion on the bubble dynamics. Subsequently, the simulations performed on the bubble dynamics and the droplet generating device have been fully investigated. Given these details, the absence of a numerical model for cavitation-induced microjet generated by liquid confining devices was noted.

- Microbubble dynamics are varied by liquid pressure, the initial pressure of the gas trapped in the bubble and fluid properties. An accurate understanding of the dynamics of these bubbles is essential. In the current biomedical applications, microbubbles are commonly created in confined geometry. The bubble expansion in the confined geometry increases the liquid pressure around the bubble and consequently prevents the bubble from free expansion (i.e. self-limiting effect). In this thesis, the effect of liquid pressure increase generated by bubble expansion on bubble dynamics was experimentally investigated. For this purpose, we created bubbles in the sealed reservoirs filled with water. Keeping the bubble energy constant, we recorded the bubble dynamics and the liquid pressure in the reservoirs simultaneously with a needle hydrophone. The results showed 0.5-fold decrease in the bubbles size and fourfold decrease in their lifetime compared to those generated in non-sealed containers. In addition, it was found that the liquid pressure depends on the volume of the reservoirs and the laser energy that was used to create the bubble. This pressure increases with decrease in the reservoir volume and/or with increase in the laser energy. For the examined settings, it was concluded that the maximum amplitude of the liquid pressure wave was 3.8 bar for the smallest reservoir (0.3 mL) with maximum laser energy ( $\sim 3.25$  mJ).
- In all analytical models presented to describe the bubble dynamics, the effect of liquid pressure in the reservoir has been considered as constant. However, the bubble expansion leads to the liquid pressure wave in the reservoir (time-dependent liquid pressure). In this thesis, an updated analytical model was proposed to implement the experimental liquid pressure profile in the equations to describe the self-limiting bubble dynamics. For this purpose, KM equation

was used to compute the bubble dynamics. The bubble dynamics extracted from KM equation were in good agreement with those measured experimentally.

- This thesis presented a generalized model of laser-induced droplet generators using COMSOL Multiphysics and MATLAB. In the first step, RP model was adapted for the laser-induced bubbles generated in the confining devices by coupling RP and Tait equations. Subsequently, the interaction between the bubble, the fluid and the membrane were simulated in the fluid-structure interaction (FSI) module to compute the membrane dynamics. The droplet dynamics were then examined in the two-phase flow (TPF) module knowing the membrane dynamics.
- The effect of laser energy and geometrical parameters were investigated to obtain efficient conditions for printing purposes. The results showed that, with 200  $\mu\text{m}$  thick membrane, droplets were deposited regardless of laser energies. However, low laser energies ( $< 70 \mu\text{J}$ ) did not provide sufficient pressure for droplet generation with the 400 and 600  $\mu\text{m}$ -thick membranes. Investigation on the droplet dynamics in 50, 75 and 150  $\mu\text{m}$  nozzle diameters presented that the droplets cannot detach from the 150  $\mu\text{m}$  nozzle tip at low laser energy. Therefore, the laser energy was scanned between 25 and 450  $\mu\text{J}$  for the 200  $\mu\text{m}$  thick membrane and 50 and 75  $\mu\text{m}$  nozzle to explore the droplet dynamics. For 50  $\mu\text{m}$ -nozzle, the velocity of microjet varied between 4.1 to 48.4 m/s and the volume of the resulting droplets was between 0.097 and 5.49 nL. Since the droplet detachment time was between 240 and 605  $\mu\text{s}$ , the droplet had a generation potential of between 1.65 and 4.05 kHz. For a 75  $\mu\text{m}$ -nozzle, the droplet velocity was between 0.94 and 19.91 m/s, which resulted in a droplet with a volume between 0.49 and 7.68 nL. Also, the droplet detachment time (210-837  $\mu\text{s}$ ) potentially indicated a generation frequency between 1.19 and 4.76 kHz. Although this research focused on printing applications, the modeling approach presented here can be widely adapted for designing and optimizing needle-free drug injectors and other similar microfluidic devices.
- The main goal of this thesis is to develop a bioprinting approach that can print viscous bioink, along with the high viability of the printed cells. Having micrometric resolution and high printing speed were the other features that

were addressed in this thesis. For development purposes, the elastic membrane was removed; and the laser light was focused directly on the bioink. These modifications facilitate the development and preparation steps of the device presented in the simulation. The bioink was locally ionized by focusing the laser beam in the middle of the capillary, consequently generating a bubble. The resulting bubble propelled the bioink towards the capillary opening and formed a droplet. In this study, the droplets dynamics were recorded using a high-speed camera for laser energies between 90 and 130  $\mu\text{J}$ . The results showed that the average droplet velocity varied between 3.2 and 11.60 m/s. Also, the change in the laser energy led to the change in the volume of the printed droplets between 1.675 and 6.1 nL (which corresponds to a diameter between 165 and 325  $\mu\text{m}$ ).

- Fluorescence microscopy images of the cells were recorded after staining with Hoechst 33342 and Calcein AM. A MATLAB algorithm was developed to detect living and dead cells using microscopic images. The results depict that the LIST-printed HUVECs have viability between 96.5% and 93.1% right after the printing. There is a marginal decrease in cell viability at higher energies. It can be explained by the thermomechanical impact on the cell at the higher laser energy. To evaluate the cell functionality after the printing, it was examined whether the printed cells were able to make intercellular junctions. The LIST-printed HUVECs and the control were stained on the third day of printing using DAPI, CD 31 and VE-Cadherin. The results showed the two groups form similar intercellular junctions. From the viability and functionality tests, it can be said that LIST has the ability to print primary cells (e.g. HUVECs) with high viability without losing the functionality.
- To evaluate high-speed printing potential of the developed device, printing was performed at 10, 20 and 30 Hz with a laser energy of 100  $\mu\text{J}$ . The viability of the cells was recorded after printing and the results showed the difference in the cell viability at different speeds to be within the experimental errors. The velocity of the droplets did not differ significantly from each other in these three speeds. Since at all speeds, the droplets detached from the capillary end within 400  $\mu\text{s}$ , the device has the stability needed to potentially print at speeds of up to 2500 droplets per second.

- Owing to the key demand in achieving printing vascular network for regenerating functional organs, in this research, the focus was on printing HUVECs for tubulogenesis application. The ideal matrix/bioink combination for tubulogenesis was found to be HUVECs and fibrinogen as bioink and Matrigel mixed with Thrombin as the matrix. The diffusion of Thrombin in Matrigel solidified fibrinogen droplets and ultimately helped in maintaining the printing pattern. The Matrigel matrix provided a suitable environment for the printed HUVECs to facilitate the angiogenesis/tubulogenesis processes. On the day after printing, the cells could form tube-like formations in 3D. To estimate the size of lumen generated by HUVECs, the confocal images were segmented with the MATLAB algorithm presented in this thesis. The estimation indicated that on an average,  $\sim 20\%$  of the printed lines were lumen.
- In order to increase the lumen length, the printed HUVEC lines were treated with pro- and anti-angiogenic factors. BMP9 as the only effective factor has been able to increase the lumen length up to 60%. The study showed that pro-angiogenic factors could significantly increase the number of sproutings compared to control. FLT1-FC significantly increased the length of the sprouting created around the printed lines. Given the fact that the pro- and anti-angiogenic factors affect the number of sprouts and their length in LIST-printed lines, these could be a promising alternative for conventional angiogenesis assay.

## 6.2 Limitations

- Creating bubbles in the capillary requires sufficient absorption of laser energy by bioink. For this purpose, the food dye (Allura Red AC) was added to the bioink before printing. The dye absorbed the laser energy resulting in cavitation. After the droplets were printed on the matrix, the food dye in the droplets was rinsed by adding the cell medium. The cells were exposed to the dye only for a short duration. The presence of red dye in bioink is one of the limitations of the LIST printing approach. It should be verified if the dye is washable after the printing and if the dye causes damage to the printed biomaterials. While this was verified for the HUVECs in this work, the effect is unknown for other cell types. Given the fact that LIST printing requires washing protocol, direct

printing into the living tissue/organ with this technique is quite challenging.

- The cells in the bioink move towards the capillary outlet and accumulate at the capillary outlet after an hour due to the gravity and vertical orientation of the capillary. It leads to blockage and reduces printability.
- LIST can potentially generate 2500 droplets per second. Given the fact that printing the droplets (diameter  $\sim 250 \mu\text{m}$ ) with zero overlap needs a stage with an average velocity of 625 mm/s. However, in this work the mechanical stage had a maximum speed of 10 mm/s and the maximum frequency of the laser was 30 Hz.
- In cases that viscous bioink is used for printing, it is necessary to create large bubbles to propel the bio-ink for droplet generation purposes. To increase the size of the bubble, the laser energy must be increased. Since part of the laser light is absorbed by the wall of the glass capillary, the increase in the laser energy can lead to breakage of the capillary.

### 6.3 Future studies

In this thesis, bubble dynamics in confining reservoirs were comprehensively investigated. Fluid dynamics models for laser-induced droplet generating devices were also presented for simulation. Then, with the development of LIST, the efficiency of the printed HUVECs was analyzed and finally, by LIST-printing of HUVECs on Matrigel, tube-like formations were created. Given the achievements presented, engineering and biology aspects of the project can obtain further development as discussed henceforth:

Modeling:

- Working on a hybrid numerical/analytical model that simulates the dynamics of bubbles and droplets in the capillary tubes
  - Conducting the parametric studies on the geometry, properties of the fluid such as viscosity and the effect of the Newtonian and non-Newtonian nature of the simulated fluid (effect on printing capacity)

- The presence of a static mixer to mix the bioinks can affect the dynamics of the droplets during the printing. Therefore, simulation of the bioprinter head with a static mixer will be beneficial.

Device development:

- In some applications, two or more cell types or biomaterials need to be printed in order. With the proposed approach, the addition of capillaries parallel to the initial capillary and with modification in the bioprinter control algorithm, multiplexing can be attained in the future.
- In this thesis, the cells were printed on the matrices in 2D and created a tube-like formation. Due to the potential of the bioprinter to move the matrices in the z-direction and with the addition of other capillaries, 3D structures can be printed in layers.

It is important to note that due to the long printing time (especially while printing in 3D), the need for temperature, humidity and CO<sub>2</sub> control enclosure is required. Therefore, the design and fabrication of an incubator are required.

- For specific purposes, mixing bioinks just before printing is required. Installation of a static mixer in the bioprinter head makes this method print a broader range of biomaterials.

Biology:

- In this study, only HUVECs were printed to form a tube-like formation. The structures of the vessel include different layers such as smooth muscle layers. To bring the printed structure closer to the real vessels, it is suggested that smooth muscle cells are printed in the desired pattern along with HUVECs.
- Alternatively, the transplantation of the tube-shaped construct of LIST-printed HUVECs in mice causes this structure to be surrounded by the muscle cells of the host body and finally to connect to their blood supply network.
- It is suggested that after equipping the device with 3D printing capability, smooth muscle and endothelial cells be intertwined and printed in 3D with the desired gels. It results in the fabrication of a tube structure of various sizes with this approach.

# Bibliography

- [1] C. Mandrycky, Z. Wang, K. Kim, and D.-H. Kim, “3D bioprinting for engineering complex tissues,” *Biotechnol. Adv.*, vol. 34, pp. 422–434, jul 2016.
- [2] C. C. Chang, E. D. Boland, S. K. Williams, and J. B. Hoying, “Direct-write bioprinting three-dimensional biohybrid systems for future regenerative therapies,” *J. Biomed. Mater. Res. Part B Appl. Biomater.*, vol. 98B, pp. 160–170, jul 2011.
- [3] D. A. Foyt, M. D. A. Norman, T. T. L. Yu, and E. Gentleman, “Exploiting Advanced Hydrogel Technologies to Address Key Challenges in Regenerative Medicine,” *Adv. Healthc. Mater.*, vol. 7, p. 1700939, apr 2018.
- [4] I. T. Ozbolat and M. Hospodiuk, “Current advances and future perspectives in extrusion-based bioprinting,” *Biomaterials*, vol. 76, pp. 321–343, jan 2016.
- [5] T. Billiet, E. Gevaert, T. De Schryver, M. Cornelissen, and P. Dubruel, “The 3D printing of gelatin methacrylamide cell-laden tissue-engineered constructs with high cell viability,” *Biomaterials*, vol. 35, no. 1, pp. 49–62, 2014.
- [6] D. Kang, G. Ahn, D. Kim, H. W. Kang, S. Yun, W. S. Yun, J. H. Shim, and S. Jin, “Pre-set extrusion bioprinting for multiscale heterogeneous tissue structure fabrication,” *Biofabrication*, vol. 10, no. 3, 2018.
- [7] A. Bhattacharyya, G. Janarthanan, H. N. Tran, H. J. Ham, J. H. Yoon, and I. Noh, “Bioink homogeneity control during 3D bioprinting of multicomponent micro/nanocomposite hydrogel for even tissue regeneration using novel twin screw extrusion system,” *Chem. Eng. J.*, vol. 415, no. December 2020, p. 128971, 2021.

- [8] J. Visser, B. Peters, T. J. Burger, J. Boomstra, W. J. Dhert, F. P. Melchels, and J. Malda, “Biofabrication of multi-material anatomically shaped tissue constructs,” *Biofabrication*, vol. 5, no. 3, 2013.
- [9] S. Khalil, J. Nam, and W. Sun, “Multi-nozzle deposition for construction of 3D biopolymer tissue scaffolds,” *Rapid Prototyp. J.*, vol. 11, no. 1, pp. 9–17, 2005.
- [10] R. Chang, J. Nam, and W. Sun, “Effects of dispensing pressure and nozzle diameter on cell survival from solid freeform fabrication-based direct cell writing,” *Tissue Eng. - Part A.*, vol. 14, no. 1, pp. 41–48, 2008.
- [11] H. Gudapati, M. Dey, and I. Ozbolat, “A comprehensive review on droplet-based bioprinting: Past, present and future,” *Biomaterials*, vol. 102, pp. 20–42, 2016.
- [12] C. Xu, W. Chai, Y. Huang, and R. R. Markwald, “Scaffold-free inkjet printing of three-dimensional zigzag cellular tubes,” *Biotechnol. Bioeng.*, vol. 109, no. 12, pp. 3152–3160, 2012.
- [13] T. Xu, J. Jin, C. Gregory, J. J. Hickman, and T. Boland, “Inkjet printing of viable mammalian cells,” *Biomaterials*, vol. 26, no. 1, pp. 93–99, 2005.
- [14] S. Tasoglu and U. Demirci, “Bioprinting for stem cell research,” *Trends Biotechnol.*, vol. 31, pp. 10–19, jan 2013.
- [15] W. Lee, J. C. Debasitis, V. K. Lee, J.-H. Lee, K. Fischer, K. Edminster, J.-K. Park, and S.-S. Yoo, “Multi-layered culture of human skin fibroblasts and keratinocytes through three-dimensional freeform fabrication,” *Biomaterials*, vol. 30, pp. 1587–1595, mar 2009.
- [16] A. Faulkner-Jones, S. Greenhough, J. A King, J. Gardner, A. Courtney, and W. Shu, “Development of a valve-based cell printer for the formation of human embryonic stem cell spheroid aggregates,” *Biofabrication*, vol. 5, p. 015013, feb 2013.
- [17] U. A. Gurkan, R. El Assal, S. E. Yildiz, Y. Sung, A. J. Trachtenberg, W. P. Kuo, and U. Demirci, “Engineering Anisotropic Biomimetic Fibrocartilage Microenvironment by Bioprinting Mesenchymal Stem Cells in Nanoliter Gel Droplets,” *Mol. Pharm.*, vol. 11, pp. 2151–2159, jul 2014.

- [18] A. Faulkner-Jones, C. Fyfe, D. J. Cornelissen, J. Gardner, J. King, A. Courtney, and W. Shu, “Bioprinting of human pluripotent stem cells and their directed differentiation into hepatocyte-like cells for the generation of mini-livers in 3D,” *Biofabrication*, vol. 7, no. 4, 2015.
- [19] B. Derby, “Bioprinting: inkjet printing proteins and hybrid cell-containing materials and structures,” *J. Mater. Chem.*, vol. 18, no. 47, p. 5717, 2008.
- [20] H. Wijshoff, “The dynamics of the piezo inkjet printhead operation,” *Phys. Rep.*, vol. 491, pp. 77–177, jun 2010.
- [21] Y. Nishiyama, M. Nakamura, C. Henmi, K. Yamaguchi, S. Mochizuki, H. Nakagawa, and K. Takiura, “Development of a Three-Dimensional Bioprinter: Construction of Cell Supporting Structures Using Hydrogel and State-Of-The-Art Inkjet Technology,” *J. Biomech. Eng.*, vol. 131, pp. 1–6, mar 2009.
- [22] X. Cui and T. Boland, “Human microvasculature fabrication using thermal inkjet printing technology,” *Biomaterials*, vol. 30, no. 31, pp. 6221–6227, 2009.
- [23] T. Xu, H. Kincaid, A. Atala, and J. J. Yoo, “High-Throughput Production of Single-Cell Microparticles Using an Inkjet Printing Technology,” *J. Manuf. Sci. Eng.*, vol. 130, pp. 0210171–0210175, apr 2008.
- [24] K. Christensen, C. Xu, W. Chai, Z. Zhang, J. Fu, and Y. Huang, “Freeform inkjet printing of cellular structures with bifurcations,” *Biotechnol. Bioeng.*, vol. 112, pp. 1047–1055, may 2015.
- [25] K. Pataky, T. Braschler, A. Negro, P. Renaud, M. P. Lutolf, and J. Brugger, “Microdrop printing of hydrogel bioinks into 3d tissue-like geometries,” *Advanced Materials*, vol. 24, no. 3, pp. 391–396, 2012.
- [26] S. Yamaguchi, A. Ueno, Y. Akiyama, and K. Morishima, “Cell patterning through inkjet printing of one cell per droplet,” *Biofabrication*, vol. 4, p. 045005, dec 2012.
- [27] A. Yusof, H. Keegan, C. D. Spillane, O. M. Sheils, C. M. Martin, J. J. O’Leary, R. Zengerle, and P. Koltay, “Inkjet-like printing of single-cells,” *Lab Chip*, vol. 11, no. 14, p. 2447, 2011.

- [28] M. S. Onses, E. Sutanto, P. M. Ferreira, and A. G. Alleyne, “Mechanisms , Capabilities , and Applications of,” *Small*, vol. 11, no. 34, pp. 4237–4266, 2015.
- [29] J.-U. Park, M. Hardy, S. J. Kang, K. Barton, K. Adair, D. K. Mukhopadhyay, C. Y. Lee, M. S. Strano, A. G. Alleyne, J. G. Georgiadis, P. M. Ferreira, and J. A. Rogers, “High-resolution electrohydrodynamic jet printing,” *Nat. Mater.*, vol. 6, pp. 782–789, oct 2007.
- [30] E. Sutanto, K. Shigeta, Y. K. Kim, P. G. Graf, D. J. Hoelzle, K. L. Barton, A. G. Alleyne, P. M. Ferreira, and J. A. Rogers, “A multimaterial electrohydrodynamic jet (E-jet) printing system,” *J. Micromechanics Microengineering*, vol. 22, no. 4, 2012.
- [31] R. Gauvin, Y.-C. Chen, J. W. Lee, P. Soman, P. Zorlutuna, J. W. Nichol, H. Bae, S. Chen, and A. Khademhosseini, “Microfabrication of complex porous tissue engineering scaffolds using 3D projection stereolithography,” *Biomaterials*, vol. 33, pp. 3824–3834, may 2012.
- [32] Z. Wang, R. Abdulla, B. Parker, R. Samanipour, S. Ghosh, and K. Kim, “A simple and high-resolution stereolithography-based 3D bioprinting system using visible light crosslinkable bioinks,” *Biofabrication*, vol. 7, p. 045009, dec 2015.
- [33] F. Guillemot, A. Souquet, S. Catros, and B. Guillotin, “Laser-assisted cell printing: principle, physical parameters versus cell fate and perspectives in tissue engineering,” *Nanomedicine*, vol. 5, no. 3, pp. 507–515, 2010.
- [34] C. Boutopoulos, I. Kalpyris, E. Serpetzoglou, and I. Zergioti, “Laser-induced forward transfer of silver nanoparticle ink: time-resolved imaging of the jetting dynamics and correlation with the printing quality,” *Microfluidics and nanofluidics*, vol. 16, no. 3, pp. 493–500, 2014.
- [35] M. Makrygianni, I. Kalpyris, C. Boutopoulos, and I. Zergioti, “Laser induced forward transfer of Ag nanoparticles ink deposition and characterization,” *Appl. Surf. Sci.*, vol. 297, pp. 40–44, apr 2014.
- [36] C. Boutopoulos, C. Pandis, K. Giannakopoulos, P. Pissis, and I. Zergioti, “Polymer/carbon nanotube composite patterns via laser induced forward transfer,” *Appl. Phys. Lett.*, vol. 96, p. 041104, jan 2010.

- [37] S. V. Murphy and A. Atala, “3d bioprinting of tissues and organs,” *Nature biotechnology*, vol. 32, no. 8, pp. 773–785, 2014.
- [38] H.-R. Lee, S. M. Jung, S. Yoon, W. H. Yoon, T. H. Park, S. Kim, H. W. Shin, D. S. Hwang, and S. Jung, “Immobilization of planktonic algal spores by inkjet printing,” *Sci. Rep.*, vol. 9, p. 12357, dec 2019.
- [39] J. Nie, Q. Gao, J. Fu, and Y. He, “Grafting of 3D Bioprinting to In Vitro Drug Screening: A Review,” *Adv. Healthc. Mater.*, vol. 9, p. 1901773, apr 2020.
- [40] J. E. Snyder, Q. Hamid, C. Wang, R. Chang, K. Emami, H. Wu, and W. Sun, “Bioprinting cell-laden matrigel for radioprotection study of liver by pro-drug conversion in a dual-tissue microfluidic chip,” *Biofabrication*, vol. 3, p. 034112, sep 2011.
- [41] J. U. Lind, T. A. Busbee, A. D. Valentine, F. S. Pasqualini, H. Yuan, M. Yadid, S.-J. Park, A. Kotikian, A. P. Nesmith, P. H. Campbell, J. J. Vlassak, J. A. Lewis, and K. K. Parker, “Instrumented cardiac microphysiological devices via multimaterial three-dimensional printing,” *Nat. Mater.*, vol. 16, pp. 303–308, mar 2017.
- [42] Y. S. Zhang, A. Arneri, S. Bersini, S.-R. Shin, K. Zhu, Z. Goli-Malekabadi, J. Aleman, C. Colosi, F. Busignani, V. Dell’Erba, C. Bishop, T. Shupe, D. Demarchi, M. Moretti, M. Rasponi, M. R. Dokmeci, A. Atala, and A. Khademhosseini, “Bioprinting 3D microfibrinous scaffolds for engineering endothelialized myocardium and heart-on-a-chip,” *Biomaterials*, vol. 110, pp. 45–59, dec 2016.
- [43] Z. Ma, S. Koo, M. A. Finnegan, P. Loskill, N. Huebsch, N. C. Marks, B. R. Conklin, C. P. Grigoropoulos, and K. E. Healy, “Three-dimensional filamentous human diseased cardiac tissue model,” *Biomaterials*, vol. 35, pp. 1367–1377, feb 2014.
- [44] J. S. Miller, K. R. Stevens, M. T. Yang, B. M. Baker, D.-H. T. Nguyen, D. M. Cohen, E. Toro, A. A. Chen, P. A. Galie, X. Yu, R. Chaturvedi, S. N. Bhatia, and C. S. Chen, “Rapid casting of patterned vascular networks for perfusable engineered three-dimensional tissues,” *Nat. Mater.*, vol. 11, pp. 768–774, sep 2012.

- [45] L. E. Bertassoni, J. C. Cardoso, V. Manoharan, A. L. Cristino, N. S. Bhise, W. A. Araujo, P. Zorlutuna, N. E. Vrana, A. M. Ghaemmaghami, M. R. Dokmeci, and A. Khademhosseini, “Direct-write bioprinting of cell-laden methacrylated gelatin hydrogels,” *Biofabrication*, vol. 6, p. 024105, apr 2014.
- [46] T. Q. Huang, X. Qu, J. Liu, and S. Chen, “3D printing of biomimetic microstructures for cancer cell migration,” *Biomed. Microdevices*, vol. 16, pp. 127–132, feb 2014.
- [47] Y. Zhao, R. Yao, L. Ouyang, H. Ding, T. Zhang, K. Zhang, S. Cheng, and W. Sun, “Three-dimensional printing of Hela cells for cervical tumor model in vitro,” *Biofabrication*, vol. 6, p. 035001, apr 2014.
- [48] C. H. Choi, J. H. Jung, Y. W. Rhee, D. P. Kim, S. E. Shim, and C. S. Lee, “Generation of monodisperse alginate microbeads and in situ encapsulation of cell in microfluidic device,” *Biomed. Microdevices*, vol. 9, no. 6, pp. 855–862, 2007.
- [49] M. Xie, Q. Gao, H. Zhao, J. Nie, Z. Fu, H. Wang, L. Chen, L. Shao, J. Fu, Z. Chen, and Y. He, “Electro-Assisted Bioprinting of Low-Concentration GelMA Microdroplets,” *Small*, vol. 15, no. 4, pp. 1–10, 2019.
- [50] H. Zhao, Y. Chen, L. Shao, M. Xie, J. Nie, J. Qiu, P. Zhao, H. Ramezani, J. Fu, H. Ouyang, and Y. He, “Airflow-Assisted 3D Bioprinting of Human Heterogeneous Microspheroidal Organoids with Microfluidic Nozzle,” *Small*, vol. 14, no. 39, pp. 1–7, 2018.
- [51] L. Shao, Q. Gao, H. Zhao, C. Xie, J. Fu, Z. Liu, M. Xiang, and Y. He, “Fiber-Based Mini Tissue with Morphology-Controllable GelMA Microfibers,” *Small*, vol. 14, no. 44, pp. 1–8, 2018.
- [52] Y. Zuo, X. He, Y. Yang, D. Wei, J. Sun, M. Zhong, R. Xie, H. Fan, and X. Zhang, “Microfluidic-based generation of functional microfibers for biomimetic complex tissue construction,” *Acta Biomater.*, vol. 38, pp. 153–162, 2016.

- [53] Y. Cheng, F. Zheng, J. Lu, L. Shang, Z. Xie, Y. Zhao, Y. Chen, and Z. Gu, “Bioinspired multicompartamental microfibers from microfluidics,” *Adv. Mater.*, vol. 26, no. 30, pp. 5184–5190, 2014.
- [54] K. C. Hribar, K. Meggs, J. Liu, W. Zhu, X. Qu, and S. Chen, “Three-dimensional direct cell patterning in collagen hydrogels with near-infrared femtosecond laser,” *Scientific reports*, vol. 5, no. 1, pp. 1–7, 2015.
- [55] A. Shpichka, P. Bikmulina, M. Peshkova, N. Kosheleva, I. Zurina, E. Zahmatkesh, N. Khoshdel-Rad, M. Lipina, E. Golubeva, M. Vosough, and P. Timashev, “Engineering a Model to Study Viral Infections: Bioprinting, Microfluidics, and Organoids to Defeat Coronavirus Disease 2019 (COVID-19),” *Int. J. Bioprinting*, vol. 6, pp. 1–20, aug 2020.
- [56] A. Seyfoori, M. Amereh, S. M. H. Dabiri, E. Askari, T. Walsh, and M. Akbari, “The role of biomaterials and three dimensional (3D) in vitro tissue models in fighting against COVID-19,” *Biomater. Sci.*, vol. 9, no. 4, pp. 1217–1226, 2021.
- [57] J. Chakraborty, I. Banerjee, R. Vaishya, and S. Ghosh, “Bioengineered in Vitro Tissue Models to Study SARS-CoV-2 Pathogenesis and Therapeutic Validation,” *ACS Biomater. Sci. Eng.*, vol. 6, pp. 6540–6555, dec 2020.
- [58] C. Kryou, V. Leva, M. Chatzipetrou, and I. Zergioti, “Bioprinting for Liver Transplantation,” *Bioengineering*, vol. 6, p. 95, oct 2019.
- [59] T. Grix, A. Ruppelt, A. Thomas, A.-K. Amler, B. Noichl, R. Lauster, and L. Kloke, “Bioprinting Perfusion-Enabled Liver Equivalents for Advanced Organ-on-a-Chip Applications,” *Genes (Basel)*, vol. 9, p. 176, mar 2018.
- [60] N. S. Bhise, V. Manoharan, S. Massa, A. Tamayol, M. Ghaderi, M. Miscuglio, Q. Lang, Y. Shrike Zhang, S. R. Shin, G. Calzone, N. Annabi, T. D. Shupe, C. E. Bishop, A. Atala, M. R. Dokmeci, and A. Khademhosseini, “A liver-on-a-chip platform with bioprinted hepatic spheroids,” *Biofabrication*, vol. 8, p. 014101, jan 2016.
- [61] N. Vermeulen, G. Haddow, T. Seymour, A. Faulkner-Jones, and W. Shu, “3D bioprint me: a socioethical view of bioprinting human organs and tissues,” *J. Med. Ethics*, vol. 43, pp. 618–624, sep 2017.

- [62] I. T. Ozbolat and Y. Yu, “Bioprinting toward organ fabrication: Challenges and future trends,” *IEEE Trans. Biomed. Eng.*, vol. 60, no. 3, pp. 691–699, 2013.
- [63] I. T. Ozbolat, W. Peng, and V. Ozbolat, “Application areas of 3D bioprinting,” *Drug Discov. Today*, vol. 21, no. 8, pp. 1257–1271, 2016.
- [64] V. Lee, G. Singh, J. P. Trasatti, C. Bjornsson, X. Xu, T. N. Tran, S. S. Yoo, G. Dai, and P. Karande, “Design and fabrication of human skin by three-dimensional bioprinting,” *Tissue Eng. - Part C Methods*, vol. 20, no. 6, pp. 473–484, 2014.
- [65] N. Cubo, M. Garcia, J. F. Del Cañizo, D. Velasco, and J. L. Jorcano, “3D bioprinting of functional human skin: Production and in vivo analysis,” *Biofabrication*, vol. 9, no. 1, 2017.
- [66] P. He, J. Zhao, J. Zhang, B. Li, Z. Gou, M. Gou, and X. Li, “Bioprinting of skin constructs for wound healing,” *Burn. Trauma*, vol. 6, pp. 1–10, 2018.
- [67] X. Cui, K. Breitenkamp, M. G. Finn, M. Lotz, and D. D. D’Lima, “Direct human cartilage repair using three-dimensional bioprinting technology,” *Tissue Eng. - Part A*, vol. 18, no. 11-12, pp. 1304–1312, 2012.
- [68] D. Nguyen, D. A. Hgg, A. Forsman, J. Ekholm, P. Nimkingratana, C. Brantsing, T. Kalogeropoulos, S. Zaunz, S. Concaro, M. Brittberg, A. Lindahl, P. Gatenholm, A. Enejder, and S. Simonsson, “Cartilage Tissue Engineering by the 3D Bioprinting of iPS Cells in a Nanocellulose/Alginate Bioink,” *Sci. Rep.*, vol. 7, no. 1, pp. 1–10, 2017.
- [69] A. Sorkio, L. Koch, L. Koivusalo, A. Deiwick, S. Miettinen, B. Chichkov, and H. Skottman, “Human stem cell based corneal tissue mimicking structures using laser-assisted 3D bioprinting and functional bioinks,” *Biomaterials*, vol. 171, pp. 57–71, 2018.
- [70] D. F. Duarte Campos, M. Rohde, M. Ross, P. Anvari, A. Blaeser, M. Vogt, C. Panfil, G. H. F. Yam, J. S. Mehta, H. Fischer, P. Walter, and M. Fuest,

- “Corneal bioprinting utilizing collagen-based bioinks and primary human keratocytes,” *J. Biomed. Mater. Res. - Part A*, vol. 107, no. 9, pp. 1945–1953, 2019.
- [71] S. S. Mahdavi, M. J. Abdekhodaie, H. Kumar, S. Mashayekhan, A. Baradaran-Rafii, and K. Kim, “Stereolithography 3D Bioprinting Method for Fabrication of Human Corneal Stroma Equivalent,” *Ann. Biomed. Eng.*, vol. 48, no. 7, pp. 1955–1970, 2020.
- [72] A. K. Miri, A. Khalilpour, B. Cecen, S. Maharjan, S. R. Shin, and A. Khademhosseini, “Multiscale bioprinting of vascularized models,” *Biomaterials*, vol. 198, pp. 204–216, apr 2019.
- [73] P. Datta, B. Ayan, and I. T. Ozbolat, “Bioprinting for vascular and vascularized tissue biofabrication,” *Acta Biomater.*, vol. 51, pp. 1–20, 2017.
- [74] V. K. Lee, A. M. Lanzi, H. Ngo, S. S. Yoo, P. A. Vincent, and G. Dai, “Generation of multi-scale vascular network system within 3D hydrogel using 3D bio-printing technology,” *Cell. Mol. Bioeng.*, vol. 7, no. 3, pp. 460–472, 2014.
- [75] W. Wu, A. Deconinck, and J. A. Lewis, “Omnidirectional printing of 3D microvascular networks,” *Adv. Mater.*, vol. 23, no. 24, pp. 178–183, 2011.
- [76] D. B. Kolesky, R. L. Truby, A. S. Gladman, T. A. Busbee, K. A. Homan, and J. A. Lewis, “3D Bioprinting of Vascularized, Heterogeneous Cell-Laden Tissue Constructs,” *Adv. Mater.*, vol. 26, pp. 3124–3130, may 2014.
- [77] M. Nakamura, Y. Nishiyama, C. Henmi, S. Iwanaga, H. Nakagawa, K. Yamaguchi, K. Akita, S. Mochizuki, and K. Takiura, “Ink jet three-dimensional digital fabrication for biological tissue manufacturing: Analysis of alginate microgel beads produced by ink jet droplets for three dimensional tissue fabrication,” *J. Imaging Sci. Technol.*, vol. 52, no. 6, pp. 0602011–0602016, 2008.
- [78] P. Wu and B. Ringeisen, “Development of human umbilical vein endothelial cell (huvec) and human umbilical vein smooth muscle cell (huvsmc) branch/stem structures on hydrogel layers via biological laser printing (biolp),” *Biofabrication*, vol. 2, no. 1, p. 014111, 2010.

- [79] R. K. Pirlo, P. Wu, J. Liu, and B. Ringeisen, "Plga/hydrogel biopapers as a stackable substrate for printing huvec networks via biolp™," *Biotechnology and bioengineering*, vol. 109, no. 1, pp. 262–273, 2012.
- [80] O. K  rour  dan, J.-M. Bourget, M. R  my, S. Crauste-Manciet, J. Kalisky, S. Catros, N. B. Th  baud, and R. Devillard, "Micropatterning of endothelial cells to create a capillary-like network with defined architecture by laser-assisted bioprinting," *Journal of Materials Science: Materials in Medicine*, vol. 30, no. 2, p. 28, 2019.
- [81] R. Gaebel, N. Ma, J. Liu, J. Guan, L. Koch, C. Klopsch, M. Gruene, A. Toelk, W. Wang, P. Mark, *et al.*, "Patterning human stem cells and endothelial cells with laser printing for cardiac regeneration," *Biomaterials*, vol. 32, no. 35, pp. 9218–9230, 2011.
- [82] R. Xiong, Z. Zhang, W. Chai, Y. Huang, and D. B. Chrisey, "Freeform drop-on-demand laser printing of 3d alginate and cellular constructs," *Biofabrication*, vol. 7, no. 4, p. 045011, 2015.
- [83] K. C. Hribar, P. Soman, J. Warner, P. Chung, and S. Chen, "Light-assisted direct-write of 3d functional biomaterials," *Lab on a chip*, vol. 14, no. 2, pp. 268–275, 2014.
- [84] W. Zhu, X. Qu, J. Zhu, X. Ma, S. Patel, J. Liu, P. Wang, C. S. E. Lai, M. Gou, Y. Xu, K. Zhang, and S. Chen, "Direct 3D bioprinting of prevascularized tissue constructs with complex microarchitecture," *Biomaterials*, vol. 124, pp. 106–115, apr 2017.
- [85] A. P. Zhang, X. Qu, P. Soman, K. C. Hribar, J. W. Lee, S. Chen, and S. He, "Rapid Fabrication of Complex 3D Extracellular Microenvironments by Dynamic Optical Projection Stereolithography," *Adv. Mater.*, vol. 24, pp. 4266–4270, aug 2012.
- [86] N. E. Fedorovich, H. M. Wijnberg, W. J. Dhert, and J. Alblas, "Distinct tissue formation by heterogeneous printing of osteo-and endothelial progenitor cells," *Tissue Eng. - Part A*, vol. 17, no. 15-16, pp. 2113–2121, 2011.

- [87] J. W. Lee, Y.-J. Choi, W.-J. Yong, F. Pati, J.-H. Shim, K. S. Kang, I.-H. Kang, J. Park, and D.-W. Cho, “Development of a 3d cell printed construct considering angiogenesis for liver tissue engineering,” *Biofabrication*, vol. 8, no. 1, p. 015007, 2016.
- [88] Y. Zheng, J. Chen, M. Craven, N. W. Choi, S. Totorica, A. Diaz-Santana, P. Kermani, B. Hempstead, C. Fischbach-Teschl, J. A. López, and A. D. Stroock, “In vitro microvessels for the study of angiogenesis and thrombosis,” *Proc. Natl. Acad. Sci. U. S. A.*, vol. 109, no. 24, pp. 9342–9347, 2012.
- [89] D. B. Kolesky, K. A. Homan, M. A. Skylar-Scott, and J. A. Lewis, “Three-dimensional bioprinting of thick vascularized tissues,” *Proceedings of the national academy of sciences*, vol. 113, no. 12, pp. 3179–3184, 2016.
- [90] X. Ma, B. Huang, X. Zhao, Y. Wang, Q. Chang, S. Qiu, X. Fu, and G. Wang, “Comparisons of spark-charge bubble dynamics near the elastic and rigid boundaries,” *Ultrasonics sonochemistry*, vol. 43, pp. 80–90, 2018.
- [91] K. Tan and S. Yeo, “Bubble dynamics and cavitation intensity in millimeter-scale channels under an ultrasonic horn,” *Ultrasonics sonochemistry*, vol. 58, p. 104666, 2019.
- [92] L. Yusuf, M. D. Symes, and P. Prentice, “Characterising the cavitation activity generated by an ultrasonic horn at varying tip-vibration amplitudes,” *Ultrasonics Sonochemistry*, vol. 70, p. 105273, 2021.
- [93] R. Petkovšek and P. Gregorčič, “A laser probe measurement of cavitation bubble dynamics improved by shock wave detection and compared to shadow photography,” *J. Appl. Phys.*, vol. 102, no. 4, p. 044909, 2007.
- [94] B. Han, K. Köhler, K. Jungnickel, R. Mettin, W. Lauterborn, and A. Vogel, “Dynamics of laser-induced bubble pairs,” *Journal of Fluid Mechanics*, vol. 771, pp. 706–742, 2015.
- [95] X. Liu, Y. Hou, X. Liu, J. He, J. Lu, and X. Ni, “Oscillation characteristics of a laser-induced cavitation bubble in water at different temperatures,” *Optik*, vol. 122, no. 14, pp. 1254–1257, 2011.

- [96] E.-A. Brujan and A. Vogel, “Stress wave emission and cavitation bubble dynamics by nanosecond optical breakdown in a tissue phantom,” *Journal of Fluid Mechanics*, vol. 558, pp. 281–308, 2006.
- [97] T.-H. Wu, Y. Chen, S.-Y. Park, J. Hong, T. Teslaa, J. F. Zhong, D. Di Carlo, M. A. Teitell, and P.-Y. Chiou, “Pulsed laser triggered high speed microfluidic fluorescence activated cell sorter,” *Lab on a Chip*, vol. 12, no. 7, pp. 1378–1383, 2012.
- [98] T.-H. Wu, L. Gao, Y. Chen, K. Wei, and P.-Y. Chiou, “Pulsed laser triggered high speed microfluidic switch,” *Applied Physics Letters*, vol. 93, no. 14, p. 144102, 2008.
- [99] Y. Chen, T.-H. Wu, Y.-C. Kung, M. A. Teitell, and P.-Y. Chiou, “3d pulsed laser-triggered high-speed microfluidic fluorescence-activated cell sorter,” *Analyst*, vol. 138, no. 24, pp. 7308–7315, 2013.
- [100] T.-h. Han and J. J. Yoh, “A laser based reusable microjet injector for transdermal drug delivery,” *Journal of Applied Physics*, vol. 107, no. 10, p. 103110, 2010.
- [101] H.-j. Jang, H. Yu, S. Lee, E. Hur, Y. Kim, S.-H. Lee, N. Kang, and J. J. Yoh, “Towards clinical use of a laser-induced microjet system aimed at reliable and safe drug delivery,” *Journal of biomedical optics*, vol. 19, no. 5, p. 058001, 2014.
- [102] J. J. Yoh, H.-j. Jang, M.-a. Park, T.-h. Han, and J.-m. Hah, “A laser syringe aimed at delivering drug into the outer layer of human skin,” in *AIP Conference Proceedings*, vol. 1464, pp. 524–531, American Institute of Physics, 2012.
- [103] J. J. Yoh, H.-j. Jang, M.-a. Park, T.-h. Han, and J.-m. Hah, “A bio-ballistic micro-jet for drug injection into animal skin using a nd: Yag laser,” *Shock Waves*, vol. 26, no. 1, pp. 39–43, 2016.
- [104] T.-h. Han, J.-m. Hah, and J. J. Yoh, “Drug injection into fat tissue with a laser based microjet injector,” *Journal of Applied Physics*, vol. 109, no. 9, p. 093105, 2011.

- [105] H.-c. Ham, H.-j. Jang, and J. J. Yoh, “A check valve controlled laser-induced microjet for uniform transdermal drug delivery,” *AIP Advances*, vol. 7, no. 12, p. 125206, 2017.
- [106] C. Boutopoulos, P. Andreakou, D. Kafetzopoulos, S. Chatzandroulis, and I. Zergioti, “Direct laser printing of biotin microarrays on low temperature oxide on si substrates,” *physica status solidi (a)*, vol. 205, no. 11, pp. 2505–2508, 2008.
- [107] M. Mohammadzadeh, J. M. Mercado, and C.-D. Ohl, “Bubble dynamics in laser lithotripsy,” in *Journal of Physics: Conference series*, vol. 656, p. 012004, IOP Publishing, 2015.
- [108] L. A. Hardy, J. D. Kennedy, C. R. Wilson, P. B. Irby, and N. M. Fried, “Analysis of thulium fiber laser induced bubble dynamics for ablation of kidney stones,” *Journal of biophotonics*, vol. 10, no. 10, pp. 1240–1249, 2017.
- [109] D. A. Gonzalez, L. A. Hardy, T. C. Hutchens, P. B. Irby, and N. M. Fried, “Thulium fiber laser-induced vapor bubble dynamics using bare, tapered, ball, hollow steel, and muzzle brake fiber optic tips,” *Optical Engineering*, vol. 57, no. 3, p. 036106, 2018.
- [110] T. Lee, W. Luo, Q. Li, H. Demirci, and L. J. Guo, “Laser-induced focused ultrasound for cavitation treatment: Toward high-precision invisible sonic scalpel,” *Small*, vol. 13, no. 38, p. 1701555, 2017.
- [111] Y. Chen, T.-H. Wu, and P.-Y. Chiou, “Scanning laser pulses driven microfluidic peristaltic membrane pump,” *Lab on a Chip*, vol. 12, no. 10, pp. 1771–1774, 2012.
- [112] R. Dijkink and C.-D. Ohl, “Laser-induced cavitation based micropump,” *Lab on a Chip*, vol. 8, no. 10, pp. 1676–1681, 2008.
- [113] S.-Y. Park, T.-H. Wu, Y. Chen, M. A. Teitell, and P.-Y. Chiou, “High-speed droplet generation on demand driven by pulse laser-induced cavitation,” *Lab on a Chip*, vol. 11, no. 6, pp. 1010–1012, 2011.
- [114] Y. Tagawa, N. Oudalov, C. W. Visser, I. R. Peters, D. van der Meer, C. Sun, A. Prosperetti, and D. Lohse, “Highly focused supersonic microjets,” *Physical review X*, vol. 2, no. 3, p. 031002, 2012.

- [115] Y. Tagawa, N. Oudalov, A. El Ghalbzouri, C. Sun, and D. Lohse, “Needle-free injection into skin and soft matter with highly focused microjets,” *Lab on a Chip*, vol. 13, no. 7, pp. 1357–1363, 2013.
- [116] P. Rohilla and J. Marston, “Feasibility of laser induced jets in needle free jet injections,” *International journal of pharmaceutics*, vol. 589, p. 119714, 2020.
- [117] J. Krizek, F. De Goumoëns, P. Delrot, and C. Moser, “Needle-free delivery of fluids from compact laser-based jet injector,” *Lab on a Chip*, vol. 20, no. 20, pp. 3784–3791, 2020.
- [118] P. Delrot, S. P. Hauser, J. Krizek, and C. Moser, “Depth-controlled laser-induced jet injection for direct three-dimensional liquid delivery,” *Applied Physics A*, vol. 124, no. 9, pp. 1–8, 2018.
- [119] J. Krizek, P. Delrot, and C. Moser, “Repetitive regime of highly focused liquid microjets for needle-free injection,” *Scientific reports*, vol. 10, no. 1, pp. 1–9, 2020.
- [120] P. Delrot, M. A. Modestino, F. Gallaire, D. Psaltis, and C. Moser, “Inkjet printing of viscous monodisperse microdroplets by laser-induced flow focusing,” *Physical Review Applied*, vol. 6, no. 2, p. 024003, 2016.
- [121] M. SHAN, B. CHEN, C. YAO, Q. HAN, C. ZHU, and Y. YANG, “Electric characteristic and cavitation bubble dynamics using underwater pulsed discharge,” *Plasma Sci. Technol.*, vol. 21, p. 074002, jul 2019.
- [122] P. Gregorčič, R. Petkovšek, and J. Možina, “Investigation of a cavitation bubble between a rigid boundary and a free surface,” *Journal of applied physics*, vol. 102, no. 9, p. 094904, 2007.
- [123] B. Han, K. Köhler, K. Jungnickel, R. Mettin, W. Lauterborn, and A. Vogel, “Dynamics of laser-induced bubble pairs,” *J. Fluid Mech.*, vol. 771, pp. 706–742, may 2015.
- [124] K. Murakami, *Spherical and Non-spherical Bubble Dynamics in Soft Matter*. PhD thesis, University of Michigan, 2020.

- [125] M. S. Plesset and A. Prosperetti, “Bubble dynamics and cavitation,” *Annual review of fluid mechanics*, vol. 9, no. 1, pp. 145–185, 1977.
- [126] J. B. Keller and M. Miksis, “Bubble oscillations of large amplitude,” *J. Acoust. Soc. Am.*, vol. 68, pp. 628–633, aug 1980.
- [127] Z. Hu, J. Xu, and T. A. Bigelow, “Comparison of Gilmore-Akulichev’s, Keller-Miksis’s and Rayleigh-Plesset’s equations on therapeutic ultrasound bubble cavitation,” *J. Acoust. Soc. Am.*, vol. 136, pp. 2280–2280, oct 2014.
- [128] C. C. Church, “A theoretical study of cavitation generated by an extracorporeal shock wave lithotripter,” *J. Acoust. Soc. Am.*, vol. 86, pp. 215–227, jul 1989.
- [129] R. A. Van Gorder, “Dynamics of the Rayleigh–Plesset equation modelling a gas-filled bubble immersed in an incompressible fluid,” *J. Fluid Mech.*, vol. 807, pp. 478–508, nov 2016.
- [130] E. Klaseboer and B. C. Khoo, “A modified Rayleigh–Plesset model for a non-spherically symmetric oscillating bubble with applications to boundary integral methods,” *Eng. Anal. Bound. Elem.*, vol. 30, pp. 59–71, jan 2006.
- [131] E. M. Englert, A. McCarn, and G. A. Williams, “Luminescence from laser-induced bubbles in water-glycerol mixtures: Effect of viscosity,” *Phys. Rev. E*, vol. 83, p. 046306, apr 2011.
- [132] F. Hegedűs, S. Koch, W. Garen, Z. Pandula, G. Paál, L. Kullmann, and U. Teubner, “The effect of high viscosity on compressible and incompressible Rayleigh–Plesset-type bubble models,” *Int. J. Heat Fluid Flow*, vol. 42, pp. 200–208, aug 2013.
- [133] F. A. Godínez and M. Navarrete, “Effect of liquid density on the Rayleigh-Taylor instability of sonoluminescing bubbles,” *Rev. Mex. Física*, vol. 59, no. February, pp. 76–82, 2013.
- [134] B. Rahmatizadeh, M. T. H. Beheshti, M. Azadegan, and M. Najafi, “Stability analysis and sliding mode control of a single spherical bubble described by Keller–Miksis equation,” *Int. J. Dyn. Control*, vol. 9, pp. 1757–1764, dec 2021.

- [135] K. Johansen, J. H. Song, and P. Prentice, “Validity of the Keller-Miksis equation for “non-stable” cavitation and the acoustic emissions generated,” in *2017 IEEE Int. Ultrason. Symp.*, pp. 1–4, IEEE, sep 2017.
- [136] E. Zilonova, M. Solovchuk, and T. Sheu, “Bubble dynamics in viscoelastic soft tissue in high-intensity focal ultrasound thermal therapy,” *Ultrason. Sonochem.*, vol. 40, pp. 900–911, jan 2018.
- [137] M. de Icaza-Herrera, F. Fernández, and A. M. Loske, “Combined short and long-delay tandem shock waves to improve shock wave lithotripsy according to the Gilmore–Akulichev theory,” *Ultrasonics*, vol. 58, pp. 53–59, apr 2015.
- [138] T. Požar, V. Agrež, *et al.*, “Laser-induced cavitation bubbles and shock waves in water near a concave surface,” *Ultrasonics Sonochemistry*, vol. 73, p. 105456, 2021.
- [139] E.-A. Brujan, T. Noda, A. Ishigami, T. Ogasawara, and H. Takahira, “Dynamics of laser-induced cavitation bubbles near two perpendicular rigid walls,” *Journal of Fluid Mechanics*, vol. 841, pp. 28–49, 2018.
- [140] E.-A. Brujan, K. Nahen, P. Schmidt, and A. Vogel, “Dynamics of laser-induced cavitation bubbles near an elastic boundary,” *Journal of Fluid Mechanics*, vol. 433, pp. 251–281, 2001.
- [141] D. Horvat, U. Orthaber, J. Schille, L. Hartwig, U. Löschner, A. Vrečko, *et al.*, “Laser-induced bubble dynamics inside and near a gap between a rigid boundary and an elastic membrane,” *International Journal of Multiphase Flow*, vol. 100, pp. 119–126, 2018.
- [142] W. Lauterborn, C. Lechner, M. Koch, and R. Mettin, “Bubble models and real bubbles: Rayleigh and energy-deposit cases in a tait-compressible liquid,” *IMA Journal of Applied Mathematics*, vol. 83, no. 4, pp. 556–589, 2018.
- [143] C. Lechner, M. Koch, W. Lauterborn, and R. Mettin, “Pressure and tension waves from bubble collapse near a solid boundary: A numerical approach,” *The Journal of the Acoustical Society of America*, vol. 142, no. 6, pp. 3649–3659, 2017.

- [144] K. Sasaki, T. Nakano, W. Soliman, and N. Takada, “Effect of pressurization on the dynamics of a cavitation bubble induced by liquid-phase laser ablation,” *Applied Physics Express*, vol. 2, no. 4, p. 046501, 2009.
- [145] B.-b. Li, H.-c. Zhang, J. Lu, and X.-w. Ni, “Experimental investigation of the effect of ambient pressure on laser-induced bubble dynamics,” *Optics & Laser Technology*, vol. 43, no. 8, pp. 1499–1503, 2011.
- [146] M. S. Brown, C. F. Brasz, Y. Ventikos, and C. B. Arnold, “Impulsively actuated jets from thin liquid films for high-resolution printing applications,” *Journal of Fluid Mechanics*, vol. 709, pp. 341–370, 2012.
- [147] A. Kalaitzis, M. Makrygianni, I. Theodorakos, A. Hatzia Apostolou, S. Melamed, A. Kabla, F. de la Vega, and I. Zergioti, “Jetting dynamics of newtonian and non-newtonian fluids via laser-induced forward transfer: Experimental and simulation studies,” *Applied Surface Science*, vol. 465, pp. 136–142, 2019.
- [148] N. Kyriazis, P. Koukouvinis, and M. Gavaises, “Numerical investigations on bubble-induced jetting and shock wave focusing: application on a needle-free injection,” *Proceedings of the Royal Society A*, vol. 475, no. 2222, p. 20180548, 2019.
- [149] I. R. Peters, Y. Tagawa, N. Oudalov, C. Sun, A. Prosperetti, D. Lohse, and D. van der Meer, “Highly focused supersonic microjets: numerical simulations,” *Journal of fluid mechanics*, vol. 719, pp. 587–605, 2013.
- [150] A. Dadvand, M. T. Shervani-Tabar, and B. C. Khoo, “A note on spark bubble drop-on-demand droplet generation: simulation and experiment,” *The International Journal of Advanced Manufacturing Technology*, vol. 56, no. 1, pp. 245–259, 2011.
- [151] K. Sato, Y. Tomita, and A. Shima, “Numerical analysis of a gas bubble near a rigid boundary in an oscillatory pressure field,” *The Journal of the Acoustical Society of America*, vol. 95, no. 5, pp. 2416–2424, 1994.
- [152] E. Ory, H. Yuan, A. Prosperetti, S. Popinet, and S. Zaleski, “Growth and collapse of a vapor bubble in a narrow tube,” *Physics of fluids*, vol. 12, no. 6, pp. 1268–1277, 2000.

- [153] M. Mohammadzadeh, F. Li, and C.-D. Ohl, “Shearing flow from transient bubble oscillations in narrow gaps,” *Physical Review Fluids*, vol. 2, no. 1, p. 014301, 2017.
- [154] C. Turangan, A. Jamaluddin, G. Ball, and T. Leighton, “Free-lagrange simulations of the expansion and jetting collapse of air bubbles in water,” *Journal of Fluid Mechanics*, vol. 598, pp. 1–25, 2008.
- [155] A. Lopez-Villa, A. Medina, and F. Higuera, “Bubble growth by injection of gas into viscous liquids in cylindrical and conical tubes,” *Physics of Fluids*, vol. 23, no. 10, p. 102102, 2011.
- [156] H. Ebrahimi Orimi, L. Arreaza, S. Narayanswamy, and C. Boutopoulos, “Self-limited nanosecond laser-induced bubble growth in sealed containers,” *Appl. Phys. Lett.*, vol. 119, p. 064101, aug 2021.
- [157] H. E. Orimi, S. Narayanswamy, and C. Boutopoulos, “Hybrid analytical/numerical modeling of nanosecond laser-induced micro-jets generated by liquid confining devices,” *Journal of Fluids and Structures*, vol. 98, p. 103079, 2020.
- [158] H. E. Orimi, S. S. H. Kolkooh, E. Hooker, S. Narayanswamy, B. Larrivé, and C. Boutopoulos, “Drop-on-demand cell bioprinting via laser induced side transfer (list),” *Scientific reports*, vol. 10, no. 1, pp. 1–9, 2020.
- [159] K. Rink, G. Delacréta, and R. Salathé, “Fragmentation process induced by microsecond laser pulses during lithotripsy,” *Applied physics letters*, vol. 61, no. 3, pp. 258–260, 1992.
- [160] B. Dollet, P. Marmottant, and V. Garbin, “Bubble dynamics in soft and biological matter,” *Annual Review of Fluid Mechanics*, vol. 51, pp. 331–355, 2019.
- [161] T. Fourest, J.-M. Laurens, E. Deletombe, J. Dupas, and M. Arrigoni, “Confined rayleigh–plesset equation for hydrodynamic ram analysis in thin-walled containers under ballistic impacts,” *Thin-Walled Structures*, vol. 86, pp. 67–72, 2015.

- [162] A. Vogel, J. Noack, K. Nahen, D. Theisen, S. Busch, U. Parlitz, D. Hammer, G. Noojin, B. Rockwell, and R. Birngruber, “Energy balance of optical breakdown in water at nanosecond to femtosecond time scales.,” *Applied Physics B: Lasers & Optics*, vol. 68, no. 2, 1999.
- [163] A. Vogel, S. Busch, and U. Parlitz, “Shock wave emission and cavitation bubble generation by picosecond and nanosecond optical breakdown in water,” *The Journal of the Acoustical Society of America*, vol. 100, no. 1, pp. 148–165, 1996.
- [164] A. Philipp and W. Lauterborn, “Cavitation erosion by single laser-produced bubbles,” *Journal of fluid mechanics*, vol. 361, pp. 75–116, 1998.
- [165] E. Brujan, *Cavitation in Non-Newtonian fluids: with biomedical and bioengineering applications*. Springer Science & Business Media, 2010.
- [166] I. Aplitz and A. Vogel, “Material ejection in nanosecond er: Yag laser ablation of water, liver, and skin,” *Applied Physics A*, vol. 81, no. 2, pp. 329–338, 2005.
- [167] C. Boutopoulos, D. P. Papageorgiou, I. Zergioti, and A. G. Papathanasiou, “Sticking of droplets on slippery superhydrophobic surfaces by laser induced forward transfer,” *Applied Physics Letters*, vol. 103, no. 2, p. 024104, 2013.
- [168] K. Zhang, A. Jian, X. Zhang, Y. Wang, Z. Li, and H.-y. Tam, “Laser-induced thermal bubbles for microfluidic applications,” *Lab on a Chip*, vol. 11, no. 7, pp. 1389–1395, 2011.
- [169] H. Tan, “An adaptive mesh refinement based flow simulation for free-surfaces in thermal inkjet technology,” *International Journal of Multiphase Flow*, vol. 82, pp. 1–16, 2016.
- [170] I. Akhatov, O. Lindau, A. Topolnikov, R. Mettin, N. Vakhitova, and W. Lauterborn, “Collapse and rebound of a laser-induced cavitation bubble,” *Physics of Fluids*, vol. 13, no. 10, pp. 2805–2819, 2001.
- [171] A. De Bonis, M. Sansone, L. D’Alessio, A. Galasso, A. Santagata, and R. Teghil, “Dynamics of laser-induced bubble and nanoparticles generation during ultra-short laser ablation of pd in liquid,” *Journal of Physics D: Applied Physics*, vol. 46, no. 44, p. 445301, 2013.

- [172] F. Hegedűs, S. Koch, W. Garen, Z. Pandula, G. Paál, L. Kullmann, and U. Teubner, “The effect of high viscosity on compressible and incompressible rayleigh–plesset-type bubble models,” *International journal of heat and fluid flow*, vol. 42, pp. 200–208, 2013.
- [173] J. Lam, J. Lombard, C. Dujardin, G. Ledoux, S. Merabia, and D. Amans, “Dynamical study of bubble expansion following laser ablation in liquids,” *Applied Physics Letters*, vol. 108, no. 7, p. 074104, 2016.
- [174] W. Soliman, T. Nakano, N. Takada, and K. Sasaki, “Modification of rayleigh–plesset theory for reproducing dynamics of cavitation bubbles in liquid-phase laser ablation,” *Japanese Journal of Applied Physics*, vol. 49, no. 11R, p. 116202, 2010.
- [175] Y. Tomita, M. Tsubota, K. Nagane, and N. An-Naka, “Behavior of laser-induced cavitation bubbles in liquid nitrogen,” *Journal of Applied Physics*, vol. 88, no. 10, pp. 5993–6001, 2000.
- [176] L. Xiu-Mei, H. Jie, L. Jian, and N. Xiao-Wu, “Growth and collapse of laser-induced bubbles in glycerol–water mixtures,” *Chinese Physics B*, vol. 17, no. 7, p. 2574, 2008.
- [177] S. S. Paulsen, “Pressure systems stored-energy threshold risk analysis,” tech. rep., Pacific Northwest National Lab.(PNNL), Richland, WA (United States), 2009.
- [178] S. Egerev, “In search of a noncontact underwater acoustic source,” *Acoustical Physics*, vol. 49, no. 1, pp. 51–61, 2003.
- [179] M. S. Hutson and X. Ma, “Plasma and cavitation dynamics during pulsed laser microsurgery in vivo,” *Physical review letters*, vol. 99, no. 15, p. 158104, 2007.
- [180] C. Sun, E. Can, R. Dijkink, D. Lohse, and A. Prosperetti, “Growth and collapse of a vapour bubble in a microtube: the role of thermal effects,” *Journal of fluid mechanics*, vol. 632, pp. 5–16, 2009.
- [181] V. Venugopalan, A. Guerra III, K. Nahen, and A. Vogel, “Role of laser-induced plasma formation in pulsed cellular microsurgery and micromanipulation,” *Physical review letters*, vol. 88, no. 7, p. 078103, 2002.

- [182] A. Vogel, S. Busch, K. Jungnickel, and R. Birngruber, “Mechanisms of intraocular photodisruption with picosecond and nanosecond laser pulses,” *Lasers in surgery and medicine*, vol. 15, no. 1, pp. 32–43, 1994.
- [183] J. R. Macdonald, “Some simple isothermal equations of state,” *Reviews of Modern Physics*, vol. 38, no. 4, p. 669, 1966.
- [184] A. Vogel, W. Lauterborn, and R. Timm, “Optical and acoustic investigations of the dynamics of laser-produced cavitation bubbles near a solid boundary,” *Journal of Fluid Mechanics*, vol. 206, pp. 299–338, 1989.
- [185] D. Obreschkow, M. Tinguely, N. Dorsaz, P. Kobel, A. De Bosset, and M. Farhat, “The quest for the most spherical bubble: experimental setup and data overview,” *Experiments in Fluids*, vol. 54, no. 4, pp. 1–18, 2013.
- [186] B. Thornton, T. Takahashi, T. Ura, and T. Sakka, “Cavity formation and material ablation for single-pulse laser-ablated solids immersed in water at high pressure,” *Applied Physics Express*, vol. 5, no. 10, p. 102402, 2012.
- [187] J. Tomko, S. O’Malley, C. Trout, J. Naddeo, R. Jimenez, J. C. Griepenburg, W. Soliman, and D. Bubb, “Cavitation bubble dynamics and nanoparticle size distributions in laser ablation in liquids,” *Colloids and Surfaces A: Physicochemical and Engineering Aspects*, vol. 522, pp. 368–372, 2017.
- [188] J. Schoppink and D. F. Rivas, “Jet injectors: Perspectives for small volume delivery with lasers,” *Advanced drug delivery reviews*, p. 114109, 2022.
- [189] K. Roversi, H. Ebrahimi Orimi, M. Falchetti, E. Lummertz da Rocha, S. Talbot, and C. Boutopoulos, “Bioprinting of Adult Dorsal Root Ganglion (DRG) Neurons Using Laser-Induced Side Transfer (LIST),” *Micromachines*, vol. 12, p. 865, jul 2021.
- [190] I. T. Ozbolat, *3D Bioprinting: fundamentals, principles and applications*. Academic Press, 2016.
- [191] T. Xu, C. A. Gregory, P. Molnar, X. Cui, S. Jalota, S. B. Bhaduri, and T. Boland, “Viability and electrophysiology of neural cell structures generated

- by the inkjet printing method,” *Biomaterials*, vol. 27, no. 19, pp. 3580–3588, 2006.
- [192] A. Antoshin, S. Churbanov, N. Minaev, D. Zhang, Y. Zhang, A. Shpichka, and P. Timashev, “Lift-bioprinting, is it worth it?,” *Bioprinting*, vol. 15, p. e00052, 2019.
- [193] A. Panwar and L. P. Tan, “Current status of bioinks for micro-extrusion-based 3d bioprinting,” *Molecules*, vol. 21, no. 6, p. 685, 2016.
- [194] N. R. Schiele, D. T. Corr, Y. Huang, N. A. Raof, Y. Xie, and D. B. Chrisey, “Laser-based direct-write techniques for cell printing,” *Biofabrication*, vol. 2, no. 3, p. 032001, 2010.
- [195] C. Boutopoulos, E. Touloupakis, I. Pezzotti, M. T. Giardi, and I. Zergioti, “Direct laser immobilization of photosynthetic material on screen printed electrodes for amperometric biosensor,” *Applied Physics Letters*, vol. 98, no. 9, p. 093703, 2011.
- [196] M. Colina, P. Serra, J. M. Fernández-Pradas, L. Sevilla, and J. L. Morenza, “Dna deposition through laser induced forward transfer,” *Biosensors and Bioelectronics*, vol. 20, no. 8, pp. 1638–1642, 2005.
- [197] S. Catros, F. Guillemot, A. Nandakumar, S. Ziane, L. Moroni, P. Habibovic, C. van Blitterswijk, B. Rousseau, O. Chassande, J. Amédée, *et al.*, “Layer-by-layer tissue microfabrication supports cell proliferation in vitro and in vivo,” *Tissue Engineering Part C: Methods*, vol. 18, no. 1, pp. 62–70, 2012.
- [198] L. Koch, A. Deiwick, S. Schlie, S. Michael, M. Gruene, V. Coger, D. Zychlinski, A. Schambach, K. Reimers, P. M. Vogt, *et al.*, “Skin tissue generation by laser cell printing,” *Biotechnology and bioengineering*, vol. 109, no. 7, pp. 1855–1863, 2012.
- [199] N. T. Kattamis, P. E. Purnick, R. Weiss, and C. B. Arnold, “Thick film laser induced forward transfer for deposition of thermally and mechanically sensitive materials,” *Applied Physics Letters*, vol. 91, no. 17, p. 171120, 2007.

- [200] J. A. Barron, D. B. Krizman, and B. R. Ringeisen, “Laser printing of single cells: statistical analysis, cell viability, and stress,” *Annals of biomedical engineering*, vol. 33, no. 2, pp. 121–130, 2005.
- [201] Y. Lin, G. Huang, Y. Huang, T.-R. J. Tzeng, and D. Chrisey, “Effect of laser fluence in laser-assisted direct writing of human colon cancer cell,” *Rapid Prototyping Journal*, 2010.
- [202] L. Koch, M. Gruene, C. Unger, and B. Chichkov, “Laser assisted cell printing,” *Current pharmaceutical biotechnology*, vol. 14, no. 1, pp. 91–97, 2013.
- [203] L. Koch, S. Kuhn, H. Sorg, M. Gruene, S. Schlie, R. Gaebel, B. Polchow, K. Reimers, S. Stoelting, N. Ma, *et al.*, “Laser printing of skin cells and human stem cells,” *Tissue Engineering Part C: Methods*, vol. 16, no. 5, pp. 847–854, 2010.
- [204] A. Kiyama, N. Endo, S. Kawamoto, C. Katsuta, K. Oida, A. Tanaka, and Y. Tagawa, “Visualization of penetration of a high-speed focused microjet into gel and animal skin,” *Journal of Visualization*, vol. 22, no. 3, pp. 449–457, 2019.
- [205] C. Boutopoulos, M. Chatzipetrou, A. G. Papathanasiou, and I. Zergioti, “Time-resolved imaging and immobilization study of biomaterials on hydrophobic and superhydrophobic surfaces by means of laser-induced forward transfer,” *Laser Physics Letters*, vol. 11, no. 10, p. 105603, 2014.
- [206] F. Kawecki, W. P. Clafshenkel, F. A. Auger, J.-M. Bourget, J. Fradette, and R. Devillard, “Self-assembled human osseous cell sheets as living biopapers for the laser-assisted bioprinting of human endothelial cells,” *Biofabrication*, vol. 10, no. 3, p. 035006, 2018.
- [207] A. Ovsianikov, M. Gruene, M. Pflaum, L. Koch, F. Maiorana, M. Wilhelmi, A. Haverich, and B. Chichkov, “Laser printing of cells into 3d scaffolds,” *Biofabrication*, vol. 2, no. 1, p. 014104, 2010.
- [208] B. Guillotin, A. Souquet, S. Catros, M. Duocastella, B. Pippenger, S. Bellance, R. Bareille, M. Rémy, L. Bordenave, J. Amédée, *et al.*, “Laser assisted bioprinting of engineered tissue with high cell density and microscale organization,” *Biomaterials*, vol. 31, no. 28, pp. 7250–7256, 2010.

- [209] N. Senturk, A. Bedir, B. Bilgici, F. Aydin, A. Okuyucu, Z. Ozmen, and A. Turanli, “Genotoxic effects of 1064-nm nd: Yag and 532-nm ktp lasers on fibroblast cell cultures,” *Clinical and Experimental Dermatology: Experimental dermatology*, vol. 35, no. 5, pp. 516–520, 2010.
- [210] E. Epifanov, E. Migal, F. Potemkin, A. Antoshin, V. Yusupov, and N. Minaev, “An apparatus for forming three-dimensional structures by the method of two-photon femtosecond polymerization with simultaneous spatiotemporal focusing,” *Instruments and Experimental Techniques*, vol. 64, no. 6, pp. 891–897, 2021.
- [211] H. Yang, K.-H. Yang, R. J. Narayan, and S. Ma, “Laser-based bioprinting for multilayer cell patterning in tissue engineering and cancer research,” *Essays in Biochemistry*, vol. 65, no. 3, pp. 409–416, 2021.
- [212] S. B. Balani, S. H. Ghaffar, M. Chougan, E. Pei, and E. Şahin, “Processes and materials used for direct writing technologies: A review,” *Results in Engineering*, vol. 11, p. 100257, 2021.
- [213] H.-G. Yi, H. Kim, J. Kwon, Y.-J. Choi, J. Jang, and D.-W. Cho, “Application of 3d bioprinting in the prevention and the therapy for human diseases,” *Signal Transduction and Targeted Therapy*, vol. 6, no. 1, pp. 1–17, 2021.
- [214] C. Tomasina, T. Bodet, C. Mota, L. Moroni, and S. Camarero-Espinosa, “Bio-printing Vasculature: Materials, Cells and Emergent Techniques,” *Materials (Basel)*, vol. 12, p. 2701, aug 2019.
- [215] J. Rouwkema and A. Khademhosseini, “Vascularization and Angiogenesis in Tissue Engineering: Beyond Creating Static Networks,” *Trends Biotechnol.*, vol. 34, pp. 733–745, sep 2016.
- [216] R. K. Jain, P. Au, J. Tam, D. G. Duda, and D. Fukumura, “Engineering vascularized tissue,” *Nat. Biotechnol.*, vol. 23, pp. 821–823, jul 2005.
- [217] A. Negro, T. Cherbuin, and M. P. Lutolf, “3D Inkjet Printing of Complex, Cell-Laden Hydrogel Structures,” *Sci. Rep.*, vol. 8, p. 17099, dec 2018.

- [218] J. A. Park, S. Yoon, J. Kwon, H. Now, Y. K. Kim, W.-J. Kim, J.-Y. Yoo, and S. Jung, “Freeform micropatterning of living cells into cell culture medium using direct inkjet printing,” *Sci. Rep.*, vol. 7, p. 14610, dec 2017.
- [219] Y. K. Kim, J. A. Park, W. H. Yoon, J. Kim, and S. Jung, “Drop-on-demand inkjet-based cell printing with 30-  $\mu$  m nozzle diameter for cell-level accuracy,” *Biomicrofluidics*, vol. 10, p. 064110, nov 2016.
- [220] T. J. Hinton, Q. Jallerat, R. N. Palchesko, J. H. Park, M. S. Grodzicki, H.-J. Shue, M. H. Ramadan, A. R. Hudson, and A. W. Feinberg, “Three-dimensional printing of complex biological structures by freeform reversible embedding of suspended hydrogels,” *Science advances*, vol. 1, no. 9, p. e1500758, 2015.
- [221] F. Maiullari, M. Costantini, M. Milan, V. Pace, M. Chirivì, S. Maiullari, A. Rainer, D. Baci, H. E.-S. Marei, D. Seliktar, *et al.*, “A multi-cellular 3d bioprinting approach for vascularized heart tissue engineering based on huvecs and ipsc-derived cardiomyocytes,” *Scientific reports*, vol. 8, no. 1, pp. 1–15, 2018.
- [222] L. Xu, M. Varkey, A. Jorgensen, J. Ju, Q. Jin, J. H. Park, Y. Fu, G. Zhang, D. Ke, W. Zhao, *et al.*, “Bioprinting small diameter blood vessel constructs with an endothelial and smooth muscle cell bilayer in a single step,” *Biofabrication*, vol. 12, no. 4, p. 045012, 2020.
- [223] M. A. Skylar-Scott, S. G. M. Uzel, L. L. Nam, J. H. Ahrens, R. L. Truby, S. Damaraju, and J. A. Lewis, “Biomufacturing of organ-specific tissues with high cellular density and embedded vascular channels,” *Sci. Adv.*, vol. 5, sep 2019.
- [224] W. Jia, P. S. Gungor-Ozkerim, Y. S. Zhang, K. Yue, K. Zhu, W. Liu, Q. Pi, B. Byambaa, M. R. Dokmeci, S. R. Shin, and A. Khademhosseini, “Direct 3D bioprinting of perfusable vascular constructs using a blend bioink,” *Biomaterials*, vol. 106, pp. 58–68, nov 2016.
- [225] D. Takagi, W. Lin, T. Matsumoto, H. Yaginuma, N. Hemmi, S. Hatada, and M. Seo, “High-precision three-dimensional inkjet technology for live cell bioprinting,” *International Journal of Bioprinting*, vol. 5, no. 2, 2019.

- [226] M. Yanez, J. Rincon, A. Dones, C. De Maria, R. Gonzales, and T. Boland, “In Vivo Assessment of Printed Microvasculature in a Bilayer Skin Graft to Treat Full-Thickness Wounds,” *Tissue Eng. Part A*, vol. 21, pp. 224–233, jan 2015.
- [227] J.-M. Bourget, O. K erour edan, M. Medina, M. R emy, N. B. Th ebaud, R. Bareille, O. Chassande, J. Am ed ee, S. Catros, and R. Devillard, “Patterning of Endothelial Cells and Mesenchymal Stem Cells by Laser-Assisted Bioprinting to Study Cell Migration,” *Biomed Res. Int.*, vol. 2016, pp. 1–7, 2016.
- [228] O. K erour edan, D. Hakobyan, M. R emy, S. Ziane, N. Dusserre, J. C. Fricain, S. Delmond, N. B. Th ebaud, and R. Devillard, “In situ prevascularization designed by laser-assisted bioprinting: Effect on bone regeneration,” *Biofabrication*, vol. 11, no. 4, 2019.
- [229] C. Viallard, C. Audiger, N. Popovic, N. Akla, K. Lanthier, I. Legault-Navarrete, H. Melichar, S. Costantino, S. Lesage, and B. Larriv ee, “Bmp9 signaling promotes the normalization of tumor blood vessels,” *Oncogene*, vol. 39, no. 14, pp. 2996–3014, 2020.
- [230] K. P. Mouillesseaux, D. S. Wiley, L. M. Saunders, L. A. Wylie, E. J. Kushner, D. C. Chong, K. M. Citrin, A. T. Barber, Y. Park, J.-D. Kim, *et al.*, “Notch regulates bmp responsiveness and lateral branching in vessel networks via smad6,” *Nature communications*, vol. 7, no. 1, pp. 1–12, 2016.
- [231] B. Larriv ee, C. Prahst, E. Gordon, R. del Toro, T. Mathivet, A. Duarte, M. Simons, and A. Eichmann, “ALK1 Signaling Inhibits Angiogenesis by Cooperating with the Notch Pathway,” *Dev. Cell*, vol. 22, pp. 489–500, mar 2012.
- [232] L. David, C. Mallet, S. Mazerbourg, J.-J. Feige, and S. Bailly, “Identification of BMP9 and BMP10 as functional activators of the orphan activin receptor-like kinase 1 (ALK1) in endothelial cells,” *Blood*, vol. 109, pp. 1953–1961, mar 2007.
- [233] A. Benn, C. Hiepen, M. Osterland, C. Sch utte, A. Zwijsen, and P. Knaus, “Role of bone morphogenetic proteins in sprouting angiogenesis: differential BMP receptor-dependent signaling pathways balance stalk vs . tip cell competence,” *FASEB J.*, vol. 31, pp. 4720–4733, nov 2017.

- [234] M. N. Nakatsu, R. C. Sainson, J. N. Aoto, K. L. Taylor, M. Aitkenhead, S. Pérez-del Pulgar, P. M. Carpenter, and C. C. Hughes, “Angiogenic sprouting and capillary lumen formation modeled by human umbilical vein endothelial cells (huvec) in fibrin gels: the role of fibroblasts and angiopoietin-1,” *Microvascular research*, vol. 66, no. 2, pp. 102–112, 2003.
- [235] D. Donovan, N. Brown, E. Bishop, and C. Lewis, “Comparison of three in vitro human ‘angiogenesis’ assays with capillaries formed in vivo,” *Angiogenesis*, vol. 4, no. 2, pp. 113–121, 2001.
- [236] A.-C. Vion, S. Alt, A. Klaus-Bergmann, A. Szymborska, T. Zheng, T. Perovic, A. Hammoutene, M. B. Oliveira, E. Bartels-Klein, I. Hollfinger, P.-E. Rautou, M. O. Bernabeu, and H. Gerhardt, “Primary cilia sensitize endothelial cells to BMP and prevent excessive vascular regression,” *J. Cell Biol.*, vol. 217, pp. 1651–1665, may 2018.
- [237] H. Hall, T. Baechi, and J. A. Hubbell, “Molecular properties of fibrin-based matrices for promotion of angiogenesis in vitro,” *Microvascular research*, vol. 62, no. 3, pp. 315–326, 2001.
- [238] K. T. Morin and R. T. Tranquillo, “In vitro models of angiogenesis and vasculogenesis in fibrin gel,” *Experimental cell research*, vol. 319, no. 16, pp. 2409–2417, 2013.
- [239] V. Ranta, T. Mikkola, O. Ylikorkala, L. Viinikka, and A. Orpana, “Reduced viability of human vascular endothelial cells cultured on matrigel™,” *Journal of cellular physiology*, vol. 176, no. 1, pp. 92–98, 1998.
- [240] G. Haralabopoulos, D. Grant, H. Kleinman, and M. Maragoudakis, “Thrombin promotes endothelial cell alignment in matrigel in vitro and angiogenesis in vivo,” *American Journal of Physiology-Cell Physiology*, vol. 273, no. 1, pp. C239–C245, 1997.
- [241] D. C. Darland and P. A. D’amore, “TGF $\beta$  is required for the formation of capillary-like structures in three-dimensional cocultures of 10T1/2 and endothelial cells,” *Angiogenesis*, vol. 4, no. 1, pp. 11–20, 2001.

- [242] A. P. Hall, “Review of the pericyte during angiogenesis and its role in cancer and diabetic retinopathy,” *Toxicol. Pathol.*, vol. 34, no. 6, pp. 763–775, 2006.
- [243] H. Zhao and J. C. Chappell, “Microvascular bioengineering: a focus on pericytes,” *J. Biol. Eng.*, vol. 13, p. 26, dec 2019.
- [244] K.-J. Oh, H. S. Yu, J. Park, H.-S. Lee, S. A. Park, and K. Park, “Co-culture of smooth muscle cells and endothelial cells on three-dimensional bioprinted polycaprolactone scaffolds for cavernosal tissue engineering,” *Aging Male*, vol. 23, pp. 830–835, dec 2020.
- [245] C. Piard, A. Jeyaram, Y. Liu, J. Caccamese, S. M. Jay, Y. Chen, and J. Fisher, “3D printed HUVECs/MSCs cocultures impact cellular interactions and angiogenesis depending on cell-cell distance,” *Biomaterials*, vol. 222, p. 119423, nov 2019.
- [246] M. Yeo and G. Kim, “Micro/nano-hierarchical scaffold fabricated using a cell electrospinning/3D printing process for co-culturing myoblasts and HUVECs to induce myoblast alignment and differentiation,” *Acta Biomater.*, vol. 107, pp. 102–114, apr 2020.

# Appendix A

## Supplementary of chapter 2

### A.1 Complete schematic of the experimental setup

Figure A.1 presents the complete schematic of the experimental setup for bubble dynamics study in sealed containers.

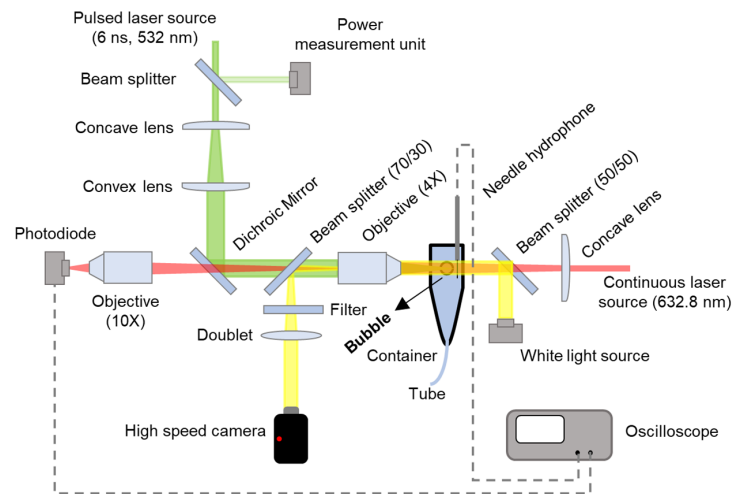


Figure A.1: Complete schematic of the experimental setup used to capture bubble dynamics and liquid pressure increase in sealed containers.

## A.2 Container preparation, degassing and sealing protocol

We used modified microcentrifuge tubes (MCT-170-C & MCT-060-C, Axygen Scientific, VWR) as containers. MCT-170-C served as 1.9 ml containers, MCT-060-C as 0.6 ml containers, and volume reduced (with partial glue (AA 3951, Loctite, Henkel) filling) MCT-060-C as 0.3 ml containers. First, the lids were separated from the tubes. Next, to build optical windows, we made side holes all the way through on the microcentrifuge tubes and installed round coverslips (CA48380-046, VWR) using a light cure adhesive (AA 3951, Loctite, Henkel). Furthermore, we installed a pressure release silicon tube (TYGON ND-100-65), which enabled lid closure underwater. The tube was attached to a 20-gauge metallic tube, fixed at the bottom of the modified microcentrifuge tube. A small hole has made to the lid to facilitate the insertion of the needle hydrophone. An O-ring and blu tack adhesive were appropriately added to so that the whole seals with the needle hydrophone inside the container (see step 10). The degassing protocol consisted in the following steps:

1. Coat containers with hydrophilic mixture (1,1,3,3-tetramethylguanidine was dissolved in ethylene glycol, 20 % (v/v)), leave for 2 hours in the mixture, then remove the mixture and leave to dry thoroughly for 6 hours.
2. Fill the container with distilled water and submerge in a 50 mL centrifuge tube also filled with distilled water.
3. Ensure that opening of the container is facing downward and the tube is full of water. Use syringe to fill the tube if necessary.
4. Place the centrifuge tube in the centrifuge for 5 minutes, at 1000 rpm
5. Obtain the tube from centrifuge, check to see if any bubble visible in the container. If bubbles are present, repeat 3 and 4, otherwise take the centrifuge tube out.
6. Fill a large clean beaker with  $\approx 800$  mL distilled water.
7. Put on powder-free gloves to prevent water contamination.

8. Carefully immerse the centrifuge tube in the large beaker and remove the modified microcentrifuge tube.
9. While the modified microcentrifuge tube chamber is submerged, ensure no gas bubbles in the modified microcentrifuge tube.
10. While underwater, insert the hydrophone into the lid opening. Ensure sealing and the then place the lid back to the modified microcentrifuge tube.
11. Tie a knot in the pressure release tube and tighten.
12. Remove the sealed container from the large beaker and wrap parafilm around the boundary of container body, hydrophone and lid.
13. Inspect again for air bubbles inside the chamber, if there are none, proceed.

### A.3 Cavitation threshold and energy balance

Figure A.2 shows cavitation threshold and energy balance versus laser pulse energy.

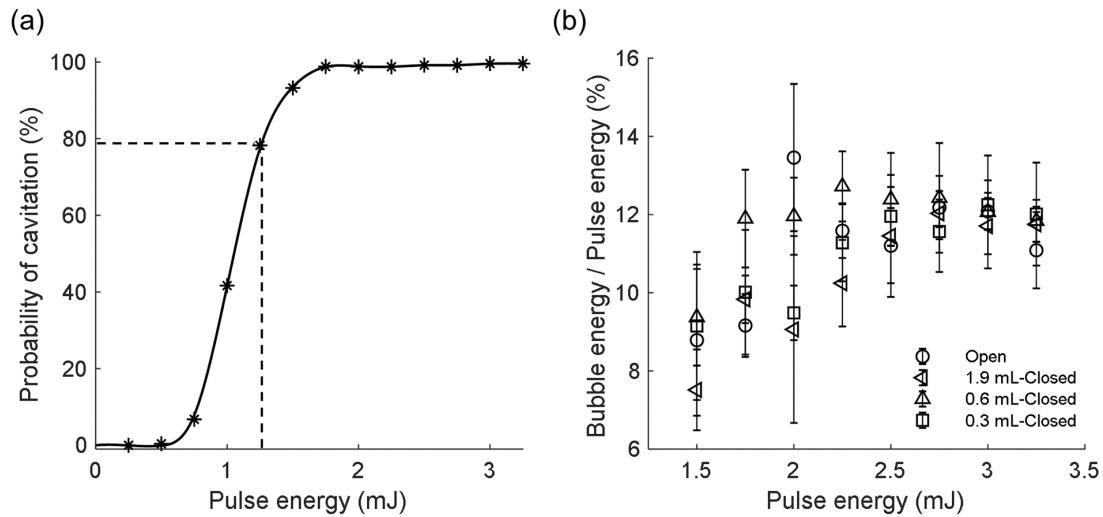


Figure A.2: (a) Cavitation probability versus pulse energy (b) Laser to bubble energy conversion versus laser pulse energy.

## A.4 Calculation of $R_0$

We considered a focused Gaussian beam to calculate the bubble initial radius,  $R_0$ . We assumed that  $R_0$  corresponds to the laser focal volume at which the laser irradiance exceeds the optical breakdown threshold. The optical breakdown threshold equals to  $2.5 \times 10^7$  mJ/cm<sup>2</sup> for ns laser ( $\lambda = 532$  nm) cavitation in water. We used a Gaussian function (Eq. 25) to calculate the irradiance distribution,  $I_G(r,z)$ :

$$I_G(r, z) = I_0 \left( \frac{W_0}{W_z} \right)^2 \exp\left[-2 \left( \frac{r^2}{W_z^2} \right)\right] \quad (25)$$

where ( $W_0$ ) is the spot size at the focus,  $r$  is the coordinate in the radial direction,  $W_z$  is the laser beam width at position  $z$  along the beam propagation axis, and  $I_0$  is the peak irradiance.  $W_0$  and  $I_0$  can be calculated using the following equations (Eq. 26 and Eq. 27):

$$W_0 = \frac{1.22 \lambda}{NA} \quad (26)$$

$$I_0 = 2I_{av} = \frac{2E_l}{\pi W_0^2} \quad (27)$$

Where  $\lambda$  is the laser wavelength, NA is the numerical aperture of the lens and  $E$  is the laser energy.  $W_z$  can be calculated by Eq. 28.

$$W = W_0 \sqrt{1 + \left( \frac{Z}{Z_r} \right)^2} \quad (28)$$

Where  $Z_r$  is the Rayleigh range (Eq. 29):

$$Z_r = \frac{\pi W_0^2}{\lambda} \quad (29)$$

Figure A.3a presents the irradiance distribution for  $\lambda = 532$  nm, NA = 0.1 and  $E = 1.75$  mJ. The equivalent focal volume considered for the  $R_0$  calculation is shown in Figure A.3b.

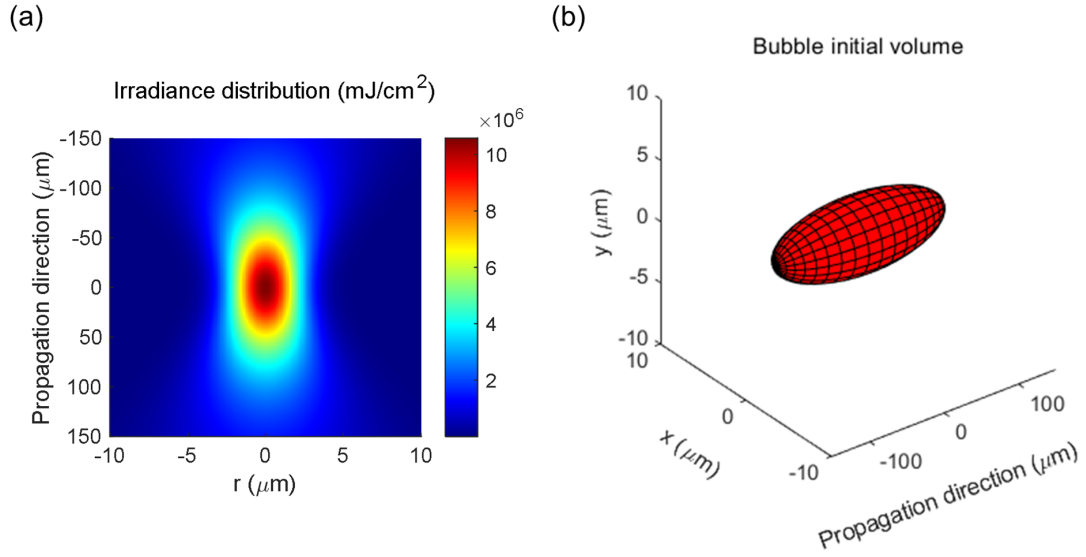


Figure A.3: (a) Irradiance distribution and (b) representation of the bubble initial volume for  $\lambda = 532$  nm, NA = 0.1 and  $E = 1.75$  mJ.

## A.5 Calculation of $P_g$

Knowing  $R_0$ , we varied  $P_g$  in the KM equation to get the best match between the lifetime recorded for open 50 mL reservoir and the calculated one by the KM equation for a given laser energy.

## A.6 Initial conditions and constants used in Keller-Miksis model

Table A.1 and table A.2 present the initial conditions ( $P_g$  and  $R_0$ ) and constants used in Keller-Miksis equation, respectively.

Table A.1: The initial conditions used in the Keller-Miksis model.

Laser energy (mJ)	$P_g$ (GPa)	$R_0$ ( $\mu\text{m}$ )
1.5	13.74	8.67
1.75	16.56	8.87
2	22.42	9.13
2.25	22.83	9.36
2.5	24.95	9.56
2.75	25.25	9.74
3	28.28	9.91
3.25	28.79	10.06

Table A.2: Constants used in the Keller-Miksis model.

Symbol	Description	Value
$\gamma$	Heat capacity ratio of vapor	1.33
$\nu$	Kinematic viscosity	$1.005 \times 10^{-6}$ ( $\text{m}^2/\text{s}$ )
$\sigma_l$	Surface tension	0.072 N/m
$\rho_l$	Liquid density	1000 $\text{kg}/\text{m}^3$
$P_v$	Saturated vapor pressure in the bubble	2330 Pa
$c$	Speed of sound in the liquid	1498 m/s

# Appendix B

## Supplementary of chapter 3

### **B.1 Video S1**

<https://bit.ly/3jzTXRG>

### **B.2 Video S2**

<https://bit.ly/3lKI3qG>

### **B.3 Video S3**

<https://bit.ly/3fGQgZn>

### **B.4 Video S4**

<https://bit.ly/37toevC>

# Appendix C

## Supplementary of chapter 4

### C.1 HUVECs migration post LIST-printing

Figure C.1 presents the migration of LIST-printed HUVECs.

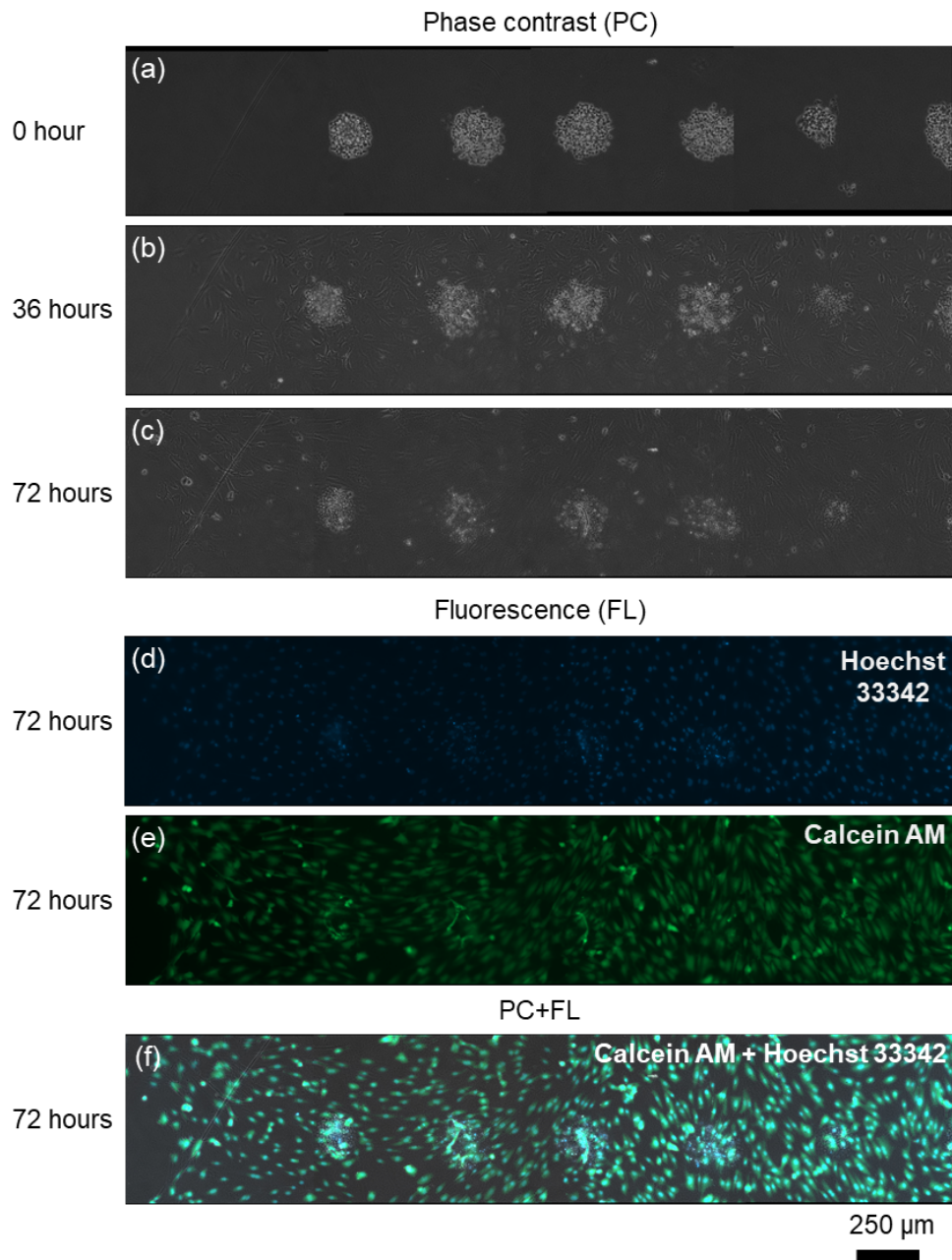


Figure C.1: HUVECs migration post LIST printing. (a-c) Phase contrast (PC) optical microscopy images of LIST-printed ( $100 \mu\text{J}$ ) HUVECs 0 h, 36 h and 72 h post printing. (d-e) Fluorescence (FL) microscopy and (f) combined BF/PC images 72 h post printing. Calcein AM (green) stains live cells and Hoechst 33342 (blue) stains all cells.

## C.2 Time point to the first frame

Figure C.2 shows the algorithm for computing the time point of the first frame.

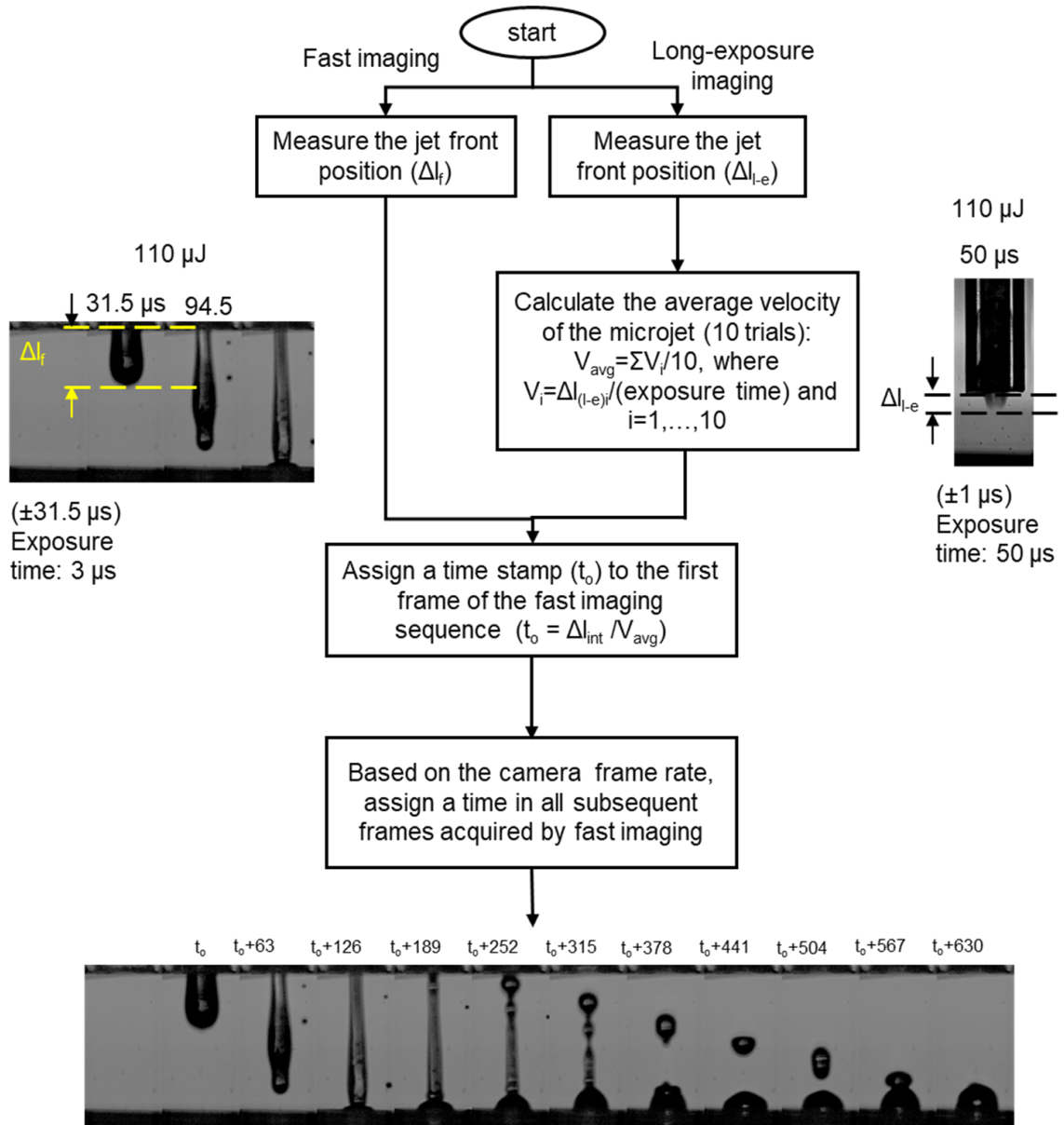


Figure C.2: Flow chart showing the steps implemented to assign a time point to the first frame of an image sequence acquired by fast imaging.

# Appendix D

## Supplementary of chapter 5

### D.1 Allura red dye toxicity test with dye exclusion method

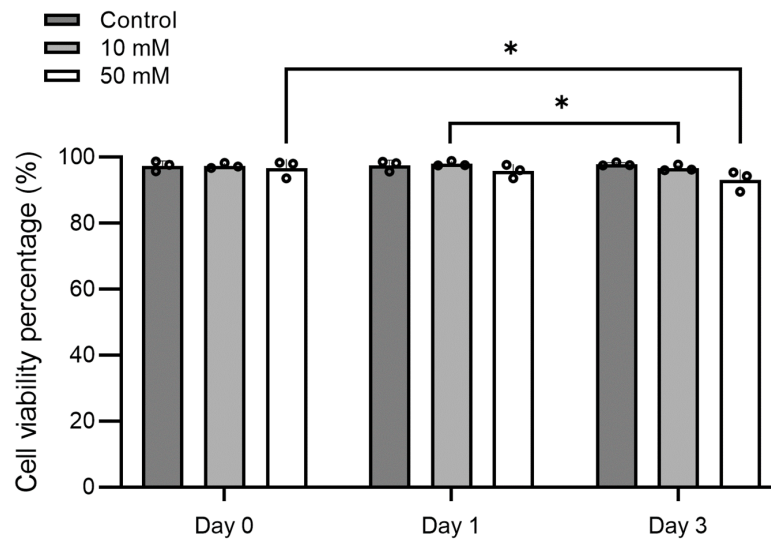


Figure D.1: Evaluating potential cytotoxicity effects for Allura red. The effect of the Allura red dye (10 mM and 50 mM) on HUVECs viability for 0-, 1- and 3-days post exposure. Error bars represent standard deviation (N=3). Two-way ANOVA test was used for comparison ( $P < 0.01 = *$ ).

## D.2 HUVECs network formation study on Fibrin, Matrigel and Matrigel/thrombin using conventional cell seeding

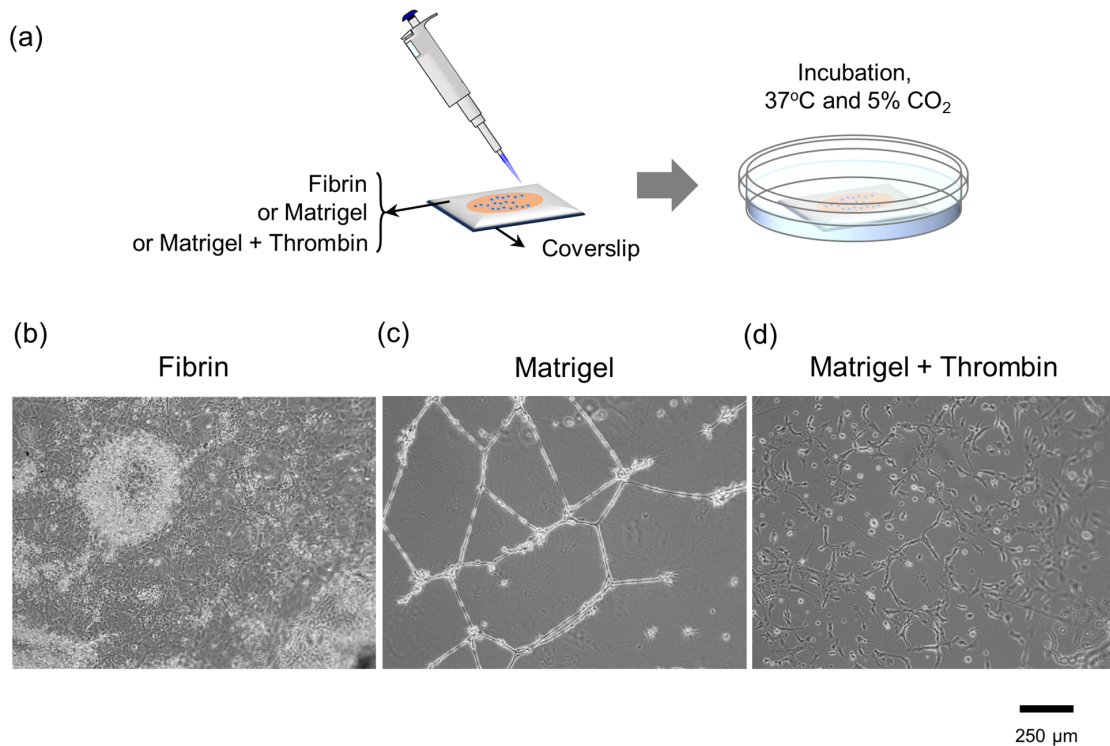


Figure D.2: HUVECs network formation on Fibrin, Matrigel and Matrigel/thrombin using conventional cell seeding, (a) schematic of conventional HUVECs seeding on three different matrices (left). After seeding the samples were placed into an incubator for further analysis (right); HUVECs (2-days after seeding) on (b) fibrin, (c) Matrigel, and (d) Matrigel/thrombin.

### D.3 Conventional assays for similar conditions show random or no network formation

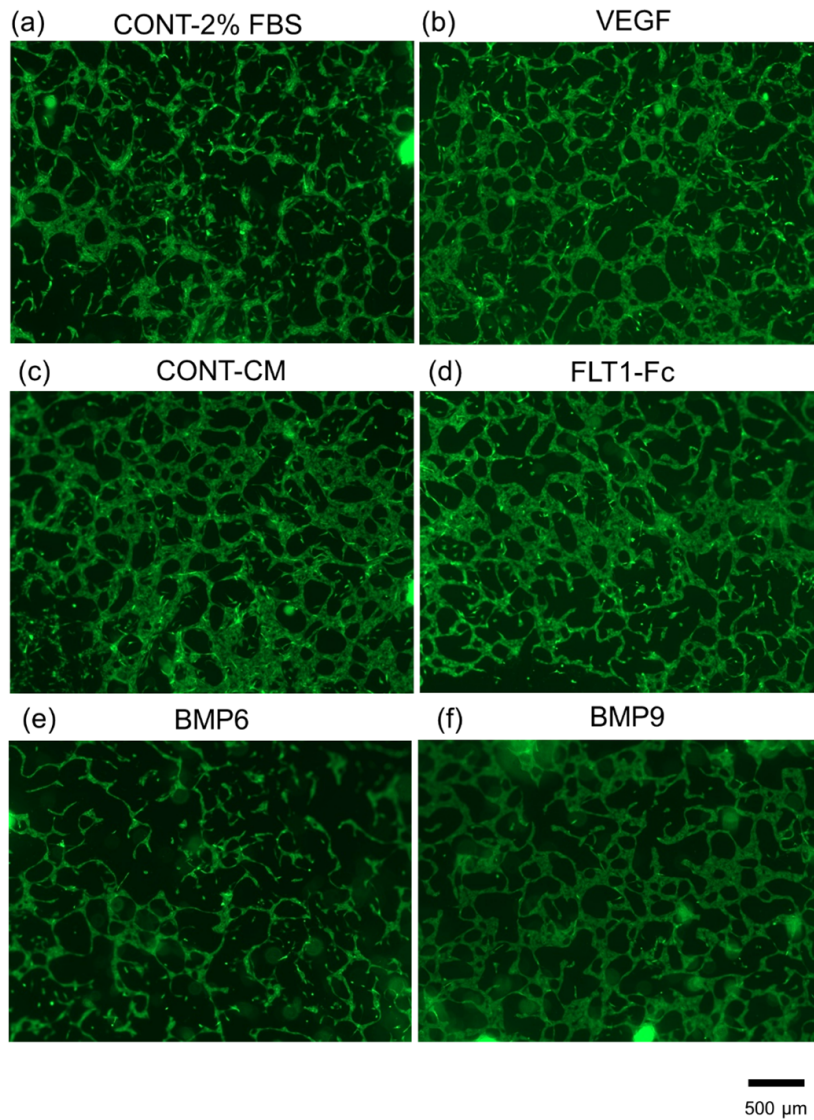


Figure D.3: Verifying the effect of anti- (BMP9 and FLT1-Fc) and pro- angiogenic (VEGF and BMP6) compounds using a conventional angiogenesis assay. Indicative fluorescence images of random HUVECs networks on fibrin stained with Calcein AM.

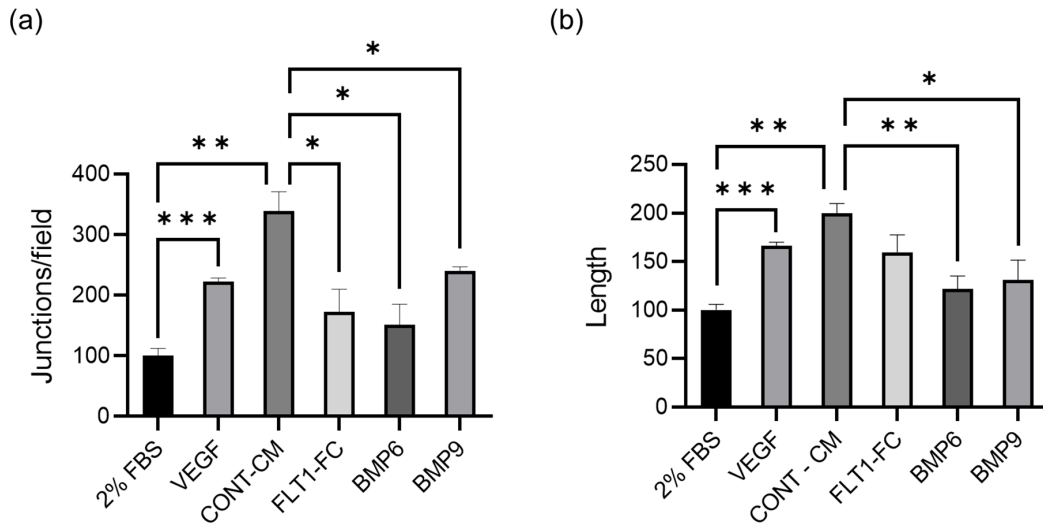


Figure D.4: Verifying the effect of anti- (BMP9 and FLT1-Fc) and pro- angiogenic (VEGF and BMP6) compounds using a conventional angiogenesis assay. (a) number of junctions per field and (b) total length in a conventional angiogenesis assay for treatments with by pro- and anti- angiogenic factors. Significant differences are indicated by asterisks ( $P < 0.05 = *$ ,  $P < 0.01 = **$  and  $P < 0.001 = ***$ ).